Investigation Of Hybrid Opto-electronic Devices Based On Graphene-Transition Metal Dichalcogenides Heterostructures

Thesis
Submitted For the Degree of

Doctor of Philosophy (Science)
in
Physics (Experimental)

By

Shubhrasish Mukherjee

Department of Physics

University of Calcutta

2023

Dedicated to baba……

List of Publications

1. High-Responsivity Gate-Tunable Ultraviolet−Visible Broadband Phototransistor Based on Graphene−WS_2 Mixed-Dimensional (2D-0D) Heterostructure, **Shubhrasish Mukherjee**, Didhiti Bhattacharya, Sumanti Patra, Sanjukta Paul, Rajib Kumar Mitra, Priya Mahadevan, Atindra Nath Pal and Samit Kumar Ray, ACS Appl. Mater. Interfaces 2022, 14, 4, 5775–5784.

2. High-Performance Broad-Band Photodetection Based on Graphene−$MoS_{2x}Se_{2(1-x)}$ Alloy Engineered Phototransistors, **Shubhrasish Mukherjee**, Didhiti Bhattacharya, Samit Kumar Ray and Atindra Nath Pal, ACS Appl. Mater. Interfaces 2022, 14, 34875−34883.

3. Exciton-Plasmon Coupling Mediated Superior Photoresponse In 2D Hybrid Phototransistors, **Shubhrasish Mukherjee**, Didhiti Bhattacharya, Samit Kumar Ray and Atindra Nath Pal. (Communicated).

4. Superior Photoresponse of a Bilayer MoS_2 Phototransistor, **Shubhrasish Mukherjee**, Atindra Nath Pal and Samit Kumar Ray. (Manuscript under preparation).

List of Publications not Covered in this Thesis

1. Two-Dimensional $Mo_xW_{1-x}S_2$ Alloys for Nanogenerators Producing Record Piezo-Output and Coupled Photodetectors for Self-Powered UV Sensor, Didhiti Bhattacharya, **Shubhrasish Mukherjee**, Atindra Nath Pal, Rajib Kumar Mitra and Samit Kumar Ray, Adv. Optical Mater. 2022, 2200353.

2. G Phonon Mode Splitting in Doped Bilayer Graphene Probed by in-situ Transport Measurement and Raman Spectroscopy, Shubhadip Moulick, **Shubhrasish Mukherjee**, Shreyan Raha, Achintya Singha and Atindra Nath Pal. (Manuscript under preparation).

Acknowledgement

From conception to completion, this thesis took nearly five years, and it was like climbing a high peak step by step, accompanied by bitterness, hardships, and countless cycles of inquiry, exploration, confusion, and encouragement. Though words will never be enough to express my gratitude to everyone who assisted me on this journey, I would like to express my heartfelt gratitude to everyone.

First and foremost, I would like to express my heartfelt gratitude to my supervisors, Prof. Samit Kumar Ray, and Dr. Atindra Nath Pal, for exposing me to a very exciting and interesting field of research and installing confidence in me. Their invaluable advice and discussions constantly provide me with a fresh perspective on how to approach the challenges I face with my research, and their moral support, optimism, and ongoing encouragement serve as my source of inspiration. Their new perspectives on science and upbeat attitude have always been energizing. I am grateful to them for their suggestions and critical comments, which helped me shape my thesis.

I am thankful to S.N. Bose National Centre for Basic Sciences for providing a beautiful campus and good research facilities with friendly environment. Also, I am very much grateful to DST INSPIRE fellowship (IF170929), Govt. of India.

It was quite a unique experience in helping setting-up the lab from the scratch. I would like to express my heartfelt gratitude to my past and present labmates including Shubhadip da, Biswajit, Rafiqul, Didhiti, Riju, Taniya, Soumili, Tausif, Buddhadeb da, Gaurav, Subhankar, and Dayal, for providing me a homely environment and lively company on numerous occasions. We four (Shubhadip da, Rafiqul, Biswajit, and me) have wonderful memories together after joining almost at the same time. They provide unwavering encouragement and motivation, which made this PhD a joy to complete. For example, the heterostructure setup was developed with the active participation of Shubhadip da. Riju assisted in optimizing photolithography for device fabrication. Rafiqul is always available to assist with any LabVIEW and interfacing related issues. Didhiti is the most serious person I have ever met. Her enthusiasm and never-ending assistance enriched me throughout my doctoral studies. I have learned many things from her. To me, Biswajit is more than just a lab mate. It has been nearly 11 years since the undergraduate years when we first got together. I would like to thank my seniors like Dr. Sayan Bayan, Dr. Buddhadeb Pal, Dr. Sk md Obaidulla and Dr. Sujoy Kumar Ghosh for their valuable comments and supports. They are all very cooperative in

maintaining a good research environment within the laboratory. It will never be easy to complete my PhD work without all of them. I extend my gratitude to the faculty members of SNBNCBS, specially Prof. Rajib Kumar Mitra and Prof. Priya Mahadevan for their collaborative supports and some fruitful discussions.

I am thankful to every colleague of the SNB family. Special thanks to Piya di, Dipanjan da, Debayan, Subrata da, Dipika di, Sankar da, Sudipta da, Supriyo da, Mehebub da, Keshab da, Koushik da, Arnab da, Riya, Amrita, Jayanta, Dhrubojyoti, Abhik, Indrani, Rahul, Pratap, Amrit da for their amazing company. Piya di, Dipanjan da, and Debayan are like extended lab members and are always there for me when I am in trouble.

Excluding the lab, I will miss SNB cricket the most. The auction and the chaos of the SNB cricket tournament are something, I will never forget. My memories of SNB ground with Supriya da, Mehebub da, Souvanik da, Shubhasis da, Rakesh da, Sumanta da, Subrata da, Kesab da, Dipanjan da, Kaushik da, Panda, Subham, Pratap, Biswajit Panda, Biswajit Kumar, Gaurav Patel, and Anirban will always make me happy.

Shakti da, Amit da, Joy da, Urmi di, Dipanyan da, Debargya da, Sourav da (Centre facility labs), and Amit da (mechanical workshop) deserve special thanks for their technical assistance during my research at SNBNCBS. I would also like to thank all of the staff members, including the cleaners, gardeners, and mess crew, for making my stay here memorable. Swarup da and Nivedita mam deserve special thanks for their unwavering support with the fellowship and contingency grant arrangements.

I am extremely fortunate to have a select group of friends who make my stay enjoyable, including Sumanta, Sukalyan, Siddhartha, Arghya, Raktim, Sukanya, Bratati, and Raju. I hope we can keep the tours and plans going as they were. I also want to express my gratitude to my childhood friends Taslim, Honda, Raja, Somnath, Sanju, and Chandan for always sticking by my side. I will always remember the days I spent with Sourav, Kishalay, Babusona, Biswajit in Burdwan. They will always hold a special place in my heart.

All of my teachers from school, college, and university deserve my sincere gratitude, but in particular Bikash babu, Chanchal babu, Arup sir, Debasish sir (D.B sir), Tanmoy sir (T.B sir), and Partha sir (P.M sir). I want to thank you for inspiring me to study physics and giving me the confidence to pursue research.

Last but not least, I would like to thank my family, especially my mother (Chandana Mukherjee), elder sister (Shantashree Mukherjee) and bother-in-law (Ayan Mukherjee) for their faith in me and for constantly motivating me. I am extremely grateful to other family members such as Runu pisi, uncle (Nilkamal Mukherjee), aunt (Rupa Mukherjee), and sister (Tamalika Mukherjee) for their unwavering support and assistance. My father, who I lost on my journey, will always be missed along with my Takuma and Choto-dadu. He served as my inspiration, and I have always made an effort to emulate him. Everything I have accomplished today is solely due to him. This thesis is dedicated to him. I consider myself fortunate to have a family that has always shown me unconditional love and support. Without their blessing, none of this would have been possible.

Finally, I owe a debt of gratitude to the almighty for allowing me to sail the journey of my life and making it possible by being with me through the ups and downs.

Shubhrasish Mukherjee

S. N. Bose National Centre for Basic Sciences

Abstract

Photodetectors that can convert light into electrical signals are at the heart of technologies that affect our daily lives. Two-dimensional (2D) layered materials (graphene, TMDCs etc.) offer a new viable alternative to the conventional semiconductors used in photodetector devices (Si, Ge, ZnO etc.) due to their promising electronic and optical properties. While graphene is considered as an outstanding channel material for a transistor due to its ultrahigh charge carrier mobility (~up to 60000 cm^2 /VS, at room temperature on a substrate), it has limitations in the field of optoelectronics because of its gapless nature, low absorption cross-section etc. Among various possibilities, a popular strategy is to create a noble device structure by incorporating light absorbing nanomaterials like Si quantum dots, nanostructured PbS, ZnO etc. into graphene. In this typical hybrid structure, graphene is used for carrier transport channel and interaction between the photosensitive material and graphene is the prime factor for the ultrasensitive photodetection. Being layered semiconductors, some members of the transition metal dichalcogenide (TMDC) family (MX_2; M = Mo, W; X = S, Se) are natural partners of graphene for optically active heterostructures. In this aspect, solution processed TMDC QDs are found to be suitable for fabrication of graphene-based broadband, highly stable photodetectors because of their broad absorbance band, direct and tunable band gap, easy synthesis process and higher stability. However, these binary TMDCs suffer from intrinsic defects like chalcogen vacancies, which strongly affect their intrinsic electronic and optical properties leading to localized deep-level defect states (DLDSs). Alloying is a potential solution to overcome such difficulties as it offers lower deep level densities, conversion of deep to shallow levels of defects and better thermal stability. Hence, for the broad applications in integrated devices, growth of these bandgap engineered 2D ternary alloys may provide realistic solution to improve the device performance. Also, several attempts have been made to improve the optical properties of such TMDCs by coupling surface plasmon (SP) modes of some metal nanostructures. The localized surface plasmon resonance (LSPR) of a metal nanostructure (nanoparticles, nanowires etc.) can be excited by an incident electromagnetic radiation and it depends on the carrier density, size, and shape of the nanostructures and on the external surrounding. The SP of the metal nanostructures can couple with the excitons of TMDCs, which may result in an enhanced absorbance, emission and improved photodetection capabilities.

Contents

Chapter 1

Introduction

The general introduction to the research projects covered in this dissertation is highlighted in this chapter. The motivation behind selecting the materials and the specific device structures is the focus of this chapter. It provides a brief overview of the fundamentals of van der Waals 2D materials, physics of the cutting-edge photodetector technology, and the potential application of such 2D materials and heterostructures as broadband photodetectors. This chapter also provides a thorough examination of graphene-based hybrid phototransistors.

The semiconductor industry has been dominated for several decades due to its low cost, abundance, high quality native oxide, and moderate device processing temperature range. However, as the demand for lower power miniaturised electronic and photonic circuits increased, research on nanostructure devices with new functionalities has taken a leap. In 2004, graphene was discovered experimentally and opened-up a new research field for scientists from a variety of disciplines[1]. Beyond graphene, there are several two-dimensional (2D) materials in nature that allow the exfoliation of atomically thin individual layers because of the weak van der Waals coupling[2]. It was quickly established that such 2D systems can be used for a variety of electronic and optoelectronic applications as well as the study of exotic physics such as the relativistic physics of Dirac Fermions[3], Berry phase and the quantum hall effect[4], neutral and charged exciton dynamics[5], Polaritons[6], Coulomb drag[7], and anomalous lattice vibrations[8] etc. The potential for high-speed electronic applications with low power consumption is one of the key features of such van der Waals (vdW) materials. These materials could also be used to create transparent and flexible devices, among other possibilities. As the silicon-based 3D technology has almost reached to its limit, it cannot fulfil the demand of further miniaturization with lower power consumption, the need for new technology possibly with new functional low dimensional materials is an absolute necessity. Numerous studies have demonstrated that vdW devices can be coupled with silicon chips, realising a variety of exciting device functionality, including optical modulators, mode-locked ultrafast lasers, and ultrafast photodetectors.

Hence, this chapter gives a brief introduction about the basic of vdW 2D materials like their electronic structure, band structure, electronic, optoelectronic, vibrational properties, the state-of-the-art photodetector technology, and the potential application of such 2D materials and their heterostructures as a broadband photodetector. Also, this chapter gives a comprehensive review of the graphene-based hybrid phototransistors. The conclusion of the thesis contains a detailed description of the thesis objectives and organisation.

1.1 Graphene

The fundamental component of graphite, known as graphene, consists of covalently connected carbon atoms with a hexagonal pattern[9,10]. Graphene is the thinnest and strongest material ever tested. Even at room temperature, its charge carriers have almost zero effective mass and can travel micrometre-long distances without scattering[11]. Also, graphene has twice the current density and thermal conductivity in comparison to copper along with enormous stiffness. A Dirac-like equation describes electron transport in graphene, allowing researchers to investigate relativistic quantum phenomena in a table-top experiment. We will go over its crystal structure, band structure and electronic properties briefly in this section.

1.1.1 Crystal structure

Graphene is made up of carbon atoms arranged in hexagonal arrays. Six electrons make up each carbon atom: two are in the inner core shell 1s and four are in the energy levels 2s, $2p_x$, $2p_y$, and $2p_z$. The sp^2 hybridized orbitals result from the combination of the orbitals 2s, $2p_x$, $2p_y$ in graphene. The hexagonal planar lattice structure of graphene is created when these three σ states form covalent bonds with their three closest neighbours. The remaining $2p_z$ orbital is

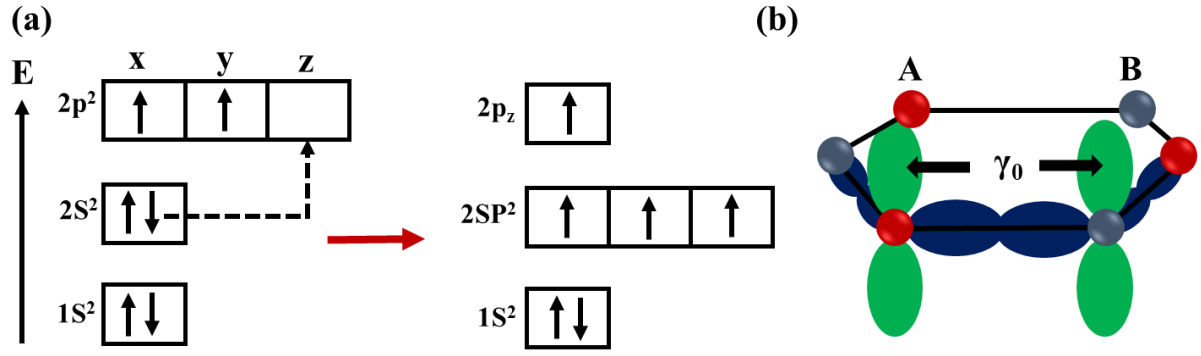

Figure 1.1: *Orbitals and hybridization in graphene. (a) Formation of sp^2 hybridization in graphene. (b) Orbitals and nearest neighbour hopping in graphene. Navy represents the σ bonding and green represents the π bonding. γ_0 is the nearest neighbour hopping parameter.*

positioned perpendicular to the lattice plane and can hop to the neighbouring $2p_z$ orbitals resulting in π bond formation. Since $2p_z$ only contains one electron, the π bonds are half filled and leading the unusual electronic properties of graphene.

The honeycomb lattice is not a Bravais lattice from a crystallographic perspective since it has two inequivalent neighbouring lattice sites. Yet, two atoms (A and B) can be arranged in a unit cell to create a triangular lattice. The unit cell is a rhomboid and contains two atoms, one from each sublattice (as shown by the red dotted area in **Figure 1.2a**). The primitive lattice vectors are denoted by,

$$\overrightarrow{a_1} = \frac{a_0}{2}(3,\sqrt{3}) \ , \overrightarrow{a_2} = \frac{a_0}{2}(3,-\sqrt{3}) \quad \ldots\ldots\ldots\ldots\ldots\ldots \quad (1.1)$$

Where, a_0 represents the distance between two nearest neighbour carbon atoms (1.42 Å here). Similarly, the reciprocal lattice vectors can be written as

$$\overrightarrow{b_1} = \frac{2\pi}{3a}(1,\sqrt{3}), \ \overrightarrow{b_2} = \frac{2\pi}{3a}(1,-\sqrt{3}) \quad \ldots\ldots\ldots\ldots\ldots\ldots \quad (1.2)$$

Also, the nearest neighbouring vectors can be written as

$$\overrightarrow{\delta_1} = \frac{a}{2}(1,\sqrt{3}), \ \overrightarrow{\delta_2} = \frac{a}{2}(1,-\sqrt{3}), \ \overrightarrow{\delta_3} = -a\,(1,0) \ \ldots\ldots\ldots\ldots\ldots\ldots \quad (1.3)$$

Figure 1.2b represents the first Brillouin zone of the reciprocal lattice where, Γ, K, K' and M represent the important high symmetry points. The K and K′ points are the inequivalent

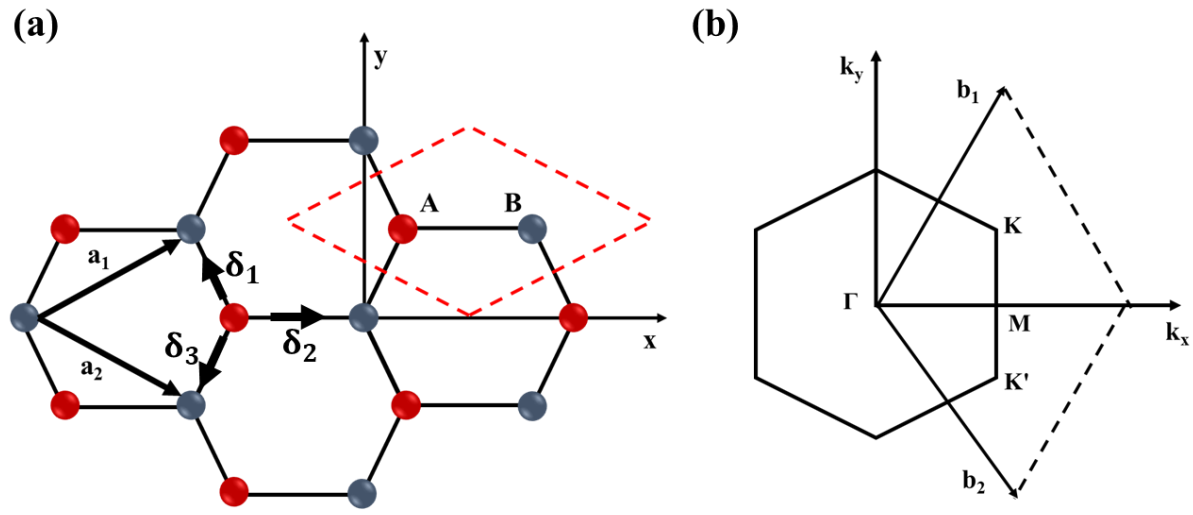

Figure 1.2: *Crystal structure of graphene. (a) Hexagonal honeycomb like crystal structure of graphene. The red dotted lines with rhombus shape define the unit cell with two atom basis (A and B).* $\overrightarrow{a_1}$ *and* $\overrightarrow{a_2}$ *are the primitive lattice vectors. (b) The first Brillouin zone of graphene, with high symmetry points at, K, K', and M.* $\overrightarrow{b_1}$ *and* $\overrightarrow{b_2}$ *are the reciprocal lattice vectors.*

neighbouring vertices of the Brillouin zone edge, whereas the Γ point represents the centre. The position of K, K′ and M in momentum space can be written as

$$\overrightarrow{K} = \frac{2\pi}{3a_0}\,(1, \frac{1}{\sqrt{3}}),\;\; \overrightarrow{K'} = \frac{2\pi}{3a_0}\,(1, -\frac{1}{\sqrt{3}}),\;\; M = \frac{2\pi}{3a_0}\,(1, 0) \;\ldots\ldots\ldots\ldots\ldots\ldots\; (1.4)$$

These inequivalent points (K and K′) are known as the Dirac points and have a significant importance in the transport properties of graphene.

1.1.2 Electronic band structure

By using tight-binding formulation the electronic band structure of graphene was first calculated by P. R. Wallec[12] in 1947. Here by using second quantization, various hopping energies were used to calculate the band dispersion analytically. Assuming the nearest neighbour interaction, the tight binding Hamiltonian in graphene can be written as[13,14]

$$H = -\gamma_0 \sum_{i,j,\sigma}(a^{\dagger}_{\sigma,i} b_{\sigma,j} + h.c) \;\ldots\ldots\ldots\ldots\ldots\ldots\ldots\ldots\ldots\ldots\; (1.5)$$

Where, γ_0 represents the nearest neighbour hopping parameter, $a_{\sigma,i}$ and $a^{\dagger}_{\sigma,i}$ define the annihilation and creation operator of an electron in sublattice A. Similarly, $b_{\sigma,j}$ is for sublattice B.

Solving this tight-binding Hamiltonian, the energy dispersion relation becomes

$$E_{\pm}(k) = \pm\gamma_0 \sqrt{3 + f(k)} \;\ldots\ldots\ldots\ldots\ldots\ldots\ldots\ldots\ldots\ldots\ldots\; (1.6)$$

where,

$$f(k) = 2\cos\left(\sqrt{3}\,k_y a_0\right) + 4\cos\left(\frac{\sqrt{3}}{2}\,k_y a_0\right)\cos\left(\frac{3}{2}\,k_x a_0\right) \;\ldots\ldots\; (1.7)$$

The ‘+’ and ‘-’ sign correspond to the conduction and the valance band respectively.

The electronic band structure of monolayer graphene is represented in **Figure 1.3a** where the valance bands (VB) and the conduction bands (CB) are touching each other at 6 different points in the Brillouin zone. These K and K' points are known as Dirac points. Therefore, monolayer graphene is a zero-band gap material. Now, near to the Dirac point (K or K') the Taylor series expansion gives,

$$E_{\pm}(k) = \pm\hbar v_F\,|k| + O\,(k^2) \;\ldots\ldots\ldots\ldots\ldots\ldots\ldots\ldots\ldots\ldots\; (1.8)$$

Where, $v_F = 3\gamma_0 a/2\hbar$ is the Fermi velocity in graphene and the electron wave vector k can be found from the Dirac points. Neglecting the higher order terms

$$E_{\pm}(k) = \pm\hbar v_F\,|k| \;\ldots\ldots\ldots\ldots\ldots\ldots\ldots\ldots\ldots\ldots\ldots\ldots\; (1.9)$$

So, near to the K point graphene has a linear dispersion relation with zero effective mass of electrons and relativistic velocity ($v_F \sim c/300$). Thus, the quasiparticles in graphene can be described as massless Dirac Fermions. The density of states (DOS) of graphene near to the Dirac point and its zoomed view are shown in **Figure 1.3b**. For low energy massless Dirac fermions, Equation 1.9 describes to the spectrum of the Dirac like Hamiltonian near to the K point as

$$H_K = \begin{pmatrix} 0 & k_x - ik_y \\ k_x + k_y & 0 \end{pmatrix} = \hbar v_F \vec{\sigma}.\vec{k} \quad \ldots\ldots\ldots\ldots\ldots\ldots\ldots \quad (1.10)$$

And close to the K' point the equation 1.10 becomes $H_{K'} = \hbar v_F \overrightarrow{\sigma^*}.\vec{k}$. Where σ is the Pauli spin matrix and σ^* is the complex conjugate. It should be noted that σ is not true electronic spin, but rather originates due to graphene's two carbon atoms per unit cell. Thus, σ can be referred to as pseudospin. So, in addition to the spin and orbital indices, graphene carriers have a pseudospin index. Now, $N(E) = \sum_n \delta(E - E_n)$ can be used to express the total number of quantum states (k_x^n, k_y^n) with energies E_n, where $\delta(E)$ is the Dirac delta function. The DOS, which can be derived from the constant energy surfaces, is now described as the total number of states per unit volume per unit energy at energy E. Near the Dirac point, the energy contours for two-dimensional graphene are circular. Thus, the DOS can be written as

$$\rho(\epsilon)d\epsilon = 2\pi \frac{|k|dk}{(2\pi)^2} \ldots\ldots\ldots\ldots\ldots\ldots\ldots\ldots\ldots\ldots\ldots\ldots\ldots \quad (1.11)$$

So,

$$\rho(\epsilon) = \frac{4\epsilon}{2\pi\gamma^2} \quad \ldots\ldots\ldots\ldots\ldots\ldots\ldots\ldots\ldots\ldots\ldots\ldots\ldots\ldots\ldots \quad (1.12)$$

Where factor four handles two spin degeneracy and two valley degeneracy. As shown in **Figure 1.3b**, the DOS increases linearly with energy and reaches zero at E = 0. Then, from equation 1.12 the total carrier concentration can be calculated at T=0K as $n = \int_0^{E_F} \rho(\epsilon)d\epsilon$

i.e.

$$n = \frac{E_F^2}{\pi(\hbar v_F)^2} \quad \ldots\ldots\ldots\ldots\ldots\ldots\ldots\ldots\ldots\ldots\ldots\ldots\ldots\ldots\ldots \quad (1.13)$$

Where E_F is the Fermi energy.

The mass (m^*) can be determined by

$$m^* = \frac{1}{2\pi}\left(\frac{\delta A(E)}{\delta(E)}\right)_{E=E_F} \ldots\ldots\ldots\ldots\ldots\ldots\ldots\ldots\ldots\ldots\ldots\ldots\ldots \quad (1.14)$$

Where $A(E) = \pi(E/v_F)^2$ is the effective area in the k space. Then from equation 1.1.3 and 1.14, m^* can be written as

$$m^* = \frac{E_F}{v_F} = \frac{\hbar\sqrt{\pi}}{v_F}\sqrt{n} \quad \ldots\ldots\ldots\ldots\ldots\ldots\ldots\ldots\ldots\ldots\ldots\ldots \quad (1.15)$$

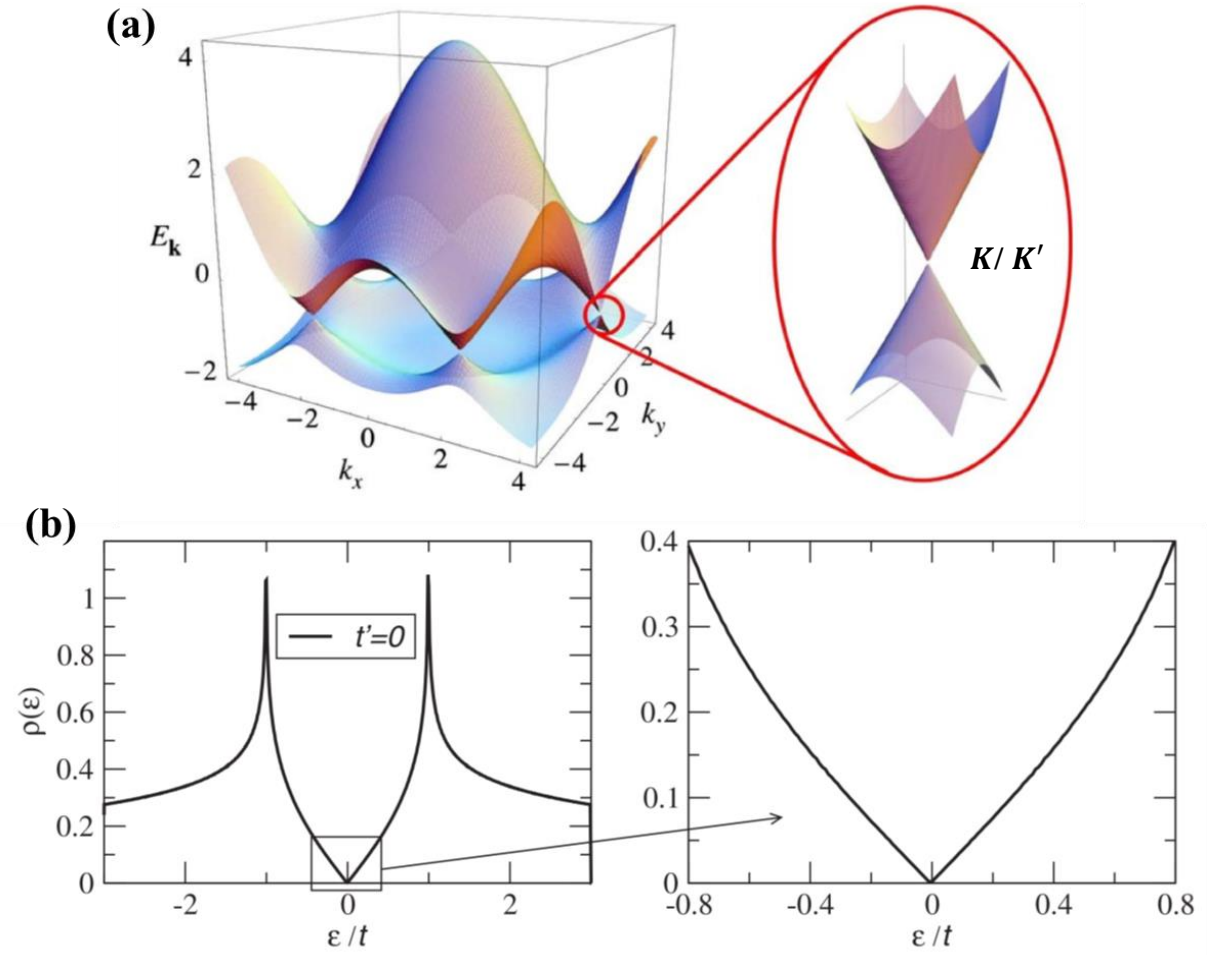

Figure 1.3: *Electronic band structure of graphene. (a) The conduction (CB) and valence band (VB) touch at the six corners of the Brillouin zone. The linear Dirac cone is visible in this enlargement of the band structure near the K or K′ point. (b) Density of states (DOS) of graphene near to the Dirac point. The zoomed view shows the linear DOS at lower energies, Figures are adapted from Ref.13.*

1.1.3 Electrical transport in graphene transistor

Graphene physics research has made spectacular advances in the last 15 years, beginning with the fabrication of gated monolayer graphene device, and progressing to the observation of fractional quantum Hall effect, spin Hall effect and Klein tunnelling etc[15]. The lack of a gap in the graphene dispersion results in a direct transition from electron-like to hole-like metallic transport as the gate voltage is tuned through the charge neutral Dirac point, resulting in ambipolar transport[10]. **Figure 1.4a** depicts a typical back gated graphene field effect transistor (GFET). In most cases, silicon dioxide (SiO_2) is used as an insulating substrate on top of the

highly doped silicon (p^+ or n^+) to transfer or deposit graphene flakes (produced by mechanical exfoliation, CVD, epitaxially, etc.). The "back" gate electrode is made of the doped silicon. Electron-beam lithography, photo lithography or shadow masking are used to form the electrical contacts on the graphene flakes, and after that, a bilayer of Ti/Au is deposited to metalize the contacts. According to convention, the electrodes of GFETs are referred to as "Source," "Drain," and "Gate": The graphene flake is directly contacted with the "Source" and "Drain" electrodes. Typically, devices are made in two probe, four probe, and hall bar geometry.

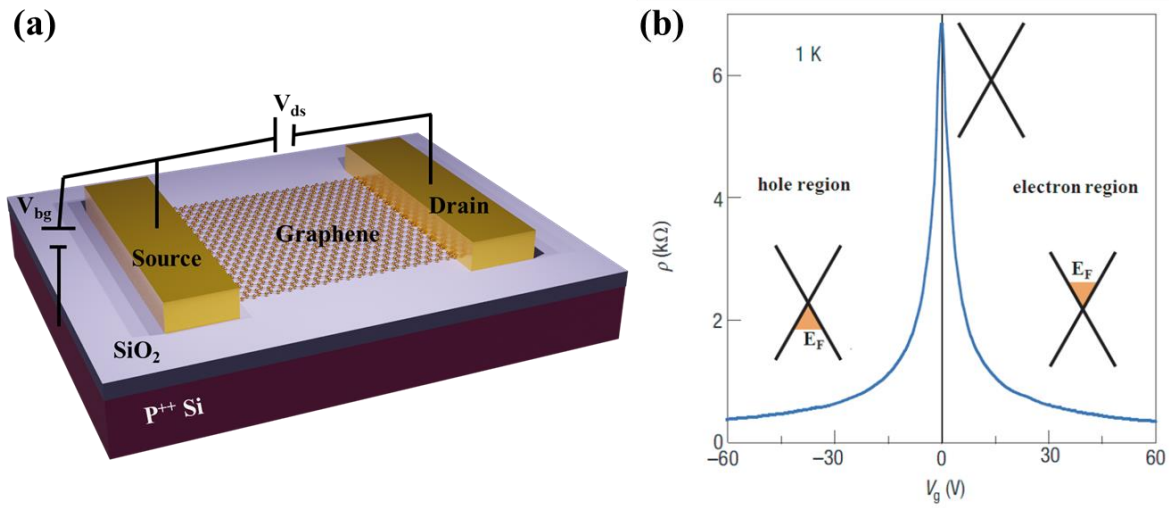

Figure 1.4: *Electronic transport in graphene field effect transistor (FET). (a) Schematic of back gated graphene FET. (b) Gate voltage (Vg) dependent resistivity (ρ) in graphene transistor. The shaded area represents the Fermi level in the valence band (Left) and the conduction band (Right) depending on the gate voltages. Near the maximum of the curve (Dirac point), the charge neutral band structure is also shown. Figure 1.4b is adapted from Ref. 10.*

With an external electric field between the gate and the source (drain) electrodes, the charge carrier densities of such graphene devices can be easily tuned. A typical transfer characteristics for a monolayer graphene transistor with SiO_2 as the back gate dielectric is depicted in **Figure 1.4b**. Resistivity (ρ) should ideally diverge (or conductivity should be zero), but there will always be some thermally generated carriers and spatial inhomogeneity in the form of charge puddles (n). The resistivity decreases almost linearly away from the Dirac point before reaching saturation. The resistivity can be found from

$$\rho = \frac{\left(\frac{W}{L}\right)V_{ds}}{I_{ds}} \quad \ldots\ldots\ldots\ldots\ldots\ldots\ldots\ldots\ldots\ldots\ldots\ldots \quad (1.16)$$

Where, V_{ds} is the applied bias voltage between two electrodes, and I_{ds} is the measured current. W and L represent the width and the length of the device respectively. Normally, the devices are several micrometre in length and graphene has a ballistic length of a few hundred nanometres[16], the mobility can be determined using the conventional expression of diffusive transport theory.

$$\sigma = ne\mu \quad (1.17)$$

Where, σ, n and e represents the conductivity, the carrier density, and the electronic charge respectively.

Also, σ can be found out from equation (1.16) as

$$\sigma = \frac{1}{\rho} = \frac{I_{ds}}{V_{ds}}\frac{L}{W} \quad (1.18)$$

The carrier density (n) can be tuned by applying the gate voltages (V_{bg}) and can be calculated by using a parallel plate capacitor model, i.e.

$$n = \frac{C_{bg}}{e}\,(V_{bg} - V_D) \quad (1.19)$$

Where c_{bg} is the gate capacitance of the device.

By using these equations (1.17), (1.18) and (1.19) the carrier mobility (μ) can be calculated.

At V_{bg}=V_D, the carrier density should ideally become zero (n→0). However, in real experiments, it is not possible to achieve n→0. Because of charge impurities (n_{imp}), the sample contains electron and hole puddles[17,18]. The trapped charges at the interface of graphene layer and the SiO_2 substrate could be responsible for these charge impurities. The consideration of charge impurities is critical because it explains the linear dependence of on n, the variation of minimum conductivity, and why remains constant near the V_D. At low density, Coulomb scattering dominates, resulting in a linear density dependence in conductivity, whereas at high density, short-range scattering becomes important, causing conductivity to become nonlinear with density.

1.1.4 Optical properties

The linear Dirac cone and the absence of an energy gap in the band structure of graphene result a uniform absorption across a broad electromagnetic spectrum. Above the far-infrared, graphene's optical response is mainly dominated by direct valence band to conduction band (FIR)[19] transition. **Figure 1.5a** depicts an optical image of graphene layers (mono and bilayer)

on a metal framework, with each layer absorbing approximately 2.3% of the light. **Figure 1.5b** shows that this value is frequency independent within the linear energy range. This universal conductance can be calculated using fundamental constants using the tight-binding model i.e. $\sigma\,(w) = \frac{\pi e^2}{2h}$ resulting an absorbance of $A\,(w) = \frac{4\pi}{c}\,\sigma\,(w)$ ~ 2.3 %. The Fermi energy of graphene can be shifted by hundreds of meV by electrical doping which may change optical absorption dramatically via Pauli blocking. Optical transitions are suppressed in this scenario for photon energies less than $|2E_F|$.

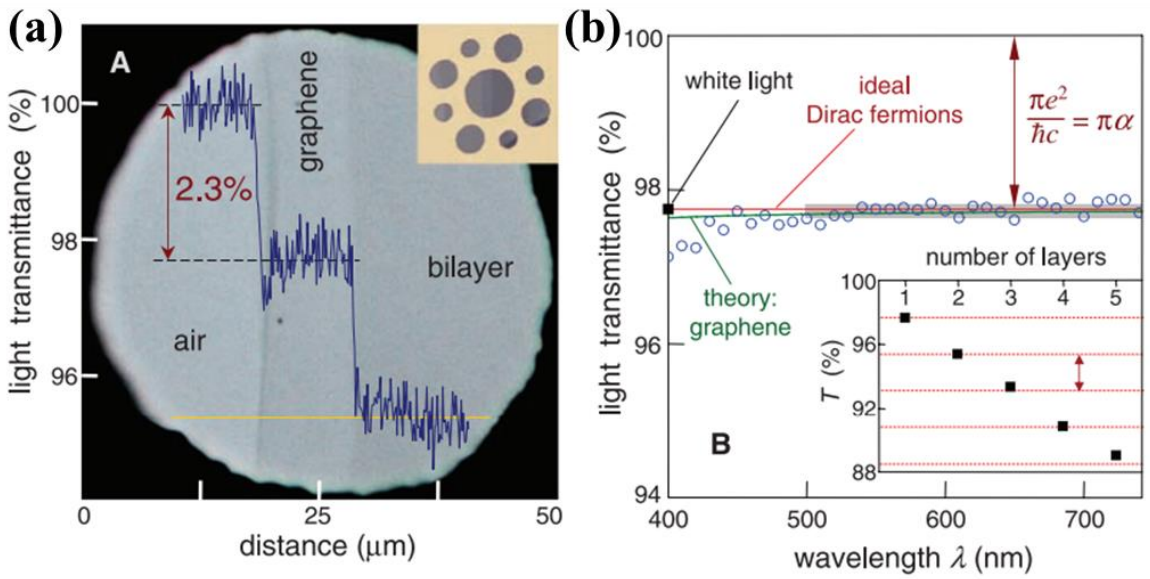

Figure 1.5: *Optical properties of graphene. (a) Mono and bilayer graphene on metal substrate (Inset). Along the yellow line, the transmittance is shown by line scan profile. (b) Transmittance (open circles) is spectrally dependent. Behavior for perfect Dirac fermions is shown by the red (green) line (graphene). Transmittance is depicted as a function of layer number in the inset. Adopted from Ref. 19.*

1.1.5 Vibrational properties

The unit cell of single layer graphene has two atom bases (A and B). Its atoms are capable of both in-plane and out-of-plane motion. Thus, there are 3 degrees of freedom in all (x, y, z). As a result, there will be a total of six branches: three optical and three acoustic. Using density functional theory (DFT) the phonon dispersion of a single layer graphene along the high symmetry lines is shown in **Figure 1.6a**. LO (in-plane longitudinal optic mode), TO (in-plane transverse optic mode) and ZO (optical mode in perpendicular direction) are the optical branches. Similarly, LA (in plane longitudinal acoustic mode), TA (in-plane transverse acoustic mode) and ZA (acoustic mode in perpendicular direction) are the acoustic branches[20].

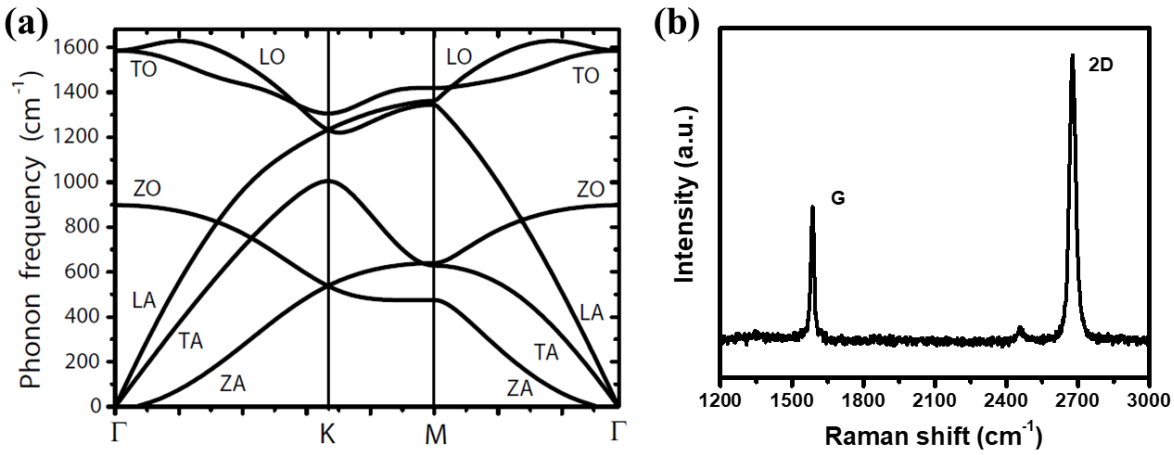

Figure 1.6: *Vibrational properties of monolayer graphene. (a) Phonon dispersion in monolayer graphene using density functional theory (DFT). (b) Raman spectra of monolayer graphene. Figure 1.6a is adapted from Ref. 20.*

For characterising sp^2 and sp^3 carbon materials such graphite, diamond, poly-aromatic compounds, carbon nanotubes, and fullerenes the Raman spectroscopy has been an effective, non-invasive, and non-destructive instrument. It has been uniquely used to determine the number of graphene layers. Raman fingerprints of single, bilayer graphene differ and have been studied by numerous groups[21–24].

Figure 1.6b depicts a typical Raman spectrum of monolayer graphene with 532 nm laser excitation. The symmetry allows E_{2g} mode at Γ point, which is commonly referred to as G mode appearing at 1583 cm^{-1}. Regardless of the number of layers, the G-band frequency remains constant. The 2D-band is the most distinguishing feature of the Raman spectrum, depending on the number of layers. The layer dependency (n = 1, 2, 3, 4 etc.) of graphene 2D-band is represented in **Figure 1.7**. The 2D-band in single layer graphene is a single band with a width at half maximum (FWHM) of ~ 25 cm^{-1} and a wavelength of 2685 cm^{-1}. In contrast, the 2D-band in bilayer graphene may be successfully deconvoluted into the four Lorentzians depicted in **Figure 1.8** as $2D_{uu}$, $2D_{ul}$, $2D_{lu}$, and $2D_{ll}$. The 2D band is decomposed into six components for 3-layers (n = 3) and for n>5, the 2D mode is indistinguishable from HOPG, which can be divided into two components. The double resonance (DR) mechanism, which incorporates the layer dependent electronic band structure, can explain the dependence of the Raman 2D-band lineshape on the number of layers. The DR process for single layer graphene is depicted in **Figure 1.7b**, which explains the origin of single 2D-band. However, for the bilayer graphene, inter-layer coupling splits the conduction and valence bands at the K and K'

points, as shown in **Figure 1.7c**. The four sub-bands in the 2D spectrum result from four possible intervalley transitions in the "e-h" process, involving the upper (u) and lower (l) bands. The stacking sequence can also be determined using the 2D-band. For example, when comparing ABC stacked trilayer to ABA (Bernal stacking) stacking, the peaks are blue shifted[25].

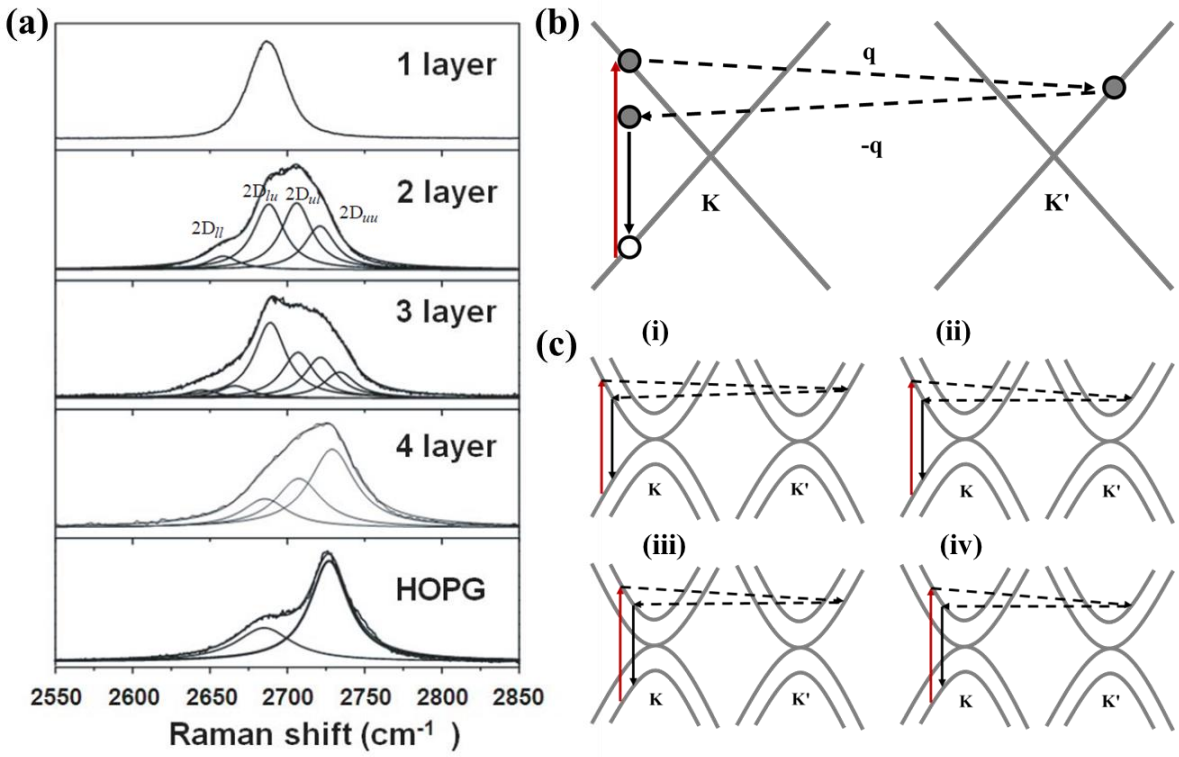

***Figure 1.7**: Raman spectra of graphene layers. (a) Evaluation of graphene 2D-band with layer number. (b) Second order Raman process of 2D mode in monolayer graphene. (c) Origin of four peaks in 2D band of a bilayer graphene. Figure 1.7a is adapted from Ref. 25.*

1.2 Transition metal dichalcogenides (TMDCs)

Like graphene, transition metal dichalcogenides (TMDCs) can also be exfoliated into atomically thin crystals. Semiconducting TMDCs are of special interest because of their energy gap in the band structure has a significant impact on both electrical and optical properties[26]. MoS_2 and WS_2 are two well-known members of the TMDC family that are widely used for their potential applications. Both bulk crystals have an indirect bandgap of ~1.2eV, but when they reach the monolayer limit, they switch back to a direct bandgap semiconductor with a bandgap of ~ 2eV[27]. Because of the finite bandgap in the visible range, the TMDCs are suitable

for optoelectronic applications. It can also be used on low-energy circuits due to its sharp on-off ratio.

1.2.1 Crystal structure

A class of materials known as TMDCs has the formula MX_2, where M is an element from the transition metal group IV (Ti, Zr, Hf, and so on), group V (Nb or Ta), or group VI (Mo, W, and so on), and X is a chalcogen (S, Se or Te)[28–30]. These substances come together to form the layered structural unit X-M-X, which is composed of two hexagonal planes of chalcogen and one plane of metal atoms (**Figure 1.8a**). In TMDC, to form the bulk crystal, adjacent layers are held together by weak van der-Waals interactions. There are three different crystal structures of TMDCs depending on the variance in stacking orders and metal atom coordination (**Figure 1.8b**). 2H is the most stable of the three. Since the 2H stacking stands for the hexagonal symmetry and follows the ABA structure in the c-direction with two layers per repeated unit[31]. 3R possesses rhombohedral symmetry, trigonal prismatic coordination and three layers per repeated unit denoted by 3. Compared to the other two phases, this one is uncommon. The octahedral 1T phase of TMDC is a metallic metastable polymorph with an ABC stacking. The 1T phase can be formed using alkali-ion intercalation techniques or strain engineering in van

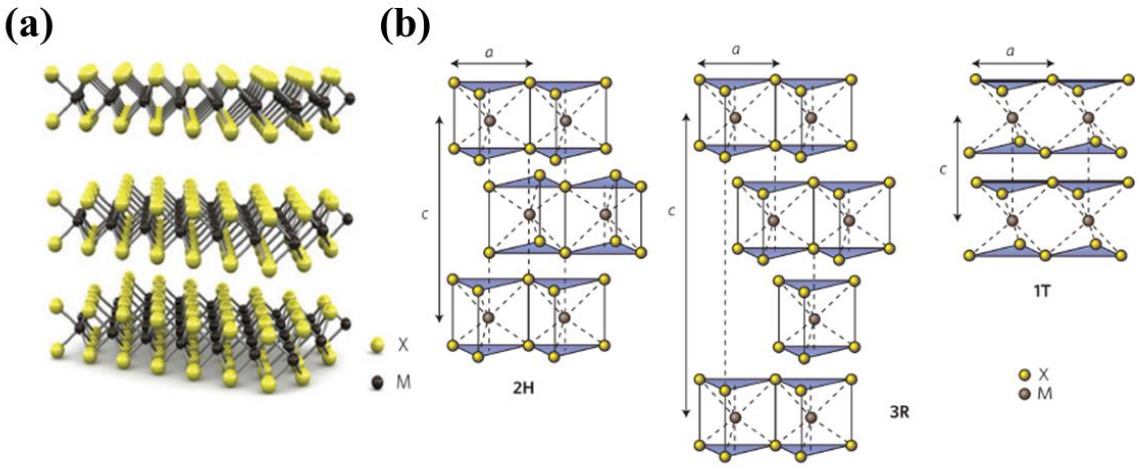

Figure 1.8: *Crystal structure of TMDC materials. (a) A three-dimensional schematic illustration of the MX_2 structure, showing the metal atoms (M) and chalcogen atoms (X). (b) Schematic structures with different phases: 2H (hexagonal symmetry, two layers per repeat unit, trigonal prismatic coordination), 3R (rhombohedral symmetry, three layers per repeat unit, trigonal prismatic coordination) and 1T (tetragonal symmetry, one layer per repeat unit, octahedral coordination). Figures are adapted from Ref. 46.*

der Waals heterostructures, but it slowly relaxes into the 2H phase with heating or as time passes[32]. It has tetragonal symmetry, which is denoted by T, and one layer per repeated unit, which is denoted by 1. It is a diamagnetic, indirect bandgap semiconductor with properties comparable to the 2H structure[33].

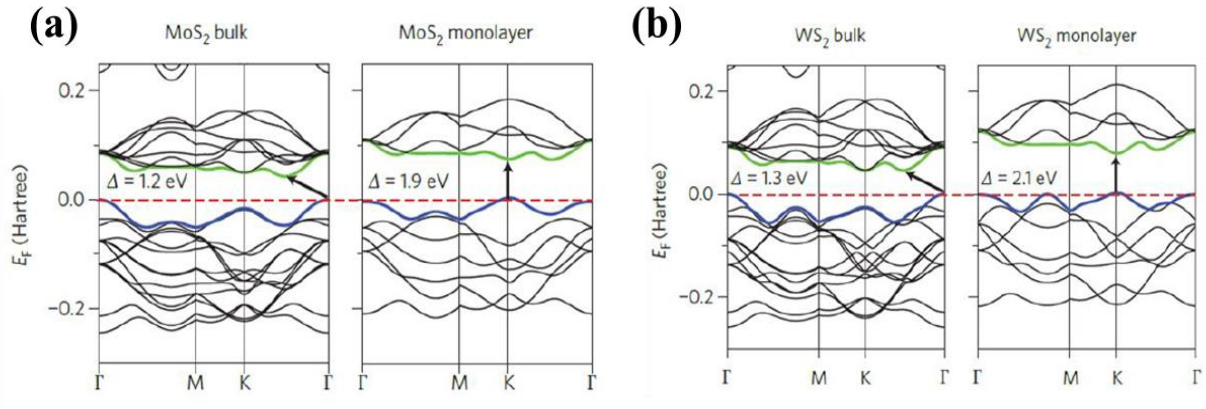

Figure 1.9: *Calculated band structures of TMDCs with first-principles density functional theory (DFT). For bulk and monolayer (**a**) MoS_2 and (b) WS_2. Adapted from Ref. 28.*

1.2.2 Electronic band structure

TMDCs that are semiconductors show a direct bandgap in the monolayer and an indirect bandgap in the bulk. The primary cause of the observed photoluminescence from monolayer MX_2, which has made optoelectronic applications possible, is the direct bandgap[27,33]. First-principles calculations, tight-binding approximations, and measurements are used to determine the band structures of bulk and monolayer MX_2s. DFT calculations show that the bulk crystal's valence band maxima are located at Γ-point[34]. It is an indirect bandgap semiconductor because the conduction band minima are located at the Q-point (halfway between Γ and K). The theoretical analysis shows that the electronic states near the K-point are caused by localised d-orbitals of W(Mo) atoms, which are unaffected by interlayer coupling because they are sandwiched between Se(S) atoms. However, the states near the Γ-point are sensitive to interlayer interactions and arise from the p_z-orbitals of the Se(S) atoms and the d-orbitals of the W (Mo) atoms. As a result, as the layer number changes, the direct excitonic states near the K-point remain relatively unchanged, but the transition at the Γ point shifts significantly from indirect to direct. With decreasing layer numbers, all MoX_2 and WX_2 compounds are expected to undergo a similar indirect-to-direct bandgap transformation[35,36]. **Figure 1.9a** and **1.9b** shows the calculated band structure of bulk and monolayer MoS_2 and WS_2 respectively.

1.2.3 Electrical transport in TMDC transistor

Kis's group successfully studied the electronic properties of single layer MoS_2 FETs for the first time in 2011[37]. The device was fabricated by using mechanically exfoliated monolayer MoS_2 with HfO_2 as top gate (**Figure 1.10a**). The transfer characteristic of ultrathin layers of MoS_2 reveals that it is an n-type semiconductor (**Figure 1.10b**). As expected, the MoS_2 transistors exhibits a very high on/off ratio of 10^8 and a subthreshold swing of close to 74 mV per decade (**Figure 1.10b**. The superior electrical properties of the MoS_2 layer have been widely studied, making them a potential candidate for electronic and optoelectronic applications such as modulator and logic transistors, as well as ultrafast photonic devices for optical communication[38]. With a two-terminal device configuration, the field-effect mobility is approximated by extracting the slope in the linear regime. The field effect mobility μ is given by conventional MOSFET theory as

$$\mu = \frac{dI_{ds}}{dV_{bg}} \frac{L}{WC_{OX}V_{ds}} \quad \ldots\ldots\ldots\ldots\ldots\ldots\ldots\ldots\ldots\ldots\ldots\ldots\ldots\ldots \quad (1.20)$$

Where, I_{ds} is the drain-source current, V_{bg} is the back gate voltage, L and W represent the length and the width of the device, V_{ds} is the applied bias voltage and C_{OX} is the gate capacitance. The best single layer MoS_2 mobilities that have been reported up to this point are still below 100 cm^2/Vs, despite theoretical predictions of phonon-limited mobilities up to 410 cm^2/Vs at ambient temperature[39]. The effect of charged impurities at the MoS_2/oxide interface and defects such sulphur vacancies are frequently assumed[40]. The efficient suppression of phonon and impurity-scattering has recently been achieved in fully encapsulated MoS_2 layers sandwiched

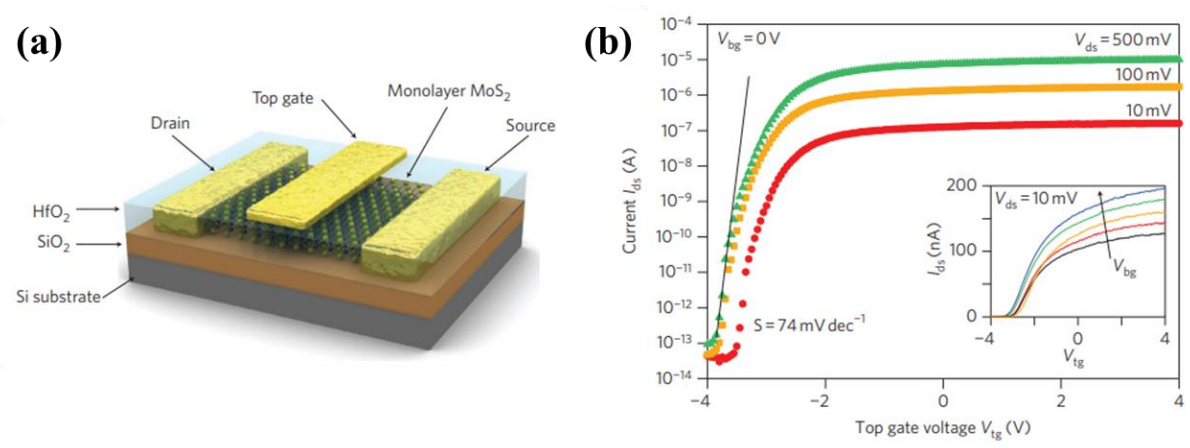

Figure 1.10: *Electrical transport in MoS_2 transistor. (a) Schematic of a top gated monolayer MoS_2 transistor. (b) I_{ds}-V_{tg} curve recorded for a bias voltage ranging from 10 mV to 500 mV. Measurements are performed at room temperature with the back gate grounded. Adapted from Ref. 134.*

between boron nitride (hBN) layers, with record low-temperature mobilities of 10^3-10^4 cm^2/VS for 1-6 layers[41]. Nonetheless, there is still opportunity for improvement due to the significantly decreased room temperature mobility of 40 to 120 cm^2/VS[42].

1.2.4 Optical properties

The previously described electronic band structures of TMDCs have a direct influence on their optical properties. Changes in photoconductivity, absorption spectra, and photoluminescence for MoS_2 indicate a shift from indirect to direct bandgap and an increase in bandgap energy[27,43]. The optical absorption spectra of bulk MoS_2 exhibits two prominent peaks that are exciton-related, known as the A and B excitons: direct-gap transitions at the K-point of the Brillouin zone between the maxima of split valence bands and the minimum of the conduction band (**Figure 1.11a**). The band splitting in such TMDCs (which is estimated to be separated by about 160 meV in the VB of monolayer MoS_2)[44] happens due to the spin-orbit coupling, primarily coming from the d-orbits of heavy Mo atoms. Calculations have revealed that the A and B excitons match the predicted gap energies at the K-point. Unlike the largely unchanged absorption spectra, the PL spectra for changing the number of layers show a significant difference. The PL shows a dramatic improvement when transitioning from a dark, indirect-gap bulk crystal to a bright, direct-gap monolayer limit. As shown in **Figure 1.11b**, the major peak of the monolayer MoS_2 photoluminescence spectrum is the direct-gap luminescence characteristic at 1.9 eV. Few-layer MoS_2 also includes additional peaks corresponding to the indirect-gap luminescence and direct-gap hot luminescence[27].

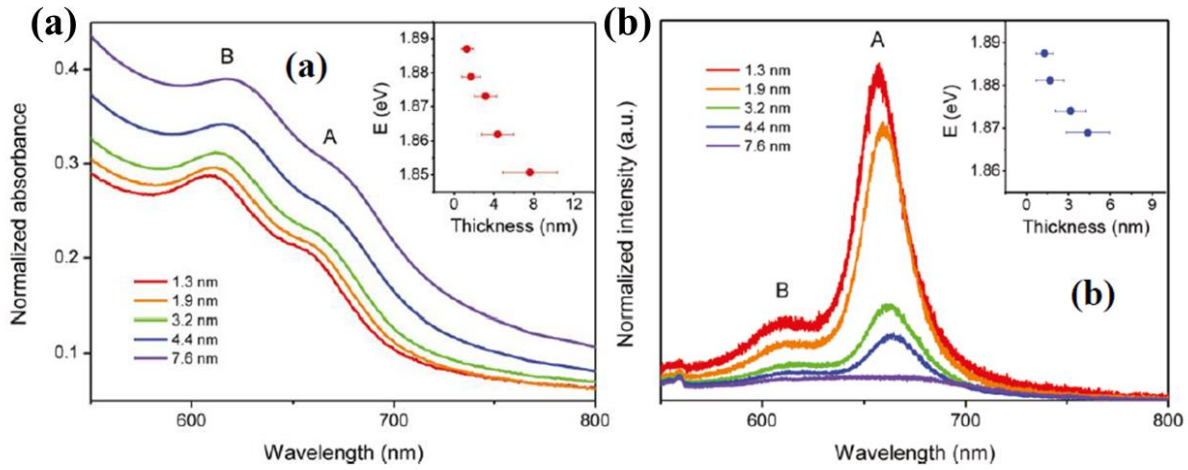

Figure 1.11: *Optical properties of MoS_2. (a) Absorption and (b) photoluminescence spectra of MoS_2 thin films with average thicknesses ranging from 1.3 to 7.6 nm. Inset shows the thickness dependent bandgap shift of MoS_2. Figures are adapted from Ref. 42.*

1.2.5 Vibrational properties

Raman spectroscopy is the most direct and non-invasive method for determining the properties and layer number of 2D layered materials. The main Raman peaks are the in-plane E^1_{2g} and E_{1u} phonon modes, as well as the out-of-plane A_{1g} mode (**Figure 1.12a**)[45]. When layer thickness is reduced, the frequency of the A_{1g} mode of MoS_2 near 406 cm^{-1} decreases while the frequency of the E^1_{2g} mode near 382 cm^{-1} increases (**Figure 1.12b**). This shift in the peak position allows Raman spectroscopy to determine layer thicknesses. The shift is primarily caused by the influence of neighbouring layers on the effective restoring forces on atoms, as well as an increase in dielectric screening of long-range Coulomb interactions. For example, The E^1_{2g} and A_{1g} modes for monolayer MoS_2 are located at 385 cm^{-1} and 404.5 cm^{-1}, respectively, with a value of about 19.5 cm^{-1}. The frequency of A_{1g} mode blue shifts (stiffens) as the number of layers increases, while E^1_{2g} red shifts (softens). As a result, for the bilayer, becomes 22.5 cm^{-1}. When the number of layers is greater than 4, there is no further discernible change, and converges to the value of bulk crystal (26 cm^{-1}), as shown in **Figure 1.12c**. The findings provide a simple and dependable method for determining layer thickness, which has been widely applied to MoS_2 research[46].

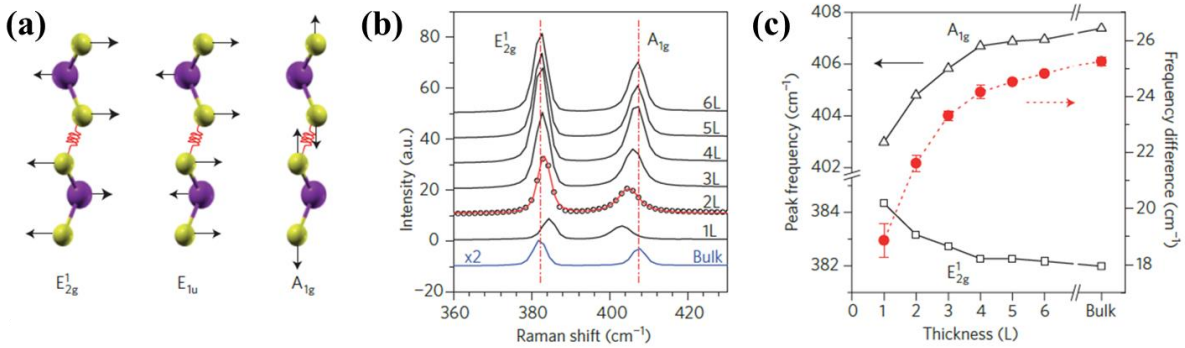

Figure 1.12: *Vibrational properties of MoS_2. (a) The in-plane phonon modes E^1_{2g} and E_{1u}, as well as the out-of-plane phonon mode A_{1g} of MoS_2 are depicted schematically (analogously for WS_2). (b) Thickness-dependent Raman spectra for MoS_2. (c) Peak position and frequency difference for the E^1_{2g} and A_{1g} modes as a function of MoS_2 layer thickness. Adapted from Ref. 46.*

1.3 Synthesis of 2D layered materials

There are several methods for the reliable production of atomically thin layered 2D TMDCs like top-down and bottom-up synthesis procedure[38]. Micromechanical exfoliation and chemical exfoliation are well-known techniques for preparing 2D nanosheets using the top-down

approach. Chemical vapour deposition (CVD) is widely used in the bottom-up approach to produce ultrathin layered 2D nanomaterials. We have used the two above mentioned techniques in this thesis work, while there are other techniques like atomic layer deposition (ALD), Pulsed laser deposition (PLD), thermolysis are also used to produce two-dimensional materials.

1.3.1 Mechanical Exfoliation

Micro-mechanical cleavage is a well-known traditional method for exfoliating layered bulk crystals to obtain layer 2D flakes[3]. Using adhesive tape on target substrates, atomically thin flakes of TMDCs can be peeled from their bulk parent crystals. This mechanical exfoliation produces highly pure and clean nanoflakes, which are suitable for studying their fundamental properties and fabricating high quality-controlled devices. However, the yield of this method is low, it is not scalable, and there is no control over the size and thickness of the nanoflake.

1.3.2 Chemical Exfoliation

The liquid phase exfoliation[47,48] method is widely used chemical method to exfoliate layered nanosheets from bulk material, with the exfoliated ultrathin layers dispersed in a specific solvent. Here, ultrasonic vibrations break the interlayer weak van der Waals bond but not the covalent bonds of each layer, and the choice of solvent is critical in exfoliation. This method enables the production of large quantities of crystalline, layered 2D nanosheets at a low cost and lithium intercalation, hydrothermal technique are famous chemical exfoliation technique.

1.3.3 Chemical Vapour Deposition (CVD)

Chemical vapour deposition[49,50] is a bottom-up synthesis method for producing high-quality ultrathin two-dimensional layered flakes. The given substrate is exposed to a reactive precursor under specific conditions (temperature and pressure), and the precursor is decomposed or reacted to form an ultrathin layer on the given substrate. This method yields a large-scale crystalline two-dimensional TMDC material with tunable thickness and excellent electronic properties, albeit, with multiple grain boundaries. While this method is promising for the realistic application, significant research on the controlled growth and device fabrication are required to improve the device performance.

1.4 TMDC quantum dots

Two-dimensional (2D) materials are transformed into zero-dimensional (0D) materials when their lateral sizes are decreased below their Bohr radius. Because of the emergence of edge sites and quantum confinement effects, these 0D materials exhibit new or improved properties over their two-dimensional counterparts[51,52]. However, these 0 D materials (quantum dots) continue to retain their natural 2D parent characteristics. This new class of 0D materials offers more tunable physio-chemical properties, a higher surface-to-volume ratio, and more functionalization options. To obtain the quantum dots (QDs) of TMDCs (MX_2), the in-plane covalent (X-M-X) bond must be broken, resulting in abundant edge atoms (M or X)[53]. 0D TMDCs are a promising candidate for catalytic applications due to the presence of edge states. TMDC QDs can be dispersed in appropriate solvents and exhibit strong emissive properties, making them suitable for bio-imaging and optoelectronic applications. TMDC QDs have a tunable band gap due to the quantum confinement effect, as well as a wider direct band gap and higher quantum yield than their 2D layered counterparts. The bandgap is strongly influenced by defects, functional groups, and additional dopants during the synthesise time, in addition to the size dependent quantum confinement effect. Size-variable TMDC quantum dots show promise in optical sensing, photovoltaics, catalysis, bio-imaging, energy storage and conversion.

1.5 TMDC alloys

The binary TMDCs (MoS_2, WS_2 etc) have intrinsic defects such as chalcogen vacancies, which have a significant impact on their intrinsic electronic and optical properties, resulting in localised deep-level defect states (DLDSs)[54,55]. These numerous mid-gap defect states can significantly degrade the electronic and optoelectronic performances of the TMDC devices. Many techniques have been developed to reduce deep level defects inside semiconductors by introducing additional impurity through doping, strain engineering, and other techniques. The introduction of foreign dopants suppresses deep-level defects inside the semiconductor via donor-acceptor level repulsion, but the dopant solubility and donor-acceptor level symmetry have a significant impact on the efficacy of this method. The formation of passivated impurity states can alter the host band structure, causing the deep level to become shallower. However, the host material's intrinsic band structure changes significantly, which can cause additional issues. As a result, developing new approaches to reduce deep level defect density while maintaining the electronic properties of the host material is highly desirable. Alloying is being

developed as a new approach for defect engineering in semiconductors, and the alloys' bandgap can be tuned by controlling component concentration. Alloying is a method of suppressing the deep level defect states of a semiconductor while retaining its basic properties. TMDC (MX_2) materials can be alloyed by replacing either the transition metal (M) or chalcogen (X) sites[56]. Common semiconductor alloys have a positive enthalpy formation energy, whereas TMDC semiconductor alloys have a negative enthalpy value, indicating higher atomic ordering[57]. This atomic ordering is critical in determining the properties of the alloy. DFT calculations show the stabilities and electronic properties of the TMDC alloys ($Mo_xW_{1-x}S_2$, $MoS_{2x}Se_{2(1-x)}$ etc.) and show that alloy formation is favourable at room temperature[58]. Chemical vapour deposition, solvothermal methods, or exfoliation in layered structure from bulk crystals can all be used to synthesize these materials.

1.6 Exciton-plasmon coupling

Surface plasmons are coherent and collective oscillations of free electrons that occur on the surface of metal nanostructures when excited by incident light[59]. Surface plasmons can be classified into two modes based on the propagation length: localised surface plasmon resonance (LSPR) and surface plasmon polaritons (SPPs)[60–62]. Excitations of the conduction electrons in metallic nanostructures that are non-propagating and might be coupled to the electromagnetic field are known as LSPR. The form, size, and surrounding dielectric of metallic nanostructures can actively tune their LSPR frequency. Unlike LSPR, excitations in the SPPs mode, can propagate along the interface between a metal and a dielectric, and can be controlled by the surrounding environment in the vicinity of the metal/dielectric interface. Two-dimensional (2D) semiconductors, such as atomically thin films of transition metal dichalcogenides (TMDCs), are gaining popularity as a new platform for studying and exploiting exciton-plasmon coupling[63–65]. Several recent studies have demonstrated that hybridizing monolayer TMDC with metal nanostructures results in varying degrees of exciton-plasmon coupling and increased light absorption and emission. As a result, the strong light-matter interactions at the ultimate atomic-scale thickness allow TMDCs to be used in ultrafast photodetectors, ultrathin photovoltaics, optical communications, and light-emitting devices etc[60,66].

1.7 Van der Waals heterostructures

Conventional semiconductor heterostructures are important in many fields, including the fabrication of LASER, high electron mobility transistors (HEMT), heterojunction bipolar transistors, and so on. The formation of a triangular quantum well at the interface of two dissimilar materials allows electrons to be confined in two dimensions, leading to the formation of a 2D electron gas. A clean interface enables high electron mobility, which is essential for studying various interesting quantum confinement phenomena in condensed matter physics, such as integer and fractional quantum hall effects[67], quantum spin hall effects[68,69], Bloch oscillations of electrons[70], exciton-polariton condensation[71], and so on. However, the cost of fabricating such junctions is high due to the requirement of costly fabrication techniques such as molecular bean epitaxy (MBE) or complex chemical vapour deposition (CVD) among others.

The success of conventional heterostructures prompted the idea of stacking various van der Waals materials in the desired order to investigate a new set of 2D hybrid materials. Whereas complex epitaxial growth techniques are required to create a clean interface in a conventional heterostructure, the stability of atomically thin van der Waals materials can be used to create high quality interfaces by simply stacking one atomic layer on top of the other. A mechanical attachment process like this does not require any lattice matching criteria. As a result, multiple layered materials with different lattice constants are contacted with one another, forming heterostructures. To stack multiple layers, similar attachment processes can be used[72,73]. Van der Waals interactions in layered materials are not limited to interplanar interactions. Indeed, van der Waals forces interact with any passivated, dangling-bond-free surface. As a result, any layered 2D material can be combined with a variety of different dimensional materials to form mixed-dimensional vdW heterostructures. Such 2D+nD (n = 0, 1, and 3) material combinations have begun to emerge, representing a much broader class of vdW heterostructures for further investigation[74].

1.8 Photodetection mechanism

Conventional photodetectors function as light sensors, producing an electrical signal when exposed to light. A variety of physical mechanisms can be involved to convert an optical signal into electrical signals, such as, photoconducting effect, photogating effect, photovoltaic effect, photothermoelectric effect, bolometric effect, plasma wave assisted photo detection. The

governing detection mechanism is determined by the design scheme and materials used. The underlying physical mechanism of photodetection determines detection ability and detection speed. The sections that follow provide a brief description of various photodetection mechanisms.

1.8.1 Photoconducting effect

When photons are absorbed, the electrical conductivity of conventional semiconductors is modified. Carrier densities reach a steady state value as a result of the equilibrium between electron-hole (e-h) pair generation and recombination in the presence of light. A typical photoconductor is made up of a semiconductor channel between two ohmic contacts. In dark condition, the channel is allowed to flow only a small source-drain current (dark current, I_{dark}) under an applied bias (V_{ds}) between the electrodes. Under illumination, photons with energies greater than the semiconductor's bandgap are absorbed, resulting in the formation of electron-hole pairs. The electric field due to the applied bias then separates the photoexcited electron-hole pairs, and the free charge carriers drift in opposite direction and are collected in the source/drain electrodes. This process causes a net increase in channel current. As the change in electrical conductivity depends on the photocarrier densities involved in electrical transport, this phenomenon is known as the photoconductivity effect[38]. For photodetection, various semiconductor-based photodetectors such as Silicon, Germanium, CdS, and others rely on this photoconductivity effect.

1.8.2 Photogating effect

In photogating effect[75], the effective Fermi energy (E_F) of the main conducting channel varies with light illumination. In the presence of light, a pseudo gate voltage appears and shifts the effective Fermi energy, resulting in a change in the channel's net conductivity. A light insensitive material (channel/receiver) is typically attached to a light sensitive material (detector). When light is present, one type of photogenerated carrier (e/h) is transferred to the conducting channel (receiver), leaving the photoactive material charged. The interfacial electric field (E), which may develop due to the initial Fermi energy (E_F) difference between the two materials, causes selectivity in the charge transfer process. An external electric field generated by a gate voltage applied to the channel (field effect transistor (FET) configuration) can also influence the electric field. Efficient charge separation via photogating effect exhibits

extremely high gain, resulting in extremely high photosensitivity. However, the device speed may be constrained by a sluggish charge carrier dynamics in the photoactive material.

1.8.3 Photovoltaic effect

In photovoltaic effect, a built-in electric field is used to separate photogenerated charge carriers and travel in opposite directions. Normally, the built-in electric field is generated at a junction (depletion region) where the work functions of the materials differ significantly. Photodetectors that use the photovoltaic effect are commonly referred to as photodiodes. In general, the photodiode family includes PN photodiodes and the Schottky barrier photodiodes. The PN photodiodes are formed by two oppositely doped semiconductors and for the Schottky barrier photodiodes a semiconductor and a metal interface are needed. In the dark, a photodiode typically exhibits an asymmetric current-voltage characteristic (rectifying behaviour), whereas under illumination, the device can function in two modes: photovoltaic (at zero bias) and photoconductive (under reverse bias). In photovoltaic mode[76,77], the built-in electric field separates photogenerated electron-hole pairs which are collected at opposite electrodes, resulting in a significant photocurrent (short-circuit current, I_{SC}). The electrical output can also be photovoltaic (open-circuit voltage, V_{OC}) if the circuit is kept open. The lowest dark current is achieved by a photodiode operating in this mode, which improves detectivity and maximises linearity and sensitivity. When operating in photoconductive mode, the built-in and external electric fields have the same general direction, increasing the separation efficiency of the electron-hole pairs as well as the response speed due to a shorter carrier transit time and decreased diode capacitance. A photodiode typically has a maximum unity gain, which is much lower than the photoconductive or photogating effect.

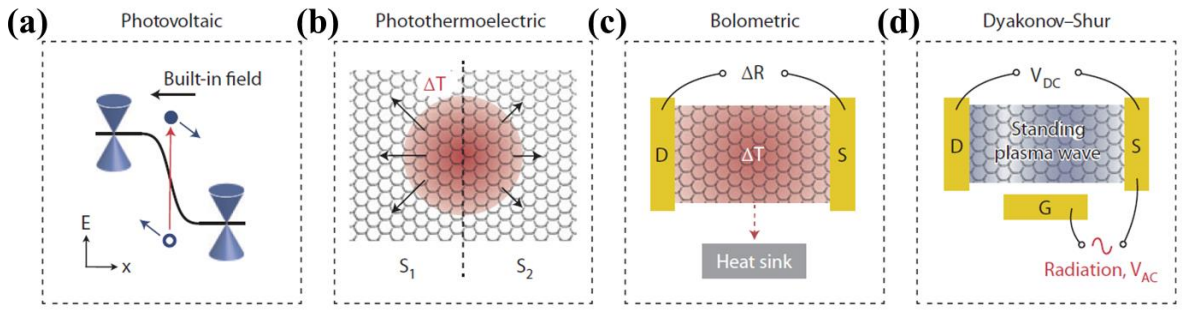

Figure 1.13: *Mechanisms of light detection. Schematic presentation of various types of photo signal detection like (a) photovoltaic, (b) photothermoelectric, (c) bolometric, (d) plasma wave assisted photodetection. Figures are adapted from Ref. 75.*

1.8.4 Photo-thermoelectric effect

The local temperature difference of the charge carriers, which causes them to diffuse to the relatively cool side and produce a voltage, is the source of the photo-thermoelectric effect[78,79]. Through the Seebeck effect (or thermoelectric effect)[78], voltage difference can be found due to this temperature difference, namely the photothermoelectric voltage (V_{PTE}). The generated photo-thermoelectric voltage V_{PTE} can be written as

$$V_{PTE} = (S_1 - S_2)\Delta T \quad \ldots\ldots\ldots\ldots\ldots\ldots\ldots\ldots\ldots\ldots \quad (1.21)$$

Where, S_1 and S_2 denote the Seebeck coefficients of the two substances and ΔT is the temperature difference. The photo-thermoelectric effect cannot exist in a uniform semiconductor because negligible temperature gradients. In order to obtain temperature gradients, a device must either be locally illuminated or globally illuminated if different parts of the device have different absorption coefficients.

1.8.5 Bolometric effect

Bolometers display the change in conductance caused by a change in material temperature (T). In such detectors, incident radiation power (P) generates heat. Temperature dependent conductivity is measured by measuring current while using a constant external biassing voltage. The thermal resistance, defined as $R_{TH} = \frac{dT}{dP}$, determines the sensitivity of these detectors. The response time can be determined by the heat capacity (C) of the material using the formula $\tau = R_{TH} \times C$. As a result, a material with a lower volume density will have a lower C, and thus a shorter response time, allowing for faster signal detection[80].

1.8.6 Plasma wave assisted photodetection

A cavity for plasma waves is formed by a field effect transistor (FET) made of 2D electron gas. Plasma waves travel faster than momentum relaxation time between drain-source contacts in a weakly damped condition. As a result, constructive interference can occur, resulting in a resonantly amplified response. Even though the plasma wave is alternating current (AC), rectification occurs due to the nonlinear electrical response of the 2D electron gas in the transistor channel, resulting in a net DC voltage between the source-drain terminals. The photoresponse is calculated from the peaks at odd multiples of the lowest frequency plasma waves. THz radiations can be detected using plasma coupled photodetection[81].

1.9 Photodetector figure of merits

The detection performance of photodetectors, made of various materials and geometries is typically compared using several key parameters[75,82,83]. We will provide a succinct overview of these parameters in the section that follows.

1.9.1 Photoresponsivity (R)

The ratio of the output photocurrent or photovoltage to the input optical power on the active region of the device is known as the photodetector's responsivity (R). With the help of this parameter, you can determine the photodetector's output photocurrent or photovoltage for a specific incident illumination power at a specific wavelength. The photoresponsivity of a device can be represented as

$$R = \frac{I_{ph}}{P_{Light}} \quad \ldots\ldots\ldots\ldots\ldots\ldots\ldots\ldots\ldots\ldots \quad (1.22)$$

where, I_{ph} is the generated photocurrent of the device and P_{Light} is the input optical illumination. The unit of photoresponsivity is A/W.

1.9.2 External Quantum Efficiency (EQE)

External quantum efficiency (EQE) is the ratio of the number of electron-hole pairs contributing to the photocurrent to the number of incident photons. It can be defined as

$$EQE = \frac{\frac{I_{ph}}{e}}{\frac{P_{Light}}{h\nu}} \quad \ldots\ldots\ldots\ldots\ldots\ldots\ldots\ldots\ldots\ldots \quad (1.23)$$

Where, e is the electron charge, h is the Plank's constant and ν is the frequency of the incident light. For a photodetector to have a large EQE, the optical absorption of the active layer must be high while carrier recombination and trapping before collection must be kept to a minimum.

1.9.3 Signal to Noise Ratio (SNR)

Noise is always present in a photodetection process, limiting the detection of small amounts of radiation energy by causing a random fluctuation in the device's output. Low noise is important for a photodetector to determine the lowest detectable output signal strength. Then, the SNR can be defined as

$$SNR = \frac{Signal\ power}{Noise\ power} \quad \ldots\ldots\ldots\ldots\ldots\ldots\ldots\ldots\ldots\ldots \quad (1.24)$$

To detect the output signal properly, the SNR must be greater than 1.

1.9.4 Noise equivalent power (NEP)

The least amount of optical power that must require to get a signal to noise ratio 1 at 1Hz bandwidth is called noise equivalent power (NEP). It is defined as

$$NEP = \frac{P_1}{\sqrt{\Delta f}} \quad \dots\dots\dots\dots\dots\dots\dots\dots\dots\dots\dots\dots \quad (1.25)$$

Where, P_1 is the incident optical power to get SNR 1 and Δf is the frequency bandwidth. Also, the NEP can be written as

$$NEP = \frac{\sqrt{S_I}}{R} \quad \dots\dots\dots\dots\dots\dots\dots\dots\dots\dots\dots\dots.. \quad (1.26)$$

Where, S_I is the total noise spectral density consisting of 1/f noise, thermal noise and the shot noise and R is the photoresponsivity. The unit of NEP is $W/Hz^{0.5}$.

1.9.5 Specific detectivity (D^*)

A useful parameter for comparing the detection capabilities of photodetectors with various materials and geometries is the specific detectivity (D^*). The specific detectivity is defined as

$$D^* = \frac{\sqrt{A}}{NEP} \quad \dots\dots\dots\dots\dots\dots\dots\dots\dots\dots\dots\dots\dots \quad (1.27)$$

Where, A is the effective area of the device. The D^* is independent of the area because total device noise is normally proportional to the square root of the area.

1.9.6 Response speed

The capability of a photodetector to follow a rapidly modulated optical signal is determined by its response speed. The rise time τ_{Rise} and fall time τ_{Fall} are commonly used to characterise a photodetector's response speed. The rise time τ_{Rise} (and the fall time τ_{Fall}) are defined as the time interval required for the response to rise (decay) from 10% (90%) to 90% (10%) of its peak value. In certain applications, like optical communication, a photodetector with a fast response speed is important. In general, a photodetector's overall response speed is determined by its bandwidth Δf, which includes intrinsic bandwidth and radio frequency (RC) circuit-limited bandwidth.

1.10 Noise mechanism in photodetectors

The understanding of noise and its mechanism is important in electronic devices like photodetectors[84]. The magnitude of noise in an electrical signal determines the lowest value of signal that can be reliably detected. A low signal-to-noise ratio (SNR) gives low detection

capabilities. The noise in the output signal is caused by the uncertain (probabilistic) nature of the physical processes underlying the photodetection mechanism. In photodetector devices, a variety of noises, including flicker noise, thermal noise and shot noise may be present. The origin and the role of different type of noises are discussed in this section.

1.10.1 Flicker noise (1/f noise)

Flicker noise, also known as 1/f noise, is one of the most common sources of noise when working at low frequencies[85,86]. The trapping-detrapping mechanism of charge carriers is the primary source of 1/f noise in metal oxide semiconductor field-effect transistors (MOSFET)[87], graphene field effect transistors, or other semiconductor based devices. The presence of trap states in the oxide can change the carrier density (n) by adding or removing carriers from the channel. Random variations in carrier density causes conductivity fluctuations, which result in noise with a 1/f frequency. Moreover, these charge fluctuations may cause the fluctuations in the mobility as a result of the fluctuations in the Coulomb potential leading to low frequency resistance noise. Hooge's empirical formula is often used to quantify this noise arising primarily from the mobility fluctuations and is thus known as the Hooge model[85]. Since both these mechanisms are present in realistic devices, various models are proposed based on correlated number and mobility fluctuations. The normalised noise in voltage (V) or current (I) is inversely proportional to the total number of electrons (N) present in the conductor. The flicker noise power spectral density (PSD) can be written as

$$S_I(1/f) = \frac{\gamma_H I^2}{N f^{\alpha}} \quad \ldots\ldots\ldots\ldots\ldots\ldots\ldots\ldots\ldots\ldots \quad (1.28)$$

where, γ_H is the Hooge parameter, I is the measured current in the device, α is the exponent which is equal to 1 when the noise source is purely 1/f in nature.

1.10.2 Thermal noise

Any typical electrical conductor experiences a small but discernible change (noise) in the electrical current flowing through it due to the thermal motion of the charge carriers. In their respective experimental and theoretical findings, Johnson and Nyquist quantified this noise value using an electrical analogue of gas pressure[88]. The thermal motion of charge carriers was assumed to agitate the electrical modes of oscillation. A conductor of resistance R is simplified as a lossless transmission line with a resistance of value R at each end. The electrical analogue of gas pressure allows considering the thermodynamic equipartition law and gives the energy per mode of oscillation to be k_BT, where K_B is the Boltzmann constant and T is the conductor's

temperature. The total current noise due to thermal agitation in a conductor of resistance value R is estimated using Nyquist's derivation as,

$$S_I\,(Thermal) = \frac{4K_BT}{R} \quad \ldots\ldots\ldots\ldots\ldots\ldots\ldots\ldots \quad (1.29)$$

The formula also shows that the noise value (S_I (Thermal)) is solely determined by the resistance value (R) of the conductor and is unaffected by the shape or material of the conductor.

1.10.3 Shot noise

Walter Schottky first proposed the concept of shot noise in 1918 while studying current fluctuations in vacuum tubes due to the photoelectric effect. Shot noise in electrical circuits occurs because current is carried by a discrete number of charges (electrons). The shot noise (SI (Shot)) of an electronic device can be defined as

$$S_I(Shot) = \sqrt{2qI_{dark}} \quad \ldots\ldots\ldots\ldots\ldots\ldots\ldots\ldots \quad (1.30)$$

Where, I_{dark} is the current flowing through the device in dark condition. When compared to other noise sources like thermal noise or flicker noise values, S_I (Shot) is typically much lower. Shot noise should be considered for low current values where the number of charge carriers contributing to conduction becomes comparable with the uncertainty in the number of electron injection events across the current-probes.

1.11 Photodetection with van der Waals heterostructures

With strong light-matter interactions, layer-dependent bandgaps, high in-plane carrier mobility, excellent stretchability/flexibility, high transparency, and high current-carrying capacity, 2D van der Waals materials have proven to be promising photodetection candidates, generating considerable research interest from both academic and industrial communities[89].

1.11.1 Graphene photodetectors

High carrier mobility, band-structure dependent electronic noise, and sources of unconventional information like valley hybridization, among other superior electronic properties of graphene, have all confirmed the material's potential use in researching a variety of physical phenomena. Because of its zero-band gap semiconducting behaviour, graphene has ideal photoelectric properties such as wide spectral response and fast response. However, with a low light absorption rate of 2.3%, bare graphene has a limited applications in optoelectronics.

In 2011 Prof. Pablo Jarillo-Herrero and his group first demonstrate the use of graphene's electron-phonon interaction, one of its fundamental properties, in a photodetector[90]. The generation of electron hole pairs is caused by photon absorption. Because of the weak electron-phonon coupling in graphene, photogenerated electrons remain hot ($E_{photoelectron} > E_F$) for a longer time (100 ps). A longer lifetime allows hot electrons to diffuse to a relatively colder region, generating a thermoelectric voltage. The presence of a p-n junction boosts thermoelectrically generated photovoltage (**Figure 1.14**). This mechanism of photovoltaic generation is also known as the Photothermoelectric effect.

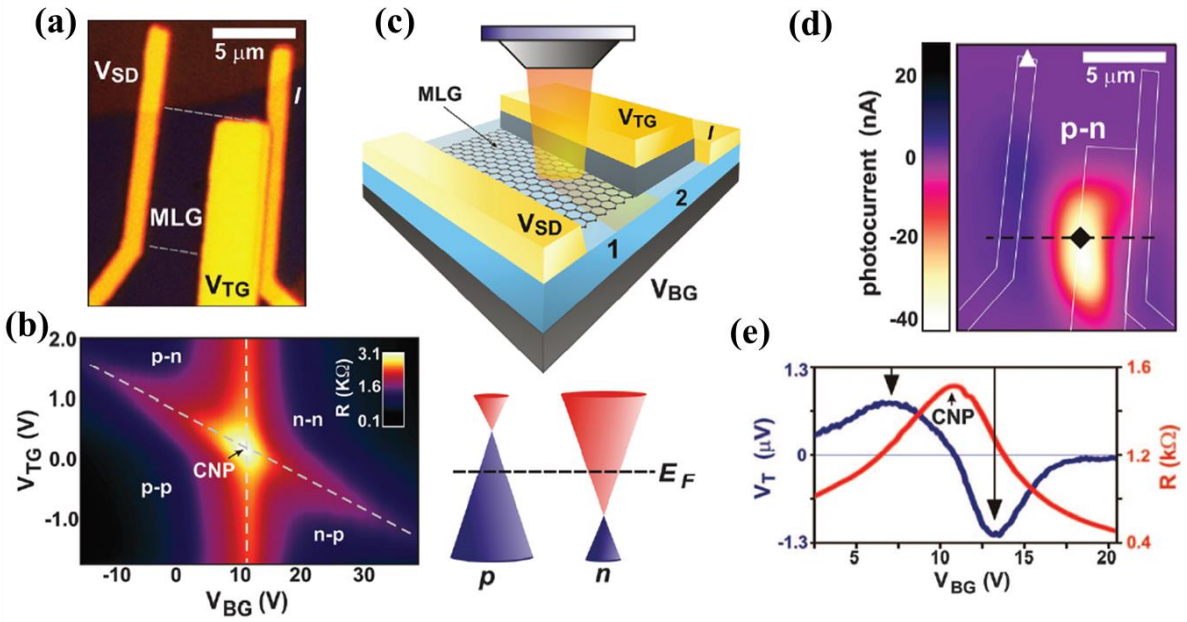

Figure 1.14: *Hot carrier assisted photoresponse in graphene. (a) Optical image of the graphene device where boron-nitride is used as top gate dielectric. MLG indicate monolayer graphene. (b) Transfer characteristics in the operational range of V_{BG} and V_{TG}. Doping types in the bottom-and-top gate region is indicated by p and n signs. (c) Scheme of the device in the p-n doped junction (top panel). Bottom panel show respective electronic band structure of monolayer graphene. E_F indicate Fermi energy. (d) Spatial dependence of photocurrent. (e) Back gate voltage dependence of thermovoltage and resistance at V_{TG} = 2.0 V, V_{SD} = 0 V, and 40 K temperature. Here 1 mW optical power is used at the triangular spot shown in (d). Figures are adapted from Ref. 90.*

Also, an ultra-broadband photodetector based on a graphene double-layer heterostructure is reported by Prof. Zhong and his group[91]. The phototransistor device is made up of two stacked graphene monolayers separated by a thin tunnel barrier. Under optical illumination, photoexcited hot carriers generated in the top layer tunnel into the bottom layer, resulting in charge accumulation on the gate and a strong photogating effect on channel conductance. The

device offers broadband photoresponse from visible to midinfrared even in the room temperature. The device schematic and the energy band diagram are represented in **Figure 1.15a** and **1.15b** respectively. In a graphene double-layer heterostructure, hot carrier tunnelling as a photodetection mechanism provides a viable route for ultra-broadband and high-sensitivity photodetection at room temperature.

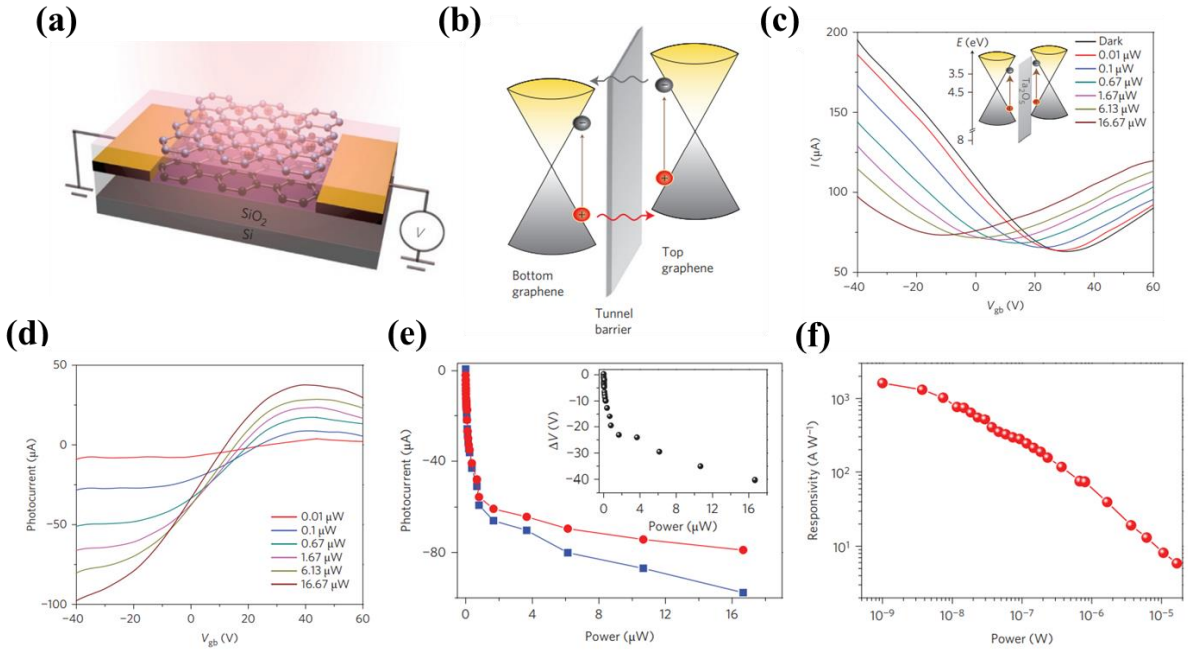

Figure 1.15: *Double-layer graphene heterostructure photodetectors. (a) Schematic of device. (b) Schematic of band diagram and photogenerated hot carrier transport under light illumination. Electrons and holes are represented by grey and red spheres, respectively. Vertical arrows represent photoexcitation, and lateral arrows represent tunnelling of hot electron (grey) and hole (red). (c) Transfer characteristics of the graphene photodetector under different illumination powers with V_{ds} = 1 V, λ = 532 nm. The energy band diagram of the graphene/Ta_2O_5 /graphene hybrid (Inset). (d) Gate dependent photocurrent under different illumination powers. (e) Illumination power dependent photocurrent at -40 V (blue squares) and -20 V (red circles) backgate voltages. Shift of Dirac point (V_D) as a function of illumination power (Inset). (f) Photoresponsivity (R) as a function of illumination power. Adapted from Ref. 91.*

Band structure engineering in nanostructures can aid in the extension of device response across a wide range of wavelengths. It can also be used to control the photocarrier generation-recombination mechanism, which determines the strength of the photo signal. Zhang et al[92].

used the concept of band structure engineering to improve the photoresponse in graphene. By patterning graphene quantum dots (GQDs) on monolayer graphene sheet, a bandgap can be created in its electronic bands (**Figure 1.16a**). The graphene channel's midgap band (MGB), created in its electronic bands (**Figure 1.16a**). The graphene channel's midgap band (MGB), which results from defects on the surface and at the edges of GQDs, is indicated by the red-shaded area (**Figure 1.16b**). Bandgap E_g is the result of quantum confinement in the electronic states of GQDs. The high photoresponsivity of these devices is attributed to the photo-electrons being trapped in MGB as the hole circulates in the conduction channel. Large photoconducting gain is made possible by the long lifetime of e-h pairs, which causes a larger photoresponse. These GQDs-based devices exhibit photoresponsivity as high as 8 A/W in the broad visible to mid-infrared region.

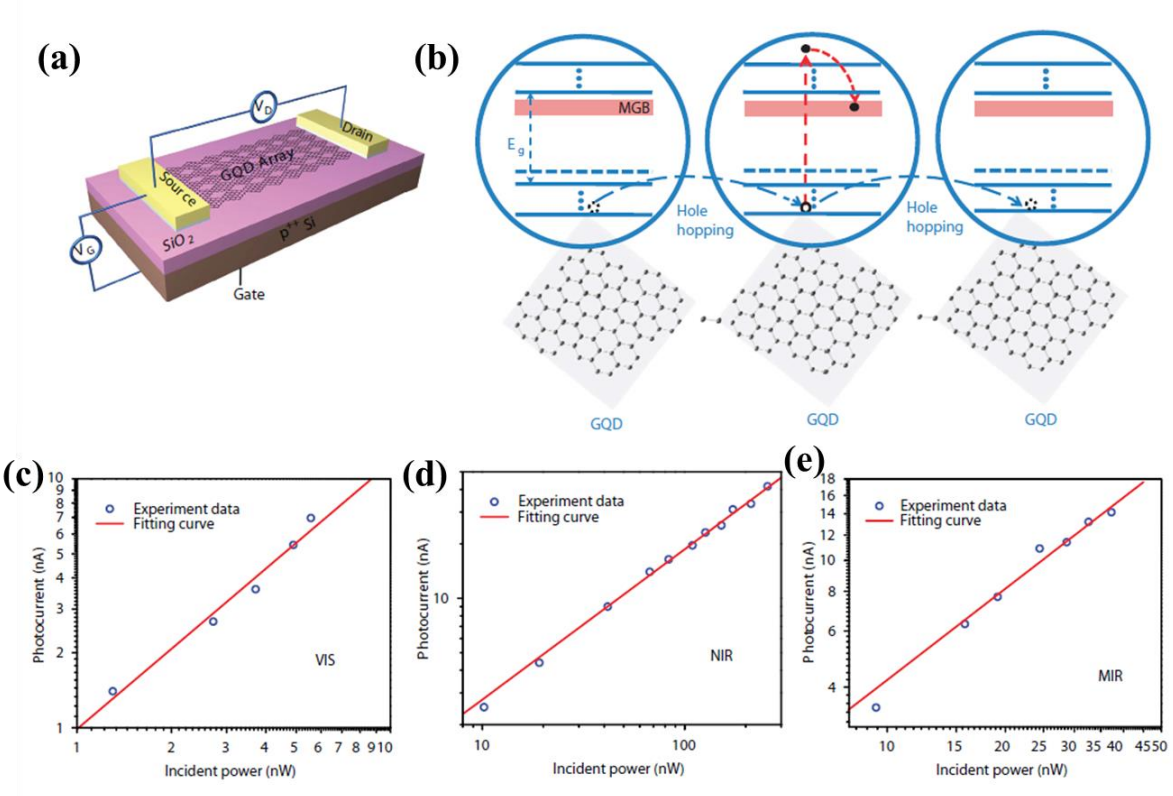

Figure 1.16: *Photoresponse in bandgap engineered graphene. (a) Schematic of the Device. (b) Schematic representation of the photocurrent generation in the device. Photocurrent as a function of illumination power with excitation of (c) 512 nm. (d) 1.4 μm. (e) 10 μm. Adapted from Ref. 92.*

1.11.2 Graphene based hybrid photodetectors

A common technique for overcoming graphene's absorbance-related limitations is to combine high light-absorbing materials with graphene to create heterostructures. When a van der Waals (vdW) material is combined with other materials to form a hybrid structure, the optoelectronic response becomes even more interesting. Depending on the application, the other materials may or may not be van der Waals materials. The interlayer hybridization in the hybrid material is critical in controlling the overall structure's response. Most importantly, such 2D materials (Graphene) can be integrated with a class of materials with different dimensionalities. In this section, a survey of mixed-dimensional vdW heterostructures is made with a focus on their use in optoelectronic devices.

1.11.2.1 2D-0D hybrid photodetectors

Based on the response spectral range, graphene-based photodetectors are classified as UV, visible, and infrared. The graphene-QDs heterostructure, with its unique advantages of light-absorption capacity, quantum effects of QDs, and high charge mobility of graphene, plays a significant role in approaching high R and D^* in all three types of graphene-based photodetectors. Carbon QDs with high UV light absorption rates have been hybridized with graphene to fabricate graphene-carbon QDs hybrid photodetectors which offers slightly higher R of 0.29 A/W than graphene photodetectors[93]. Also, to report a visible blind UV

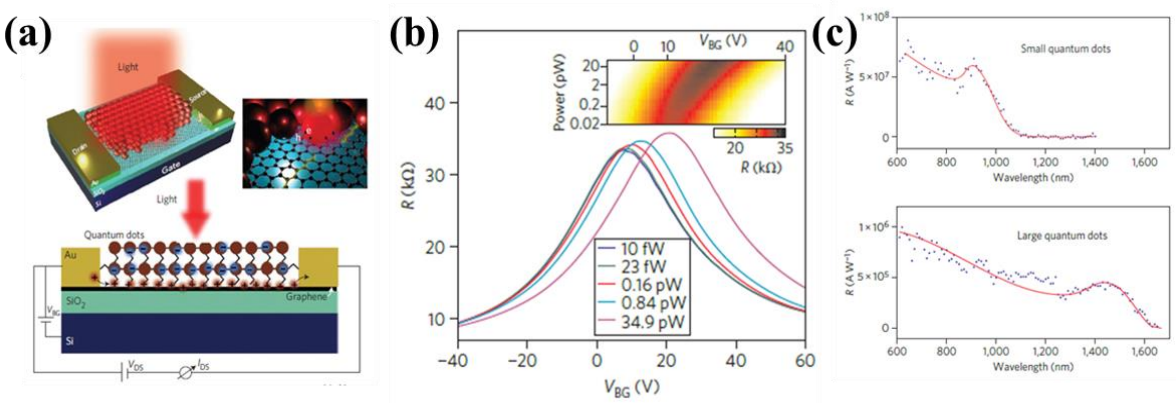

Figure 1.17: *Graphene-quantum dots hybrid phototransistors. (a) Schematic of the hybrid device where PbS quantum dots coated on a graphene flake on a Si/SiO_2 substrate. (b) Resistance (R) as a function of back-gate voltage (V_{BG}) of the hybrid device for increasing illumination intensities with λ = 500 nm. (c) spectral photoresponse of two hybrid phototransistor devices with PbS quantum dots of different sizes with exciton peaks at either 950 nm (top panel) or 1,450 nm (bottom panel). Adapted from Ref. 101.*

phototransistor, a graphene-ZnO hybrid phototransistor is created by printing ZnO quantum dots on graphene channels[94]. Also, the addition of QDs with graphene heterostructures has the potential to improve visible photodetectors' performance. High-performance visible photodetectors have been created using CdS QDs and graphene hybrids with E_g values between 1.7 and 2.4 eV (corresponding to the wavelength of visible light)[95]. When combined with graphene, some perovskite quantum dots exhibit excellent visible photoresponse[96,97]. A hybrid photodetector made of monolayer graphene covered with a thin layer of dispersive organolead halide perovskite nanodots has a high photoresponsivity of 6×10^5 A/W[97]. By combining Si QDs[98], HgTe[99], and Ti_2O_3[100] nanoparticles with graphene field effect devices, infrared photodetectors based on the same graphene-QDs hybrid structure are also reported.

Integration of another semiconductor with graphene transistor to improve the photodetection capabilities was first proposed by Konstantatos, G. *et al.*[101]. In this report, they used semiconducting quantum dots (PbS) as sensitizers in graphene field effect transistor (FET) (**Figure 1.17a**). The optical absorption of quantum dots results in photoexcited charge carriers with the holes transferred into the graphene channel and are then efficiently collected from the graphene FET channel due to high carrier mobilities, ultimately providing responses exceeding 10^7 A/W. The applied gate voltage can be used to tune this responsivity, and changing the quantum dot size can control the spectral response (**Figure 1.17b**). This phenomenon is also known as the photogating effect (**Section 1.8.2**) because the charged PbS acts as a local gate, altering conductivity by changing the effective charge carrier concentration in the graphene channel. Because of graphene's high carrier mobility, low charge carrier transit time between the source-drain channel is possible, and the long lifetime of the photogenerated e-h pairs results in a large gain in photoconductivity, resulting in a large photoresponsivity. These devices also have a high detectivity of 10^{13} Jones. Changing the response band is accomplished by using QDs of varying sizes. Because smaller QDs have a larger excitonic gap than larger QDs, the peak response appears at shorter wavelengths (950 nm) compared to 1450 nm for larger QDs (**Figure 1.17c**). This also establishes photoconductivity's tunable nature by varying the size of QDs. These studies show that photocarriers from one material (PbS) can be transferred to another (graphene) with high electronic mobility. The physical proximity of the materials and the interfacial electric field aids in the transfer of one type of charge carrier. When charge carriers are transferred to the highly mobile region, they move quickly, resulting in a low carrier transit time and a long carrier lifetime, resulting in superior photoresponse.

1.11.2.2 2D-2D hybrid photodetectors

Due to the versatile and novel properties of 2D materials, 2D-2D vdW heterostructures have been widely researched and have shown promising application in high-performance photodetectors. Because there are no dangling bonds on the surface, various 2D materials can be assembled using vdW force while ignoring the lattice mismatch. Generally, 2D-2D heterostructure can be fabricated by CVD or mechanically dry transfer method. Heterostructures that are stacked vertically can effectively capture light. The photoresponse is tuned using an external electric field in the graphene-MoS_2-graphene and graphene-MoS_2-metal type of transistors that Yu et al. presented (**Figure 1.18**)[102]. The integration of single or dual gates under the vertical heterostructure to adjust the band slope and photocurrent generation is made possible by the weak electrostatic screening effect of graphene. The graphene-MoS_2-metal type of devices achieve the highest external quantum efficiency, reaching a value of 55%, and demonstrate the highest internal quantum efficiency of 85%.

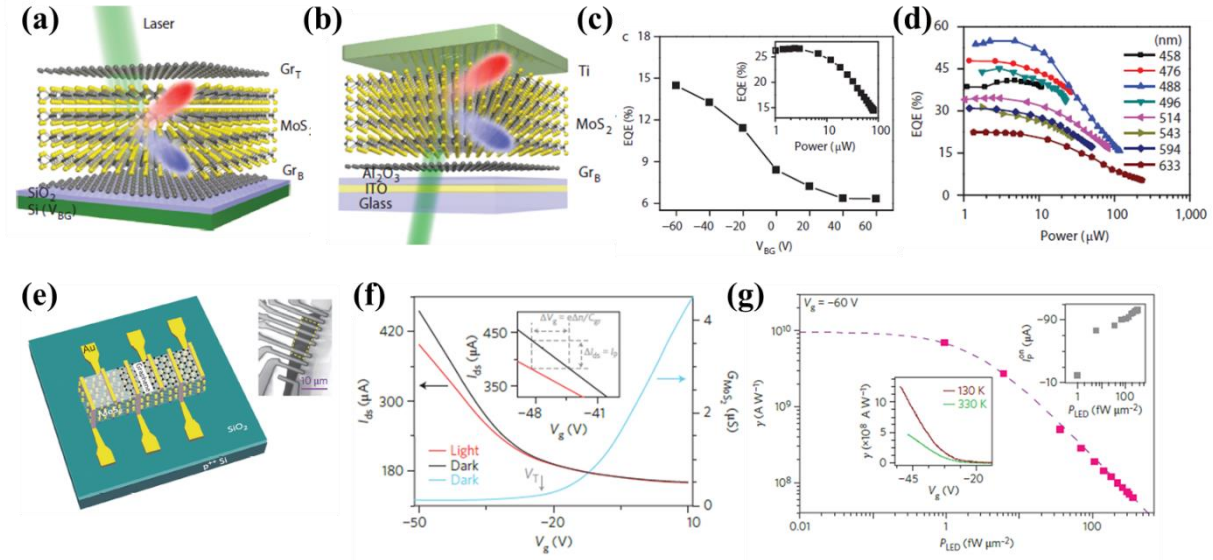

Figure 1.18: *Graphene based 2D-2D hybrid phototransistors. Schematic of hybrid (a) graphene-MoS_2-graphene, (b) graphene-MoS_2-Ti phototransistors. (c) Back gate (V_{BG}) tunable external quantum efficiency (EQE). EQE as a function of different illumination power (inset). (d) Wavelength dependent EQE. (e) schematic of the graphene-MoS_2 hybrid phototransistor. (f) Transfer characteristics of the hybrid device and the back gate tunable conductance of bare MoS_2. (g) Photoresponsivity as a function of illumination power at V_g = -60 V. Comparison of room temperature and low temperature responsivities (Bottom inset). Photocurrent as a function of illumination power. Figure 1.17a-d are adapted from Ref 102, and Figure 1.17e-g are adapted from Ref. 103.*

Graphene on few layered MoS_2 heterostructure (**Figure 1.18e**) is also reported in Roy et al.[103] and the device exhibits remarkable optoelectronic properties, including highly sensitive photodetection and gate-tunable persistent photoconductivity. The hybrid device offers photoresponsivity as high as 1×10^{10} A/W at 130 K and 5×10^{8} A/W even at room temperature (**Figure 1.18g**), making them the most sensitive graphene-based photodetectors. Also, Mehew et al.[104] reported atomically thin graphene-WS_2 heterostructure photodetectors encapsulated in an ionic polymer gate. This device offers a high responsivity of 10^6 A/W and specific detectivity (D^*) of 3.8×10^{11} Jones and able to operate at bandwidths up to 1.5 kHz.

1.11.2.3 Other hybrid photodetectors

Other aspects of mixed dimensional hybrids[74], such as 2D-1D and 2D-3D, are also reported in addition to 2D-0D and 2D-2D. Due to their novel structure and properties, 1D materials like nanowire (NWs), nanotubes, and nanobelts have attracted a lot of research in recent years. 1D materials possess many unique advantages, such as high surface-to-volume ratio, novel optoelectronic properties induced by quantum confinement effect, and superior carrier transport properties. Due to its narrow bandgap and high carrier mobility, InAs NW is a promising material for infrared photodetection. A graphene-InAs NW near-infrared photodetector was demonstrated by Miao et al.[105] Due to the built-in field, a high light to dark current ~ 5×10^2 and a good photoresponsivity 0.5 A/W have been achieved by using this device structure. Similarly, Due to its high charge carrier mobility and broadband light absorption, the single-wall carbon nanotube (SWCNT) is a promising 1D material for infrared photodetector. Planar SWCNTs film and graphene were used by Liu et al.[106] to create the heterostructure photodetector depicted in Figure 7c. Due to the broadband light absorption of SWCNTs and graphene, a photodetector using these materials was able to detect infrared light in the 400-1550 nm range. On the other hand, the combination of different 2D materials with well-developed 3D bulk semiconductors provides an advanced method for fabricating high-performance photodetector devices. Because of their unique advantages, such as easy fabrication, improved light absorption, and fast charge transfer, 2D-3D heterostructure photodetectors have received a lot of attention. Strong built-in fields in 2D-3D heterostructures can quickly separate photo-generated carriers and suppress dark current noise, resulting in high detectivity and fast response speed. For example, $PdSe_2$-Ge heterostructure photodetector has been demonstrated by Wu et al.[107] by using a few layered graphene as a transparent electrode. The device has a high responsivity in a broad spectrum covering 200-2200 nm, with a high detectivity of 1.73×10^{13} Jones and faster response time of 6.4/92.5 μs is obtained.

1.12 Motivation of the thesis

The motivation of this thesis is to fabricate large scale low-dimensional photodetector systems based on graphene and TMDCs that have high sensitivity over a wide spectral range. The bandgap of TMDCs is critical to detector performance and is central to this investigation. To create a new class of broadband photo-responsive devices that combine the superior electronic properties of graphene and the distinctive optical response of TMDCs, the primary goal has been to characterise and control the charge transfer mechanism across the graphene-TMDC interface. Transferring photogenerated carriers from TMDC to graphene is made possible by the control mechanism. The carrier transit time in the graphene channel appears to be short due to the high electronic mobility of graphene, which results in a high photo-gain and a large photoresponse. The photoresponse characteristics and corresponding physical mechanisms are studied quantitatively. The tunability of the response is confirmed using a variety of device architectures by adjusting the physical factors that affect the photoresponse. Most optoelectronic devices have been reported to use a monolayer or a few layers of graphene nanosheets, which have a very small active device area and necessitate a complex nanolithography process. As a result, wafer-scale high-performance device production for Si CMOS compatible photonic applications remains difficult. As a result, it is critical to develop a new method for producing low-cost, highly efficient devices over a large area with improved performance.

This thesis is driven by the potential to fabricate reliable, affordable, scalable, broadband photodetector devices based on graphene and TMDCs. In this aspect, solution processed TMDC QDs (WS_2 QD) are found to be suitable in compared with nanosheet counterparts for fabrication of graphene-based broadband, highly stable photodetectors because of their broad absorbance band, direct and tunable band gap, easy synthesis process and higher stability. Such comparative study on the morphology effect of TMDC nanostructures on the optoelectronic performance of graphene hybrid phototransistor is less studied. Aside from their widespread use, TMDC nanosheets face significant challenges because chalcogen vacancies in such materials cause localised deep-level defect states (DLDS), which degrade their electronic and optoelectronic properties. Composition modulation has been proposed as a potential solution for DLDS suppression, and theoretical studies have shown that ternary alloys of TMDCs are thermodynamically more favourable than their binary counterparts. Although TMDC ternary alloys outperform binary counterparts in electrical, optoelectronic, and catalytic performance,

they have received little attention in hybrid optoelectronic device fabrication also. So, integrating with graphene, these bandgap-engineered 2D ternary alloys ($MoS_{2x}Se_{2(1-x)}$) provides realistic solution to improve the device performances. Additionally, the surface plasmon of metal nanostructures can couple with TMDC excitons to produce improved optical properties like emission and absorbance which have positive impacts on optical devices. Therefore, from a fundamental as well as application standpoint, it is crucial to tune the exciton-plasmon coupling strength and combining graphene with plasmonic nanoparticles coupled TMDC (like silver nanoparticle decorated WS_2 nanosheet) has the potential to open a world of possibilities.

1.13 Aims and Objectives

The goal of this research is to gain a fundamental understanding of device functionality by developing large area graphene-TMDC based hybrid photodetector devices on rigid substrates such as Si/SiO_2 wafers. These findings indicate that these devices have the potential to compete with state-of-the-art photodetectors and that they can be used in large-scale photodetectors. To achieve this goal the following issues are addressed in this thesis:

- Development of the experimental setups to perform the experiments.
    I. Development of dry transfer setup to make artificial hybrids based on 2D van der Waals materials.
    II. Designing of photomask and optimization of photolithography down to few micron patterns.
    III. Development of high vacuum transport measurement setup with optical window.
- Fabrication of a large area graphene-WS_2 mixed dimensional phototransistor and investigation of the role of WS_2 morphology in photocurrent generation.
- Fabrication of graphene-$MoS_{2x}Se_{2(1-x)}$ alloy engineered phototransistors for UV-NIR broadband photodetection.
- Fabrication of plasmonic Ag nanoparticles coupled graphene-WS_2 hybrid phototransistors for UV-Vis broadband photodetection.

1.14 Organization of thesis

In chapter 1, a brief introduction of the material system (graphene and TMDC) are given along with their basic properties like electronic structure, band structure and their importance in optoelectronic devices. Also, we provide the introduction to the fundamental theory of photodetectors. It shortly describes the different physical mechanisms for generating photoresponse and the important figure of merits of a photodetector. A detail background of the field with discussion of the previous studies indicate that there indeed enough scope for the systemic investigation of hybrid optoelectronic devices based on graphene and TMDCs. The present dissertation contains five chapters other than the introduction with an aim to study some of these issues.

In chapter 2, we describe the various experimental methods and techniques employed to carry out the measurements. We begin this chapter starting with the detailed fabrication steps about mechanical and chemical exfoliation of 2D materials and characterization techniques. Subsequently, we describe the device fabrication process like patterning electrodes and metal deposition. Then we describes the development of optoelectronic measurement setup and discuss the details of the measurement process.

In chapter 3, a highly sensitive visible phototransistor is reported with atomically thin bilayer MoS_2. To fabricate the back gated device, the mechanically exfoliated MoS_2 sheet is first transferred to a Si/SiO_2 substrate by optical microscope based dry transferred method. At 633 nm of illumination, the fabricated phototransistor has a very high responsivity ($>10^6$ A/W), which can be further tuned by back gate voltages. In addition, when the 1/f noise is considered, the device has a low noise equivalent power (10^{-15} W/Hz$^{0.5}$) and a higher specific detectivity (10^{12} Jones).

In chapter 4, We discuss the simplest way to make a super large (0.75 mm^2), mixed-dimensional, UV-Vis broadband (365-633 nm) phototransistor with an active channel made of WS_2 QDs decorated CVD graphene. The photo-absorbing material is colloidal 0D WS_2-QDs, and the conducting channel is graphene. At a low bias voltage (V_{ds} = 1 V) and an optical power as low as 0.8 μW/cm^2, a high photoresponsivity (3.1×10^2 A/W), moderately high detectivity (8.9×10^8 Jones), and low noise equivalent power (9.7×10^{-11} W/Hz$^{0.5}$) are obtained, which can

further be tuned by modulating the gate bias. This chapter also discusses the role of WS_2 morphology in generating photocurrent in hybrid devices.

In chapter 5, We systematically investigate the photo response properties of three terminal hybrid devices by decorating large area graphene with these nanosheets (x = 0, 0.5, 1) in 2D-2D configurations by synthesising nanosheets with different composites of $MoS_{2x}Se_{2(1-x)}$ (x = 0 to 1) using simple chemical methods. Among them, the graphene-MoSSe hybrid phototransistor outperforms its binary counterparts in terms of optoelectronic properties. The device has a very high photoresponsivity (>10^4 A/W), a low noise equivalent power (10^{-14} W/$Hz^{0.5}$), and a higher specific detectivity (10^{11} Jones) in the UV-NIR (365-810 nm) range, with excellent gate tunability. This chapter concludes with a possible explanation of controllable defect engineering in MoSSe, which makes this device extremely appealing.

In chapter 6, we report a lithography-free fabrication of a large area broadband superior gate-tunable hybrid phototransistor based on monolayer graphene decorated by WS_2-Ag NPs in a three-terminal device configuration. The fabricated device exhibits extremely high photoresponsivity (up to 3.2 × 10^4 A/W) which is more than 5 times higher than the bare graphene/WS_2 hybrid device, along with a low noise equivalent power (NEP) (~10^{-13} W/$Hz^{0.5}$) and higher specific detectivity ~10^{10} Jones in the wide (325-730 nm) wavelength region. The polyvinylpyrrolidone (PVP) capped silver (Ag) nanoparticles (NPs) restricts the direct charge, energy and heat transfer and enhances the optical properties of tungsten disulphide (WS_2) by surface plasmon-exciton coupling effect. COMSOL Multiphysics simulation suggests that the electromagnetic field enhancement at the vicinity of WS_2-Ag hybrid results in the amplified optical properties of WS_2 layers and the larger photoresponse. This work demonstrates a strategy towards obtaining an environment-friendly, scalable, high-performance broadband phototransistor by tuning the exciton-plasmon coupling for new generation opto-electronic devices.

In chapter 7, we give a brief conclusion of the current thesis and gives an insight about the drawbacks and the future scope of study which can be addressed in future.

Chapter 2

Experimental Details

The various experimental methods and techniques used to perform the optical and electrical measurements are described in this chapter. This includes the detail synthesis, fabrication and lithography processes used to create various heterostructures including graphene and TMDCs. The specific features of various experimental setups, such as the dry transfer setup, high vacuum optoelectronic measurement setup are discussed. Finally, the chapter concludes with a description of various electrical measurement schemes as well as characterization tools used in this work.

2.1 Materials Synthesis and Exfoliation

Different exfoliation methods, such as mechanical exfoliation, chemical exfoliation, chemical vapour deposition (CVD), pulsed laser deposition (PLD), etc., are used for 2D materials. To obtain the desired 2D materials for this thesis, we primarily used chemical exfoliation and mechanical exfoliation techniques.

2.1.1 Liquid Phase Exfoliation

One of the most adaptable exfoliation methods for the mass production of layered nanomaterials is liquid phase exfoliation (LPE)[108]. It involves creating a few layered nanosheets with high shear or ultrasound using the right solvent and materials. When a material is exposed to ultrasound, the resulting hydrodynamic force breaks the van der Waals force and helps to exfoliate the material, the weak interlayer interactions between adjacent sheets must be overcome by introducing energy during the exfoliation process. The liquid-nanosheet interface interacts to lower the net exfoliation energy and stabilise the nanosheets' dispersion in the solvent by using the right solvent. **Figure 2.1** provides a schematic representation of this procedure. A variety of techniques, including dip coating, spin coating, spray deposition, inkjet printing, etc., can be used to process the resulting dispersions into nanostructured devices with great ease.

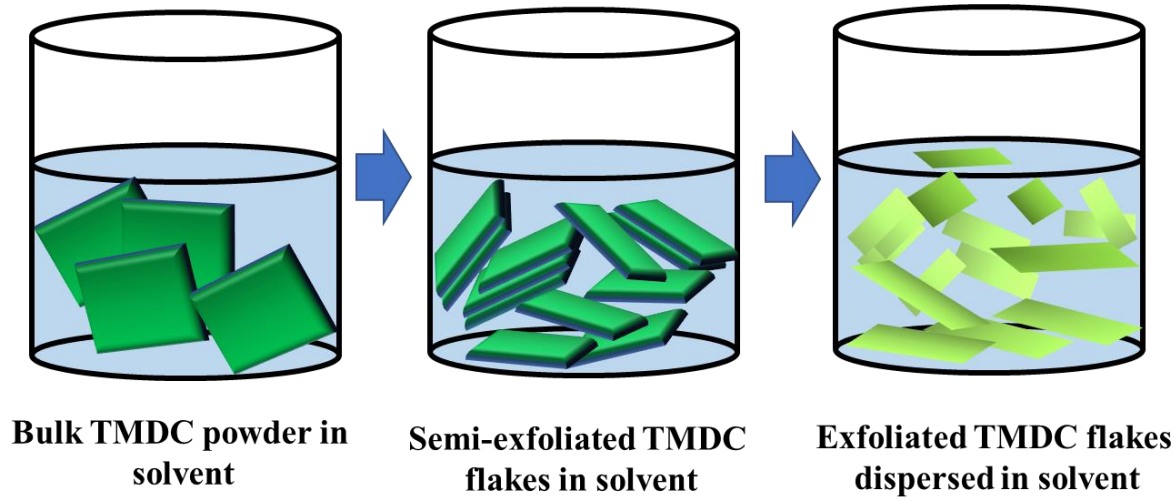

Figure 2.1: *Schematic representation of liquid phase exfoliation technique.*

2.1.2 Hydrothermal Method

One of the most common methods for preparing nanomaterials is hydrothermal synthesis[109,110]. It is essentially a solution reaction process. The chemical reactions take place in a sealed container, and the solution is heated above ambient temperature and held at a pressure greater than atmospheric pressure. The crystal growth is normally performed in an apparatus that consists of a steel pressure vessel called an autoclave and a teflon chamber kept inside the autoclave. The autoclave is typically a steel cylinder with thick walls that must endure high temperatures and pressure for an extended period. In terms of solvents, the autoclave needs to be inert. An essential component of the autoclave is the closer. Precursor that has been dissolved in solution is poured into teflon chamber so that it does not fill up more than 70% of

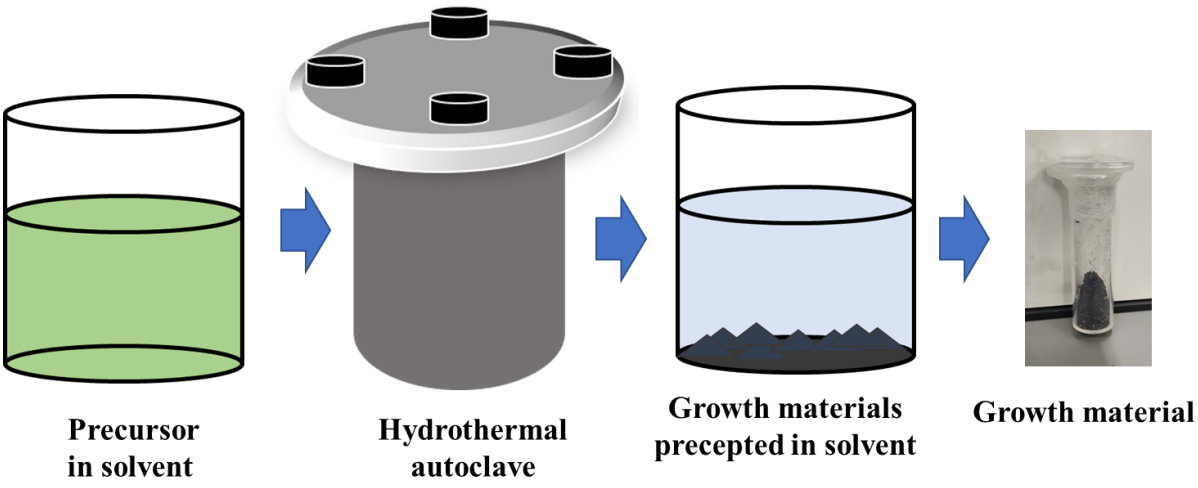

Figure 2.2: *Schematic representation of hydrothermal exfoliation technique.*

the space. The autoclave system is heated to a specific temperature, should cool to room temperature after heating, and then the material produced is stored at the bottom of the teflon chamber. **Figure 2.2** shows this schematically. Pressure and temperature play a role in the material's growth and nucleation during the hydrothermal synthesis process. For the growth of nanomaterials, the hydrothermal synthesis method has many benefits, such as relatively mild operating conditions (reaction temperature ~ 300^0 C) and minimal material loss.

2.1.3 Mechanical Exfoliation

One of the most popular and straightforward methods for producing high-quality 2D crystals is mechanical exfoliation[13,111]. Although large area samples are produced by CVD based fabrication of 2D materials like MoS_2, WSe_2, and Graphene, their lower mobility and the presence of defects and grain boundaries restrict their use for FET fabrication. As the van der Waals materials are held together by weak van der Waal forces, they can easily be exfoliated from the bulk crystal by applying a small force. Mechanical exfoliation is a simple process that involves peeling off 2D thin layers from bulk crystals with scotch tape or any other type of adhesive tape. The flakes are produced from bulk materials using a sticky tape after mechanical cleaving (exfoliation) (e.g., Scotch tape, Nitto tape etc.). Si^{++}/SiO_2 is a common substrate for exfoliation processes in which the bulk substance is physically brought into contact. The van der Waals attraction between the SiO_2 to the various materials enables some of the bulk material to be attached to SiO_2 in the form of small flakes. These flakes' typical sizes range from a few micrometres to a few tens of micrometres, and they differ significantly depending on the substrate's roughness, composition, and other factors. For instance, when obtaining a single to few layers of materials, highly polished SiO_2 exhibits lower yield than rough SiO_2. To produce better/bigger flakes, polished SiO_2 can be treated with RCA solution ($NH_4OH:H_2O_2:H_2O$=1:1:5) or O_2 plasma to increase the surface roughness. The yield of exfoliation varies depending on both the material and the substrate. Mechanical exfoliation of graphene, for example, yields significantly higher than MoS_2 (or other TMDCs) on comparable substrates. This can be attributed to either a low van der Waals force between MoS_2-SiO_2 or a strong interlayer coupling force between MoS_2 layers. To get a better yield, these TMDCs can therefore be exfoliated on other substrates, such as Polydimethylsiloxane (PMDS), and then transferred to a SiO_2 substrate. These small flakes are identified after exfoliation using a high-

resolution optical microscope (typical magnification factor 500x, 1000x). The step wish mechanical exfoliation technique is demonstrated in **Figure 2.3**.

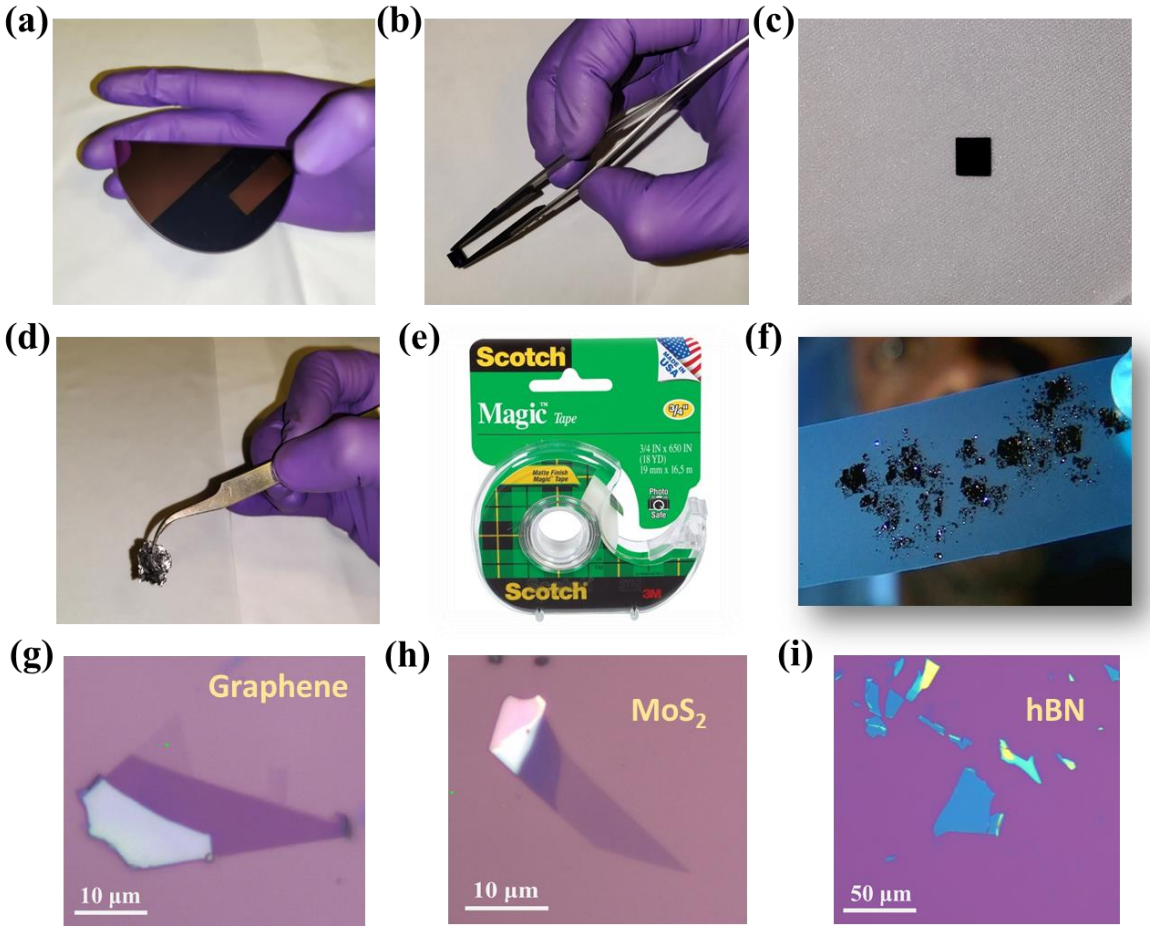

Figure 2.3: *Mechanical exfoliation technique. (a) Half-cut Si/SiO_2 wafer. (b) Small piece of Si/SiO_2 wafer (5 mm * 5 mm in dimension). (c) Clean Si/SiO_2 wafer ready for exfoliation. (d) Single crystal of 2D van der Waals material (like graphene, MoS_2 etc.). (e) Magic scotch tape for exfoliation. (f) Graphene layers on the scotch tape. Exfoliated single and few layered flakes of (g) graphene, (h) MoS_2 and (i) hBN on Si/SiO_2 wafer.*

2.2 Dry transfer and van der Waals heterostructures

2.2.1 Development of the dry transfer setup

These flakes can be transferred from one location to another while avoiding damage by using the support of a flexible substrate. A specially designed substrate coated with a sacrificial layer allows the attachment of multiple mono or multi-layer materials in any order. The attachment process is also aided by strong interlayer van der Waals attraction between different layers of

materials. A high precision mechanical micromanipulator is used to control the relative position and orientation of the layers while stacking. **Figure 2.4** depicts the dry transfer setup (micromanipulator stage). It is constructed with a commercially available optical microscope and some homemade support structures. The choice of optical microscope elements and the mechanical components are crucial in building a cost-effective setup. Here, two dry transfer setups are designed in the lab, one by using a commercially available Olympus microscope (**Figure 2.4a**) and the other by assembling various parts (**Figure 2.4b**).

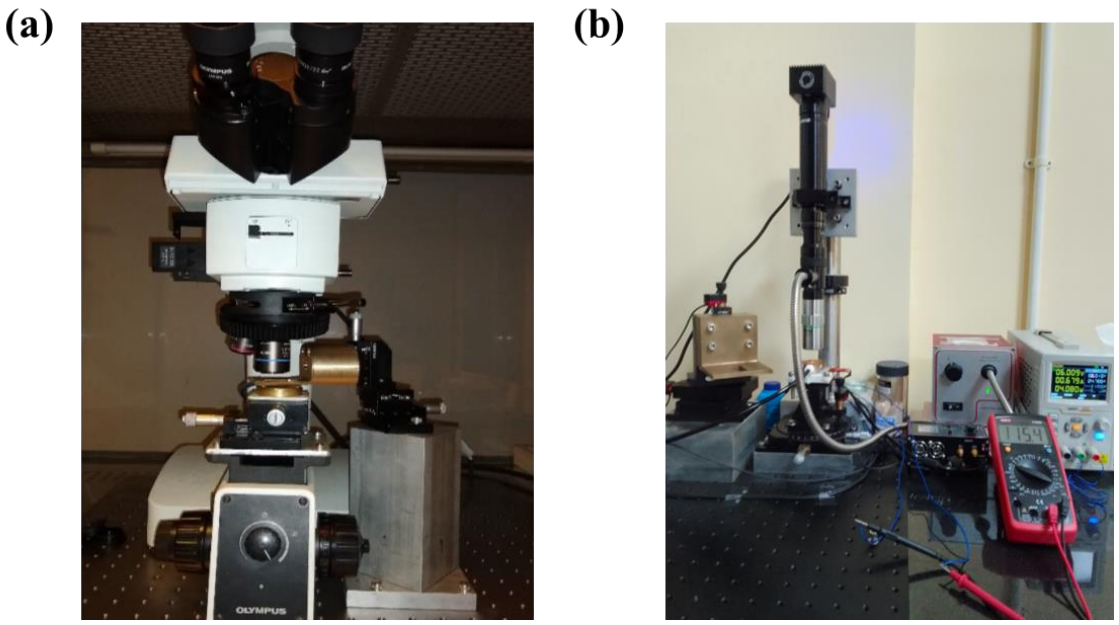

Figure 2.4: *Optical images of macroscope based dry transfer setups.*

The various components of the setups are schematically depicted in **Figure 2.5**. Using the XYZ micro controlling system, two desired samples (sample 1 and sample 2) are first vertically aligned. Both the XY stages give a precision of 1μm and help to align the materials vertically. The Z stages are critical for transferring materials for the fabrication of heterostructures. On X_1Y_1, the sample holder is mounted and heating arrangement is done for the lower sample (sample 1). The temperature of the stage is measured using a pt-100 resistance temperature sensor. When working in a closed feed-back loop, a temperature controller connected to the pt-100 and heater controls the temperature of the stage. At sample holder stage, a diaphragm pump is connected to the vacuum port, allowing for simple vacuum-and-hold mounting of the lower substrate. To prevent heat conduction to the lower XY stage, a Teflon heat isolation is used. Teflon's large thermal expansion/contraction coefficient aids in achieving extreme precision in

cooling the lower stage slowly. As a result, excellent control of the attachment is achieved, avoiding tearing/folding, and can result from the quick return of the lower stage.

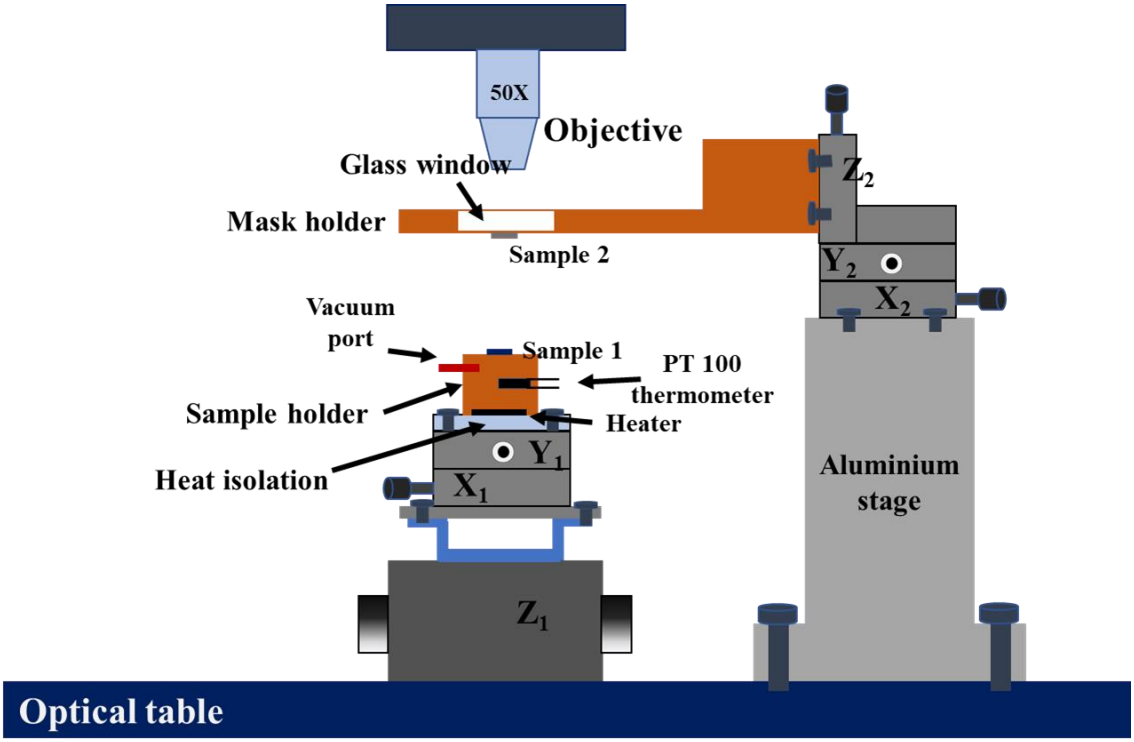

Figure 2.5: *Schematic of the dry transfer setup. The setups are developed by using a combination of components purchased from Thorlab and manufactured in the workshop.*

The second component of the setup consists of a brass-made metal mask holder and an aluminium stage that serves as the base for an identical XYZ stage (X_2, Y_2, Z_2). The mask holder has a window, and because of the step height, it can have the mask (which contains sample 2) attached at the bottom of it.

2.2.2 Making flexible mask

A flexible mask is a custom-made substrate with a sacrificial layer to support the stacking flakes during transfer. It is made up of a spherical cap on a ~ 0.5 mm transparent cover glass. The spherical surface enables us to reduce the point of contact area during pickup, allowing it to pick up only the desired flakes while avoiding the undesirable region. The substrate must be transparent so that each process can be monitored using an optical microscope. Because we are dealing with a few micrometre-sized flakes, precise control of the stacking process via a microscope is required. Furthermore, the stamp requires an adhesive sacrificial layer, the

viscosity of which can be controlled by temperature, and the residue can be removed via a solvent process after the final transfer. To make the flexible spherical cap, place a small drop of PDMS in the centre of a clean cover glass and bake for 20-30 minutes at 200^0 C. Because of the drop's high viscosity and surface tension, it spreads (before baking) over a small area on the glass plane, resulting in a natural shape like a spherical cap. The size of the cap is determined by the drop size/volume, which is chosen to keep the typical dimension of the spread on the cover glass surface within a circle of 1-2 mm diameter. A sacrificial layer (Lakme colour crush (LCC)) is used on top of the hemisphere to increase the adhesivity between the mask and the flakes. LCC is spin coated onto the mask at 8000 rpm and baked for 2 hours on a hot plate kept at 90^0 C to prepare it for the attachment process.

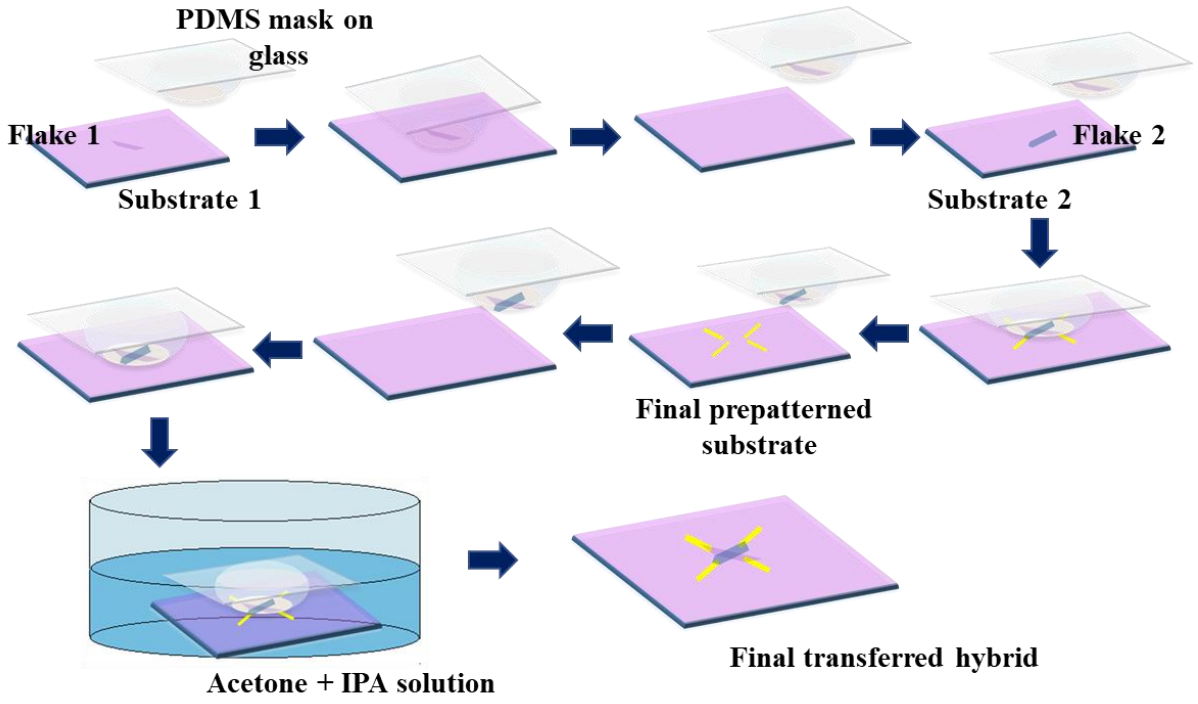

Figure 2.6: *Schematic of the process flow of dry transfer technique.*

2.2.3 Dry transfer and pick up process

Figure 2.6 depicts a step-by-step fabrication process for two-layered hybrid structures. The flexible mask, mounted to the metallic holder is first positioned downward on the top stage, making sure the concave surface is correctly aligned with the microscope's optical axis. Now, with the movement of X, Y, and Z stages, the bottom wafer containing the desired flake is

brought closer to the stamp, such that desired pickup flake comes at the centre of the stamp. The bottom stage's temperature is first raised to 80°C, and after that, by slowly moving the bottom stage in the Z direction, the flake-containing bottom stage is brought into contact with the LCC-coated stamp. After waiting for few minutes, the LCC separates from the substrate and the flake is eventually picked up by the LCC because the adhesive force of the LCC is greater than the van der Waals force of the flakes with the substrate. The entire stack is then brought into contact with a prepatterned SiO_2 wafer after all the flakes have been picked up in the desired order. The final transfer is done at a higher temperature ~ 100-120^0 C. Then the vacuum suction is removed and waited until the substrate temperature reaches room temperature. The stamp and the substrate are then immersed very carefully in 1:3 acetone-IPA mixture for 3 hours. After successfully transferred to the substrate, then hybrid samples are again immersed in pure acetone, followed by an IPA rinse for better cleanliness. For example, different hybrid stacks are shown in **Figure 2.7**.

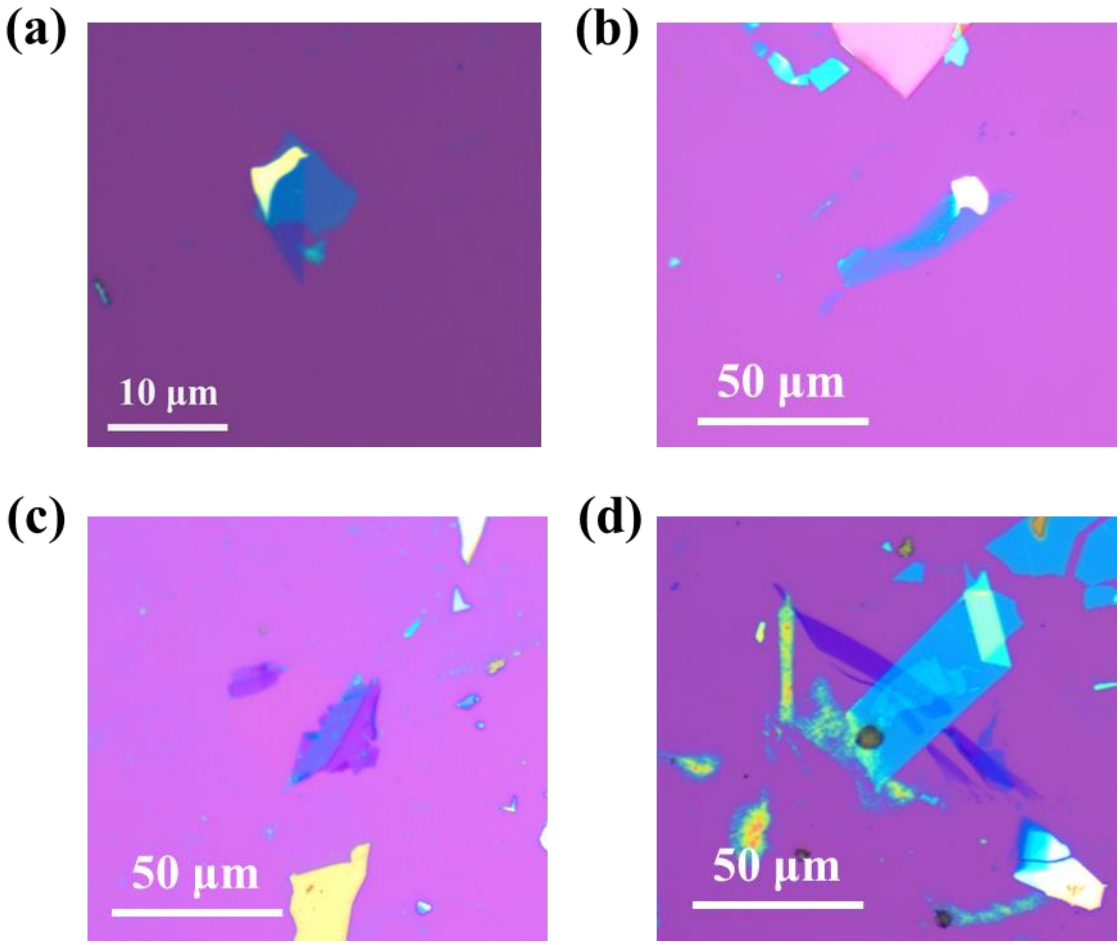

Figure 2.7: *Fabrication of different heterostructures. (a) MoS_2 on hBN, (b) hBN on MoS_2, (c) graphene on hBN and (d) graphene-hBN-MoS_2 structures.*

2.3 Materials and Interface Characterizations

2.3.1 Structural Characterizations

For newly synthesised materials, structural characterizations are critical. X-ray diffraction (XRD), scanning electron microscopy (SEM), transmission electron microscopy (TEM), and other techniques can be used to characterise the structure of a material.

2.3.1.1 X-ray Diffraction (XRD)

The crystalline material structure, including atomic arrangement, crystallite size, and defects, is investigated using the XRD technique, a non-destructive method. Here, the sample is hit by an X-ray beam that is diffracted by the atomic planes. One can determine the atomic arrangement, phase, crystallinity, thickness of films, and other different information (strain, orientations, imperfections), i.e., the overall atomic arrangements, by measuring the angles and intensities of these diffracted beams. The X-ray diffractometer is made up of an X-ray tube (the source of the X-ray), incident beam optics (before the beam hits the sample), and goniometer (The platform that holds the sample stage and detector) with a sample holder, receiving optics (the beam from the sample), and detector (which measure the intensity of X-ray scattered by the sample). A crystal is a regular array of atoms that can elastically scatter electromagnetic waves such as x-rays. According to the Bragg's condition, the scattered beams form secondary waves that can interfere constructively in certain directions and can be written as[112]

$$2dsin\theta = n\lambda \quad \ldots\ldots\ldots\ldots\ldots\ldots\ldots\ldots\ldots\ldots\ldots\ldots \quad (2.1)$$

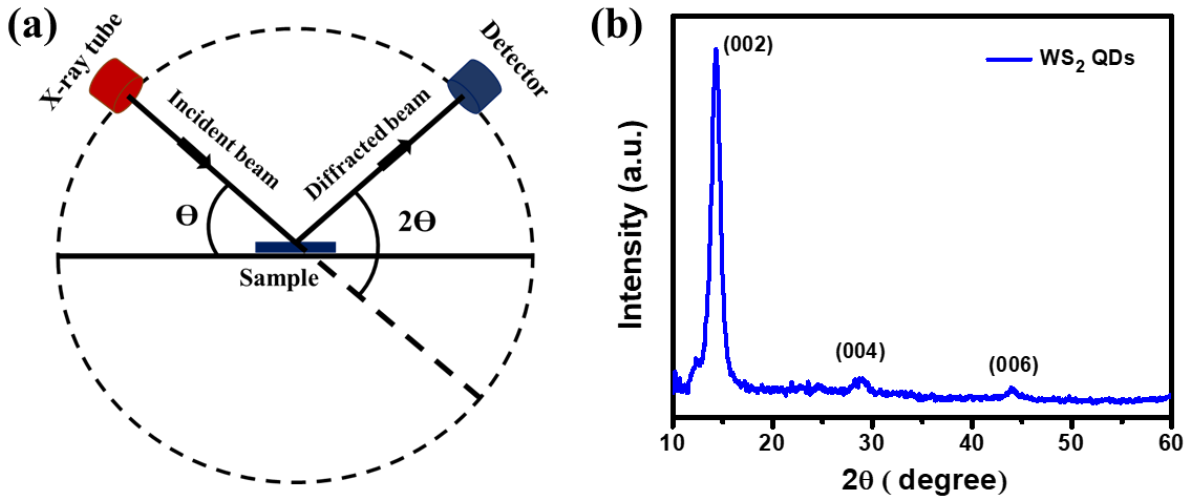

Figure 2.8: *X-ray diffraction. (a) Schematic of the working principle of x-ray diffractometer. (b) XRD pattern of WS_2 quantum dots (QDs).*

Where, d is the separation of two different planes, Θ is the incident angle, n is the integer and λ is the incident wavelength. To gather all the constructive interference that results from all potential crystalline planes, the detector scans the diffracted beam through a range of 2 angles. The crystallographic planes and d-spacing of every crystal are unique. Through Bragg's law, the X-ray diffraction peaks of a crystalline substance allowed for the calculation of the d spacing. **Figure 2.8(a)** and **2.8(b)** represent the schematic representation of the working principle of SEM and a typical XRD pattern of WS_2 quantum dots (QDs).

2.3.1.2 Scanning Electron Microscopy (SEM)

An electron beam is produced from an electron gun in the SEM instrument by thermionic emission or cold field emission. In the case of thermionic emission, electrons are produced by electrically heating the fine tip of a tungsten filament, LaB6 crystal, or a ZrO/W (Schottky emitter). These emitted electrons have a low energy and must be accelerated to a specific energy before entering the electron column. An electrostatic field maintained by applying a very high voltage between the electron source (cathode) and the anode plate accelerates and guides the electrons. At room temperature, electrons are emitted from the tungsten tip in cold field emission. Cold field emission is advantageous because the source emits a high electron yield with low chromatic aberration, making it suitable for atomic resolution imaging. A high

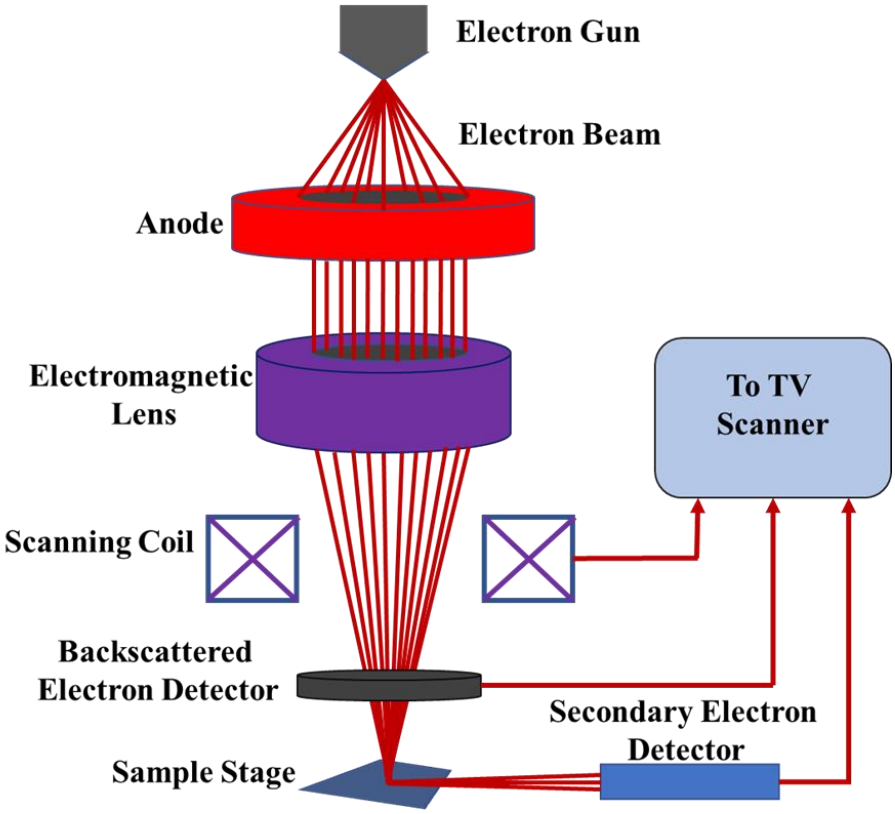

Figure 2.9: *Schematic diagram of the scanning electron microscopy (SEM).*

vacuum (10^{-7} to 10^{-10} mbar) is maintained inside the SEM to prevent the filament from burning or oxidising. Then, an electromagnetic lens made of insulated copper wire windings, a soft iron cast, and a pole piece is used to direct the accelerated electron beam. An electrical current is run through the copper winding to create an induced magnetic field, which is then directed by the lens' pole pieces. The magnetic field deflects the accelerated electrons, causing them to take a circular path as they pass through the lenses. The search coil and magnetic lenses deflect the electron beam horizontally and vertically to scan the entire surface of a specimen. The magnetic field strength inside the lens can be changed to change the focal width of the beam. SEM operates at voltages ranging from 2 to 50KV, with beam diameters ranging from 5nm to a few micrometres. Finally, an electron beam is allowed to interact with the sample surface. Secondary electrons, auger electrons, characteristic X-rays, backscattered electrons, and cathodoluminescence are all produced by the energy dissipation of primary electrons at the sample surface. Secondary and backscattered electrons are collected and distinguished by detectors based on their energy, and SEM images are constructed using these two signals via the imaging system. SEM micrographs provide detailed, three-dimensional information of the sample surface on a large scale due to the narrow beam diameter of the probing electron beam. **Figure 2.9** and **Figure 2.10** represent the schematic diagram of SEM and a typical SEM image of WS_2 QDs decorated graphene nanosheet.

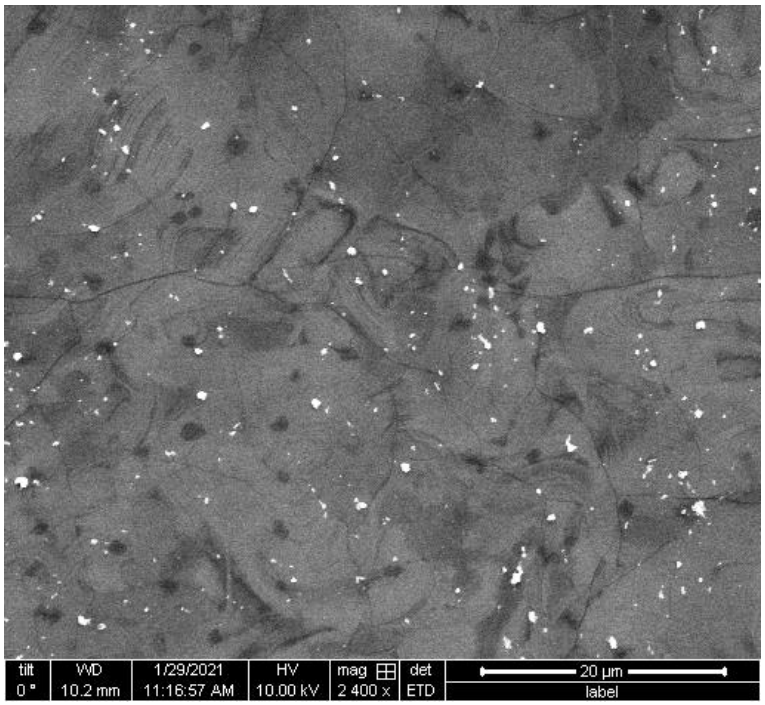

Figure 2.10: *Scanning electron microscopy (SEM) image of WS_2 QDs decorated graphene nanosheet.*

2.3.1.3 Transmission Electron Microscopy (TEM)

A highly energetic electron beam is shown through the sample in transmission electron microscopy (TEM), which uses the interaction between the electrons and the sample to reveal the sample's crystal structure and morphology through elemental analysis. TEM can be used to examine low-dimensional objects' quantity, size, and shape as well as crystal grain boundaries, structural dislocations, and other material flaws (quantum dots, nanosheets, nanowires etc.). The schematic diagram of the working principle of TEM is represented in **Figure 2.11a**. It is made up of an electron gun that produces high-energy electrons, a magnetic condensing lens that controls the amount of electrons that fall on the specimen, and other components. Between the objective lens and condensing lens is the sample. The high angle diffracted beam is blocked by the magnetic object lens, and the diffracted beam is then eliminated by the aperture, which raises the contrast of the image. In order to achieve higher magnification, the magnetic projector lens is placed above the fluorescent screen. The image can be captured using a

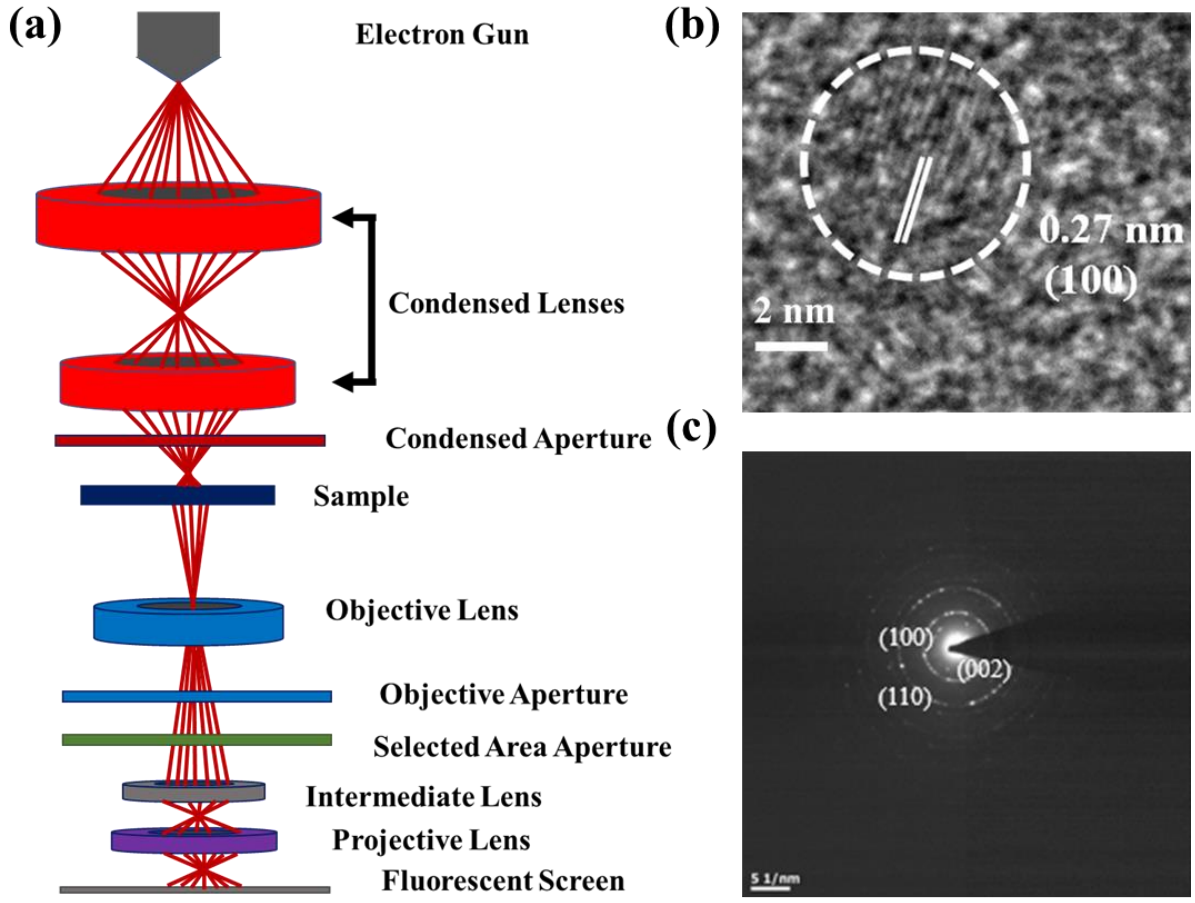

Figure 2.11: *Transmission electron microscope (TEM). (a) Schematic diagram of the transmission electron microscope (TEM). (b) HRTEM image of WS_2 QDs with interlayer spacing 0.27nm. (c) The selected area electron diffraction pattern (SAED) of WS_2 QDs.*

fluorescent screen or a CCD (charged coupled device). Many electrons experience Bragg's scattering at the various parallel atomic planes of a crystalline sample when the electron beam interacts with it. Depending on the crystalline sample's atomic spacing, these scattered electrons are collected using magnetic lenses to create either a spot pattern or a fringe pattern. This pattern reveals details about the sample's atomic arrangements, phase, crystal plan orientation, and crystallinity. A resolution of up to 0.2 nm is possible with high-resolution transmission electron microscopy (HRTEM), a type of electron diffraction imaging that is very effective at observing the lattice fringes of crystalline specimens. **Figure 2.11b** and **2.11c** represent the HRTEM image and selected area electron diffraction (SAED) pattern of a typical WS_2 QDs.

2.3.1.4 Atomic Force Microscopy (AFM)

A topographical image of the sample surface can be obtained using the atomic force microscope, a type of scanning probe microscope, through interaction between a tip and the sample surface. **Figure 2.12a** shows a schematic representation of a typical AFM, which includes a cantilever with a tip (probe) at the free end, a laser, a four-quadrant photodetector, and a scanner. The cantilever bends when the tip is near the sample surface because of interactions between the tip and sample surface's attractive and repulsive forces. A laser beam reflected off the cantilever is used to monitor the up-down and side-to-side motion of the AFM tip as it scans along the surface. The reflected beam is tracked by a position sensitive photodetector, which detects the probe's vertical and lateral motion. The surface thickness of photodetector, which detects the probe's vertical and lateral motion. The surface thickness of

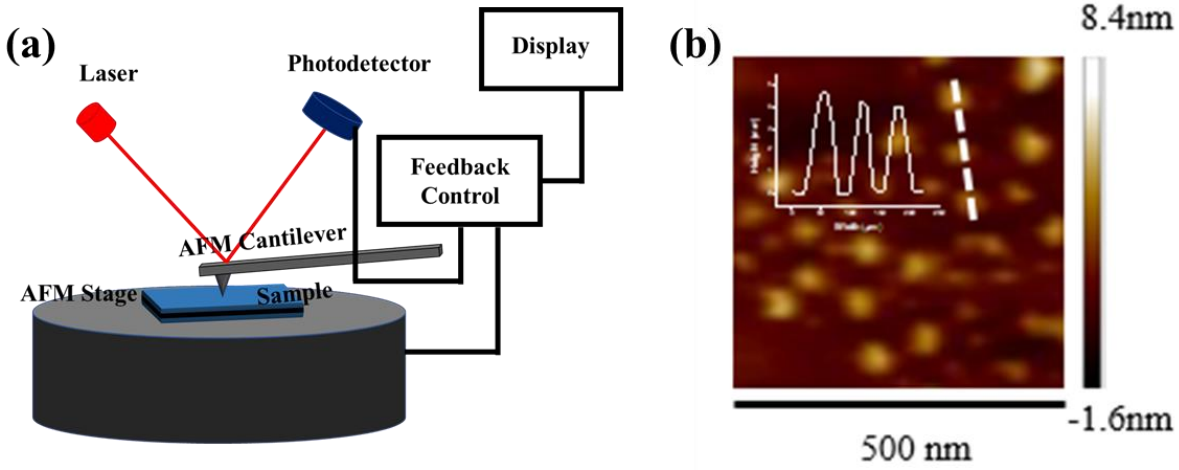

Figure 2.12: *Atomic force microscopy (AFM). (a) Schematic of the working principle of AFM. (b) A typical AFM image of WS_2 quantum dots (QDs) and the corresponding height profile.*

the sample can be estimated by calibrating the deflection sensitivity, and the resulting image is a topographical illustration of the sample surface[113]. AFM primarily employs three operational modes: (i) contact mode, in which the tip can move over the sample surface at a specific height or under a constant force, and the tip's movement is strongly influenced by frictional and adhesive forces between the tip and sample. In (ii) Tapping mode, the tip oscillates with sufficient amplitude from the sample surface (near its resonance frequency) to conserve the tip-sample interaction during scanning. The tip does not touch the sample in (iii) non-contact mode; instead, it oscillates above the sample surface during the scanning period. **Figure 2.12b** represents a typical AFM image of WS_2 QDs.

2.3.2 Spectroscopic Characterizations

The spectroscopic characterizations of newly synthesised materials are essential. Some of the important spectroscopic characterizations like UV-vis absorption spectroscopy, Raman spectroscopy and photoluminescence spectroscopy are discussed below.

2.3.2.1 UV-Vis Absorption Spectroscopy

One of the most popular and basic electronic spectroscopic techniques is UV-Vis spectroscopy, which records light that is transmitted or reflected from a material and displays data about the absorption signals caused by electronic transitions. Due to the electromagnetic spectrum's ultraviolet and visible regions being absorbed, the electronic spectra of materials can be determined. The band gap energy of semiconducting materials can also be ascertained using this method very effectively. This UV-Vis spectrometer has two modes of operation: transmission and reflection. The UV-Vis spectrometer is schematically depicted in **Figure 2.13** and consists of a light source, monochromator system, sample holder system, detector, and amplifier with recording electronic device. When a monochromatic light beam passes through a sample (absorbing materials), UV-Vis spectroscopy complies with the Lambert-Beer law, which states that the intensity of the transmitted radiation decreases after passing through the sample i.e.,

$$I = I_0\, e^{-\sigma\,(N_1 - N_2)l} \quad \ldots\ldots\ldots\ldots\ldots\ldots\ldots\ldots\ldots\ldots \quad (2.2)$$

Where, I_0 is the incident beam intensity, l is the optical path length through the sample, and N_1 and N_2 are the population densities at the initial and final energy states, respectively. The Beer-Lambert equation can be written in the form of Beer's law as

$$A = \epsilon cl = -\log_{10}\left(\frac{I}{I_0}\right) \quad \ldots\ldots\ldots\ldots\ldots\ldots\ldots \quad (2.3)$$

Where A is absorbance, I_0 is the intensity of incident radiation, I is the intensity of transmitted radiation after passing through the sample, ϵ is molar absorptivity or extinction coefficient, c is the concentration of the absorbing species and l is the path length of the sample. In the thesis, UV-visible absorption spectra were captured using a Shimadzu UV-2600 spectrometer and solutions taken in a 1 cm quartz cuvette at room temperature. **Figure 2.13b** and **2.13c** represent the UV-vis absorbance spectra of MoS_2 nanosheets (NS) and WS_2 QDs and NS respectively.

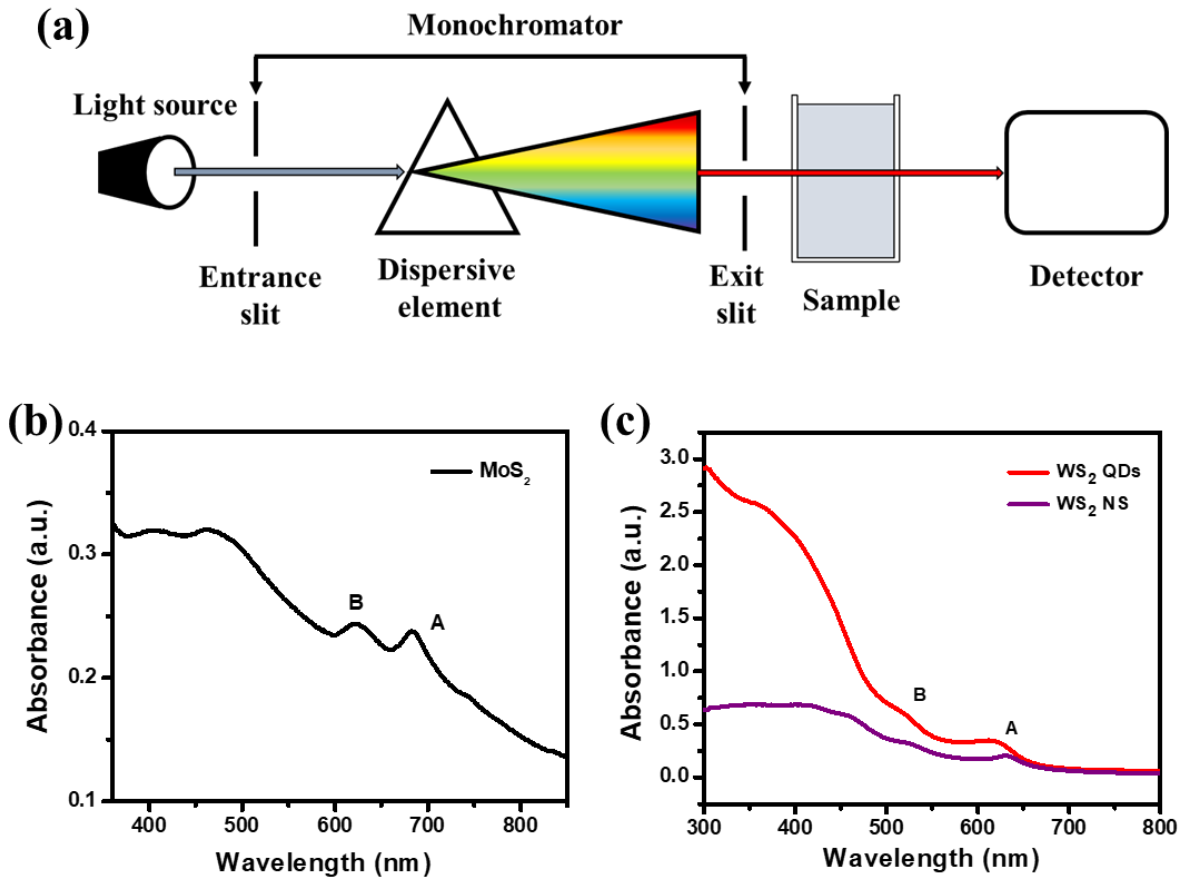

***Figure 2.13**: Absorbance spectroscopy of 2D materials. (a) Schematic representation of absorbance spectroscopy. UV-Vis absorption spectra of (b) MoS_2 and (c) WS_2 QDs and NS.*

2.3.2.2 Raman Spectroscopy

A very effective non-destructive tool for characterising the vibrational spectroscopy of c (Raman scattering) (consists of stokes and anti-stokes lines). The Raman spectrometer is schematically depicted in **Figure 2.14** and consists of three main components: (i) a laser as a source of monochromatic illumination, (ii) an objective with a sample holder, and (iii) a detector system with a display unit. To exhibit Raman shift, a material's electric dipolar

polarizability with respect to vibrational coordinate must change. When a photon excites a sample, the sample enters a virtual energy state for a brief period before the photon emits. The intensity of Raman scattering is proportional to the change in polarizability[114]. As a result, the Raman spectrum (scattering intensity as a function of frequency shifts) of that material is affected by its roto-vibronic states. The spectrum is measured with reference to the laser line, so the peaks are measured as a shift from the laser line. The vibrational energies associated with the exposed sample's bonds determine the peak positions. The Raman spectra of graphene and TMDCs (MoS_2) are discussed in the previous chapter.

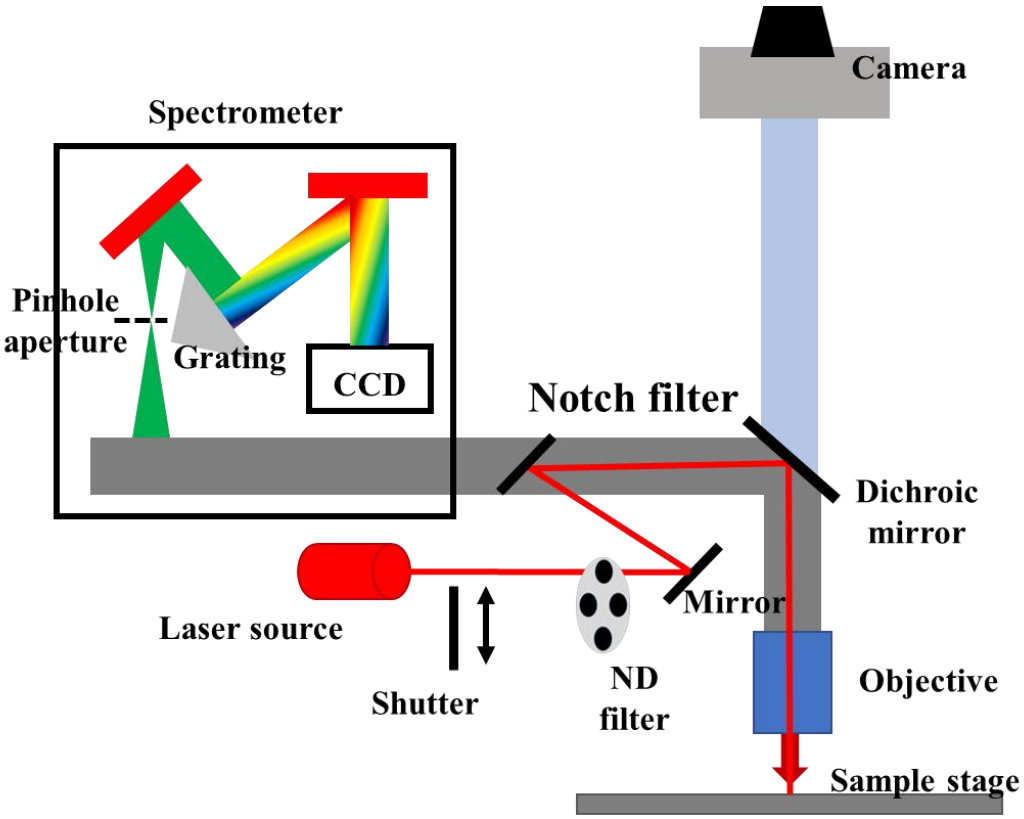

Figure 2.14: *Schematic diagram of Raman spectrometer.*

2.3.2.3 Photoluminescence Spectroscopy

Any form of matter can emit light through a process known as photoluminescence[115], or PL for short (electromagnetic radiation). Initiated by photoexcitation, or photons that excite electrons to a higher energy level in an atom, it is one of many types of luminescence (light emission), hence the prefix photo. After excitation, various relaxation processes frequently take place, during which additional photons are radiated. Absorption and emission times can range from milliseconds for phosphorescence processes in molecular systems to short femtosecond regime

for emission involving free-carrier plasma in inorganic semiconductors. In some rare cases, the delay in emission can even last for several minutes or hours. Photoluminescence spectroscopy provides information on a material's energy band gap, vacancy states, and defect levels. It is schematically shown in **Figure 2.15** and consists of a monochromatic light source (laser) to excite the sample, a focusing object with an appropriate sample compartment, a detection unit for the emission signal (spectrometer), and a display unit. When a substance goes through internal energy transitions before re-emitting the energy from the absorption event, more processes might take place. By resonantly gaining energy from the absorption of a photon or losing energy by emitting photons, electrons can change their energy states.

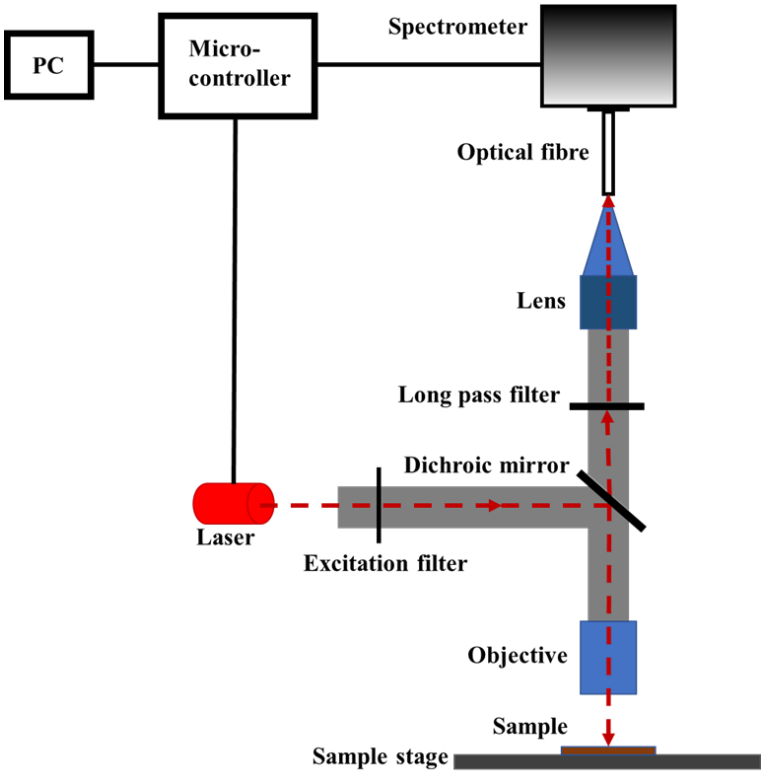

Figure 2.15: *Schematic diagram of photoluminescence spectrometer.*

2.3.2.4 Time-resolve Photoluminescence (TRPL) Spectroscopy

The lifetimes of the generated carriers were investigated using time-correlated single-photon count spectroscopy (TCSPSC). There are mainly two methods for measuring lifetime, time domain and frequency domain techniques. In time domain methods, the sample is excited with a light pulse and the resulting pulse width is as short as possible, preferably much shorter than the decay time of the sample. The TCSPC setup consists of a high repetition rate laser light source, grating monochromator, high-speed photomultiplier tubes (MCPs) and microchannel

plates (MCPs) (PMTs) as shown in simplified diagram (**Figure 2.16**). When the sample is excited by a strong pulse of light, the population density in the excited state appears and the population in the excited state decays in a particular way. Emission is a random event; each excited carrier has the same probability of emission in a given time interval. This leads to an exponential decay of the population in the excited states and from which the decay time can be calculated. Here, we used the Edinburgh Instrument with a pulsed diode laser as the excitation source for the study of time-resolved luminescence.

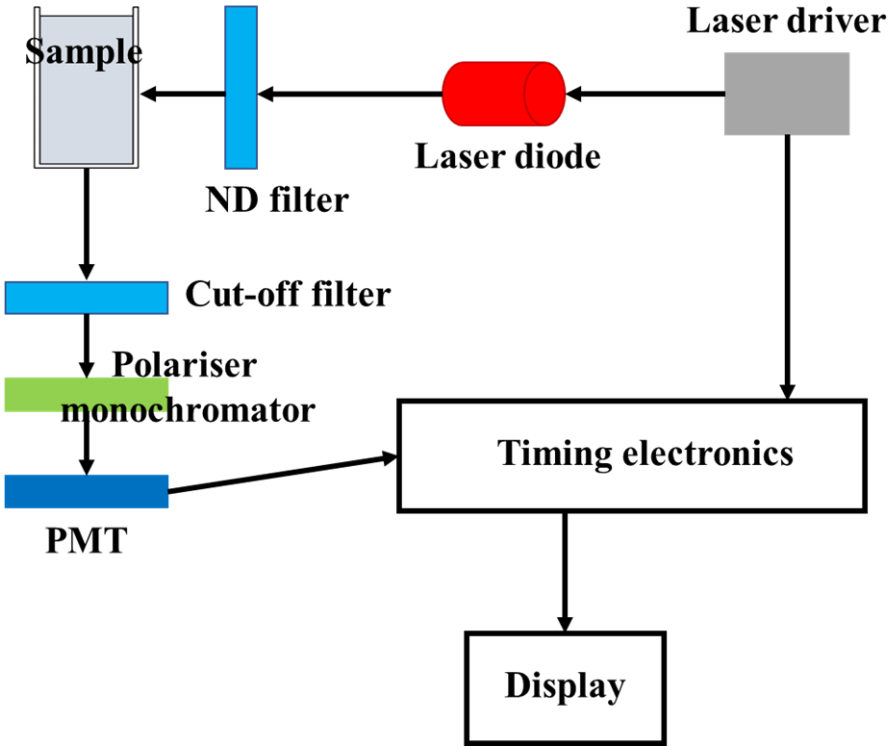

Figure 2.16: *Schematic diagram of time resolved photoluminescence spectrometer.*

2.4 Device fabrication

2.4.1 Cleaning of wafers

It is very important to clean the surface of the substrate to get better device quality. Firstly, the Si/SiO_2 wafers with 4-inch diameter are cut into small pieces (~ 5 mm * 5 mm) and thoroughly cleaned in acetone followed by isopropyl alcohol (IPA) in an ultrasonication bath for 5 minutes each to remove the micron sized particles from the wafer surface. After that, the small wafers are blow dried in nitrogen gas and kept on a hot plate at 100^0 C so that there is no moisture on SiO_2 surface prior to the device fabrication. For better cleaning O_2 plasma of dipping in buffer HF (Hydrofluoric acid) is used sometimes.

2.4.2 Photolithography

The metal contacts on the desired substrates or the materials with several micron pattern size are defined by using photolithography technique. Here, in this thesis we have used two different photolithography techniques like hard mask photolithography (MJB4, SUSS MicroTec) and laser writer photolithography (LW405D, MICROTECH). For the first one, we designed photo-mask by using different CAD software (AutoCAD, Clewin). And for the second one, there is no hard mask. We must draw the patterns according to the desire. The lithography process consists of several major steps like resist coating, baking, patterning, and development. The entire process flow is represented in **Figure 2.17** schematically and described in details below.

1. After cleaning, the sample is first spun with positive photoresist (AZ 1512 HS) for 60 seconds at 4000 rpm. The development rate during the developing process can vary from location to location depending on the resist thickness if the spin coating is not uniform. To ensure that all the solvent can evaporate and form a uniform coating, the sample is then baked for a further 1 minutes at 100°C on a hot plate (prebake).

2. After baking, the patterns are made either by using a hard mask or by direct patterning through laser writer. In both the cases, UV 405 nm laser is used. In laser written lithography, the suitable patterns are drawn by using 'Clewin' software. During the patterning, the samples are exposed at a dosh of 160-180 mJ/cm^2.

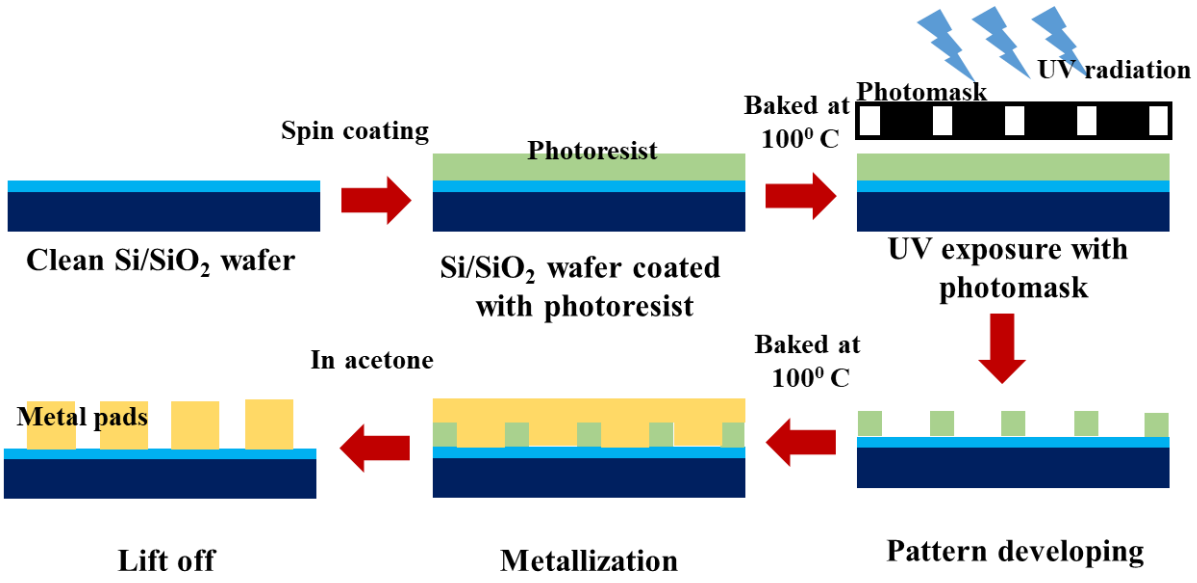

Figure 2.17: *Process flow of photolithography and metallization for device fabrication.*

3. The developing is the final step before the metal deposition. The exposed patterns are then developed in positive resist developer (AZ 326 MIF). The only exposed part of the resist is dissolved in the developer, and the unexposed part remains intact in the solution. The developing time is an important parameter; over-developing can mess up the finer pattern. The typical developing time can vary from 40-50 secs. After the developing, the sample is rinsed with DI water and blow-dried with N_2 gas. **Figure 2.18a** and **2.18b** show the photolithography (MJB4) and the laser writer setup. The e-beam evaporator setup and its main growth chamber are shown in **Figure 2.18c** and **2.18d**.

Also, we have fabricated large scale devices even without any lithography process for simplicity. Sometimes photolithography gives chemical residues (from photoresist) which may

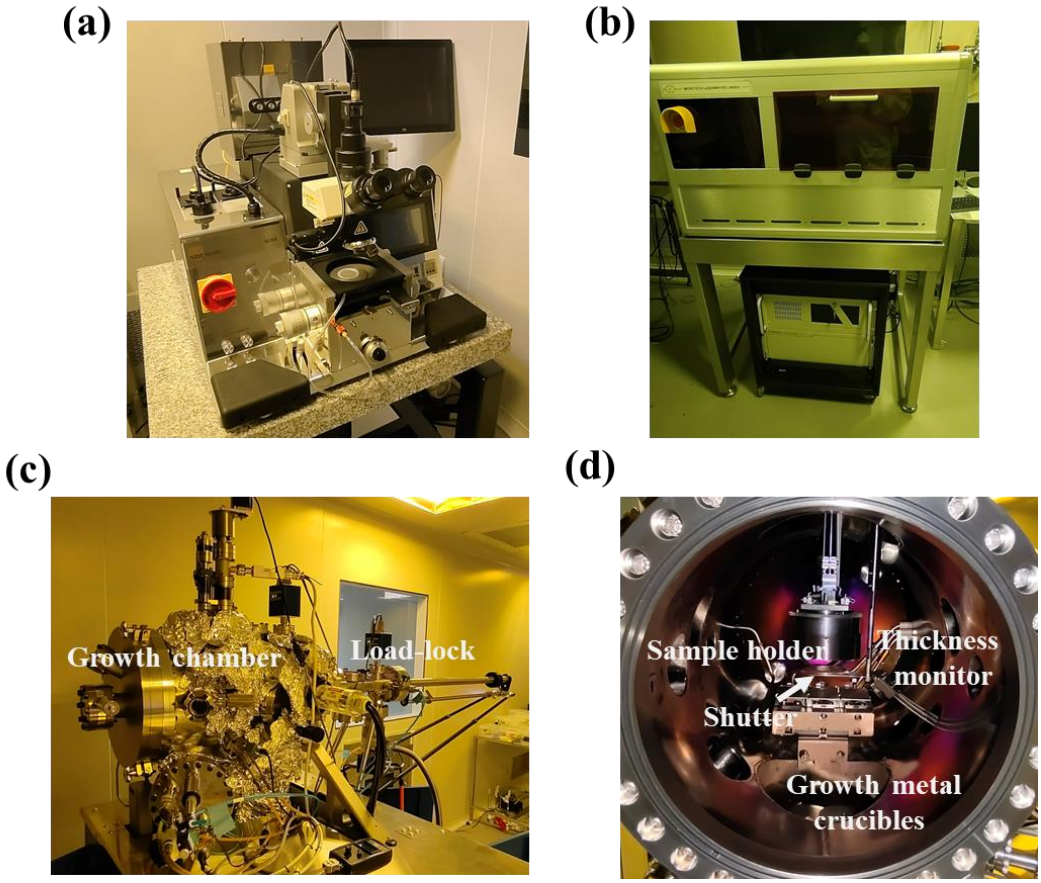

Figure 2.18: *Photolithography and metallization units. (a) Hard mask photolithography unit. (b) Laser writer lithography unit. (c) e- beam evaporation unit. (d) Growth chamber of the e-beam evaporation unit.*

hamper the charge transfer across the interfaces of the devices. For that, fabrication of lithography free devices (using metal shadow mask) are one of the objective of this thesis.

2.4.3 Metallization

Metal deposition is necessary after lithography in order to connect the metal contacts to the sample. Devices are made from a variety of metals, including Titanium (Ti), Chromium (Cr), Gold (Au). The e-beam evaporation and thermal deposition method are used to create the contacts for most of devices. The used samples are put onto a circular metal plate with the help of Kapton tape. The evaporation chamber is then pumped to ~10^{-6} mbar using a turbo-molecular pump backed by a rotary pump for few hours. A piezo base thickness monitor is used to keep track of the metal thickness and deposition rate. For Cr/Au or Ti/Au deposition, the deposition rate is optimised around 0.5A/s. The samples are removed after deposition and submerged in acetone for over four hours. Acetone dissolves the photoresist, leaving the deposited metal on the substrate behind. Acetone is injected into the sample using a syringe, aiding in the removal of unwanted Au from the substrate (lift off). The sample is then blow-dried with a nitrogen gun after being rinsed in IPA. Some of the fabricated devices are shown in **Figure 2.19**.

Figure 2.19: *Lithography patterns and devices. (a) Monolayer graphene device. (b) Two terminal MoS_2-hBN hybrid device. (c) Bare comb like patterns on Si/SiO_2.*

2.4.4 Bonding of devices

Following metallization, the devices are carefully cut with a diamond cutter to fit inside a leadless chip carrier using silver epoxy (RS Components) and heated at ~ 120^0 C. We encountered difficulties performing conventional ball/wedge bonding because the metal contacts are thin (~ 50nm). So, we bonded our device contact pads to the chip carrier with 25µm gold wire and silver epoxy blob using a HYBOND bonder.

2.5 Electrical measurement techniques

This section gives a brief introduction to the different transport measurement techniques used in this thesis, namely, two terminal current-voltage (I-V) measurement, gate dependent transfer characteristics (I_{ds} -V_{bg}) measurements and low frequency noise measurements. In this context, we have developed a high vacuum electrical measurement setup to understand the potentiality of these devices.

2.5.1 Designing of optoelectronic measurement setup

The extremely high cost of commercially available electrical transport measurement setup coupled with optical window encourages us to design a homemade low-cost setup suitable for photoresponse studies. The main goal is to perform optoelectronic transport measurements in high vacuum (~ 10^{-6} mbar) at room temperature. The schematic and the original optical picture of the setup having multiple electrical ports are shown in **Figure 2.20a** and **2.20b** respectively. The whole setup is made of brass which isolates the sample stage through a Teflon spacer. The sample holder stage is also made of brass which is connected to a wire heater connected to the setup by proper arrangements. A vacuum compatible electrical connector (containing 10 connections for sample) is used to maintain low pressure inside the cryostat while allowing the electrical connections between the sample and instruments. The vacuum isolation is done by using a rubber 'O' ring in between the brass jacket and the quartz optical window. The electrical

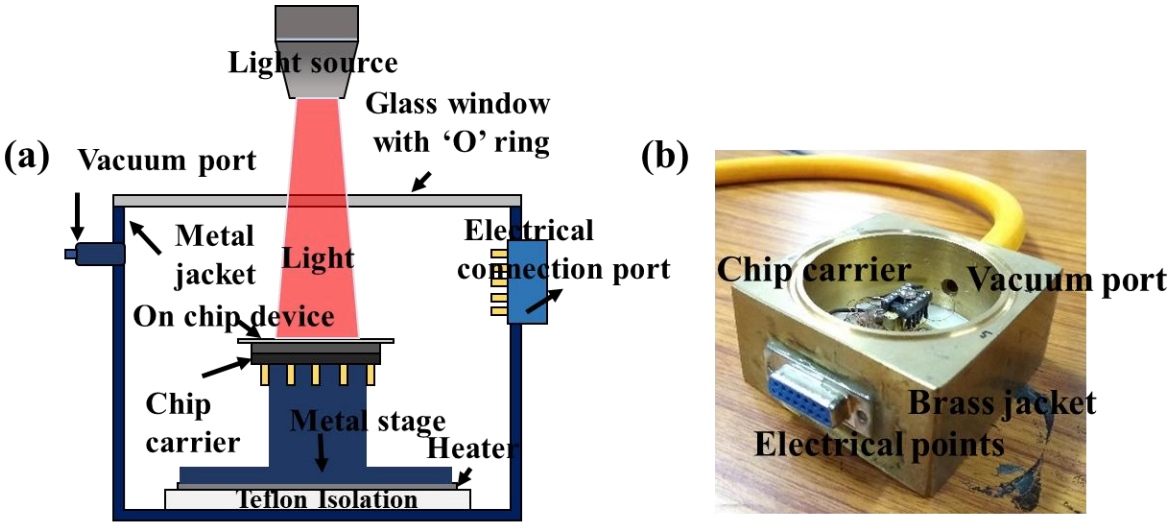

Figure 2.20 : *Homemade optoelectronic measurement setup. (a) Schematic of the experimental setup with different parts. (b) Optical image of the setup.*

connection between the chip carrier and the break-out connector is made using low resistive copper wires. Twisted pairs are used to reduce electromagnetic interference, which may originate from the large current flowing through these. All the optical experiments are done with some well calibrated Thorlab LEDs mounted by some homemade stands. The intensity profile of the LEDs are calibrated by using Flame-Ocean Optics spectrometer with integrating sphere set up.

2.5.2 Two terminal current-voltage (I-V) measurement

The output characteristics of the FET are critical in determining whether the sample is ohmic or nonohmic. The linear I-V characteristics reflect the sample's ohomic nature, whereas the output characteristics of the FET are critical in determining whether the sample is ohmic or nonohmic. The linear I-V characteristics reflect the sample's ohomic nature, whereas the non-linear I-V characteristics determine the sample's Schottky type behaviour. The configuration for measuring I-V characteristics is shown in **Figure 2.21a**. Keithley sourcemeter model 2450 is used to apply a source-drain bias (V_{ds}) at one end of the channel and ground the other end via a 50 Ω terminator. The SMU 2450 itself measures the corresponding current. The Keithley sourcemeter model 2450 is also used to measure the DC transfer characteristics of the TMDC samples, with one source metre measuring I-V and the other connected to the gate terminal (**Figure 2.21b**).

2.5.3 Gate voltage dependent ac conductance measurement

Two terminal a.c conductance is commonly used to measure the high resistance samples (semiconductors). In most cases, a lock-in amplifier is used to supply the bias voltage (V_{ds}) and measure the output current (I_{ds}) at a specific frequency. The output characteristics of a typical FET device are measured using a lock-in amplifier (MFLI, Zurich instruments) and a d.c sourcemeter (Keithley 2540). To detect weak signals and improve signal-to-noise ratio, the drain-source current (I_{ds}) is sometimes amplified by an external current amplifier (FEMTO, DLPCA 200) and measured in the A mode of lock-in amplifier. The configurations without and with amplifier are represented in **Figure 2.21c** and **2.21d** respectively.

2.5.4 Low frequency noise measurement

Low frequency 1/f noise measurement is critical for all electronic devices to understand their low-level signal detection capabilities. Because of interference from external noise sources, low frequency noise measurement is more difficult than time averaged conductivity measurement. The most important of these is the 1/f noise from the instruments, particularly the voltage preamplifier. Aside from strong interference from power line fluctuations (50 Hz in India), ground loops, long cables, impedance mismatch, and other factors can all impede unambiguous noise measurement. All our noise measurements were carried out in accordance with the method proposed by Scofield in 1987[116]. The basic idea was to modulate low frequency noise signals to relatively higher frequency f0 (f1; f2) where the preamp has the least noise (Noise floor) and then demodulate the signal using the lock-in amplifier before sampling[117]. In our measurements, we used MFLI (Zurich Instruments) lock-in amplifier at a higher frequency 2.66 KHz to get noise signal upto 150 Hz. The configurations for the low frequency 1/f noise measurements are same as the a.c conductivity and are shown in **Figure 2.21c** and **2.21d**.

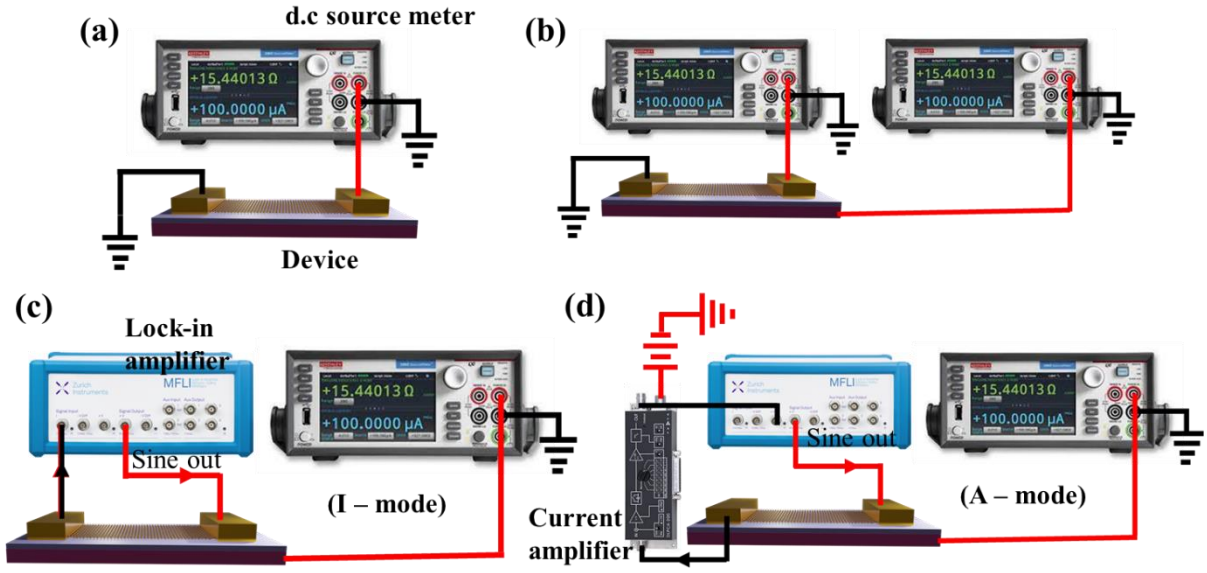

Figure 2.21: *Various electrical measurement techniques. (a) Two terminal d.c. I-V measurement. (b) I-V with different gate voltages. Gate dependent two probe a.c conductance measurements (c) without and (d) with current to voltage amplifier.*

Chapter 3

Superior Photoresponse of a Bilayer MoS_2 Phototransistor

Having an atomically thin profile, semiconducting transition metal dichalcognides (TMDC) promising two-dimensional (2D) material for electronic and optoelectronic device applications. In this work, a micron-scale phototransistor based on the mechanically exfoliated bilayer MoS_2 is fabricated, and its light-induced electric properties are investigated using a low-cost homemade optical setup. This device shows excellent switching behavior (10^4) with superior gate tunability, higher photoresponsivity (4.51×10^6 A/W) at a low bias (V_{ds} =1 V) under visible light (633 nm) illumination, making it promising for technological applications such as artificial intelligence, electronic eye, Internet of things (IoT) etc.

3.1 Introduction

Photodetectors (PDs) play critical roles in today's miniaturised electronic industry. They are critical for capturing, identifying, and visualising optical data[118,119]. Detecting light in various sub bands has a variety of applications in life, agriculture, industry, and the military. On the other hand, due to their exceptional structural, optical, and electronic characteristics, atomically thin two-dimensional (2D) transition-metal dichalcogenides (TMDCs) are becoming increasingly popular and show great promise for a variety of applications[66,120]. These 2D TMDCs are important candidates for a variety of applications because of the transition of indirect to direct bandgap as the number of layers is reduced from bulk to monolayer form[26]. Numerous studies have concentrated on the monolayer MoS_2 (1L MoS_2) among the various 2D materials because of its appealing properties, including direct band gap (1.9 eV)[27,43], high carrier mobility[37] etc. These semiconducting properties make this material highly promising for their potential applications in nanoelectronics and optoelectronics[26], including photodetectors[121], light emitting diodes[122], and flexible field-effect transistors[123] etc.

In this work, a highly sensitive visible phototransistor is reported with atomically thin bilayer MoS_2. Since the optical absorbance of bilayer MoS_2 is higher than monolayer counterpart and

enhanced spin-orbit coupling improves the optoelectronic response, 2L MoS_2 is utilized here as phototransistor channel material. To fabricate the back gated device, mechanically exfoliated MoS_2 sheet is first transferred to a Si/SiO_2 substrate by the dry transferred method as described in **Chapter 2**, **Section 2.2**. At 633 nm of illumination, the fabricated phototransistor has a very high responsivity (>10^6 A/W), which can further be tuned by the back gate voltages. In addition, when the 1/f noise is considered, the device has a low noise equivalent power (10^{-15} $W/Hz^{0.5}$) and a higher specific detectivity (10^{12} Jones).

3.2 Experimental Section

In this experiment, MoS_2 samples are prepared by mechanical exfoliation from its bulk on top of a PDMS gel pack. After that it is transfer on 300 nm Si/SiO_2 substrate by standard dry transfer technique using an optical microscope. **Figure 3.1a** represent the optical microscopic image of the exfoliated bilayer MoS_2 flake. Typical Raman spectra of the MoS_2 sample is shown in **Figure 3.1b**. The frequency separation between the Raman active modes (In-plane E^1_{2g} and out-of-plane A_{1g}) are found to be 21 cm^{-1} for bilayer MoS_2 in consistent with the previous reports[8]. Also, the photoluminescence (PL) of the MoS_2 sample is measured at room temperature with 532 nm laser excitation (**Figure 3.1c**). The dominated PL peak at 676 nm (Exciton 'A') is caused by direct intra-band transition of photogenerated carriers, while the weak peak at around 625 nm (Exciton 'B') is caused by the valance band splitting in MoS_2[124].

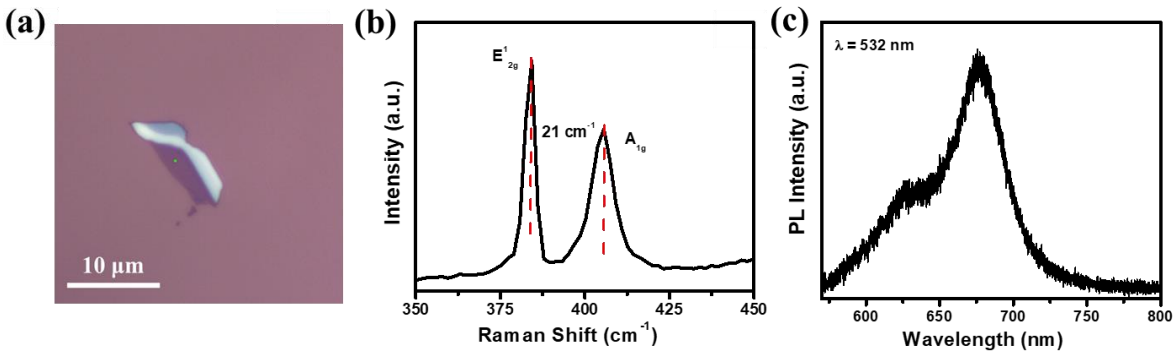

Figure 3.1: *Characterizations of mechanically exfoliated bilayer MoS_2. (a) Optical image of exfoliated bilayer MoS_2. (b) Raman and (c) photoluminescence spectra of bilayer MoS_2.*

Following the exfoliation and characterisations of MoS_2 layers, a field effect transistor is fabricated by using standard photolithography technique followed by e-beam evaporation of Ti/Au (5/70 nm). The schematic and the original images of the device are represented in **Figure 3.2a** and **3.2b** respectively where the Ti/Au contacts act as the source and the drain and the highly p^+ doped Si acts as the back gate with 300 nm SiO_2 as gate dielectric. After fabrication, the device is annealed for 3 hours at 300^0 C with $Ar+H_2$ gas to improve contacts and to get rid of the resist residues.

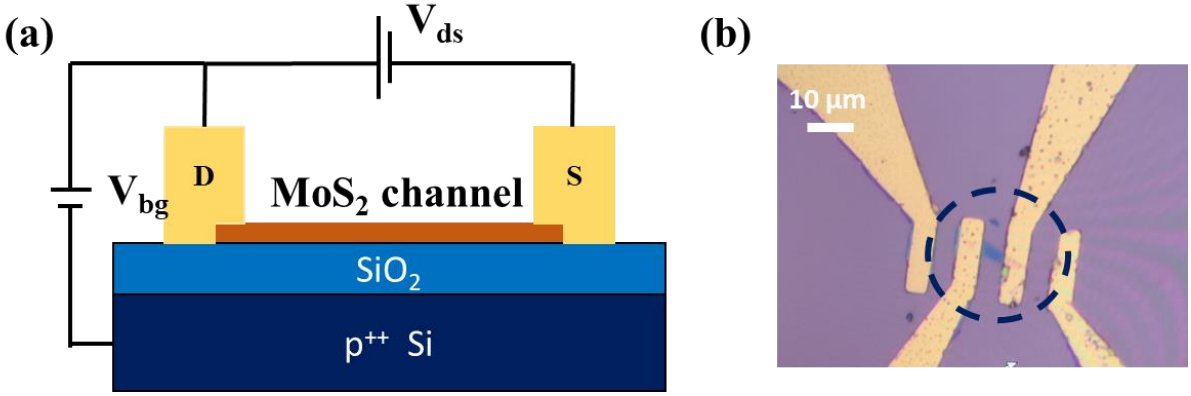

Figure 3.2: *Back gated MoS_2 field effect transistor. (a) Schematic of the back gated MoS_2 device. (b) Optical image of the device.*

3.3 Results and discussions

Figure 3.3a represents the transfer characteristics of the MoS_2 FET at a bias voltage (V_{ds}) of ~ 1 V at dark. It is seen that the fabricated single-layer MoS_2 FET has an obvious n-type semiconducting property, similar to previous reports[37,125]. Such n-type doping could be caused by impurity atoms, sulphur vacancies in MoS_2 crystals, or interstitial atoms in the MoS_2 interlayer gap which raises the total electron concentration of the host MoS_2 system, resulting in n-type doping. The threshold (V_T) voltage of the device is found to be ~ -20 V. An extremely high ON/OFF ratio ~10^4 is found in this MoS_2 FET which is comparable to some of the previously reported devices[3]. The field effect mobility (µ) of such devices can be calculated as

$$\mu = \frac{L}{W}\frac{d}{\epsilon V_{ds}}\frac{dI_{ds}}{dV_{bg}} \quad \ldots\ldots\ldots\ldots\ldots\ldots\ldots\ldots\ldots\ldots \quad (3.1)$$

where, L and W are the length and the width of the MoS_2 channel, d and ϵ are the thickness (~300 nm) and the permittivity (~ $4\times8.85\times10^{-12}$ F/m) SiO_2, respectively. V_{ds} , I_{ds} and V_{bg} are

the drain-source voltage, drain-source current and the gate voltages respectively. So, using the **Equation 3.1**, the average field effect mobility of the MoS_2 device is found to be ~ 1.38 cm^2/VS. This calculated mobility is comparable to the previously reported back-gated field effect devices[121,126]fabricated on Si/SiO_2 substrate, but it is significantly less than the top-gated FETs which could reach up to ~ 200 cm^2/VS[37]. The device also shows significant hysteresis in its transfer characteristics, which is typical for van der Waal FETs at room temperature mostly due to the interfacial trapped charges at the SiO_2/2D layer interface or adsorbed foreign impurities like gas molecules or water by the 2D active layer. **Figure 3.3b** represents the current-voltage (I-V) characteristics of the device with different gate voltages in dark.

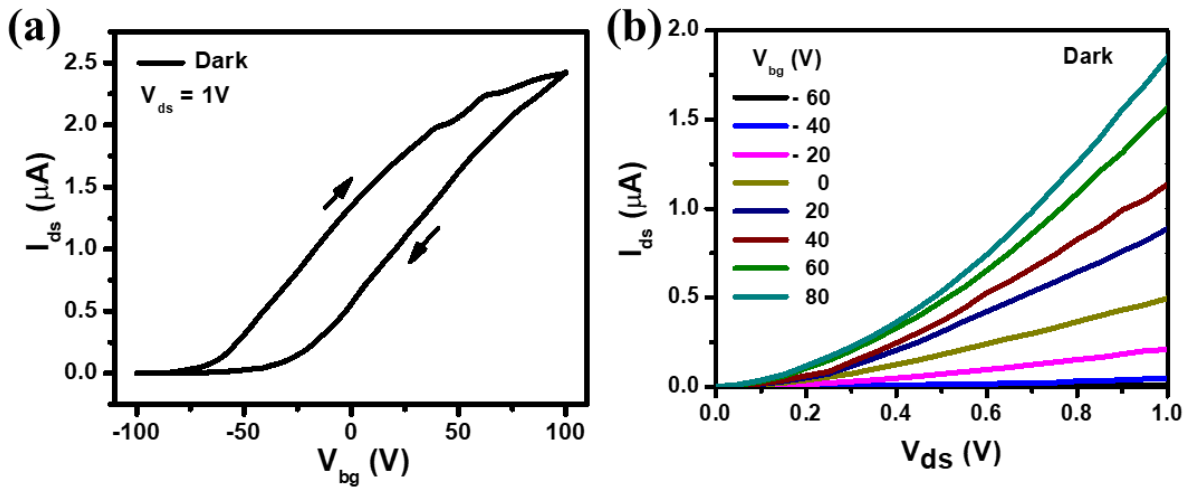

Figure 3.3: *Electronic properties of MoS_2 transistor in dark. (a) Transfer characteristics of the device. (b) I-V characteristics with different gate voltages.*

In order to investigate the optoelectronic properties of the device the transfer characteristics is recorded in presence of 633 nm illumination and in shown in **Figure 3.4a**. Here, it is observed that the drain-source current (I_{ds}) increases monotonically with the increase of optical illumination with a constant V_{ds}=1V. Upon light illumination, the photo induced electrons and holes are generated in the MoS_2 channel and transported between source and drain electrodes giving rise to the enhanced drain source current compared to its dark value. **Figure 3.4b** represents the change of threshold voltages (ΔV_T) as a function of illumination power. Here, it is seen that, as the optical intensity increases, the threshold voltage shifts toward the lower gate voltages (V_{bg}), implying the light induced electron doping in the MoS_2 channel. The calculated sensitivity of the threshold shift is ~ 9.76 V/fW at low power, making this MoS_2 phototransistor device one of the sensitive one for weak light detection.

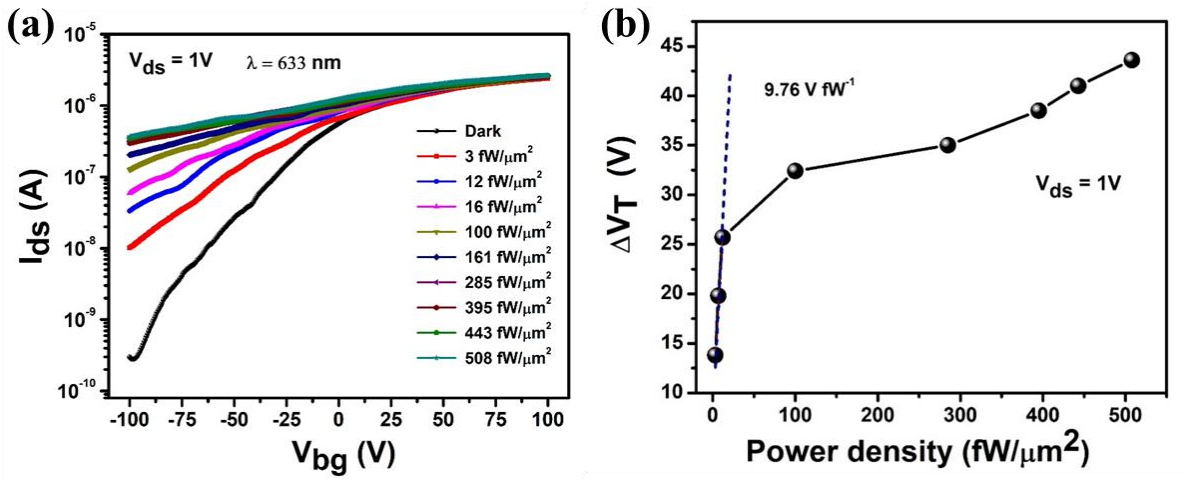

Figure 3.4: *Optoelectronic properties of MoS_2 transistor. (a) Transfer characteristics of the device with different optical illumination of 633 nm excitation. (b) Change of threshold voltage as a function of optical power density of 633 nm excitation.*

Figure 3.5a represent the photocurrent (I_{Light} -I_{Dark}) as a function of illumination power at different gate voltages. In all gate voltages, the photocurrent has a sublinear relationship with the optical power. The photoresponsivity of the devices can be calculated using photocurrent measurements. Photoresponsivity (R) is one of the important figure-of-merit of a photodetector and is defined as (see chapter 1, section 1.9)

$$R = \frac{I_{ph}}{P_{LED}} \quad \text{..... (3.2)}$$

where, I_{ph} is the measured photocurrent and P_{LED} is the illumination power density. The photoresponsivity of the device as a function of illumination power at different gate voltages and λ = 633 nm, V_{ds} = 1 V is shown in **Figure 3.5b**. With increasing $P_{LED,}$ R decreases significantly, typical characteristics of photodetectors and the device offers extremely high photoresponsivity of ~ 4.51 × 10^6 A/W for λ = 633 nm with a low optical illumination of P_{LED} ~ 3fW/μm^2 which is several orders of magnitude higher than the previously reported results[2,4]. Additionally, the device's photoresponsivity exhibits a significant gate dependence. When the gate voltage is tuned from -50 V to -20 V, the responsiveness rises; when it is tuned from -20 V to 0 V, it falls. A simple bandgap model (**Figure 3.5c** and **3.5d**) can explain these characteristics. TMDCs like MoS_2 suffer constantly from chalcogen (sulphur) vacancies that could behave like midgap states (trap state). Firstly, for $V_{bg} > V_T$, the Fermi level (E_F) becomes close to the conduction band and most of the available electron trap states are filled. When the light intensity is low, the deeper, longer-lasting hole traps fill first, and as the power rises, the

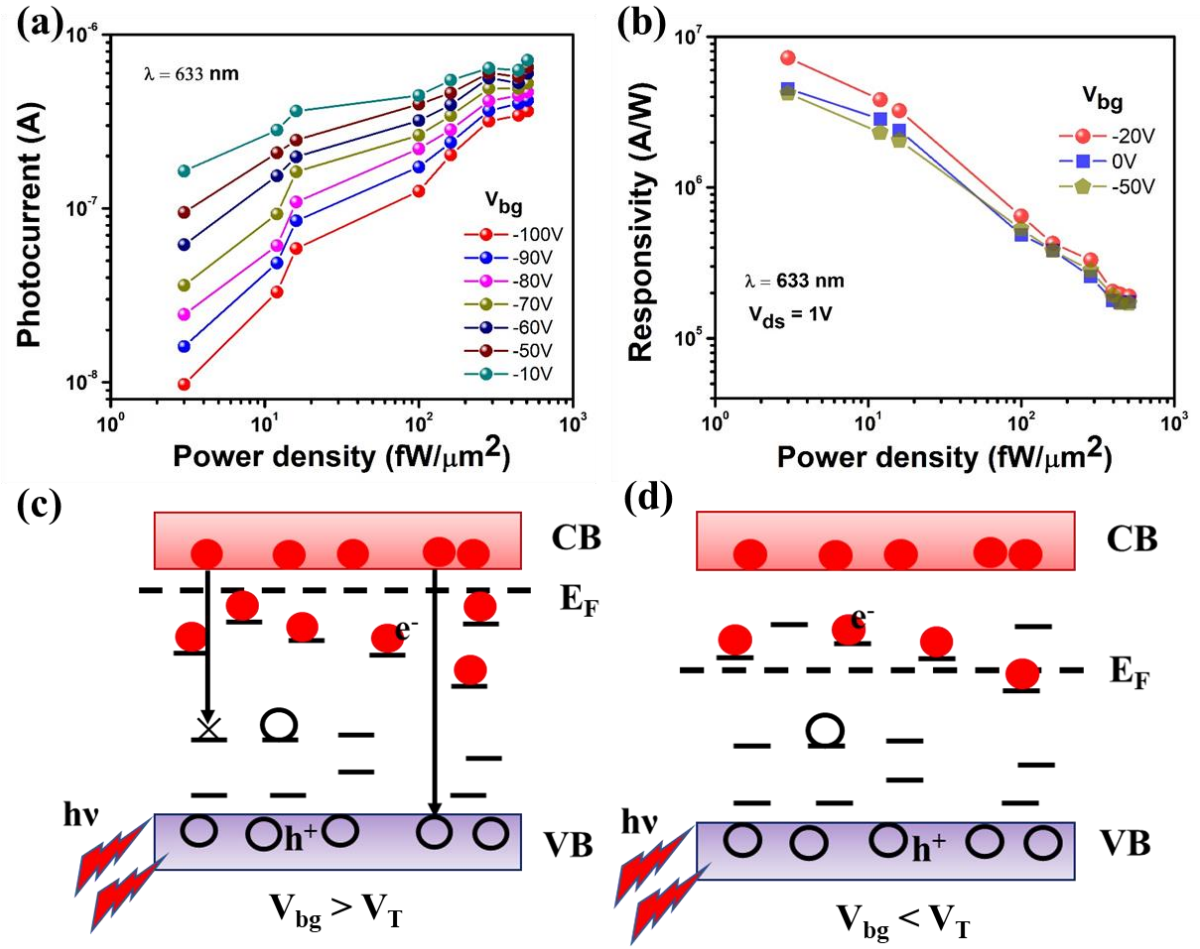

Figure 3.5: *Optoelectronic properties of MoS_2 phototransistor. (a) Illumination power dependent photocurrent at different gate voltages at λ = 633 nm, V_{ds} = 1 V. (b) Photoresponsivity (R) as a function of illumination power at different gate voltages at the same experimental conditions. (c) and (d) represent the trap related energy band model to explain the gate tunable photoresponse in the MoS_2 transistor.*

shallower trap states fill. As a result, the photoresponsivity is decreased (at V_{bg} = 0 V compared to V_{bg} = - 20 V) due to the shorter life to the dominant shorter lifetime of shallow states. At V_{bg} < V_T a different phenomenon happens. As the Fermi level E_F moves away from the conduction band at V_{bg} < V_T, more of the states above become vacant, acting as recombination centres, and lowering the photoresponsivity at V_{bg} = -50 V. This simplified trap mediated energy band model can support the experimental findings but, more complicated mechanisms are at work due to potential differences in the trap energy distribution, trap density, and carrier capture probability for electrons and holes.

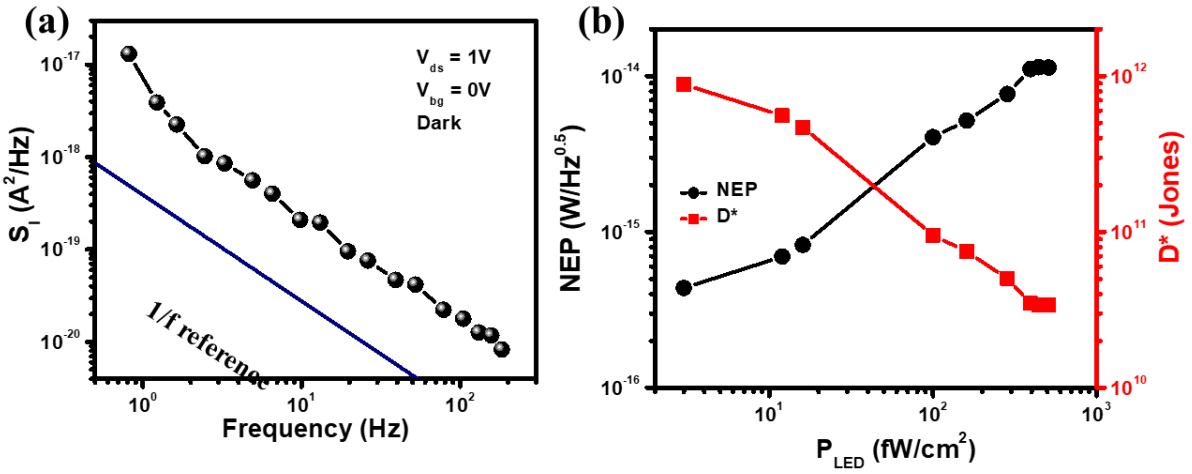

Figure 3.6: *Current noise and the detection limit of the device. (a) Current noise spectral density of the device in dark with V_{ds} = 1 V, V_{bg} = 0 V. (b) Noise equivalent power (NEP) and the specific detectivity (D^*) of the device as a function of illumination power at λ = 633 nm, V_{ds} = 1 V, V_{bg} = 0 V.*

The measurement of low frequency 1/f noise is critical in such transistor devices in order to understand the device's detection limit (See chapter 1, section 1.10). Low-frequency 1/f noise is measured in a.c. two-probe methods with bias voltage of 1 V and V_{bg} = 0 V (**Figure 3.6a**). Background noise is measured concurrently and subtracted from total noise. Along with photoresponsivity, the noise equivalent power (NEP) and specific detectivity (D^*) are two most important figures of merit for comparing photodetectors' performance. The noise equivalent power (NEP) of a device is defined as (See chapter 1, section 1.9.4)

$$NEP = \frac{\sqrt{S_I}}{R} \quad \ldots\ldots\ldots\ldots\ldots\ldots\ldots\ldots\ldots\ldots\ldots\ldots \quad (3.3)$$

Where, S_I is the total noise current of the device and R is the photoresponsivity. Also, the specific detectivity (D*) of the device can be defined as (See chapter 1, section 1.9.5)

$$D^* = \frac{\sqrt{A}}{NEP} \quad \ldots\ldots\ldots\ldots\ldots\ldots\ldots\ldots\ldots\ldots\ldots\ldots \quad (3.4)$$

Where, A is the effective device area. The illumination power dependent NEP and D* are represented in **Figure 3.6b**. The device offers NEP as low as ~ 10^{-15} W/$Hz^{0.5}$ and a higher specific detectivity ~ 10^{12} Jones at λ = 633 nm, V_{ds} = 1 V and V_{bg} = 0 V.

3.4 Summary

In summary, an ultrathin MoS_2 phototransistor is fabricated by mechanical exfoliation method. The device offers highly stable n-type doping and a superior on/off ratio (10^4). Also, the device shows excellent photoresponse characteristics in visible (633 nm) range. This fabricated MoS_2 phototransistor offers a very high photoresponsivity (>10^6 A/W), a low noise equivalent power (10^{-15} W/Hz$^{0.5}$), and a higher specific detectivity (10^{12} Jones) with excellent gate tunability which can be utilized to fabricate ultralow illumination sensitive smart devices. This result encourages one to fabricate the optoelectronic device based on layered semiconductors by a simple and affordable mechanical exfoliation method. This work creates a path for the creation of layered semiconducting materials for use in switches, memories, signal amplifiers, light-related sensors, and other functional devices in the future.

Chapter 4

Broadband Photodetection with Graphene-WS_2 Mixed Dimensional (2D-0D) Hybrid Phototransistor

Broadband photodetectors are increasingly using quantum dots (QDs) with their broadband absorption spectrum and wavelength selectivity due to recent advancements in the synthesis of highly stable, environmentally friendly, and economically viable transition metal-dichalcogenides (TMDC) quantum dots (QDs). With the solution-based processing, a super large (~0.75 mm^2), UV-Vis broadband (365-633 nm), phototransistor made of WS_2 QDs decorated CVD graphene as active channel is demonstrated with exceptional stability and durability in ambient condition (without any degradation of photocurrent till 4 months after fabrication). In this instance, graphene serves as the conducting channel and colloidal 0 D WS_2 QDs serve as the photo-absorbing material. At a low bias voltage (V_{ds} = 1 V) and an illumination of 365 nm with an optical power as low as 0.8 $\mu W/cm^2$, high photoresponsivity (3.1×10^2 A/W), moderately high detectivity (8.9×10^8 Jones), and low noise equivalent power (9.7×10^{-11} $W/Hz^{0.5}$) are obtained, which can be further tuned by modulating the gate bias. A significant increase in photocurrent is seen in the case of the QDs based device when comparing the photocurrent between two different morphologies of WS_2 (QDs and 2D nanosheets). Our observation is supported further by calculations using ab initio density functional theory, which also highlight the significance of quantum confinement in the enhanced photo response. For the next generation of optoelectronic applications, our work reveals a method for creating scalable, economical, and highly effective hybrid mixed-dimensional (2D-0D) photo detectors with graphene-WS_2 QDs.

4.1 Introduction

Photodetectors that can convert light into electrical signals are at the heart of technologies that affect our daily lives.[74,118,127] Sensitive detection of light of different wavelengths has various applications including optical communications, video-imaging, security, night-vision, optical data storage, biomedical imaging etc. In photodetectors, various photosensitive semiconductors are extensively used, such as ZnO[128], GaN for UV (< 400 nm)[129], Si for visible-NIR (~450-

1100 nm)[130], Ge for NIR–mid-IR (~1-5 μm)[131], PbS for IR (~700-1400 nm)[117], HgCdTe for MIR to far-IR (>5 μm)[119] etc. However, most of the materials suffer due to their high production cost[132] (complicated fabrication processes like molecular beam epitaxy), environmental toxicity[117,119] (Pb, Hg, Cd based materials), and stability related issues[96] (perovskites). Two dimensional (2D) layered materials (graphene[3], TMDCs[133] etc.) offer a new viable alternative due to their promising electronic and optical properties. While graphene is considered as an outstanding channel material for a transistor due to its ultrahigh charge carrier mobility (~up to 60000 $cm^2V^{-1}S^{-1}$, at room temperature on a substrate)[134], it has limitations in the field of optoelectronics because of its gapless nature, low absorption cross-section and short photogenerated carrier lifetime[111,135]. There have been attempts to increase the light absorption in graphene using plasmonic coupling[136], or microcavity confinement.[137] However, the most successful approach is by creating heterostructures and grafting a photo absorbing material on top of the graphene devices. For example, the heterostructures of graphene with PbS[138] or other quantum dots (ZnO[139], Si[98] etc.) have shown improved photoresponsivity. Also, the formation of vertical heterostructure (2D-2D) of graphene and layered transition metal dichalcogenides (TMDCs)[103,104] such as MoS_2, WS_2 can lead to very high quantum efficiency upon light illumination due to effective photoexcited carrier separation at the interface. However, the fabrication of these devices is expensive and needs delicately controlled sample transfer technique, which has low-yield and multiple lithography procedures. Graphene-based photodetectors coupled with colloidal quantum dots (QDs)[96,140,141] (PbS, CdS, Perovskite etc.) have emerged as a viable alternative due to their good detectivity, fast response time, high gain, and low production cost etc. However, most of the synthesis processes of QDs are hazardous, complex in reaction kinetics and most importantly suffer from stability issues[142]. To circumvent these difficulties, solution processed TMDC QDs[108,143] are found to be suitable for fabrication of graphene based broadband, highly stable photodetectors because of their broad absorbance band, direct and tunable band gap, easy synthesis process and higher stability. Among TMDCs, WS_2 is an emerging candidate for its outstanding optoelectronic properties. The development of a facile and simple synthesis procedure for the preparation of the crystalline WS_2 QDs[144] has opened up the possibilities to create graphene-WS_2 QDs based phototransistor devices.

In this work, we demonstrate the largest area (~0.75 mm^2) (to the best of our knowledge) lithography free, cost-effective hybrid phototransistor based on CVD graphene and chemically exfoliated WS_2 quantum dots (QDs). In this 2D-0D configuration, WS_2 QDs act as light absorber, while the CVD grown single layered graphene is the conductive channel for current

flow. This device, having a large photoactive area provides UV-visible (~365-633 nm) broadband photoresponse with good gate tunability and extra-ordinary stability. The fabricated phototransistor exhibits very high responsivity (3.1×10^2 A/W), moderately high detectivity (~8.9×10^8 Jones) and low noise equivalent power (~9.7×10^{-11} W/$Hz^{0.5}$) at a low bias voltage (V_{ds} =1 V and V_{bg} = 0 V) at an illumination of 365 nm with an optical power of ~ 0.8 μW/cm^2. We further perform a comparative study of the photoresponse between two different morphologies of WS_2 (WS_2 quantum dots (0D) and 2D WS_2 nanosheets) in same device configurations. We explain our observation through first principle calculations and show that the increased localization of the wave function due to quantum confinement effects is responsible for the enhancement of optical attributes in quantum dots. The WS_2 QDs with graphene offers a higher photoresponse than its 2D (WS_2 nanosheets (NS)) counterpart demonstrating a highly stable, low-cost graphene-based UV-visible (365-633 nm) broadband phototransistor. Adding with the simple scalable solution process for the preparation of WS_2 QDs, these results are very promising for wafer-scale phototransistor devices for future optoelectronic applications.

4.2 Experimental Section

4.2.1 Materials and Methods

All the chemicals (WS_2 powder, LiBr) and solvents (Hexane, IPA) are purchased from Sigma-Aldrich and have used without further purification.

4.2.2 Synthesis of WS_2 QDs and NS

WS_2 QDs are synthesized chemically by using Li-intercalation technique. First, for exfoliation of WS_2 nanosheets, bulk WS_2 powder 2.5 gm with anhydrous LiBr at 1:1 molar ratio is dispersed in 25 ml hexane solution. Then, using a bath sonicator, this solution is sonicated for five hours. To get rid of hexane and untreated Li ions, the black dispersion produced by the sonication process is centrifuged at 5000 rpm for 10 min. The wet sediments are cleaned by centrifuging after shaking IPA to disperse it (5000 rpm, 15 mins). By repeating this procedure three times the wet sediment of WS_2 is completely transferred in IPA solvent. Then after 1hr bath sonication, the resulting dispersion is centrifuged at 5000 rpm for 10 mins resulting a

greenish coloured exfoliated WS_2 nanosheets. To get the WS_2 QDs, the dispersion of WS_2 nanosheets in IPA is bath sonicated further for 10 hrs to achieve fragmented quantum dots (QDs), due to prolonged sonication, the lateral dimension of the WS_2 nanosheets are reduced in all directions, resulting in formation of 0D QDs. Then the resulting dispersion is centrifuged at 10000 rpm for 30 mins and the supernatant is collected which is the dispersion of WS_2 QDs in IPA.

4.2.3 Materials and interface characterizations

4.2.3.1 Microstructural characterizations

Morphology controlled WS_2 QDs and NS have been synthesized by sono-chemical exfoliation using Li-intercalation technique[144]. The colloidal semiconducting (2H-phase) WS_2 that is produced by this inexpensive, environmentally friendly exfoliation method can be easily dispersed in proper solvents[145]. **Figure 4.1a** displays the optical image of synthesized WS_2 QDs and NS dispersed in isopropanol (IPA) solution**.** The micrograph of the sample with an

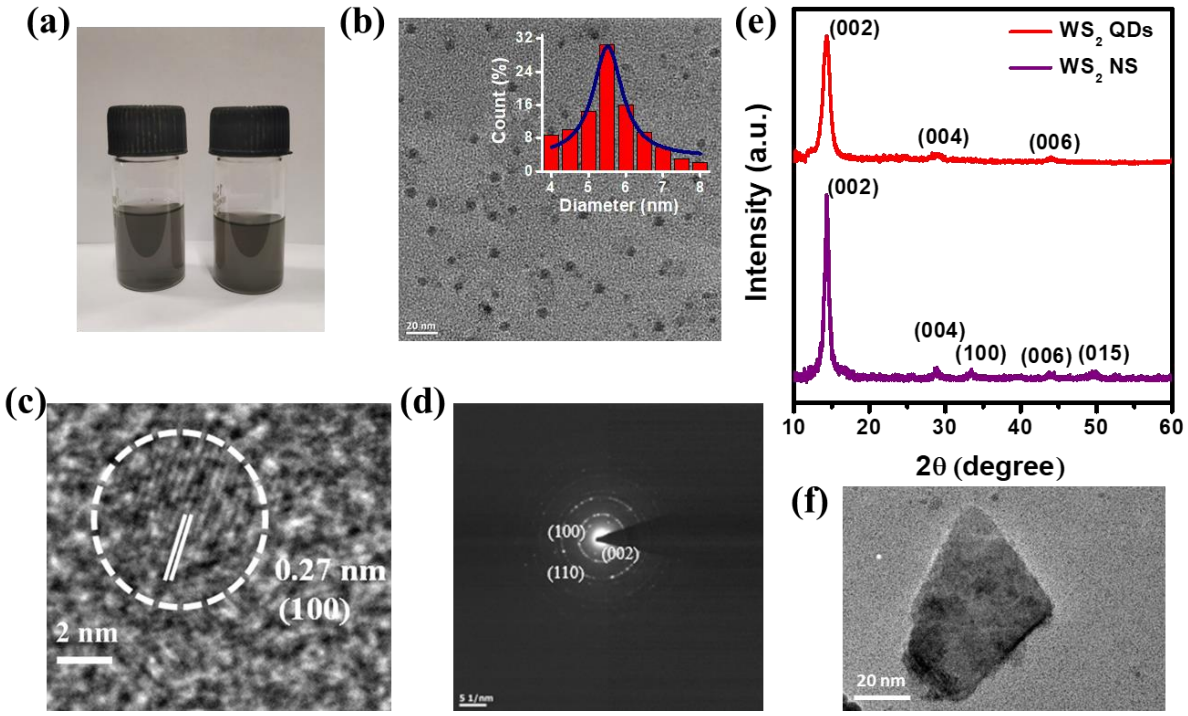

Figure 4.1: *Microstructural characterizations of morphology controlled WS_2 quantum dots (QDs) and nanosheets (NS): (a) Dispersed solution of synthesized WS_2 QDs IPA. (b) TEM image of the WS_2 QDs with size distribution of the QDs (Inset) showing the average radius of WS_2 QDs to be ~ 2.75 nm. (c) Lattice fringes with a 0.27 nm interlayer spacing are visible in this HRTEM image of WS_2 QDs. (d) The selected area electron diffraction (SAED) pattern of WS_2 QDs. (e) XRD pattern of WS_2 QDs and WS_2 NS. (f) TEM image of WS_2 NS.*

average QDs size (radius) ~2.75 nm is shown in **Figure 4.1b** and the inset figure indicates the size distribution of the WS_2 QDs. From the lattice fringes in HRTEM image (**Figure 4.1c**), the interlayer spacing is found to be 0.27 nm which reveals the formation of (100) plane in semiconducting 2H-WS_2[146]. The crystallinity of synthesized WS_2 QDs is indicated by the selected area electron diffraction (SAED) pattern shown in **Figure 4.1d**. The X-ray diffraction (XRD) pattern (**Figure 4.1e**) also supports the good crystalline 2H-phase of WS_2 QDs and NS[147].

4.2.3.2 Spectroscopic characterizations

Figure 4.2a represents the typical UV-visible absorption spectra of WS_2 QDs and NS (300-800 nm). The characteristic exciton peaks for WS_2 QDs are seen at 616 nm (A), 516 nm (B), and 630 nm (A), 524 nm for WS_2 NS. These exciton peaks are mainly arising due to the transitions between the conduction band minima and spin-orbit-coupling induced splitting of

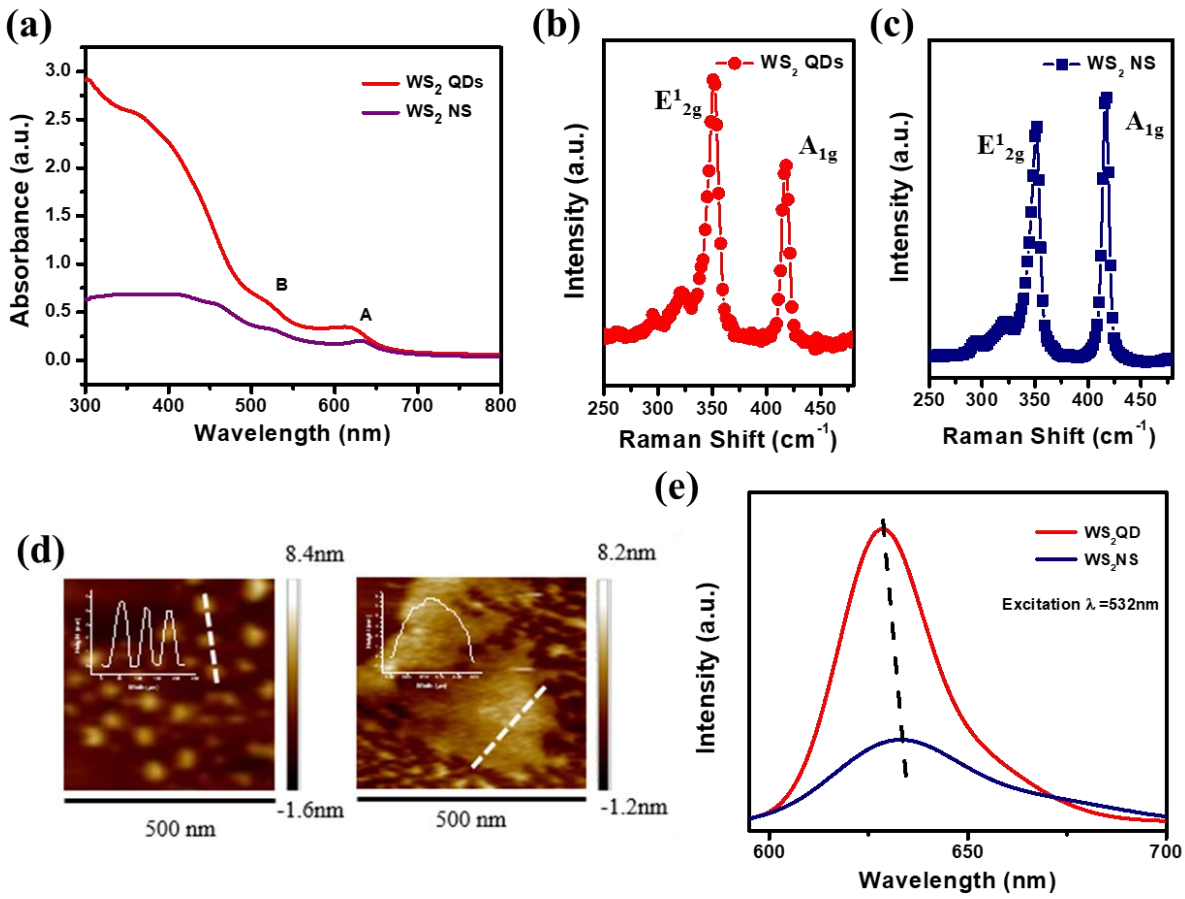

Figure 4.2: *Spectroscopic signature of morphology controlled WS_2 quantum dots (QDs) and nanosheets (NS): (a) Absorbance spectra. (b) and (c) Raman spectra. (d) AFM image along with the height profile. (e) Photoluminescence spectra of WS_2 QDs and NS respectively.*

the valence band levels[148,149]. Also, the excitonic C (~ 407 nm) and D (~ 366 nm) peaks are present in this synthesized WS_2 materials, which are attributed to the Van Hove singularities Additionally, this synthesized WS_2 material exhibits the excitonic C (407 nm) and D (366 nm) peaks, which are attributed to the Van Hove singularities producing strong absorption[150,151]. The Raman spectra of WS_2 QDs are shown in **Figure 4.2b** (bottom panel). There are two main characteristics. Peaks are observed at 351.1 and 417.2 cm^{-1}, corresponding to the in-plane (E^1_{2g}) and out-of-plane (A_{1g}) modes of vibration, respectively[152,153]. Similar modes are also observed in WS_2 NS and represented in **Figure 4.2c**. The AFM images of both the samples are represented in **Figure 4.2d** (WS_2 QDs (Left) and WS_2 NS (Right)). **Figure 4.2e** shows the photoluminescence spectra of both the samples with an excitation of 532 nm laser. It is seen that WS_2 QDs have slightly blue shifted and higher emission intensity compared to the NS system.

4.2.3.3 Interface characterizations

The interface between graphene and WS_2 QDs is characterize by Raman and photoluminescence (PL) spectroscopy. The Raman features remain unaffected in the hybrid structure (**Figure 4.3a,** top panel), indicating the good crystallinity of WS_2 QDs even in the presence of graphene. **Figure 4.3b** shows the Raman spectra of bare graphene[154] (bottom panel) and graphene-WS_2 QDs (top panel) heterostructure. A blue shift of the 2D peak position (from 2680 cm^{-1} to 2694 cm^{-1}), along with a significant enhancement of both the G (~3.2) and 2D

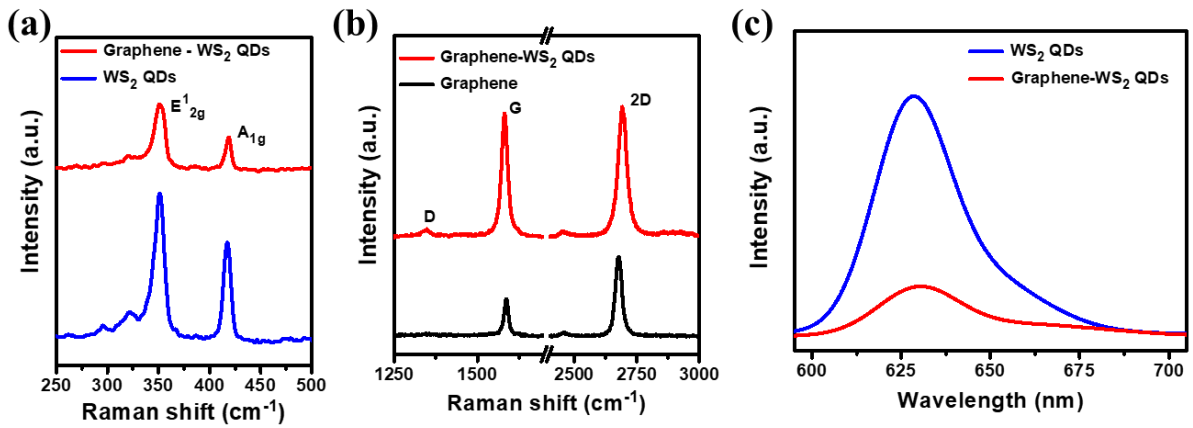

Figure 4.3: *Characterizations of the graphene-WS_2 QDs hybrid interface: (a) Raman spectra of WS_2 QDs before and after making of the heterostructure. (b) Raman spectra of graphene before and after making of the heterostructure. (c) Photoluminescence (PL) spectra of WS_2 QDs and the heterostructure with λ = 532 nm laser.*

(~1.67) peak intensities are observed in the heterostructure, indicating the injection of photo-generated holes from WS_2 QDs to graphene[155]. This enhancement of the peak intensities has also been observed in previously reported graphene-metal nanoparticles, semiconducting quantum dot system and indicates the possibility of localized surface plasmon resonance (LSPR) effect[156,157]. From the photoluminescence (PL) spectra (excitation 532 nm) of WS_2 QDs, a strong emission peak is observed (**Figure 4.3c)** at 628 nm which corresponds to the direct band gap (1.97 eV) nature[148,158]. It is observed that the emission intensity of graphene-WS_2 QDs heterostructure is quenched significantly as compared to pristine WS_2 QDs which also corroborates the charge transfer process across the heterostructure interface[97,159].

4.3 Results and discussions

4.3.1 Device fabrication and electron transport

Figure 5.4a depicts the schematic of a hybrid graphene-WS_2 QDs phototransistor, in which large area CVD graphene serves as the carrier transport channel and WS_2 QDs serve as the photon absorbing material. Gate voltages are applied to p-doped Si with a gate dielectric of 300 nm thick SiO_2. **Figure 4.4b** depicts the transfer characteristics of the field effect device (in dark) before and after quantum dot deposition. There is no charge neutrality point (CNP) in the pristine device, possibly due to the hole doping effect caused by PMMA based wet transfer and consequent adsorption of water molecules by the graphene film[160]. The deposition of WS_2 QDs

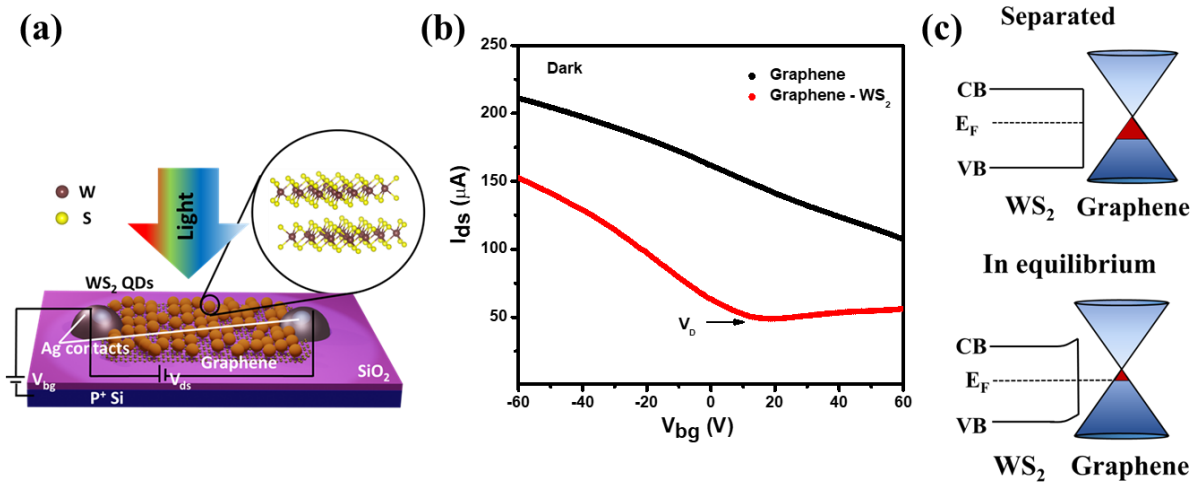

Figure 4.4: *Hybrid device and its electrical characterizations. (a) Schematic device structure of graphene-WS_2 QDs heterostructure. (b) Transfer characteristics of the graphene transistor with and without WS_2 QDs. (c) The energy band diagram before (top panel) and after formation of the heterostructure (bottom panel).*

has no effect on the transfer characteristics, indicating that graphene is the dominant carrier transport channel, but there is a significant shift in the CNP (> 60V to 18V), confirming the significant electron transfer from WS_2 quantum dots. The electrons can transfer from WS_2 QDs to graphene to equilibrate the Fermi levels leading to band bending in WS_2[138,98], as shown schematically by the energy band diagrams in the inset of **Figure 4.4c**. By simply introducing the Drude model, the field effect mobility (μ) of the hybrid graphene-WS_2 QDs transistor can be calculated as[161]

$$\mu = \frac{\sigma}{ne} \quad \ldots\ldots\ldots\ldots\ldots\ldots\ldots\ldots\ldots\ldots \quad (4.1)$$

Where, σ is the conductivity, n represents the charge carrier density and e is the electronic charge.

Here, σ is calculated from the relation,

$$\sigma = \frac{1}{R}\frac{L}{W} \quad \ldots\ldots\ldots\ldots\ldots\ldots\ldots\ldots\ldots\ldots \quad (4.2)$$

Where, R is the resistance of the device. L and W are the effective length and width of the device. Here in our device L~ 500 μm and W~ 1500 μm.

The gate voltage (V_{bg}) is converted to carrier density (n) using a parallel plate capacitor model, i.e.

$$n = \frac{C_{bg}}{e}(V_{bg} - V_D) \quad \ldots\ldots\ldots\ldots\ldots\ldots\ldots\ldots\ldots\ldots \quad (4.3)$$

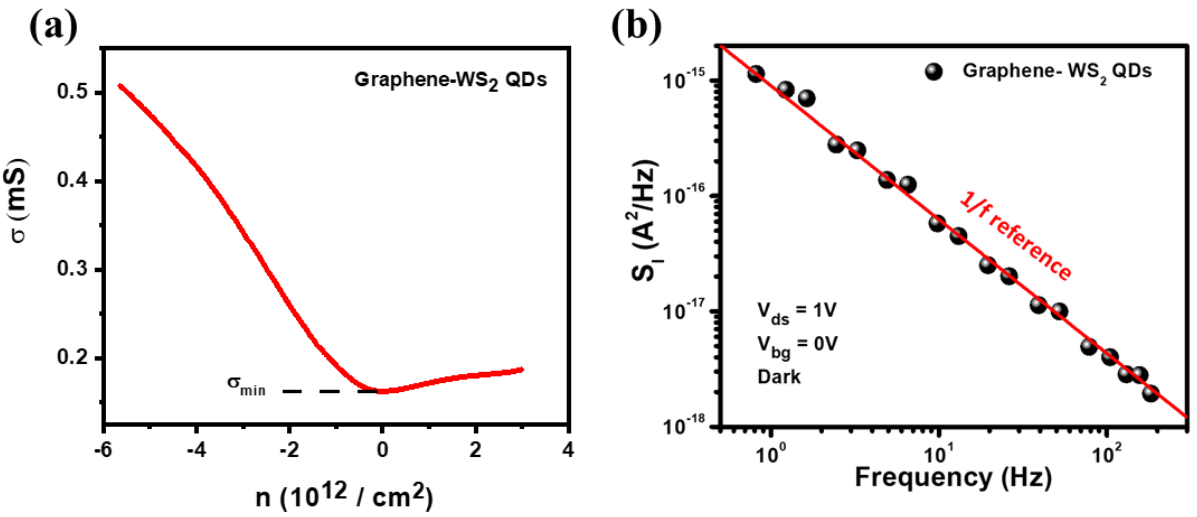

Figure 4.5: *Electrical characterizations of hybrid graphene-WS_2 QDs device. (a) Conductivity (σ) as a function of density (n) of graphene-WS_2 QDs hybrid device in dark. (b) 1/f noise spectral density of the hybrid graphene-WS_2 QDs phototransistor in dark with V_{ds} = 1 V, V_{bg} = 0 V.*

Where, $C_{bg} = 1.15\times10^{-8}$ F/ cm^2 is the backgate capacitance of 300 nm SiO_2. The n dependent σ graph is represented in **Figure 4.5a**. Using the following equations, we have calculated the field effect mobility of the charge carriers as ~ 400 cm^2/VS for holes and ~ 61 cm^2/VS for electrons in our hybrid device. The measurement of low frequency 1/f noise is very important in such graphene-based transistor devices in order to understand the detection limit of the device. Noise in the graphene devices is measured in low-frequency ac two-probe methods in a high vacuum environment with an excitation voltage bias of 1 V. The background noise is measured simultaneously, and subtracted from the total noise. In all devices, the normalized current noise PSD behaved as $SI/I^2 \sim 1/f^{\alpha}$, with α ranging from 0.9-1.1. The typical 1/f noise characteristic of a graphene-WS_2 QDs hybrid device is represented in **Figure 4.5b**.

4.3.2 Optoelectronic transport of graphene-WS_2 QDs phototransistor

4.3.2.1 UV-Vis (365-633 nm) broadband photoresponse

Figure 4.6a shows the photocurrent (I_{ph}) as a function of the drain-source bias (V_{ds}) for the hybrid device under the UV-visible (~365-633 nm) illumination of same optical power (P_{LED} ~ 470 μW/cm^2), at a gate voltage (V_{bg}) of 0 V at room temperature. The power dependent photocurrent results are presented in **Figure 4.6b** at a particular wavelength (λ = 365 nm). A significant photocurrent can be detected with a power as low as ~0.8 μW/cm^2 and a monotonic increase of photocurrent is observed with the increase of incident power. The temporal photocurrent characteristics in the broad UV-visible wavelength range (365-633 nm), with V_{ds} = 1 V, V_{bg} = 0 V for a constant optical power ~470 μW/cm^2 are shown in **Figure 4.6c**. It is found that the photocurrent (I_{ph}) can be effectively switched "on" and "off" with very good repeatability. The increased photocurrent of graphene-WS_2 QDs hybrid phototransistor for different wavelengths is in well agreement with the absorbance spectra of WS_2 QDs. Photo-responsivity (R) is one of the most important figure of merits to evaluate the performance of photodetectors which is a measure of a device's electrical response and is defined as[162]

$$R = \frac{I_{ph}}{P_{LED}} \quad \text{..... (4.4)}$$

where, I_{ph} is the photocurrent defined by (I_{light}-I_{dark}) and P_{LED} is the optical illumination power on the surface of the device. **Figure 4.6d** shows the variation of responsivity (R) with the illumination power at V_{ds} = 1 V and V_{bg} = 0 V for UV- Vis broad wavelengths. We observe an extremely high responsivity of ~3.1 × 10^2 A/W for λ = 365 nm with P_{LED} ~ 0.8 μW/cm^2. With increasing $P_{LED,}$ R decreases significantly, typical characteristics of the photodetectors[103,106,163].

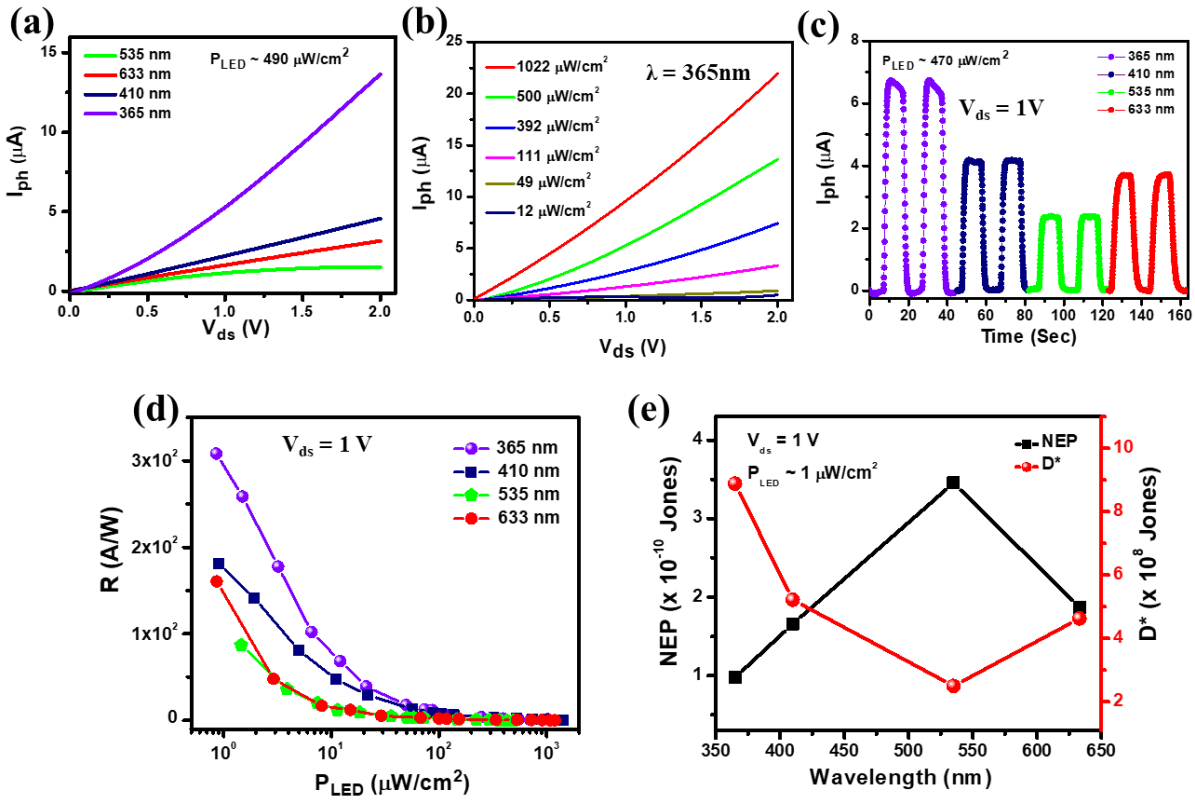

Figure 4.6: *Optoelectronic characteristics of graphene-WS_2 QDs phototransistor: (a) Photocurrent (I_{ph}) as a function of V_{ds} at V_{bg} = 0 V under UV-visible illuminations at P_{LED} ~ 470 μW/cm^2. (b) I_{ph} as a function of V_{ds} at V_{bg} = 0 V under different LED powers at λ = 365 nm. (c) Broadband temporal photoresponse of the hybrid device. (d) Photo-responsivity (R) as a function of optical powers at different wavelengths at V_{ds} = 1 V, V_{bg} = 0 V. (e) Noise equivalent power (NEP) and the specific detectivity (D^*) of the device as a function of illumination wavelength at V_{ds} = 1 V, P_{LED} ~ 1 μW/cm^2*

More importantly, significantly high responsivities are also observed for different spot wavelengths of 410 nm, 535 nm, and 633 nm, making the efficacy of our device as UV-visible broadband phototransistor. Responsivities are found to be ~ 1.81 × 10^2 and 1.6 × 10^2 A/W for 410 and 633 nm illumination, respectively for an optical power of 0.9 μW/cm^2, while R is ~ 0.87 × 10^2 A/W for 535 nm with a power of ~1 μW/cm^2. There are two main mechanisms of photocurrent either through the bound excitons or due to the photo-generated free charge carriers[164]. It is noted that the responsivity decreases from UV (365 nm) to green (535 nm) illumination by following the pattern of absorption spectrum of WS_2 QDs. It increases slightly at 633 nm due to the presence of strong exciton (A) peak, as observed in both absorbance and photoluminescence spectra. The responsivity of the fabricated graphene-WS_2 quantum dots hybrid device is significantly higher than that reported for pristine WS_2 (1.88 × 10^{-2}A/W)[165]

and graphene (0.61×10^{-2} A/W)[166] based devices as well as some of the graphene based hybrid photodetectors[167–171] (see **Table 4.1**). These results illustrate that superior large area broadband photo-transistor can be achieved by using graphene and WS_2 QDs. The figure of merits used to evaluate the capability of the detection of minimum optical illumination for a photodetector are the noise equivalent power (NEP) and the specific detectivity (D^*). The theoretical limit of the noise equivalent power (NEP) of these devices has been estimated by using the equation [120]

$$NEP = \frac{S_I}{R} \quad \text{..... (4.5)}$$

Where, S_I is the total current noise and R is the photo-responsivity of the device.

The specific detectivity can be found out from the equation, [120]

$$D^* = R\frac{A^{\frac{1}{2}}}{S_I} \quad \text{..... (4.6)}$$

Where, A is the effective area the device. Considering the dark current to be dominated by the 1/f (flicker) noise (**Figure 4.5b**), we get the limit of NEP for our devices to be ~9.7×10^{-11} W/$Hz^{0.5}$, which is presented in **Figure 4.6e** for λ = 365 nm. This low value of NEP indicates that the graphene-WS_2 QDs phototransistor may be very proficient for weak light detection. Also, considering the 1/f noise, the calculated specific detectivity (D^*) of the hybrid phototransistor is ~ 8.9×10^8 Jones for λ = 365 nm, P_{LED} ~ 0.8 μW/cm^2, V_{ds} = 1 V, V_{bg} = 0 V.

4.3.2.2 Gate tunable photoresponse

The transfer characteristics of the hybrid device both in dark and in presence of 365 nm illumination are depicted in **Figure 4.7a**. **Figure 4.7b** represents the responsivity of our device as a function of the applied back-gate voltage (V_{bg}) (at λ = 365 nm and V_{ds} = 0.1 V). It is observed that the responsivity changes from positive to negative as the gate voltage sweeps through the Dirac point (V_{bg} - V_D = 0 V). For $V_{bg} < V_D$, holes are responsible for the charge transport in graphene. With decrease of V_{bg}, the Fermi level of graphene is lowered and it enhances the built-in electric field at the interface of the heterostructure. This facilitates more photo-generated holes to be transferred from the QDs to graphene, resulting in an enhanced responsivity. Upon further decrease of V_{bg}, the responsivity shows a maximum at V_{bg}-V_D ~ -38 V and decreases thereafter. The trapped electrons in WS_2 QDs start tunnelling through the thinned barrier to graphene, leading to the decrease of the responsivity at higher negative gate voltages. Near the Dirac Point, the photoresponsivity becomes zero, that is, the device can

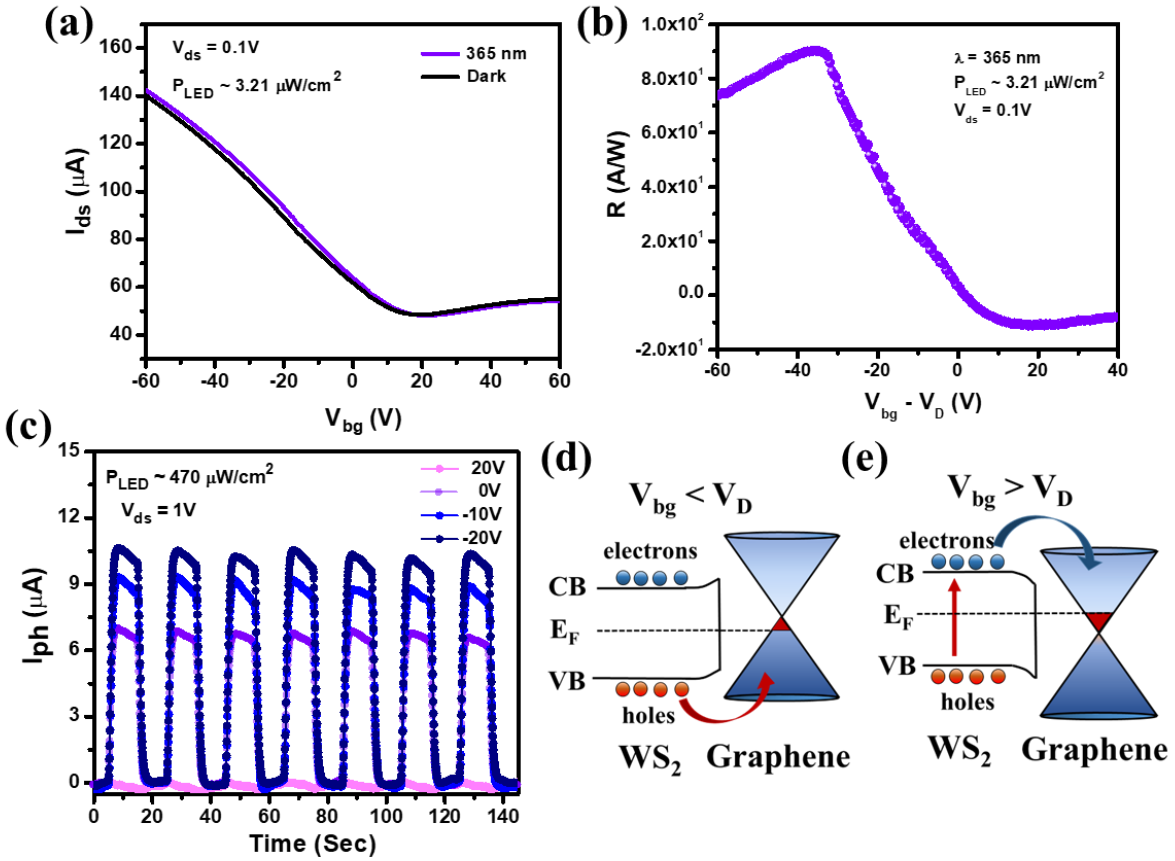

Figure 4.7: *Gate tunable photoresponse in the hybrid graphene-WS_2 QDs device: (a) Transfer characteristics of the hybrid device in dark and in illumination. V_{ds} = 0.1 V, λ = 365 nm, P_{LED} ~ 3.21 μW/cm^2. (b) Responsivity (R) as a function of V_{bg}-V_D under illumination of ~ 3.21 μW/cm^2 at λ = 365 nm, V_{ds} = 0.1 V. (c) Back gate (V_{bg}) dependent temporal photoresponse of the device under 365nm illumination at V_{ds} = 1 V. The band bending of the graphene-WS_2 QDs at (d) V_{bg} < V_D and (e) V_{bg} > V_D that illustrate the photodetection mechanism in the hybrid interface.*

effectively be turned "off" by tuning the gate voltage. At, $V_{bg} > V_D$ the electrons are the dominant charge carrier and the sign of responsivity becomes negative. The magnitude of responsivity again increases with increasing V_{bg} due to the enhanced injection of electrons from QDs to graphene. Like the hole side, a maximum in responsivity is observed at lower (V_{bg} - V_D) value (~ 15 V), possibly due to the lower mobility of electrons compared to the holes in the hybrid device. Thus, the gate voltage provides an additional functionality to switch the sign of the responsivity which demonstrates the potential of this device as a back-gate-tunable ultrahigh responsive phototransistor[98,138]. This tunability is of great importance in photodetectors because it allows to control the state (on/off) of the detector as well as to adjust the required responsivity, depending on the light intensity to be detected. Upon illumination of

λ = 365 nm, this device exhibits a large positive photocurrent of about ~7 μA which can further be modulated by varying V_{bg}. **Figure 4.7c** represents that the photocurrent (I_{ph}) increases from ~ 7 μA to ~ 11 μA with the gate voltages (V_{bg}) changing from 0V to -20 V and becomes negligibly small at V_{bg} = 20 V. The gate tunable charge transfer mechanism is schematically represented in **Figure 4.7d** for $V_{bg} < V_D$ and in **Figure 4.7e** for $V_{bg} > V_D$.

4.3.2.3 Role of confinement effect in photoresponse

A comparative study of the photoresponse is conducted on graphene-WS_2 phototransistors with two different morphologies of WS_2, namely WS_2 quantum dots (0D) and WS_2 nanosheets (2D),

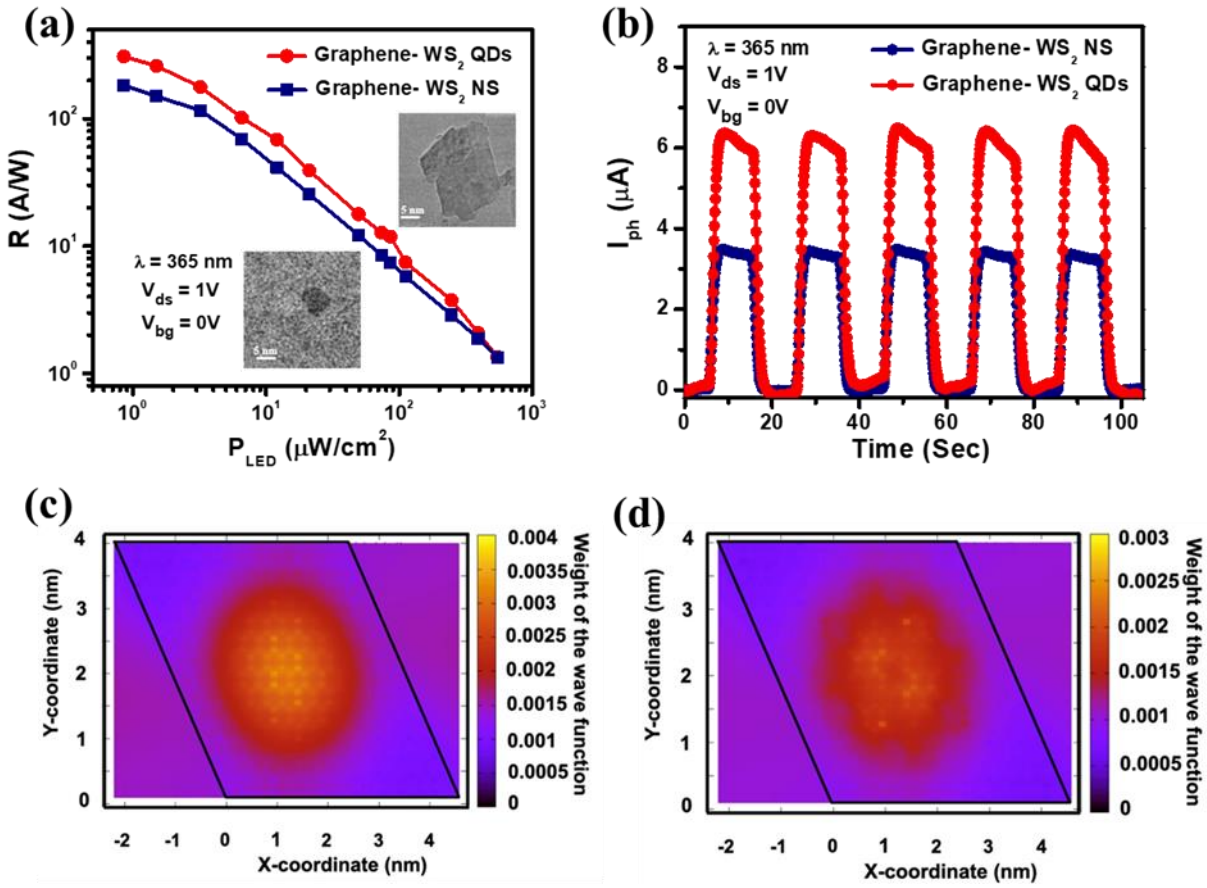

Figure 4.8: *The dependence of photoresponse on WS_2 morphology: Comparison between corresponding (a) photo responsivities (R) (the TEM image of WS_2 nanosheet and a WS_2 quantum dot) and (b) temporal photocurrents (I_{ph}) at 365 nm with V_{ds} = 1 V and V_{bg} = 0 V (c) Colour plot of the weight of the wave function corresponding to the highest occupied valence band on W atoms of the bilayer flake of lateral dimension 47.30 Å(d) Colour plot of the weight the wave function corresponding to the lowest unoccupied conduction band on W atoms of the bilayer flake of lateral dimension 47.30 Å.*

in order to gain a deeper understanding of the role of WS_2 QDs for highly sensitive photodetection (2D). The same processes are used to fabricate and measure each of these devices. **Figures 4.8a** and **4.8b** compare the photo-responsivity and temporal photocurrent for these two various devices. We find that the photoresponse (3.11×10^2 A/W) in graphene-WS_2 QDs heterostructure is significantly higher than that in graphene-WS_2 nanosheets (1.83×10^2 A/W), indicating that the morphology of WS_2 significantly affects photocurrent. The absorbance of the photo absorbing material has a significant impact on a device's photoresponse, and it has been experimentally found that WS_2 QDs have a higher absorbance than WS_2 nanosheets (**Figure 4.2a**). Ab-initio calculations of the electronic structure of quantum dots (QDs) with a size similar to our experimental result (4.7 nm) are carried out to better understand the cause of enhanced photocurrent for WS_2 QDs. **Figures 4.8c** and **4.8d**, respectively, display the calculated weights of the wave functions corresponding to the highest occupied valence band and the lowest unoccupied conduction band on each W atom in a layer of the QD. It has been discovered that the weight is not equally distributed among all the W atoms in these two states. In contrast to the infinite WS_2 nanosheet, where the weight is uniformly distributed over all the W atoms and has values of 0. 0015 at a W site for the valence band maximum and 0.0011 for the conduction band minimum, these wave functions have higher weights at the center of the quantum dot. One finds that oscillator strength for the transition will involve the weight of the valence band maximum wave function on a layer as well as the conduction band minimum wave function. This as we can see from **Figure 4.8c** leads to an enhancement of 2-3 times over what we have for the nanosheet. Similarly, **Figure 4.8d** reveals an enhancement of 2-3 times for the QD over the nanosheet. Consequently, one has an enhancement of around 9 times the oscillator strength for the QD over the nanosheets.

4.3.2.4 Role of quantum dots (QDs) concentration in photoresponse

The photoresponse of the hybrid graphene-WS_2 QDs phototransistor device also depends on the concentration of QDs. Initially, with increasing QDs concentration, the absorbance of photons is increased. A higher photon density leads to generate more electron-hole pairs which contribute to the increased photocurrent (photoresponsivity). Also, the performance of the hybrid phototransistor depends on the energy band alignment of the graphene and the WS_2 QDs, which helps to dissociate the photogenerated charge carriers. Now, with further increase in QDs concentration above the optimal value, the photogenerated excitons may get diffused within the QDs layers, which decreases the photocurrent (photoresponsivity). Here, it is found

that, the photoresponsivity of the graphene-WS_2 QDs heterostructure is highest for 2.25 mg/ml concentration of WS_2 QDs with ~ 0.75 mm^2 effective device area. The SEM images of the devices with different QDs concentrations and the photoresponsivity as a function of QDs concentration are incorporated in **Figure 4.9a** and **4.9b** respectively.

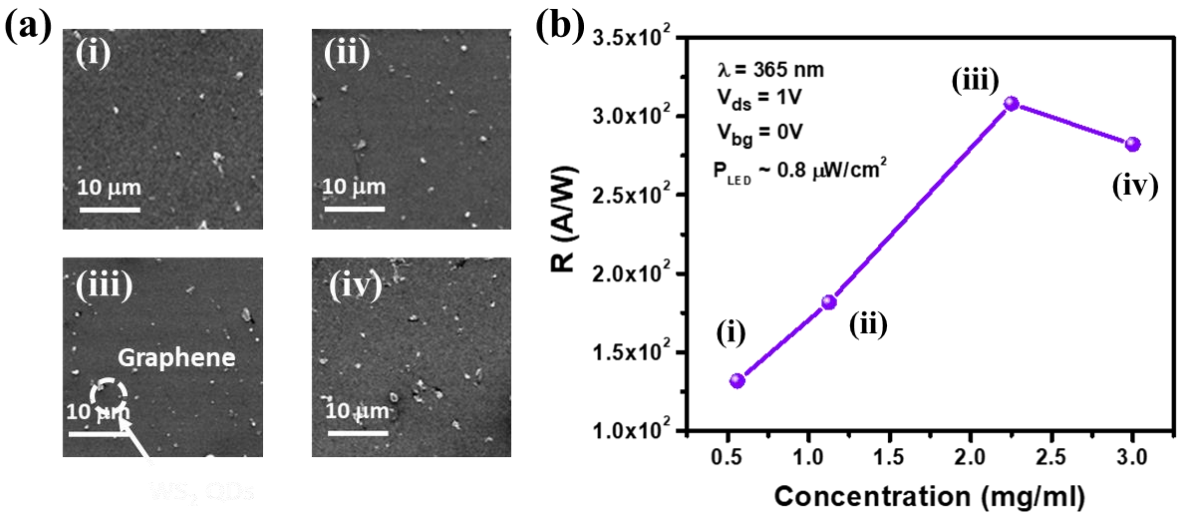

Figure 4.9: *The dependence of photoresponse on QDs concentration: (a) SEM image of the WS_2 QDs deposited CVD graphene sheets with different concentrations (i) 0.56 mg/ml (ii) 1.12 mg/ml (iii) 2.25 mg/ml (iv) 3 mg/ml (b) Variation of photoresponsivity (R) as a function of concentration of WS_2 QDs at V_{ds} = 1 V, V_{bg} = 0 V, λ = 365 nm, P_{LED} = 0.8 µW/cm^2.*

4.3.2.5 Stability

Furthermore, the stability of the device is checked (**Figure 4.10**) by measuring the same device after 4 months. No significant degradation of photocurrent is observed (I_{ph}), making it a

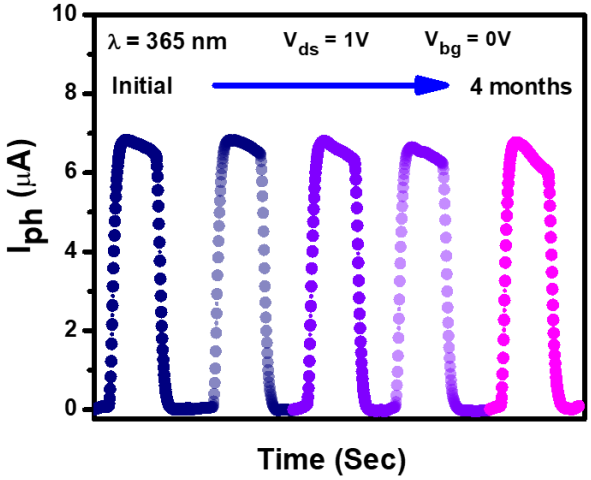

Figure 4.10: *The temporal photoresponse of the hybrid graphene-WS_2 phototransistor device after several months from the device fabrication which shows its stability.*

promising candidate for future technological applications. Also, the performance of some recently reported graphene-TMDC hybrid photodetector devices are compared in **Table 4.1** below.

Table 4.1: *Comparison of performances with reported graphene-TMDC hybrid photodetectors.*

SL No	Device structure	Channel length (μm)	Wavelength (nm)	V_{sd} (V)	V_{bg}(V)	R (A/W)	τ_{Rise} /τ_{Fall} (Sec)	Ref.
1.	Graphene-MoS_2	~ 20	632.8	0.1	-20	10	0.280/1.50	54
2.	Graphene-WS_2*	250	550	5	0	6.4	0.01/0.02	40
3.	Graphene-WS_2	-	532	5	30	121	-	55
4.	Graphene-$MoTe_2$	~10	532	-2	0	0.02	0.03/0.03	56
5.	Graphene-MoS_2-graphene	~5	405-2000	-1	40	414	0.692/ -	48
6.	Graphene-WS_2 QDs *	1000	365	5	0	1814	2.04/2.89	64
7.	Graphene-WS_2-Al_2O_3	90	340-680	2	0	950	7.85/5.61	62
8.	Graphene-BP	~ 3	655-980	0.5	-35	55.75	-/0.036	58
9.	Graphene-WS_2 QDs	~500	365-633	1	0	3.1×10^2	1.2/1.32	**This work**

*2 terminal diode configuration

4.4 Summary

In summary, we have fabricated a scalable, eco-friendly, cost effective, mixed dimensional (2D-0D) hybrid phototransistor by using a CVD grown graphene and chemically exfoliated WS_2 quantum dots without any lithographic process. Semiconducting WS_2 QDs (average radius ~ 2.75 nm) are synthesized by simple chemical exfoliation procedure, which act as a photo-absorbing material in the heterostructure device. Raman and photoluminescence measurements indicate the charge transfer between WS_2 QDs and the graphene layer, and the fabricated device shows an excellent UV-visible broadband (365-633 nm) photo response with superior gate tunability. The hybrid device exhibits moderately high detectivity (~8.9×10^8 Jones), superior photoresponsivity (3.3×10^2 A/W) and low noise equivalent power (~9.7×10^{-11} W/$Hz^{0.5}$), which are comparable or better than other available graphene based hybrid photodetectors[167]. The response time of ~1.2 sec (rise time) and ~1.32 sec (fall time) are also comparable or faster than the previously reported graphene-based hybrid photodetectors. The solution processed 0D-2D phototransistor device exhibits an extraordinary stability without any degradation of photocurrent even after 4 months of its fabrication, demonstrating its

potential for future optoelectronic devices. Furthermore, a comparative study has been done between two different morphologies of WS_2 such as graphene-WS_2 quantum dots (2D-0D) heterostructure and graphene-WS_2 nanosheets (2D-2D) heterostructure with the former device showing better photoresponse, which can be attributed to the higher absorbance of WS_2 QDs due to the quantum confinement effect. This is further explained by our first principle calculation using DFT. This superior quality large area, broadband, hybrid phototransistor has significant potential in the applications of imaging, sensing, and communication etc. The obtained results in this work demonstrate that the solution processed wafer scale WS_2 QDs based hybrid device to be a prospective candidate for the next generation low cost, high performance optoelectronic devices.

Chapter 5

Optoelectronics with Graphene – $MoS_{2x}Se_{2(1-x)}$ Alloy Engineered Phototransistors

In two-dimensional transition metal dichalcognides, alloy engineering has become a practical method for tuning the bandgap and engineering the defect levels (TMDC). The ability to chemically synthesize these ultra-thin TMDC materials has increased the likelihood of successfully fabricating hybrid multi-functional devices. We systematically investigate the photo response properties of three terminal hybrid devices by decorating large area graphene with these nanosheets (x = 0, 0.5, 1) in 2D-2D configurations, synthesising nanosheets with various composites of $MoS_{2x}Se_{2(1-x)}$ (x = 0 to 1). Among them, the graphene-MoSSe hybrid phototransistor outperforms its binary counterparts in terms of optoelectronic properties. The device has a very high photoresponsivity (>10^4 A/W), a low noise equivalent power (10^{-14} W/$Hz^{0.5}$), and a higher specific detectivity (~10^{11} Jones) in the UV-NIR (365-810 nm) range, with magnificent gate tunability. This device is extremely appealing due to its broadband light absorption and controllable defect engineering in MoSSe and ultrafast charge transport in graphene. Our work demonstrates the large area scalability of $MoS_{2x}Se_{2(1-x)}$ alloys with wafer-scale production, which has important implications for the facile and scalable fabrication of high-performance optoelectronic devices as well as providing important insights into the fundamental interactions between van der Waals materials.

5.1 Introduction

Broadband photodetectors are particularly important due to their applicability in the wide dynamic range of the electromagnetic spectrum, which improves versatility in a variety of applications such as flexible image sensing, surveillance, communication, and health monitoring[118,172]. Transition metal dichalcogenides (TMDCs), an emerging class of two dimensional (2D) layered semiconductors, become interesting because of their controllable band gap (1-2 eV) and strong light-matter interactions[27]. Various strategies like strain engineering[173] etc. are employed to widen the effective wavelength range. However, the majority of the processes are either difficult to replicate or have a negative impact on the

performance of phototransistors such as responsivity, response time, and so on[174]. Two dimensional heterostructures[175] have emerged as a powerful route towards creating high responsivity phototransistor by incorporating two different 2D layered materials in close proximity through van der Waals interaction[103]. Furthermore, the ability to create their nanostructures via relatively simple chemical routes has been shown to broaden the absorption band width and thus be useful for broadband photodetection[176]. Among various possibilities, graphene based heterostructure has shown immense prospect. In spite of having superior electronic properties[1,177] like high charge carrier mobilities, broad spectral bandwidth, ultra large specific surface area etc., it has limitations in the optoelectronic applications due to its low light absorption and gapless nature[178]. One simple strategy to overcome this shortcoming is to create a new device structure by incorporating some light absorbing (Si quantum dots[98], PbS[138], ZnO[179,180] etc) materials into graphene. In this typical device structure graphene is used as the channel to slow the charge carriers and interaction between the photoactive material and graphene is the prime factor for the ultrasensitive photodetection. Being layered semiconductors, some members of the transition metal dichalcogenide[38] (TMDC) family (MX_2 (M = Mo, W; X = S, Se) are natural partners of graphene for optically active heterostructures[103]. However, these binary TMDCs may have intrinsic defects such as chalcogen vacancies, which have a significant impact on their intrinsic electronic and optical properties resulting in localized deep-level defect states (DLDSs)[181]. Alloying is thought to be the potential solution to these problems because it provides lower deep level densities[182], conversion of deep to shallow levels of defects and also better thermal stability[183]. As a result, for the broad applications in integrated devices, the development of these bandgap engineered 2D ternary alloys may provide a feasible solution to improve the device performance. It has already been reported that $MoS_{2x}Se_{2(1-x)}$ ternary alloys can successfully be prepared[184], but the high temperature, specific atmospheric conditions, and other requirements for growing these materials limit their application related performances[168].

A systematic study of graphene-$MoS_{2x}Se_{2(1-x)}$ hybrid phototransistors with x ranging from 0 to 1 is presented in this paper. Composition-tunable ternary $MoS_{2x}Se_{2(1-x)}$ alloy nanosheets are synthesised using a simple hydrothermal synthesis followed by ultrasonication, and structural and optical investigations show that these 2D ternary alloys are highly crystalline and exhibit composition-dependent band edge emission. The higher photoresponsivity and faster response time in graphene-MoSSe phototransistors imply a lower density of deep level defects when compared to their binary counterparts. In the broad spectral region 365-810 nm, this hybrid

phototransistor fabricated with the optimised alloy has a gate tunable photoresponsivity (R) greater than 10^4 A/W and a noise equivalent power as low as 10^{-14} W/Hz$^{0.5}$. Also considering the low frequency 1/f noise measurement, the specific detectivity (D^*) of the device reaches ~10^{11} Jones, which is higher or comparable to the previously reported results[96,185]. This work demonstrates a stable, highly sensitive phototransistor that could be applied to future multifunctional devices.

5.2 Experimental Section

5.2.1 Materials

Sodium molybdate dehydrate ($Na_2MoO_4 \cdot 2H_2O$), Sulfur (S) and Selenium (Se) have been purchased from Alpha Aser, and Sodium borohydride ($NaBH_4$) has been purchased from Sigma-aldrich. All these chemicals are directly used without further purification. Deionized water is purified by a Milli-Q system.

5.2.2 Synthesis of $MoS_{2x}Se_{2(1-x)}$ alloy nanosheets

The hydrothermal method is used to synthesize ternary alloy $MoS_{2x}Se_{2(1-x)}$ nanosheets, which are then subjected to ultrasonication. $Na_2MoO_4{:}2H_2O$, S, and Se are used in this typical procedure as precursors of Mo, S, and Se, respectively, and $NaBH_4$ is used as a reducing agent. For this synthesize procedure, DI water is first used to dissolve $Na_2MoO_4 \cdot 2H_2O$, S and Se powder of proper stoichiometric amounts. The resulting solution is then homogenised using continuous magnetic stirring. Following the addition of aqueous NaBH4, which turns the

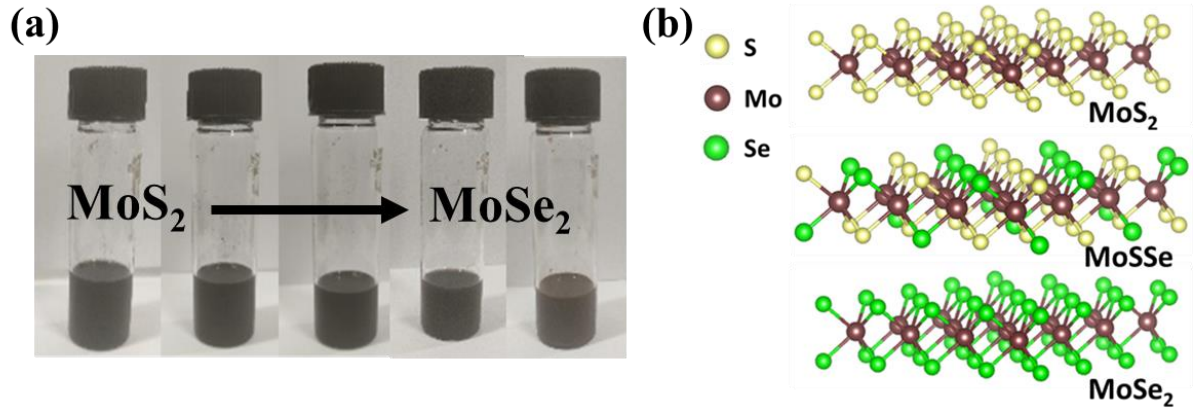

Figure 5.1: *(a) Optical image of $MoS_{2x}Se_{2(1-x)}$ dispersed solution in IPA. (b) Schematic structures of monolayer MoS_2, MoSSe and $MoSe_2$ nanosheets.*

mixture's colour brown, the mixture is kept for magnetic stirring to create a completely homogeneous, uniform mixture. This brown coloured solution is transferred into a 40 ml teflon-lined stainless autoclave and heated at 200°C. After the reaction is over, the autoclave is naturally cooled to room temperature and the finally found black powder samples are collected by repeated washing and centrifugation with DI water and IPA. To obtain the nanosheets, the cleaned wet powder sample is dried and then dissolved in IPA and sonicated in a bath before centrifugation. The ternary $MoS_{2x}Se_{2(1-x)}$ nanosheets dispersed in IPA is then used for optoelectronic experiments and characterizations. MoS_2 and $MoSe_2$ are prepared using a similar hydrothermal method assisted by ultrasonication. **Figures 5.1a** and **5.1b**, respectively, show the stable, well-dispersed colloidal $MoS_{2x}Se_{2(1-x)}$ alloy nanosheets in IPA solution and their schematic structures.

5.2.3 Materials and interface characterizations

5.2.3.1 Microstructural characterizations

All the compositions of $MoS_{2x}Se_{2(1-x)}$ alloy nanosheets are investigated by using scanning electron microscopy (SEM) equipped with energy-dispersive X-ray (EDAX) spectroscopy. The signature of Mo, S, Se can be observed in EDAX spectrum of the ternary alloys and their

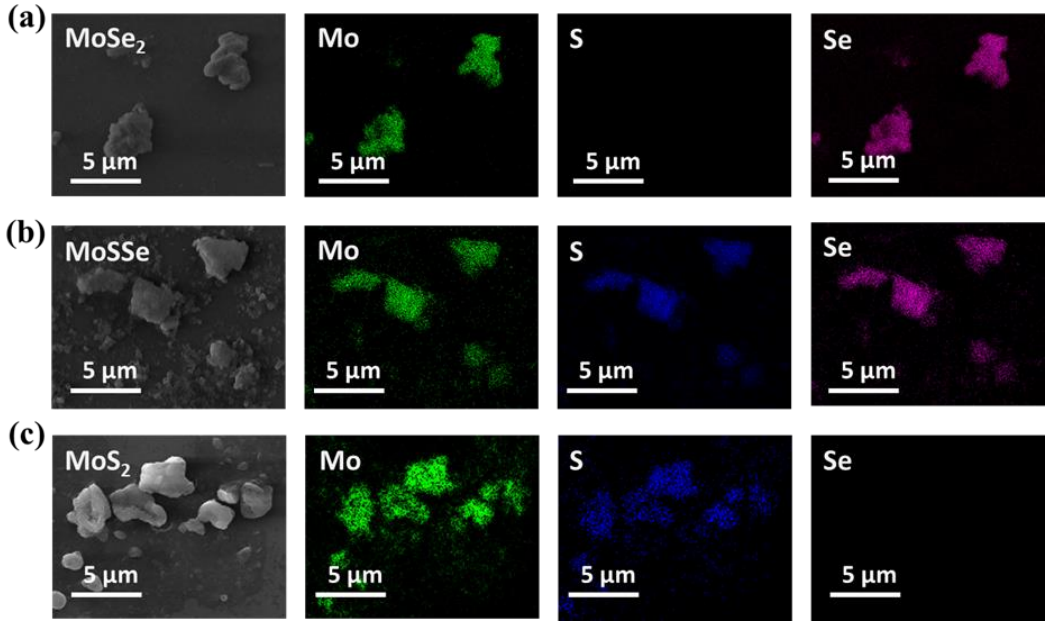

Figure 5.2: *EDAX elemental mapping of different components (Mo, S, Se) of* $MoS_{2x}Se_{2(1-x)}$ *alloys (x= 0 ,0.5, 1) (a)* $MoSe_2$ *(b) MoSSe (c)* MoS_2*.*

homogeneous distribution in the typical alloy nanosheets (for x = 0, 0.5, 1) is clearly evidenced by the elemental mapping images (**Figure 5.2**).

To crystallinity of $MoS_{2x}Se_{2(1-x)}$ with x = 0, 0.5, 1, can be well understood by high-resolution transmission electron microscopy (HRTEM) images and the selected area electron diffraction (SAED) patterns (bottom inset) as shown in **Figure 5.3a, b, c** respectively. Based on the HRTEM images, the lattice spacing of MoSSe alloy is found to be 0.28 nm, which indicates the formation of (100) plane[186] (**Figure 5.3b**). The SAED pattern of a typical MoSSe nanosheet shows bright diffraction spots with high quality hexagonal symmetry structure, with the outer and inner spots indexed as the (110) and (100) planes of 2H-MoSSe respectively[187]. With increasing Se content, the interlayer spacing for (002) plane (top Inset) is found to be increased

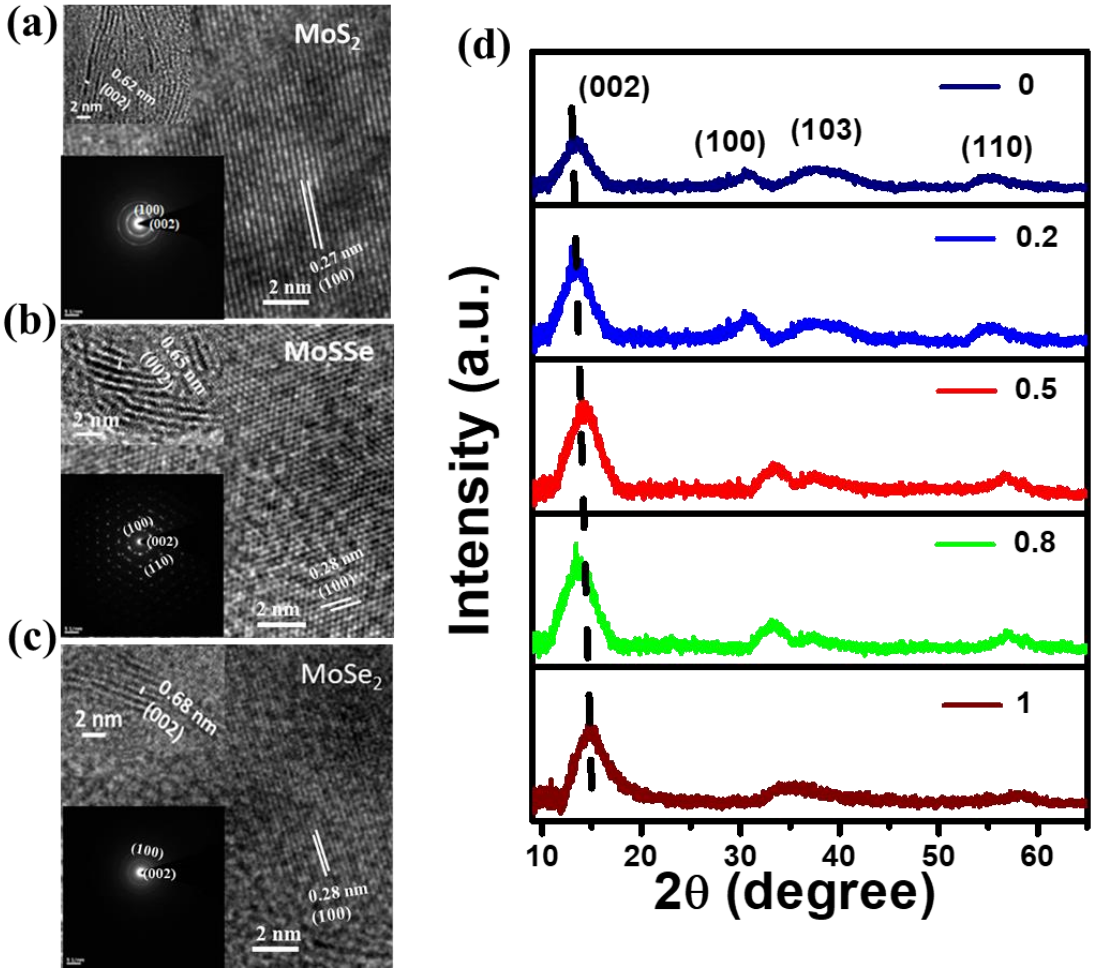

Figure 5.3: *Microstructural characteristics of $MoS_{2x}Se_{2(1-x)}$ alloys. High-resolution TEM images of (a) MoS_2, (b) MoSSe and (c) $MoSe_2$ nanosheets with corresponding interlayer spacing of (002) plane (top Inset) and SAED patterns (bottom Inset). (d) XRD patterns of different composites of $MoS_{2x}Se_{2(1-x)}$ alloys with varying S fraction (x).*

(for MoS_2~ 0.62 nm, MoSSe~ 0.65 nm, $MoSe_2$~ 0.68 nm) due to the larger atomic radius of Se than S[188]. Pristine monolayer MoS_2 ($MoSe_2$) consists of three sublayers, one layer of Mo atom sandwiched by two planes of S (Se) atoms. In the hydrothermal synthesis, the sulpho-selenide compositions S and Se's are distributed randomly, keeping the Mo atomic sites at the centre of the tetragon and maintain the hexagonal crystal symmetry, as depicted schematically in **Figure 5.1b**. The XRD patterns of all these ternary alloys (**Figure 5.3d**) along with the two binary counterparts exhibit diffraction peaks which are well consistent with the previous reports[189,190]. Decreasing the S content leads to the continuous downshift of (002) diffraction peak in $MoS_{2x}Se_{2(1-x)}$ ternary alloys. This is in accordance with the gradual expansion of lattice structure due to substitution of S atoms by larger radii Se atoms, which implies that the mixing occurs in atomic level and the obtained results from the XRD analysis agree well with the HRTEM observations.

5.2.3.2 Spectroscopic characterizations

The spectroscopic properties of the few layered as-synthesized ternary $MoS_{2x}Se_{2(1-x)}$ alloys are investigated by using UV-Vis absorption spectroscopy (**Figure 5.4a**). All the alloy composites (x = 0 to 1) show two prominent peaks, designated as exciton 'A' and 'B' peaks. These peaks originate from the direct excitonic transitions at the K and K´ points of the first Brillouin zone and the spin-orbit coupled valance bands[27,143]. It is observed that, with decreasing S (increasing Se) content both the excitonic peaks (exciton 'A' and 'B') shift to the lower energies (**Figure**

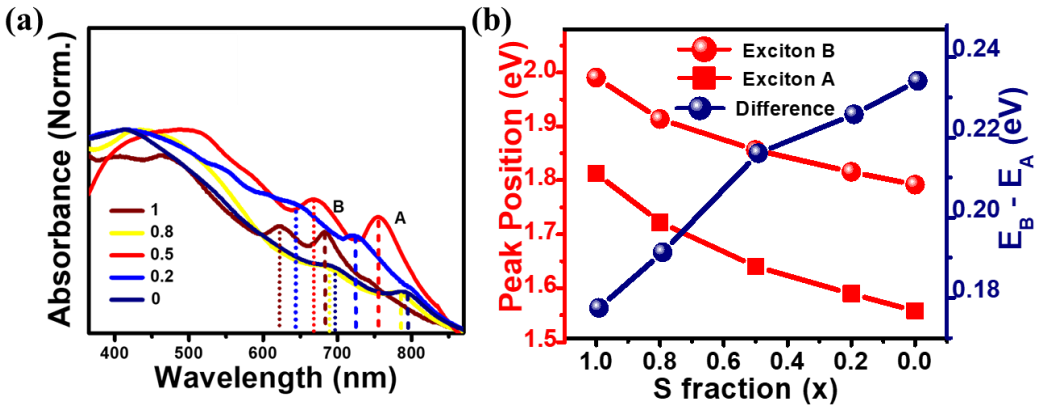

Figure 5.4: *Spectroscopic characterizations of $MoS_{2x}Se_{2(1-x)}$ alloys. (a) Normalized absorbance spectra with different x values, energy of excitonic A and B peaks (represented with dashed lines for exciton 'A' and dotted lines as exciton 'B'). (b) Evaluation of exciton 'A', 'B' and their energy gap (E_A - E_B) as a function of S fraction (x).*

5.4b). Also, the energy difference between these two peaks (E_B-E_A) increases monotonically (from 0.17 eV to 0.23 eV) with decreasing S content (from 1 to 0), which can be explained by the enhanced spin-orbit coupling strength with increasing Se content[191].

Composition tunable vibrational modes can be studied from the Raman spectra of $MoS_{2x}Se_{2(1-x)}$ alloys (**Figure 5.5a**). All these ternary alloys exhibit 4 different vibrational modes which can be assigned as A_{1g} (Se-Mo), E^1_{2g} (Se-Mo), A_{1g} (S-Mo) & E^1_{2g} (S-Mo). All of these molecular vibrational modes are in good agreement with the gradual tuning of the S or Se component in $MoS_{2x}Se_{2(1-x)}$ alloys. The modes related to the Se-Mo vibration i.e., A_{1g} (Se-Mo) and E^1_{2g} (Se-Mo), remain absent in MoS_2 (x = 1) and start to emerge with introducing Se content. Similarly, the intensity of the S−Mo related modes (E^1_{2g}(S−Mo), A_{1g}(S−Mo)) gradually decreases and disappear entirely in the binary $MoSe_2$ compound. All the vibrational modes shift to a lower frequency with decrease of S content (increase Se content), as shown in **Figure 5.5b**. With the decrease of S (increase of Se) fraction, the interaction of Se and S atoms would soften the S-Mo related modes and therefore the modes related to Se-Mo shift to lower frequencies due to the decrease in S content[192].

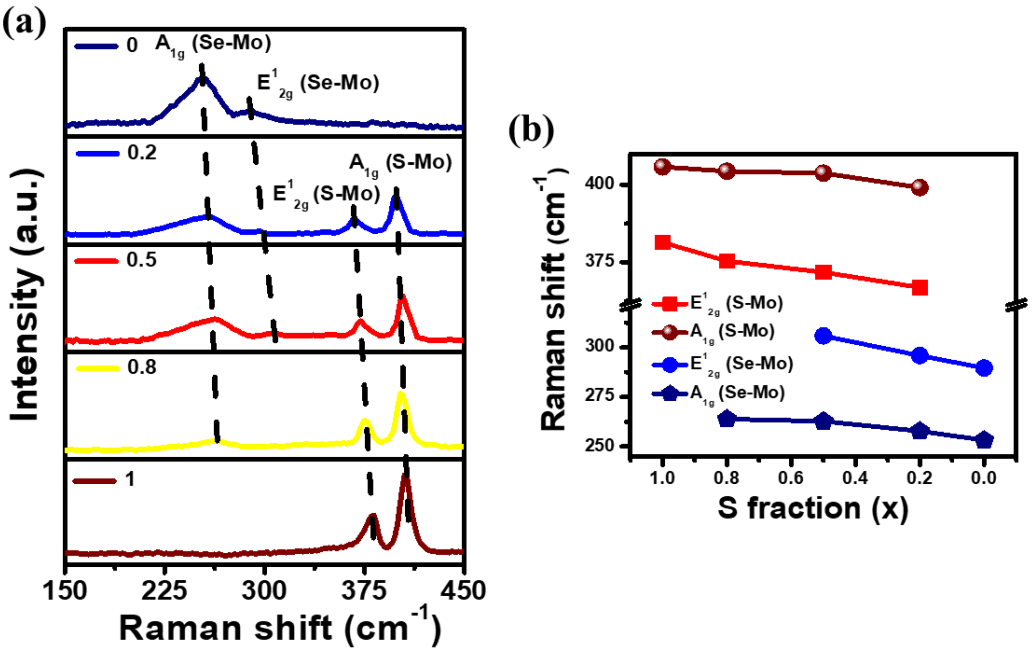

Figure 5.5: *Raman spectra of $MoS_{2x}Se_{2(1-x)}$ alloys with 532 nm laser excitation. (a) Composition tunable raman spectra of the alloys. (b) Dependence of S-Mo and Se-Mo related Raman mode shift with sulfur (S) fraction.*

The photoluminescence (PL) spectra, recorded by an excitation with 532 nm laser of $MoS_{2x}Se_{2(1-x)}$ alloys reveal (**Figure 5.6a**) that the emission spectrum can be modulated by varying the S and Se content. It is observed that the PL intensity of MoSSe alloy is greatly enhanced compared to the others. With the introduction of Se, the PL emission peak shows a red shift starting from 673 nm for pure MoS_2 to 725 nm for pure $MoSe_2$. These band edge excitonic transitions are attributed to the valance band splitting which is affected by the enhanced spin-orbit coupling due to decreasing S (increasing Se content)[193]. So, by tuning the Se and S component in the ternary alloys, the optical band gap can be modulated as it is observed from the emission peak shift in PL measurements (**Figure 5.6b).**

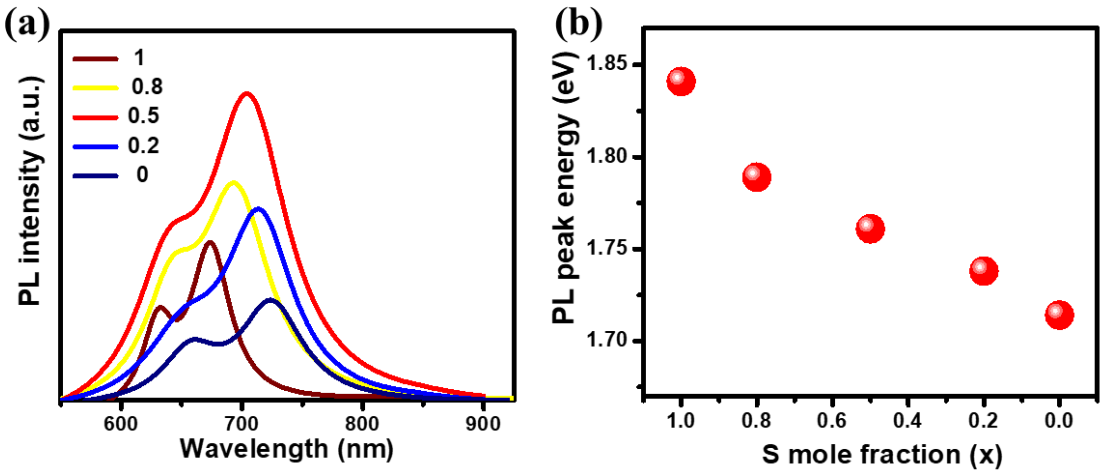

Figure 5.6: *Photoluminescence (PL) spectroscopy of $MoS_{2x}Se_{2(1-x)}$ alloys with 532 nm laser excitation. (a) Composition tunable PL spectra of the alloys. (b) The dependence of PL peak position with sulfur (S) fraction.*

5.2.3.3 Interface characterizations

The interface between graphene and MoSSe is characterized by scanning electron micrograph (SEM), Raman and PL spectroscopy. The SEM image of the graphene-MoSSe (x = 0.5) heterostructure and the corresponding EDAX spectra are shown in **Figure 5.7a** and **5.7b** respectively. Both the Raman (**Figure 5.7c**) and EDAX spectra (**Figure 5.7b**) are used as a fingerprint of the presence of graphene and the MoSSe alloy in our measured device, while the steady state PL spectra (**Figure 5.7d**) is recorded to understand the charge transfer between them.

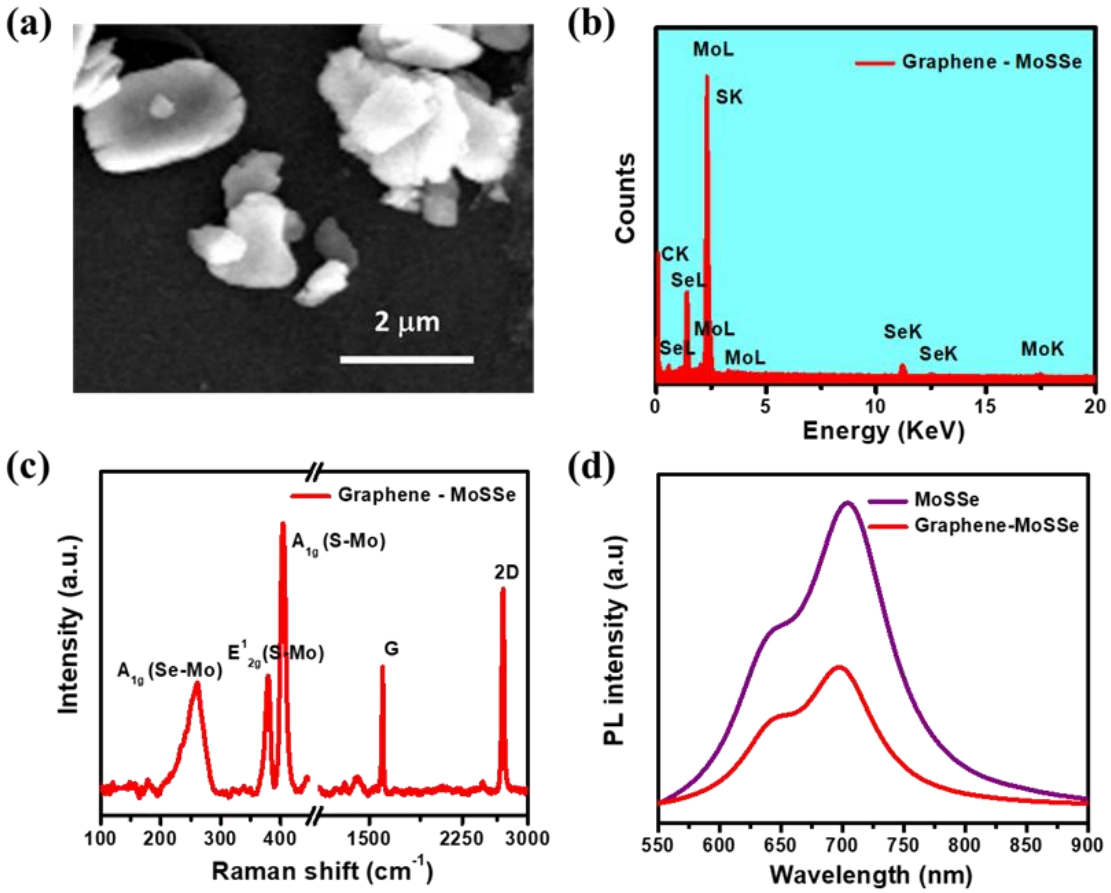

Figure 5.7: *Interfacial characterizations of graphene-MoSSe heterostructure device.* (a) *Scanning electron micrograph (SEM), (b) EDAX spectra, (c) Raman spectra and (d) PL spectra of bare MoSSe and graphene-MoSSe.*

5.3 Results and discussions

5.3.1 Fabrication of hybrid devices

The phototransistor devices are fabricated by using commercially available single-layer CVD-grown graphene on p^+ doped Si/SiO_2 (300 nm) substrates (purchased from Graphenea, USA). Then the Ti/ Au (5 nm / 60 nm) source and drain electrodes are deposited on top of the graphene film through a shadow mask by electron beam evaporation and formed a channel of W/L = 200 μm/ 70 μm. After the fabrication of the back gated graphene transistor, the chemically synthesized $MoS_{2x}Se_{2(1-x)}$ alloys (~25 μL) are drop casted on top of the graphene transistor to make the complete hybrid devices. All the devices are then annealed at 80º C for 45 mins to remove the interfacial residues. **Figure 5.8** shows the schematic of the device based on monolayer graphene and 2D TMDC alloys.

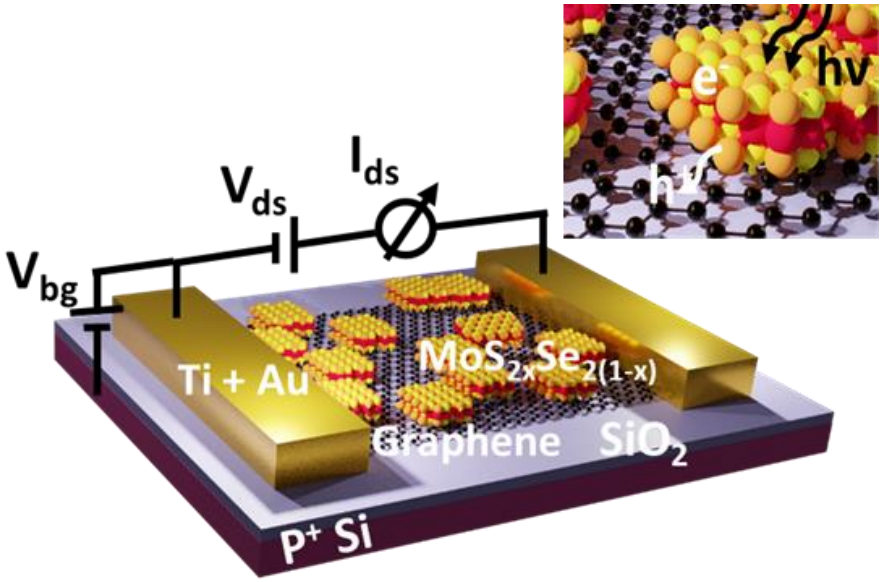

Figure 5.8: *Schematic of the hybrid graphene-MoSSe field effect transistor device. Here CVD grown graphene on Si/SiO_2 is coated with $MoS_{2x}Se_{2(1-x)}$ alloy nanosheets. Inset shows interfacial charge separation mechanism under illumination.*

5.3.2 Electronic transport of graphene-MoSSe hybrid transistor

The transfer characteristics (**Figure 5.9a**) of bare graphene and the heterostructure device (Graphene-MoSSe) reveal that the bare CVD grown graphene is a p-doped (Dirac point (V_D) > 80 V) and the Dirac point shifts to ~ 28 V due to the presence of MoSSe alloy. This means the p-type doping effect in graphene is weakened due to the effective electron transfer from MoSSe to graphene, which results from the initial work function mismatch between these two materials[194]. The field effect mobility (μ) of the hybrid graphene-MoSSe transistor can be calculated by simply introducing Drude model (as discussed in the previous chapter) which gives

$$\mu = \frac{\sigma}{ne} \quad \ldots\ldots\ldots\ldots\ldots\ldots\ldots\ldots\ldots\ldots\ldots\ldots\ldots\ldots \quad (5.1)$$

Where, σ is the conductivity, n represents the charge carrier density and e is the electronic charge.

Here, σ is calculated from the relation,

$$\sigma = \frac{1}{R}\frac{L}{W} \quad \ldots\ldots\ldots\ldots\ldots\ldots\ldots\ldots\ldots\ldots\ldots\ldots\ldots\ldots \quad (5.2)$$

Where, R is the resistance of the device. L and W are the effective length and width of the

device. The gate voltage (V_{bg}) is converted to carrier density (n) using a parallel plate capacitor model, i.e.

$$n = \frac{C_{bg}}{e}(V_{bg} - V_D) \quad \ldots\ldots\ldots\ldots\ldots\ldots\ldots\ldots\ldots\ldots \quad (5.3)$$

Where, $C_{bg} = 1.15\times10^{-8}$ F/ cm^2 is the backgate capacitance of 300 nm SiO_2.

Figure 5.9b shows the conductivity (σ) vs density (n) plot of the hybrid device at room temperature, which shows that the conductivity is linearly varying with density at low densities and deviates at higher densities. **Figure 5.9c** represents the density dependence of mobility for the hybrid device. The average hole mobility of the hybrid device is found to be ~ 216 cm^2/VS. The electron transfer from MoSSe to graphene forms a built-in electric field at the interface

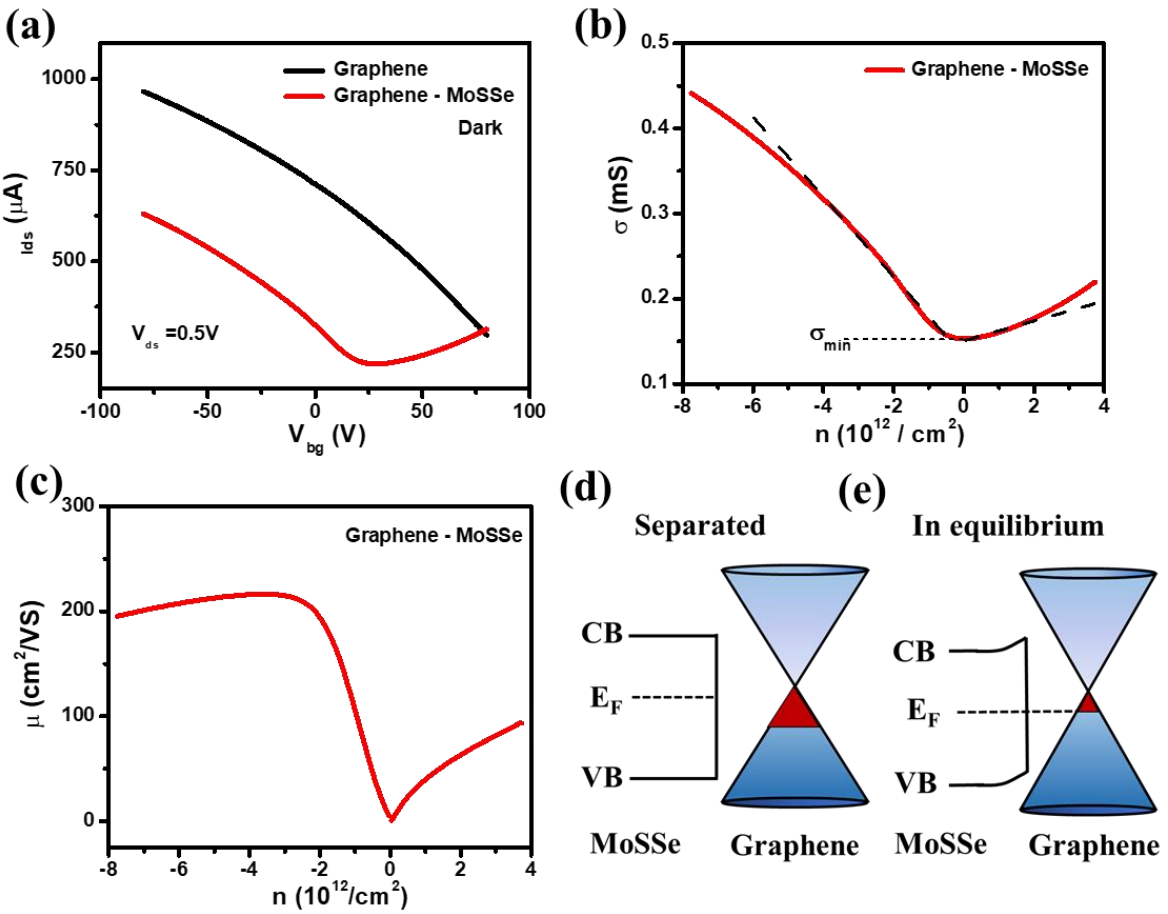

Figure 5.9: *Electrical characterizations of graphene-MoSSe heterostructure. (a) Transfer (I_{ds}-V_{bg}) characteristics of the graphene transistor with and without MoSSe nanosheets. (b) Density (n) dependent conductivity of the hybrid device. (c) Density (n) dependent average mobility (μ) of the hybrid device. (d) and (e) the schematic energy diagrams before and after the graphene being in contact with MoSSe alloy respectively.*

which leads to band bending to equilibrate the Fermi level[195] (Schematics in **Figure 5.9d** and **5.9e**).

5.3.3 Optoelectronic properties of graphene-MoSSe hybrid transistor

In order to understand the optoelectronic properties of graphene-MoSSe hybrid device I-V characteristics is recorded in room temperature. **Figure 5.10a** shows the variation of photocurrent (I_{ph}) with V_{ds} at zero gate bias (V_{bg} = 0 V) for λ = 633 nm. We see that I_{ph} grows linearly with V_{ds} and increases monotonically with the increase in optical intensity (P_{LED}). With increasing optical intensity, more numbers of charge carriers are generated in the 2D TMDC

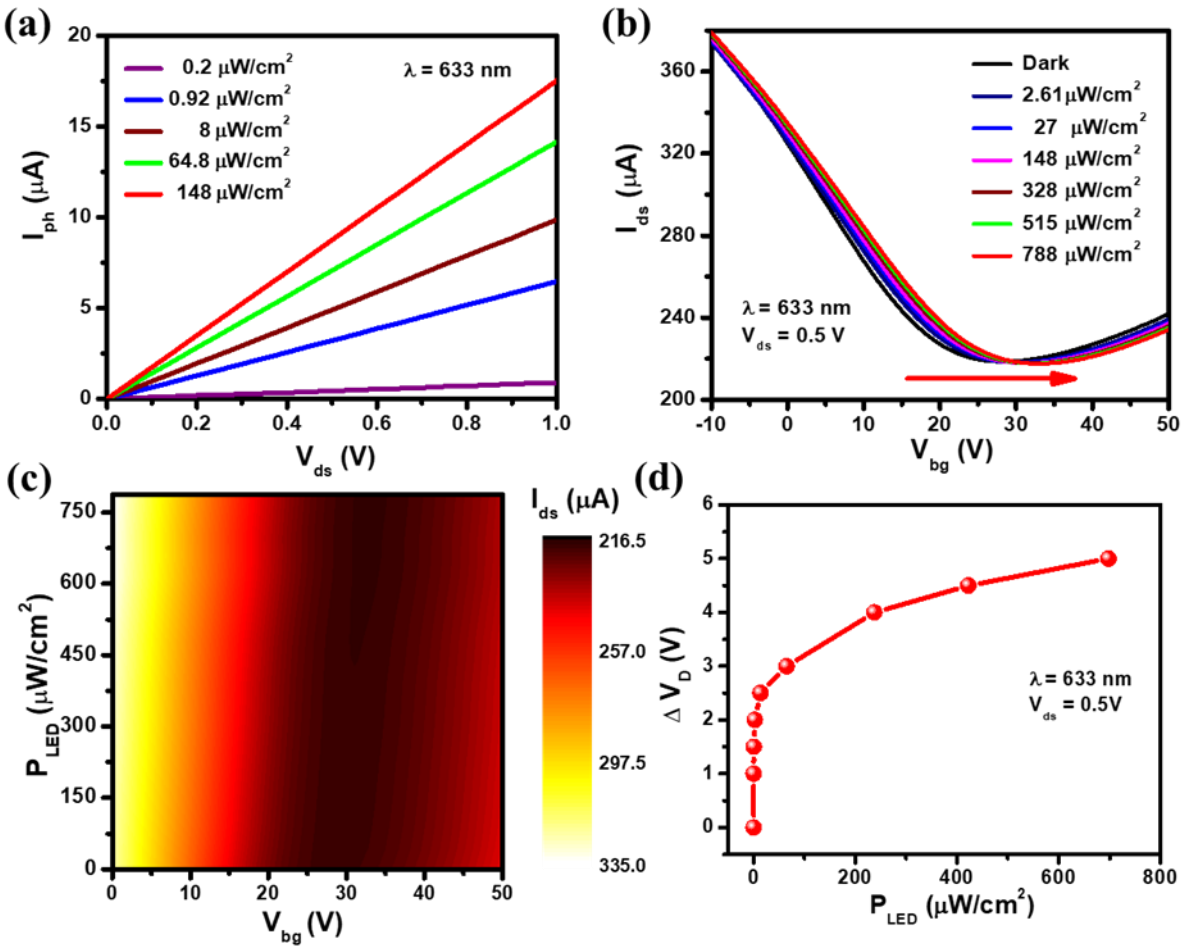

Figure 5.10: *Optoelectronic characterizations of graphene-MoSSe hybrid phototransistor. (a) Bias (V_{ds}) dependent photocurrent (I_{ph}) with different optical powers at V_{bg} = 0V, λ = 633 nm. (b) Transfer characteristics (I_{ds} -V_{bg}) for graphene-MoSSe alloy hybrid phototransistor under different illumination powers at V_{ds} = 0.5 V, λ = 633 nm. (c) Two dimensional (2D) colour plot of drain current (I_{ds}) as a function of optical power (P_{LED}) and gate voltages (V_{bg}) at V_{ds} = 0.5 V, λ = 633 nm. (d) Dependence of Dirac point (Δ V_D) with illumination power (P_{LED}) at V_{ds} = 0.5 V, λ = 633 nm.*

alloy inducing a stronger photogating effect and higher photocurrents[167,196]. **Figure 5.10b** shows the drain-source current (I_{ds}) as a function of back gate voltage (V_{bg}) under different optical excitation powers at a fixed drain source voltage (V_{ds} = 0.5 V) with λ = 633 nm. As the optical intensity increases, the Dirac point (V_D) (where the drain-source current (I_{ds}) becomes minimum) shifts toward a higher V_{bg}, implying the light induced hole doping in the graphene channel. Under illumination, electron-hole pairs are generated at MoSSe alloy and are dissociated at the graphene-MoSSe interface due to the built-in electric field. The photogenerated holes are then transferred to the graphene channel and the electrons remain trapped in MoSSe, inducing the photogating effect through capacitive coupling[138]. The photoinduced shift of the Dirac point (V_D) can be visualized in **Figure 5.10c** which represents the 2D colour plot of I_{ds} as a function of V_{bg} and the illumination intensity (P_{LED}) of λ = 633 nm. The shift of V_D with illumination intensity for λ = 633 nm and V_{ds} = 0.5 V is shown in **Figure 5.10d**.

5.3.3.1 Gate tunable photoresponse

In the hybrid device configuration, graphene offers ambipolar characteristics with excellent gate tunability. On the other hand, MoSSe nanosheets offer superior absorption in broad UV to NIR (350-850 nm) region. Combining them, the hybrid device shows strong gate tunable of the photocurrent (I_{ph}). The variation of the photocurrent (I_{ph}) with applied gate voltages (V_{bg}) and illuminating power (P_{LED}) with V_{ds} = 0.5 V, λ = 633 nm is represented in **Figure 5.11a**. The dependence of photoresponssivity (R) of graphene-MoSSe hybrid phototransistor on V_{bg}-V_D is represented in **Figure 5.11b**. Inset shows, the highest value of R increases from 3.12×10^4 A/W to 6.06×10^4 A/W when V_{bg} changes from 6 V to 13 V and again decreases to 2.05×10^4 A/W at V_{bg} = 23 V. Under illumination, electron-hole pairs are generated in MoSSe alloy and separated at the interface (due to the built-in field across graphene-MoSSe interface). For $V_{bg} < V_D$, holes are the dominated charge carriers in graphene (**Figure 5.11c**). By reducing the gate voltages (V_{bg}), the Fermi level of graphene is lowered and it enhances the built-in electric field. It helps more photo-generated holes to be transferred to the graphene channel by trapping the electrons in the TMDC layer (due to the upward band bending), resulting in an increased photoresponsivity (R) (The photoresponsivity (R) attains maximum value ~ 3500 A/W at $V_{bg} - V_D$ = -15 V, λ = 633 nm and P_{LED} ~ 13.5 μW/cm^2). With further decrease of V_{bg}, the interfacial barrier potential becomes thinner and the trapped photogenerated electrons (inside the TMDC layer) start tunnelling through it, resulting in a decreased photoresponsivity. Similarly, for $V_{bg} > V_D$, electrons are responsible for the conductivity in graphene and the increase of V_{bg}

increases the injection of photo-generated electrons to graphene from MoSSe due to the downward band bending in MoSSe (**Figure 5.11d**) resulting in a negative photoresponsivity (R). The photoresponsivity becomes negligibly small near the Dirac point (V_D ~ 28 V in this graphene- MoSSe device).

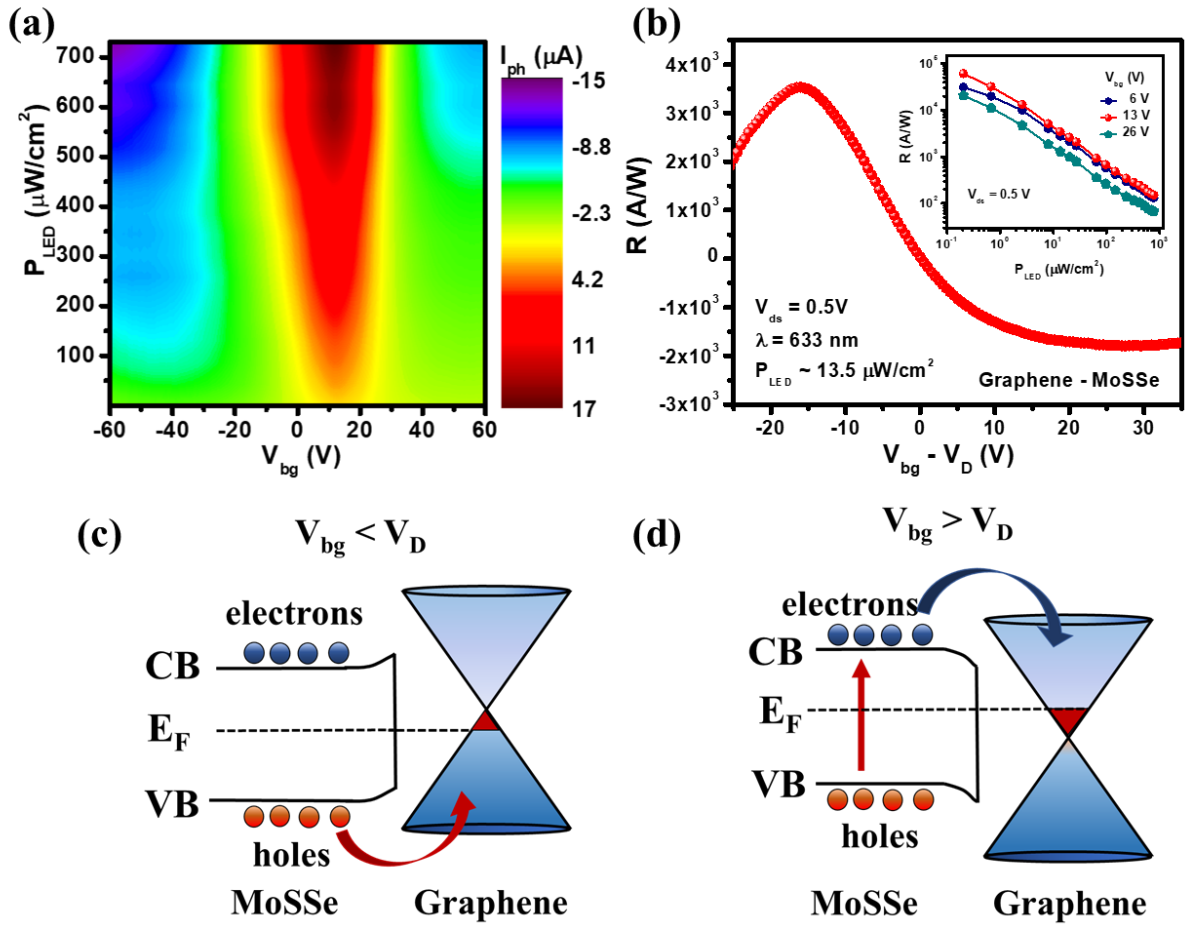

Figure 5.11: *Gate tunable photoresponse of graphene-MoSSe hybrid phototransistor. (a) Two dimensional (2D) colour plot of photocurrent (I_{ph}) as a function of applied gate voltages (V_{bg}) and optical power (P_{LED}) at V_{ds} = 0.5 V, λ = 633 nm. (b) Dependence of responsivity with illuminated power (P_{LED}) with different gate voltages at λ = 633 nm, V_{ds} = 0.5 V. The band bending at the interface of graphene-MoSSe at (c) $V_{bg} < V_D$ and (d) $V_{bg} > V_D$ illustrating the photodetection mechanism.*

5.3.3.2 Broadband photoresponse

The photoresponsivity (R)[120], $R = \frac{I_{ph}}{P_{LED}}$, of the hybrid phototransistor as a function of optical intensities (P_{LED}) are shown in **Figure 5.12a**, where all the responsivity measurements are performed under identical experimental conditions at V_{ds} = 0.5 V, V_D -V_{bg} = 15 V with the

varying wavelength of 365-810 nm. The expected inverse relationship between R and P_{LED} is also observed here and can be explained by the saturation of the photocurrent due to the lowering of the built-in field at the interface with an increase in the number of charge carriers[106]. The device offers a maximum responsivity of 6.06 $\times 10^4$ A/W for 633 nm for the minimum achievable illumination of ~ 0.2 μW/cm^2. In addition, a significantly higher photoresponsivity (R > 10^4 A/W) is obtained in the wide range of UV-NIR (365-810 nm) wavelengths. This result is comparable or superior to most of the previously reported graphene-based photodetectors[197–200]. In addition to photoresponsivity, the noise equivalent power (NEP) and the specific detectivity (D^*) are two most important figure of merits for comparing the performance of the photodetectors. NEP, i.e., the minimum optical power requires to detect the photocurrent from the noise current in a PD can be defined as[120],

$$NEP = \frac{\sqrt{S_I}}{R} \quad \ldots\ldots\ldots\ldots\ldots\ldots\ldots\ldots\ldots\ldots\ldots\ldots\ldots\ldots\ldots\ldots\ldots\ldots \quad (5.4)$$

Where, S_I is the total noise spectral density consisting of 1/f noise, thermal noise and the shot noise[201].

Considering the 1/f noise spectral density (Inset, **Figure 5.12b**), which may originate due to the trapping and detrapping of charge carriers[161], dominating the total noise power of the device, the NEP is calculated to be as low as ~10^{-14} W/Hz$^{0.5}$ in our experimental wavelength

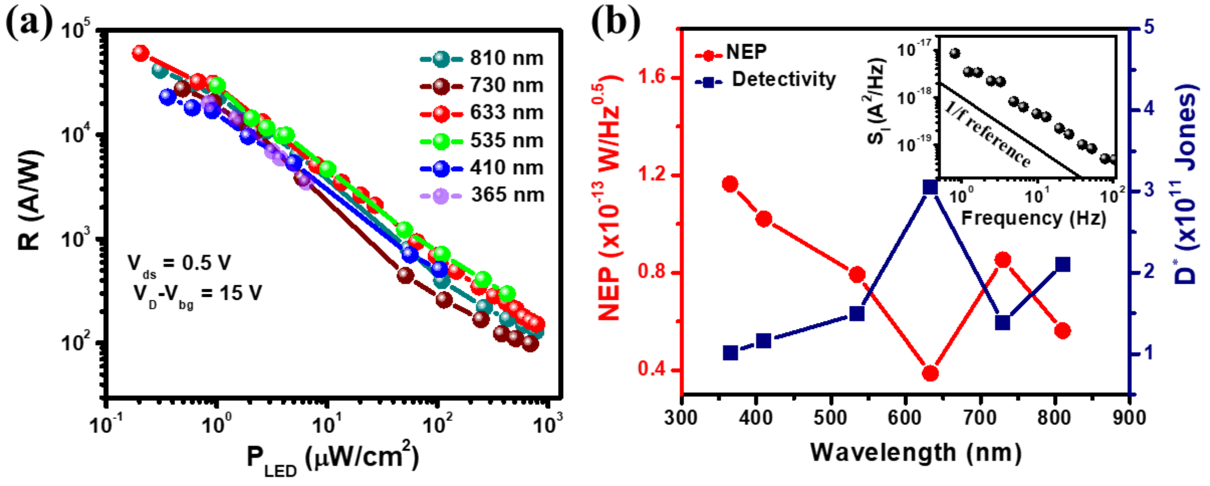

Figure 5.12: *UV-NIR Broadband photoresponse of graphene-MoSSe heterostructure. (a) Dependence of responsivity (R) with illumination power (P_{LED}) of different wavelengths for graphene-MoSSe hybrid device at V_{ds} = 0.5 V, V_D-V_{bg} = 15 V. (b) Wavelength dependent specific detectivity (D^*) and Noise equivalent power (NEP) with V_{ds} = 0.5 V, V_D -V_{bg} = 15 V. The current noise spectral density (S_I) of the device in dark at V_{ds} = 0.5 V (Inset).*

range. This significantly lower NEP value indicates the ability of the device to detect weak light. Mathematically, the specific detectivity (D^*) of a photodetector is defined as[120]

$$D^* = \frac{\sqrt{A}}{NEP} \quad \ldots\ldots\ldots\ldots\ldots\ldots\ldots\ldots\ldots\ldots\ldots\ldots\ldots\ldots\ldots\ldots\ldots\ldots \quad (5.5)$$

Where, A is the effective device area of the hybrid device. Using this equation D^* is calculated as high as ~ 3.06×10^{11} Jones for 633 nm wavelength. The calculated NEP and D^* as a function of wavelength are shown in **Figure 5.12b.**

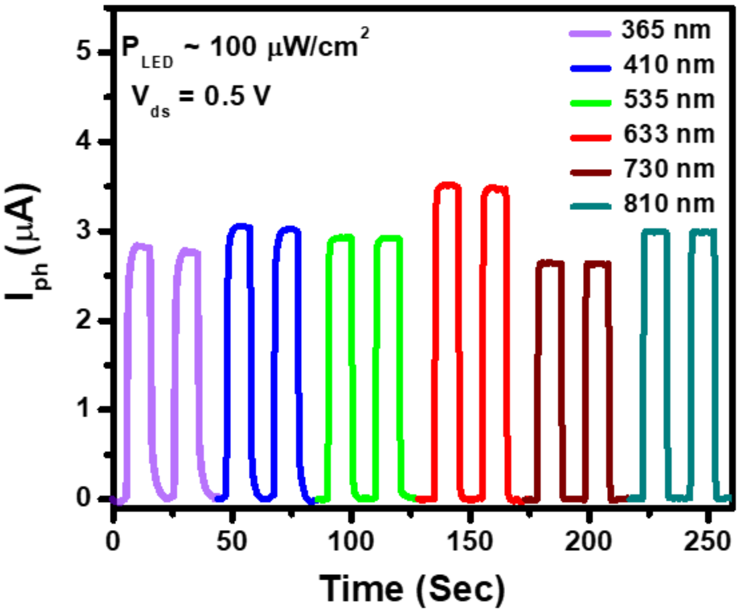

Figure 5.13: *Temporal photoresponse characteristics of graphene-MoSSe heterostructure with UV-NIR (365-810) broadband illumination at* $V_{ds} = 0.5$ *V,* $V_{bg} = 0$ *V,* P_{LED} *~ 100* μ*W/cm*^{2}*.*

Figure 5.13 represents the temporal photocurrent characteristics over the wide UV-NIR wavelength range (365-810 nm) with the same experimental condition as V_{ds} = 0.5 V and V_{bg} = 0 V for a constant illumination power of ~ 100 µW/cm^2. This hybrid graphene-MoSSe phototransistor device exhibits excellent ON/OFF modulation characteristics over a wide range of experimental wavelengths (365-810 nm) even at very low optical power and bias voltage.

5.3.3.3 Photoresponse comparison of alloy engineered hybrid phototransistors

To understand the impact of alloy engineering, it is necessary to compare the performances of three devices, i.e., graphene-MoS_2, graphene-MoSSe and graphene-$MoSe_2$ in identical device configurations. **Figure 5.14a** compares the temporal photoresponse characteristics of these P_{LED} ~ 100 µW/cm^2. All the three phototransistors show robust and reproducible photocurrent three devices under the same experimental conditions of V_{ds} = 0.5 V, V_{bg} = 0 V, λ = 633 nm,

in multiple ON/OFF cycles. The photocurrent (I_{ph}) is found to be much higher in graphene-MoSSe device compared to graphene-MoS_2 and graphene $MoSe_2$ based devices, indicating the superiority of MoSSe ternary alloy over its binary counterparts. The photocurrent dynamics of the devices are also evaluated by considering the time interval for the current changes from 10% to 90% (and vice versa) when light is turned on or off. From **Figure 5.14b**, it is seen that the rise time (τ_{rise}) and the fall time (τ_{fall}) for the graphene-MoSSe phototransistor are 430 ms and 480 ms respectively, whereas τ_{rise} becomes 480 ms and 1.32 sec and τ_{fall} becomes 570 ms and 2.98 sec for graphene-MoS_2 and graphene-$MoSe_2$ devices, respectively. The responsivity of these three phototransistors with respect to the illumination intensity are plotted in **Figure 5.14c** for the same experimental conditions of V_{ds} = 0.5 V, V_D-V_{bg} = 15 V, λ = 633 nm. The responsivity for the graphene-MoSSe phototransistor is much higher compared to other two devices, showing 6.06 ×10^4 A/W for graphene-MoSSe, 2.97×10^4 A/W for graphene-MoS_2 and 1.26×10^4 A/W for graphene-$MoSe_2$ at 633 nm with minimum achievable power of ~0.2

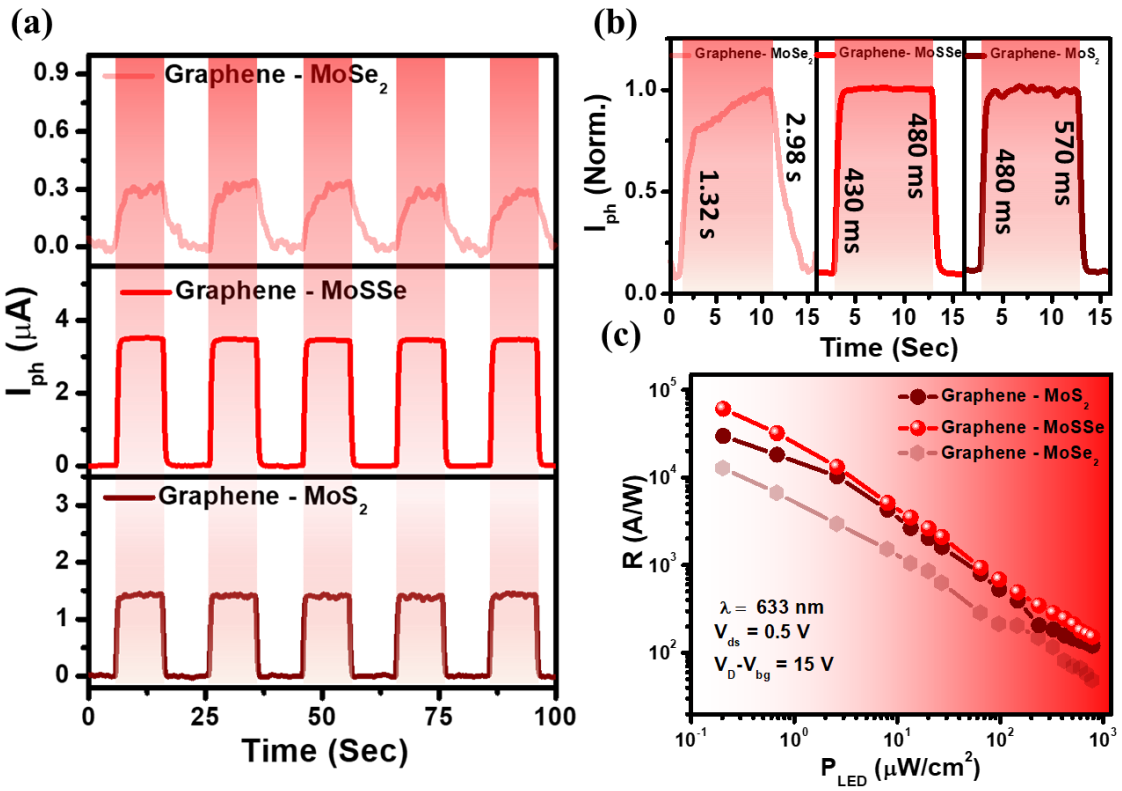

Figure 5.14: *Comparison of the photoresponse between graphene-$MoS_{2x}Se_{2(1-x)}$ hybrid devices. (a) Temporal photoresponse of graphene-$MoS_{2x}Se_{2(1-x)}$ hybrid phototransistors with x = 0, 0.5 and 1 for the same experimental conditions, V_{ds}=0.5 V, V_{bg}=0 V, λ = 633 nm, P_{LED} ~ 100 μW/cm^2. (b) Response time of the above hybrid phototransistors at V_{ds}=0.5 V, V_{bg} = 0 V, λ = 633 nm. (c) Photoresponsivity as a function of illumination power of the fabricated hybrid devices at V_{ds} = 0.5 V, V_D-V_{bg} = 15 V, λ = 633 nm.*

$\mu W/cm^2$. Higher photocurrents and the ultrahigh photoresponsivity of the MoSSe alloy-based device can be explained by the conversion of deep to shallow level defect densities by minimizing the deep level defect densities.

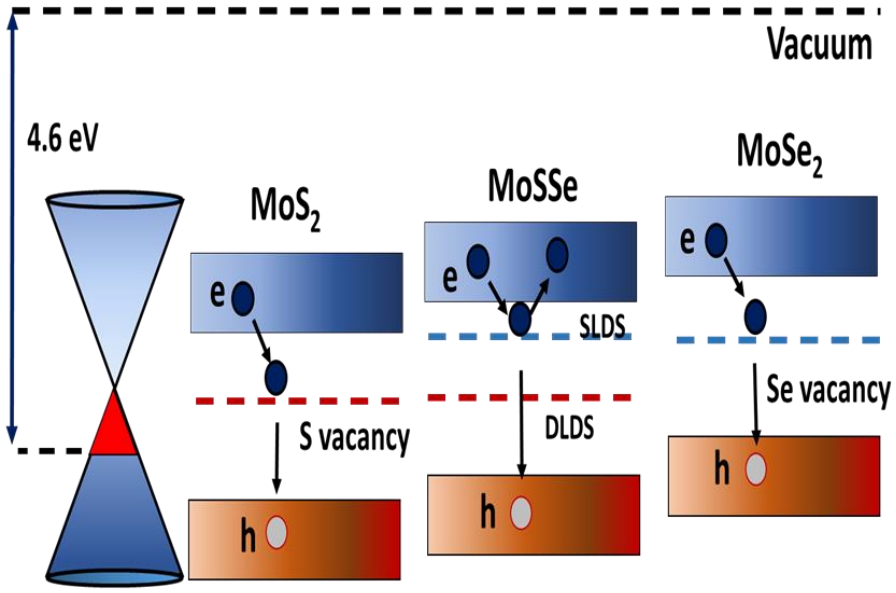

Figure 5.15: *Suggested energy band diagram for MoS_2, MoSSe, $MoSe_2$ and graphene along with the schematic localized defect states.*

Figure 5.15 illustrates the comparative energy band diagram of graphene and $MoS_{2x}Se_{2(1-x)}$ alloys with different compositions (x = 0, 0.5, 1) along with their deep level defects (DLDS) and shallow level defects (SLDS). In the binary layered TMDC materials (like MoS_2, $MoSe_2$ etc.), the unintended presence of chalcogen vacancies is available in plenty leading to the formation of localized DLDSs within the bandgap, which act as recombination trap centres for the photoexcited charge carriers and greatly affect the device performance[184]. However, the formation of ternary MoSSe alloy improves thermodynamic stability due to its low formation energy[183]. Also, the energy levels are re-localized and the intrinsic defect states are superimposed because of the coexistence of S and Se vacancies[202]. So, the harmful deep level defects in MoS_2 and $MoSe_2$ become shallow level defects in MoSSe ternary alloy[203]. **Table 5.1** gives the comparison of photoresponsivity (R), NEP, specific detectivity (D^*) and the characteristics times of the fabricated graphene-MoS_2, graphene-MoSSe and graphene-$MoSe_2$ phototransistor.

Table 5.1: *Comparison of the photodetector performance parameters for all three devices i.e., graphene –$MoSe_2$, graphene – MoSSe, graphene – MoS_2.*

Device Name	Responsivity(R) (A/W)	NEP ($W/Hz^{0.5}$)	Detectivity (D^*) (Jones)	Rise Time (τ_{Rise}) (Sec)	Fall Time (τ_{Fall}) (Sec)
Graphene-$MoSe_2$	1.26×10^4	4.68×10^{-13}	2.52×10^{10}	1.32	2.98
Graphene-MoSSe	6.06×10^4	3.87×10^{-14}	3.06×10^{11}	0.43	0.48
Graphene-MoS_2	2.97×10^4	1.30×10^{-13}	9.08×10^{10}	0.48	0.57

5.3.3.4 Stability

Stability is very important parameter for designing a photodetector device since most of the materials like BP[204,205], perovskites[96,206] are very much unstable in nature. However, even without any capping layers, our ternary alloy device offers an extraordinary stability in photocurrent switching characteristics (**Figure 5.16**) without any degradation after 4 months of its fabrication.

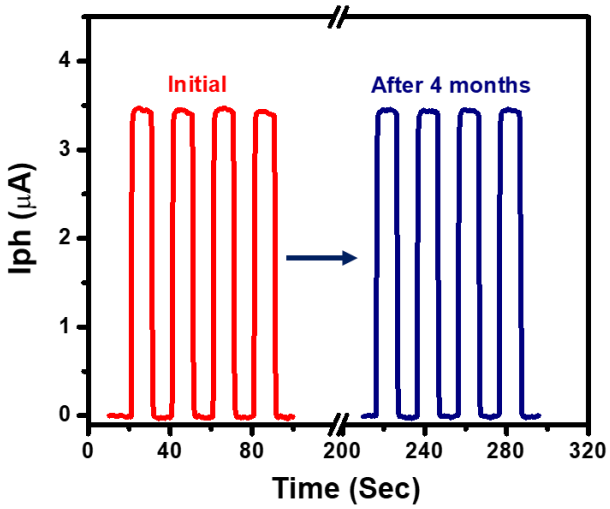

Figure 5.16: *Stability of the graphene-MoSSe hybrid phototransistor. The temporal photocurrent of the after 4 months of its fabrication with λ = 633 nm, V_{ds} = 0.5 V, V_{bg} = 0 V, P_{LED} ~ 100 $\mu W/cm^2$.*

5.4 Summary

To summarise, a cost-effective, environmentally friendly hydrothermal approach was used to demonstrate the composition-tunable synthesis of $MoS_{2x}Se_{2(1-x)}$ ternary alloy (x = 0 to 1) nanosheets. The phototransistor action of three different composites of $MoS_{2x}Se_{2(1-x)}$ (x = 0, 0.5, 1) has been studied systematically by fabricating a three terminal heterostructure device with graphene. The graphene-MoSSe hybrid phototransistor outperforms the other two devices

(MoS_2 and $MoSe_2$) in terms of photo-sensing properties, which are attributed to the suppression of deep level defects and better structural stability in MoSSe. Because of MoSSe's broad (UV-NIR) light absorption, graphene's ultrafast charge carrier transport, and the improved interfacial property at graphene-MoSSe heterostructure, this device is suitable for advanced optoelectronic devices. This graphene-MoSSe hybrid device has a very high photoresponsivity ($>10^4$ A/W), a low noise equivalent power (10^{-14} W/$Hz^{0.5}$), and a higher specific detectivity (10^{11} Jones) in the UV-NIR (365-810 nm) wavelength range with gate tunability. These findings have important implications for the facile and scalable fabrication of high-performance optoelectronic devices based on ternary 2D alloy materials, providing insight into the fundamental interaction between van-der-Waals materials.

Chapter 6

Exciton-Plasmon Coupling Mediated Superior Photoresponse in 2D Hybrid Phototransistors

The possibility of creating heterostructure of two-dimensional (2D) materials has emerged as a viable route towards realizing novel optoelectronic devices. However, the low light absorption due to their small absorption cross section, limits their realistic application. Light-matter interaction mediated by strong exciton-plasmon coupling has been demonstrated to improve absorbance and spontaneous emission in a coupled TMDC and metallic nanostructures. Here, we report a lithography-free fabrication of a large area broadband superior gate-tunable hybrid phototransistor based on monolayer graphene decorated by WS_2-Ag NPs in a three-terminal device configuration. The fabricated device exhibits extremely high photoresponsivity (up to 3.2×10^4 A/W) which is more than 5 times higher than the bare graphene/WS_2 hybrid device, along with a low noise equivalent power (NEP) (~10^{-13} W/$Hz^{0.5}$) and higher specific detectivity ~10^{10} Jones in the wide (325-730 nm) wavelength region. The additional PVP capping of Ag NPs helps to suppress the direct charge and heat transfer and most importantly, increases the device stability by preventing the degradation of WS_2-Ag hybrid system. Our work demonstrates a strategy towards obtaining an environment-friendly, scalable, high-performance broadband phototransistor by tuning the exciton-plasmon coupling for new generation opto-electronic devices.

6.1 Introduction

Two dimensional (2D) materials like graphene, transition metal dichalcognides (TMDCs) attract a lot of attention in the past 15 years because of their atomically thin profile, high transparency, higher carrier mobilities and appealing optoelectronic properties[1,38]. Most importantly, it is possible to create vertical heterostructures by using different 2D materials as they are coupled by the weak Van der Waals force in the out-of-plane direction[74,207] to introduce multiple functionalities. Graphene, a gapless semimetal having higher carrier mobilities, lacks its potential in the optoelectronic applications because of its infirm light absorption (~ 2 % of the incident light)[111,134]. In contrast, TMDCs (MoS_2, WS_2 etc.) manifest magnificent light-matter interaction characteristics primarily in the UV-Vis region and become the natural partner of graphene[89,103]. Due to the low dimensionality and the reduced dielectric

screening, the optoelectronic properties of such 2D materials are influenced by the excitons and trion[208]. Recently, several attempts have been made to improve the optical properties of such TMDCs using the surface plasmon (SP) effects of some novel metals[209,210]. The localized surface plasmon resonance (LSPR) of a metal nanostructure (nanoparticles, nanowires etc.)[211,212] can be excited by an incident electromagnetic radiation and it depends on the carrier density, size and shape of the nanostructures and also on the external surrounding[66,213]. The SP of the metal nanostructures can couple with the excitons of TMDCs and results in an enhanced absorbance, emission and improved photodetection capabilities. On the other hand, formation of van der Waals heterostructure of graphene with photo-active materials like TMDC[103,176], perovskite[214–216], semiconducting quantum dots[98,138] provides a promising scheme to design superior photodetector that combine the advantage of light absorption of the photo sensing materials and high charge mobility of graphene as the conducting channel. While there are some reports on TMDC based plasmonic phototransistors demonstrating enhanced performance based on exciton-plasmon coupling, fabrication of tunable hybrid optoelectronic devices with high quantum yield for broadband application is still missing.

In this chapter, a novel three terminal phototransistor device architecture is reported based on graphene/WS_2-Ag nanoparticles heterostructure. The polyvinylpyrrolidone (PVP) capped silver (Ag) nanoparticles (NPs) restricts the direct charge, energy and heat transfer and enhances the optical properties of tungsten disulphide (WS_2) by surface plasmon-exciton coupling effect[217]. Using monolayer graphene as a conducting channel and the Ag NPs decorated WS_2 nanosheets as the light absorbing material, the device offers superior photodetection capabilities in the broad UV-Vis (325-730 nm) region with an excellent gate tunability. The fabricated highly stable graphene/WS_2-Ag phototransistor exhibits a very high photoresponsivity (R) > 10^4 A/W, higher specific detectivity (D^*) > 10^{10} Jones and low noise equivalent power (NEP) ~ 10^{-13} W/$Hz^{0.5}$ in the overall spectrum region which is several orders of magnitude higher than the bare graphene/WS_2 control phototransistor. By tuning the exciton-plasmon coupling, the demonstrated stable, sensitive phototransistor devices have the potential for the next generation optoelectronic device applications.

6.2 Experimental Section

6.2.1 Materials

All chemicals (Tungsten disulphide, Lithium Bromide, Hexane, Isopropyl Alcohol, Polyvinylpyrrolidone, Silver Nitrate, Sodium Citrate) are brought from Sigma-Aldrich and used without any further purification.

6.2.2 Synthesis of WS_2 and WS_2-Ag (PVP) nanosheets

In this chapter, the unique properties of highly stable, solution-processed, plasmonic Ag-nanoparticles decorated and chemically exfoliated WS_2 dispersion is reported. In this regard layered WS_2 nanosheets are synthesized from bulk WS_2 by Li-intercalation assisted chemical exfoliation technique and Polyvinylpyrrolidone (PVP) coated silver nanoparticles are added in the dispersion of WS_2 to prepare WS_2-PVP encapsulated Ag nanoparticle nanocomposite. WS_2 nanosheets are synthesized chemically by using Li-intercalation technique. First, for exfoliation of WS_2 nanosheets, bulk WS_2 powder 2.5 gm with anhydrous LiBr at 1:1 molar ratio is dispersed in 25ml hexane solution. This solution is further sonicated for 6 hrs. by using bath sonicator. After sonication the resulting black dispersion is centrifuged at 5000 rpm for 15 mins to remove hexane and untreated Li ions. Then the wet sediments are washed by dispersing in IPA by shaking followed by centrifugation (5000 rpm, 15 mins). By repeating this procedure three times the wet sediment of WS_2 is completely transferred in IPA solvent. After 2 hrs. of bath sonication, the resulting dispersion is centrifuged at 5000 rpm for 10 mins and a greenish colour exfoliated WS_2 nanosheets are obtained. To prepare silver nanoparticle, PVP is dissolved in DI water and is kept for stirring at room temperature and then silver nitrate ($AgNO_3$) is added in this dispersion. After that Sodium Citrate (NaC) is used as reducing reagent, added dropwise in $AgNO_3$ dispersion and the colour of the solution is turned light orange which indicates the formation of silver nanoparticle. Thereafter different quantity silver nanoparticles are mixed with chemically exfoliated WS_2 nanosheets and kept stirring for 1 hr to get the homogeneous mixture of WS_2-PVP encapsulated Ag nanoparticle nanocomposite without any precipitation.

6.2.3 Materials characterizations

6.2.3.1 Microstructural characterizations

Figure 6.1a represents the typical TEM (transmission electron microscopy) image of chemically exfoliated WS_2 nanosheets (NS). The spherical Ag nanoparticles are encapsulated with a thin insulating polyvinylpyrrolidone (PVP) layer. The typical TEM images of Ag NPs and Ag NPs decorated WS_2 NS are represented in **Figure 6.1b** and **6.1c**. The average size of an Ag NP is ~ 10 nm in diameter (Inset, **Figure 6.1b**). The crystalline states of Ag provide a

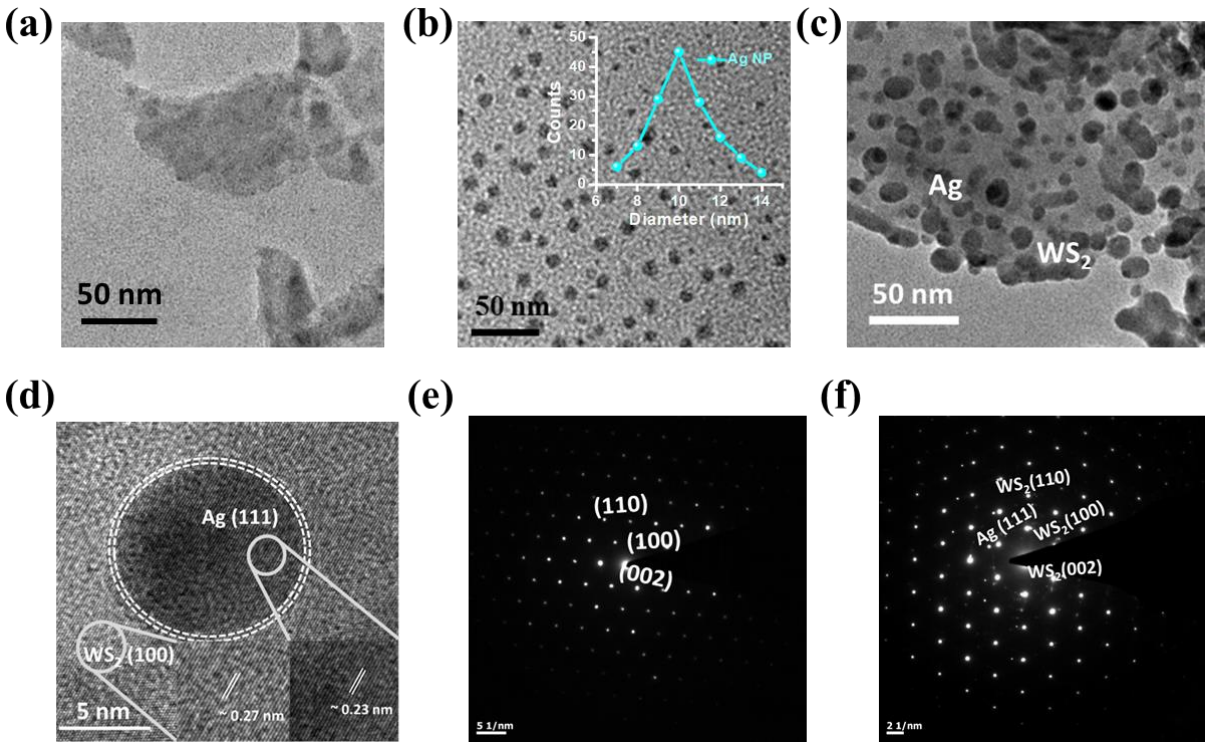

Figure 6.1: *Structural characterization of bare WS_2 and WS_2-Ag hybrid structure. Transmission electron microscopy (TEM) image of (a) bare WS_2, (b) Ag NPs (Inset height distribution of Ag NPs) and (c) Ag NPs decorated WS_2 layers. (d) HRTEM image of the hybrid indicating different lattice planes (inset) such as (100) planes of WS_2 and (111) planes of Ag NPs. SAED pattern of (e) bare WS_2 and (f) the hybrid.*

lattice spacing ~0.23nm, corresponds to (111) plane[218] of Ag, and the same for WS_2 is ~0.27 nm, indicating (100) plane[146] of WS_2, as evident from the high-resolution TEM (HRTEM) image (**Figure 6.1d**). The SAED pattern of bare WS_2 and Ag NPs decorated WS_2 nanosheets are recorded and shown in **Figure 6.1e** and **6.1f** respectively. They exhibit distinct diffraction spots which can be assigned to (100), (110) planes of WS_2 and (111) planes[219] of Ag (Which is missing in bare WS_2 (**Figure 6.1e**)). This PVP based encapsulation of the Ag nanoparticles

has multiple advantages. Firstly, it helps to supress the direct charge, energy transfer and the band gap pinning[220] and hence, the Ag nanoparticles can interact with WS_2 through localized surface plasmon resonance (LSPR) effect. Secondly, it improves the stability of Ag nanoparticles by stopping the chemical reaction between Ag and WS_2, which was reported to form Ag_2S even in the room temperature[221].

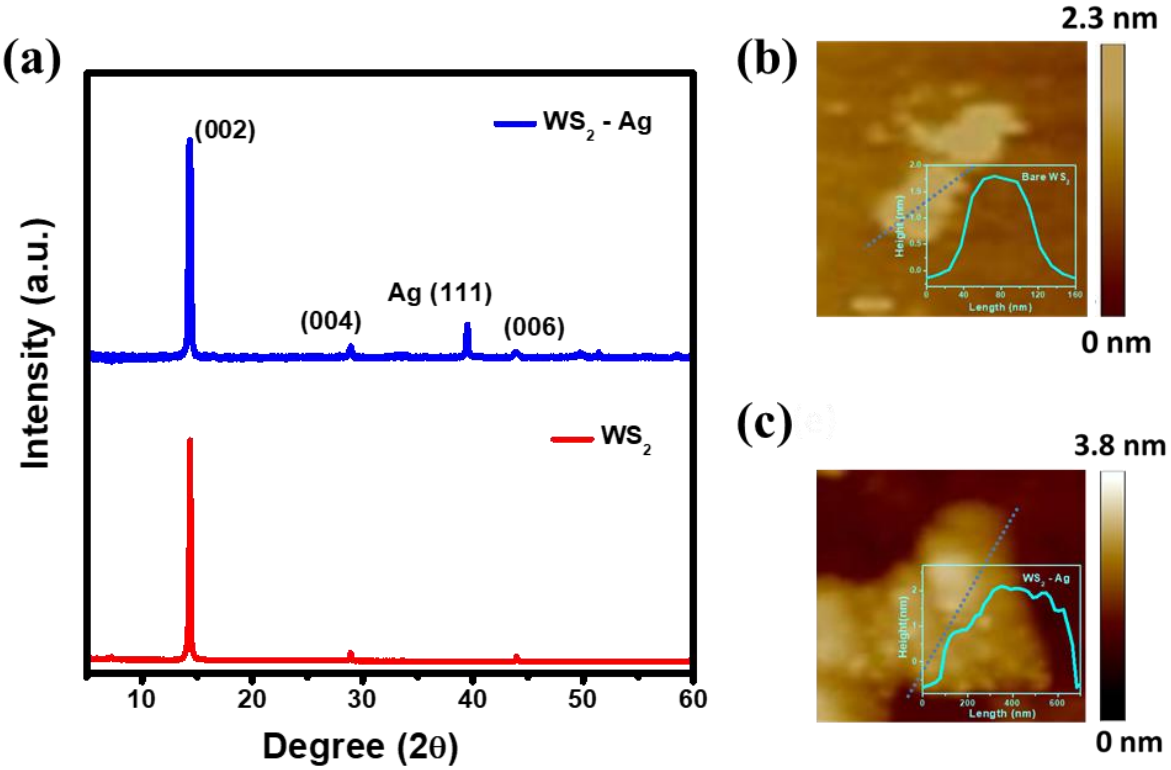

Figure 6.2: *Structural characterization of bare WS_2 and WS_2-Ag hybrid structure. (a) XRD patterns of WS_2 and the WS_2-Ag hybrid indicating the different planes. (b) and (c) AFM images and the corresponding height profile of bare WS_2 and WS_2-Ag respectively.*

The crystallinity of bare WS_2 and WS_2-Ag NS have also been examined by X-ray diffraction (XRD). The formation of (002), (004) and (006) planes is the signature of crystalline WS_2 layers[146] and the appearance of (111) plane signifies the presence of Ag in the WS_2-Ag hybrid system (**Figure 6.2a**). The Atomic Force Microscopy (AFM) images of bare WS_2 and WS_2-Ag hybrid suggest the thickness of typical nanosheets are ~ 2/3 nm suggesting the synthesized WS_2 is 3-4 layers thick. The AFM images of both the system are represented in **Figure 6.2b** and **6.2c.**

6.2.3.2 Spectroscopic characterizations

UV-Vis absorption spectra of bare WS_2, Ag NPs and WS_2-Ag hybrid are depicted in **Figure 6.3a**. The characteristics exciton 'A' and 'B' peaks of WS_2 remain intact in WS_2-Ag hybrid system[222]. The overall absorbance of WS_2 is enhanced due to the LSPR induced local electromagnetic interaction between the Ag NPs and semiconducting WS_2[223,224]. Excitonic A peak of WS_2 can be more clearly visualized in the second derivative of the absorption spectra (**Figure 6.3b**). A significant blue shift is observed in the hybrid WS_2-Ag suggesting the impact of strong exciton-plasmon coupling. The role of surface plasmon resonance of the Ag NPs can be well understood from the concentration dependent absorption spectra in WS_2-Ag hybrid structure. Interestingly it is observed that, with increasing Ag NPs density, the exciton to plasmon peak ratio decreases whereas the exciton 'A' peak intensity increases (**Figure 6.3c**), suggesting the possibilities to tune the coupling strength (exciton-plasmon) by controlling the concentration ratio of the materials.

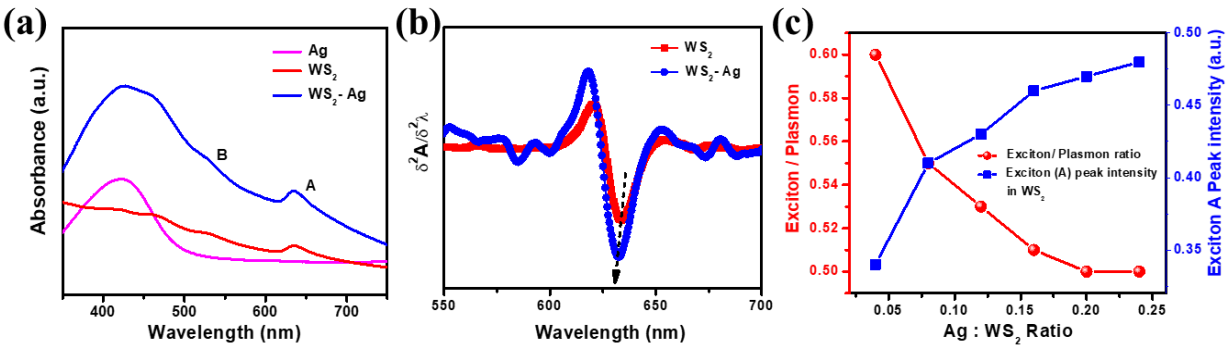

Figure 6.3: *Absorbance spectroscopy of hybrid WS_2-Ag structure. (a) Absorbance spectra of bare WS_2, Ag nanoparticles (NPs) and the plasmonic hybrid. Two distinct exciton peaks (exciton 'A' and 'B') are present in WS_2 and WS_2-Ag hybrid system. (b) Second derivative on the 'A' exciton region in the absorbance spectra of WS_2 and WS_2-Ag. (c) Dependence of exciton / plasmon ration and the exciton A peak intensity on WS_2: Ag ratio.*

The Raman spectra of few layered WS_2 sheets and WS_2-Ag hybrid are represented in **Figure 6.4a**. The in-plane (E^1_{2g}) and out-of-plane (A_{1g}) Raman modes are observed at 352 cm^{-1} and 419 cm^{-1} respectively for bare WS_2 suggesting the WS_2 are few layered thick[225]. The intensities of both the peaks are found to be enhanced significantly because of the LSPR enhancement by Ag NPs decorated on WS_2[226]. Additionally, the in-plane E^1_{2g} mode of WS_2 is red shifted due to the presence of Ag NPs as shown in **Figure 6.4b**. The red shift of E^1_{2g} mode can be ascribed to the strain relaxation due to lattice mismatch between Ag and WS_2[227,228]. The out-of-plane

A_{1g} mode behaves oppositely in the hybrid WS_2-Ag system. The strongly localized electromagnetic field of the plasmonic Ag NPs can stiffen the vertical oscillations of S atoms in WS_2, resulting in a blue shift of A_{1g} mode[229]. With increasing the Ag NPs concentration, the peak position of A_{1g} mode is blue- shifted monotonically, while the red-shifting of E^1_{2g} mode saturates after a certain Ag:WS_2 ratio (**Figure 6.4c**). The higher Ag concentration helps to increase the exciton-plasmon coupling (due to the strong surface plasmon of Ag) which results a continuous blue shift of A_{1g} peak. The saturation of E^1_{2g} mode shift is associated with the saturation of the strain effect on WS_2 layers due to the presence of Ag NPs on top.

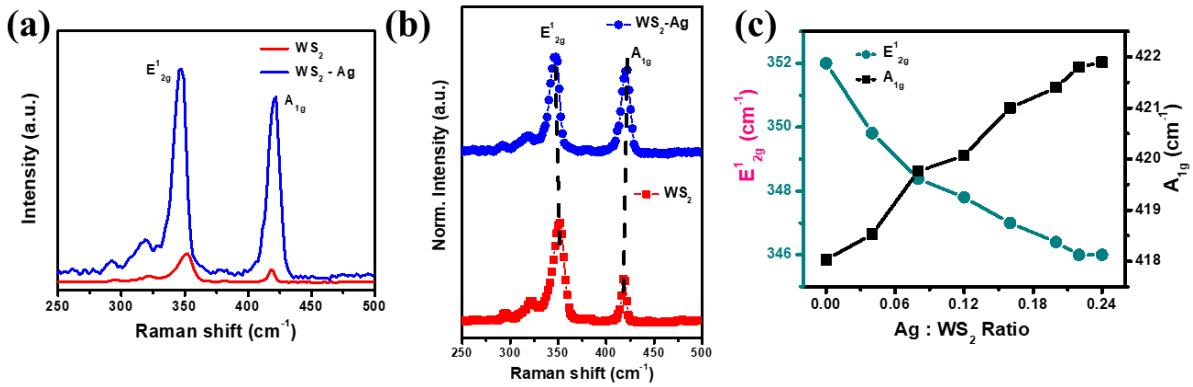

Figure 6.4: *Raman spectroscopy of hybrid WS_2-Ag structure with 532 nm laser excitation. (a) Raman spectra of WS_2 and WS_2-Ag hybrid system. (b) Normalized Raman spectra of bare WS_2 and the hybrid showing the characteristic in plane E^1_{2g} and out of plane A_{1g} peak. (c) Dependence of in-plane E^1_{2g} and out-of-plane A_{1g} Raman mode with Ag: WS_2 ratio.*

The effect of SPR on the optical properties of WS_2 is further studied through micro-Photoluminescence (PL) spectroscopy (excitation 532 nm). The PL emission spectra is dramatically enhanced in the hybrid WS_2-Ag system as shown in **Figure 6.5a**. The observed PL enhancement from the WS_2-Ag hybrid is associated with the combined contribution of the enhanced light absorption by WS_2 in the hybrid structure, the exciton-plasmon-photon conversion and plasmon enhanced exciton generation-recombination process.[230,231] Having a weak asymmetric profile, the PL spectra of WS_2 can be deconvoluted into three possible components such as neutral exciton (A^0), trion (A^T) and biexciton (A^A) (**Figure 6.5b**).[232,233] The insulating PVP layer prevents the PL quenching, band-pinning and doping by avoiding the direct metal-semiconductor contact[234,235]. The excitons in WS_2 can couple with the surface plasmon (SP) of Ag NPs due to their spatial wave-functional overlap and resulting an enhanced emission[236]. Compared to the other excitons (A^T and A^A), only the intensity of neutral exciton (A^0) dominates in the hybrid WS_2-Ag structure as shown in **Figure 6.5c**. In order to get deeper

insight of the exciton-plasmon coupling mechanism, the excitation power dependent PL emission spectra are represented in **Figure 6.5d** and **6.5e** for control WS_2 and WS_2-Ag hybrid respectively. It is observed that, the PL peak position of WS_2-Ag hybrid shifts towards shorter wavelength with increasing excitation power while the bare WS_2 shows an opposite trend. With increasing excitation power, the emission spectra of WS_2 exhibits a continuous red shift (**Figure 6.5d**), as all three excitons (A^0, A^T and A^A) contributed in the emission spectra.[233] On the other hand, the contribution of major PL emission of WS_2-Ag hybrid is dominated by neutral exciton (A^0) only.

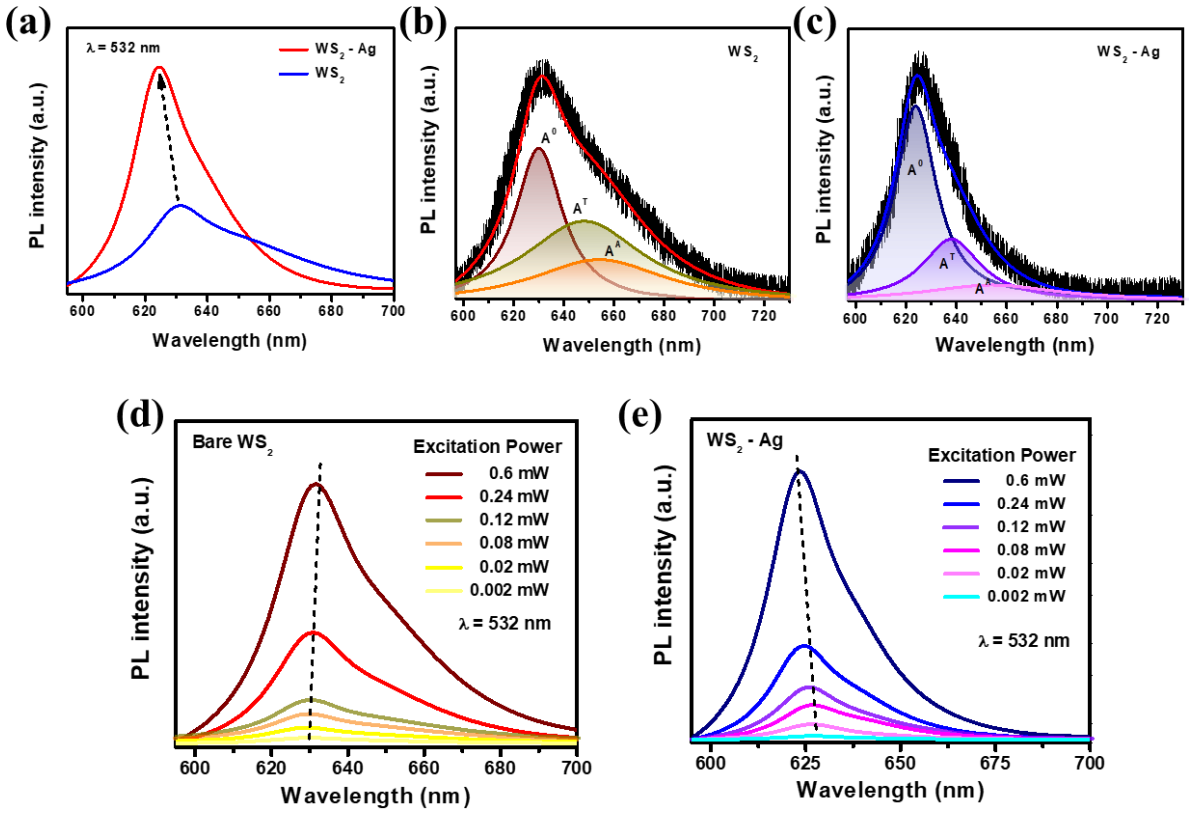

Figure 6.5: *Photoluminescence (PL) spectroscopy of hybrid WS_2-Ag structure with 532 nm laser excitation. (a) PL spectra of bare WS_2 and the WS_2-Ag hybrid structure. (b) and (c) deconvoluted and fitted PL spectra of WS_2 and the plasmonic hybrid respectively. The PL spectra for both the systems can be deconvoluted by three distinct species, called neutral exciton (A^0), trion (A^T) and biexciton (A^A). (d) and (e) power dependent PL spectra of control WS_2 layer and the WS_2-Ag hybrid structure respectively.*

The PL peaks shift with excitation power for both bare WS_2 and WS_2-Ag is depicted in **Figure 6.6a**. Also, both bare WS_2 and WS_2-Ag hybrid exhibit a monotonic increase in PL intensity as a function of illumination power (for 532 nm) which is represented in **Figure 6.6b**. The

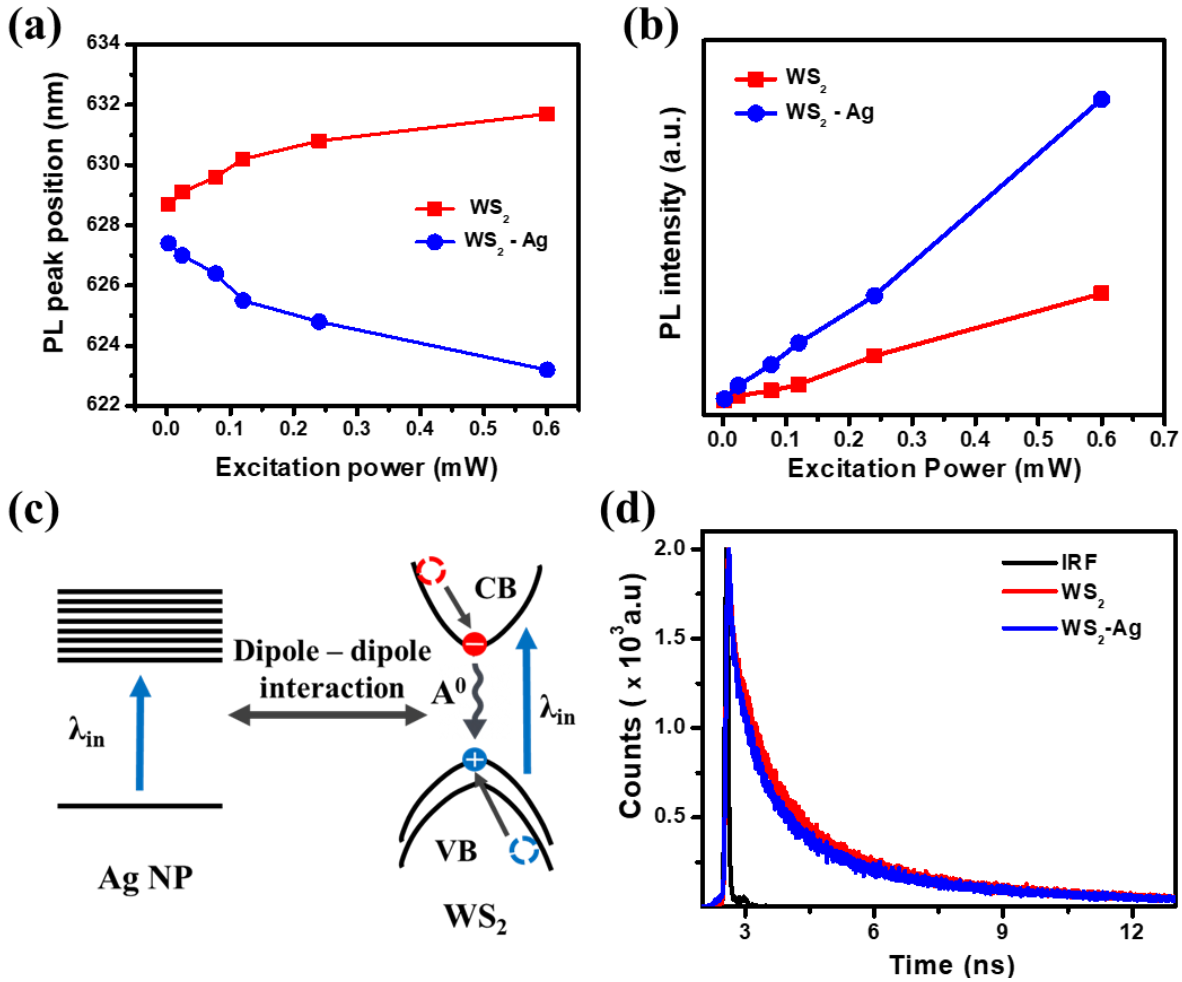

Figure 6.6: *Photoluminescence (PL) spectroscopy of hybrid WS_2-Ag structure with 532 nm laser excitation. (a) The PL peak position as a function of excitation power (λ = 532 nm) for both WS_2 and WS_2-Ag hybrid. (b) Excitation power dependent PL intensity for bare WS_2 and the hybrid system. (c) Schematic diagram of the dipole mediated exciton-plasmon coupling in the hybrid structure. (d) The time resolved PL (TRPL) decay of the pristine WS_2 and the hybrid structure.*

realization of exciton-plasmon coupling requires simultaneous spectral and spatial overlap between excitons and plasmons[61]. Thus, the confined excitons are spectrally coupled with the plasmon, with consequent strong transition dipole moments interactions. This dipolar coupling rate is dependent on the oscillator strength of excitons and the local field enhancement of SP[237,238]. The reduced band filling effect due to the dipolar interaction between the excitons of WS_2 with SP of Ag NPs results in a continuous blue shift with increasing excitation power in WS_2-Ag hybrid[211]. The dipole-dipole interaction between the exciton states and the SP is depicted schematically in **Figure 6.6c**. To estimate the lifetime of the photogenerated charge carriers, time resolved photoluminescence (TRPL) measurements are carried out for bare WS_2

and WS_2-Ag hybrid under identical conditions (excitation: 409 nm and emission at 500 nm) (**Figure 6.6d**). It is observed that the life time of bare WS_2 (1.67 ns) slightly decreases when coupled with Ag NPs. The quenched lifetime in WS_2-Ag hybrid (1.53 ns) indicates the enhancement of spontaneous emission rate of the hybrid system due to the enhanced exciton plasmon coupling. From the steady state PL, it is observed that the neutral exciton dominates in WS_2-Ag system and the spontaneous emission rate of neutral exciton is amplified by the dipole-dipole interactions (Purcell effect)[213].

6.3 Results and discussions

6.3.1 Fabrication of hybrid devices

CVD-grown monolayer graphene on p^+ doped Si/SiO_2 (300 nm) substrates (Graphenea, USA) is used to fabricate the phototransistor devices. The electrodes are deposited through a shadow mask by electron beam evaporation to make a channel of W/L = 200 µm/70 µm. P^+ doped Si acts as the back gate of the fabricated devices. After that, chemically exfoliated WS_2 and plasmonic WS_2-Ag (PVP) are simply spin coated on top of the graphene channel to make the complete hybrid devices. Finally, all the phototransistor devices are annealed at 80º C for 1 hr to improve the hybrid interfaces. The device consisting of graphene and WS_2-Ag is schematically represented in **Figure 6.7**.

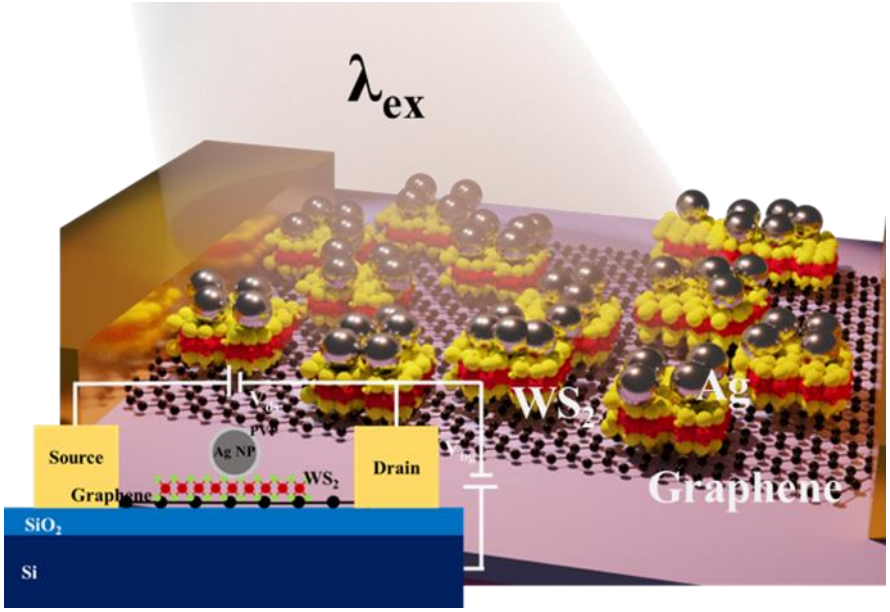

Figure 6.7: *Schematic of the hybrid graphene/WS_2-Ag phototransistor.*

6.3.2 Comparison of photoresponse characteristics in graphene/WS_2-Ag and graphene/WS_2 heterostructures

The photoresponse characteristics (I_{ph}-V_{ds}) of the graphene/WS_2-Ag and graphene/WS_2 devices with different illumination wavelengths (at a constant illumination intensity ~ 10 $\mu W/cm^2$, V_{bg} = 0 V) are shown in the **Figure 6.8a** and **6.8b** respectively. Here, it is found that, the photocurrent (I_{ph}) increases linearly with the increase of source-drain (V_{ds}) voltage varying from 0 to1 V for both the devices[176]. **Figure 6.8c** shows the spectral photoresponsivity (R) of the hybrid devices with a constant V_{ds} = 1 V, back-gate voltage (V_{bg}) of 0 V and illumination power density (P_{LED}) ~ 1 $\mu W/cm^2$ where, R can be calculated as[120]

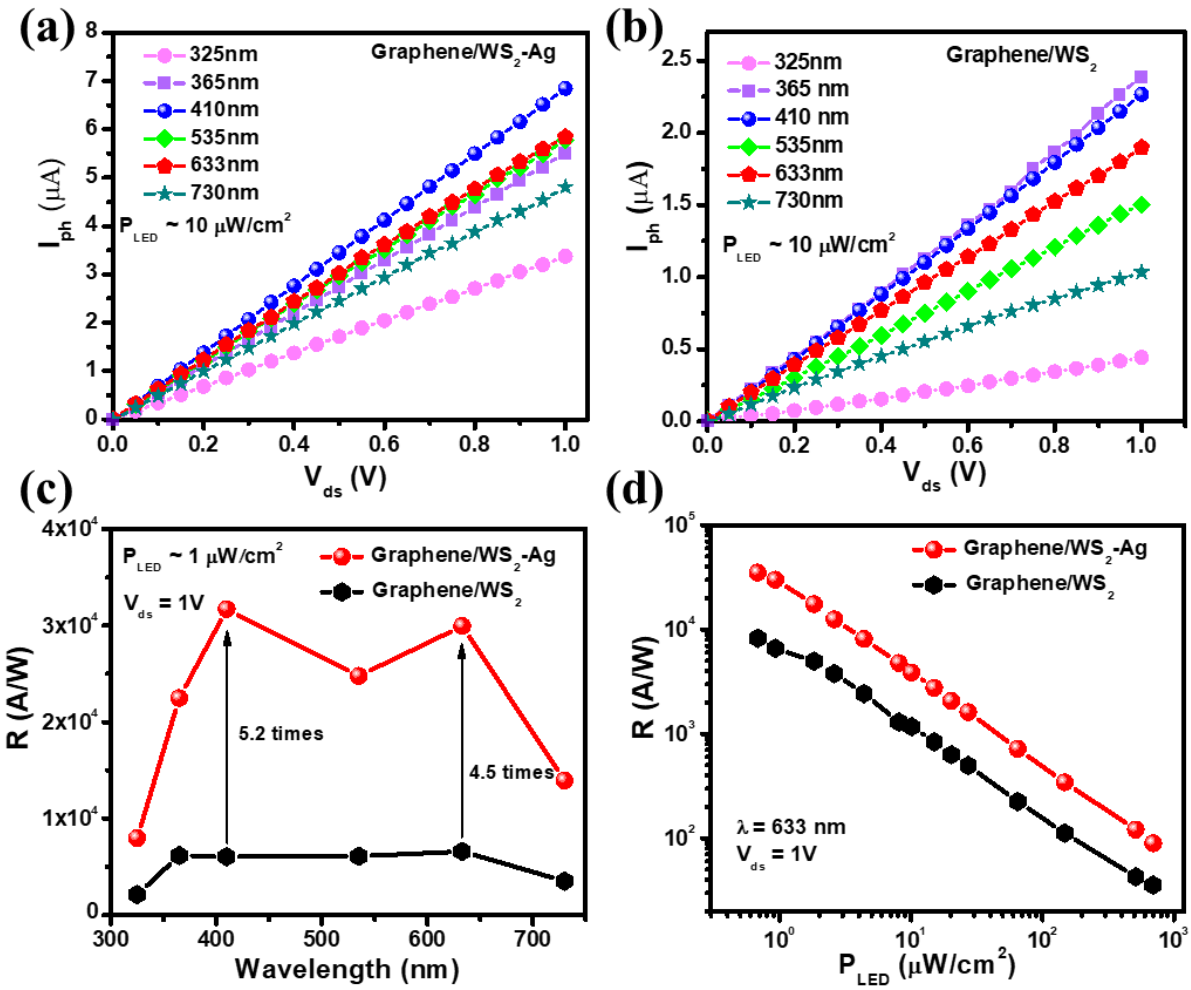

Figure 6.8: *Comparison of photoresponse characteristics of graphene/WS_2-Ag and graphene/WS_2 hybrid devices. Photocurrent (I_{ph}) as a function of applied source-drain bias (V_{ds}) voltage of (a) graphene/WS_2-Ag and (b) graphene/WS_2 devices. Photoresponsivity as a function of (c) wavelength and (d) illumination power (P_{LED}) of the plasmonic hybrid and control devices.*

$$R = \frac{I_{ph}}{P_{eff}} \quad \text{……..……} \quad (6.1)$$

Here, I_{ph} = (I_{light} - I_{dark}) is the photocurrent and P_{eff} is the effective optical illumination power on the surface of the device. Furthermore, the photoresponsivity (R) is noticeably enhanced for the plasmonic device (graphene/WS_2-Ag) in the whole UV-Vis spectrum region (325-730 nm) compared to the graphene/WS_2 control device. The enhancement of R is the highest (~5.2 times) at 410 nm of illumination. This enhanced responsivity can be attributed to the localized surface plasmon resonance effect of Ag nanoparticles which enhances the optical absorbance of the WS_2 layers. Additionally, the strong exciton-plasmon coupling of WS_2-Ag enhances the photoresponsivity significantly (~ 4.5 times) at 633 nm of illumination. **Figure 6.8d** represents a comparison of the photoresponsivity as a function optical illumination power density (P_{LED}) of the graphene/WS_2-Ag and graphene/WS_2 devices with λ = 633 nm, V_{ds} = 1 V for zero gate voltage (V_{bg} = 0 V). At a lowest illumination power of ~ 0.2 μW/cm^2 the plasmonic graphene/WS_2-Ag device offers the highest photoresponsivity (R) of ~ 3.5×10^4 A/W, whereas, in case of non-plasmonic control device, R becomes ~ 8.2×10^3 A/W at 633 nm. For both the devices, R decreases monotonically with the increase of optical power. The saturation of photocurrent (I_{ph}) due to lowering of the interfacial built-in-field reduces the responsivity with the increase of illumination power[239,240].

6.3.3 Noise, noise equivalent power (NEP) and specific detectivity (D^*)

Noise equivalent power (NEP) and specific detectivity (D^*) are two important parameters to evaluate the capability of weak signal detection of a photodetector. The NEP of a photodetector is defined as[120]

$$NEP = \frac{S_I}{R} \quad \text{……..…..} \quad (6.2)$$

Where, S_I id the total noise current considering 1/f noise, shot noise and the thermal noise of the devices and R represents the photoresponsivity.

Similarly, the specific detectivity (D^*) is defined as[120]

$$D^* = \frac{\sqrt{A}}{NEP} \quad \text{……..…..} \quad (6.3)$$

Where, A is the area of the device.

At a frequency of 1 Hz, the measured 1/f noise spectral density (S_I (1/f)) of the plasmonic graphene/WS_2-Ag and graphene/WS_2 devices are calculated to be 3.01×10^{-17} A^2/Hz and 1.11×10^{-17} A^2/Hz, respectively. This 1/f noise (inset **Figure 6.9a** and **6.9b**) clearly dominates over the other source of noises in these hybrid phototransistor devices. **Figures 6.9a** and **6.9b** show the spectral NEP and the specific detectivity (D^*) of the hybrid devices. It is seen that the plasmonic graphene/WS_2-Ag device offers lower NEP and higher specific detectivity as compared to the bare graphene/WS_2 device in overall spectrum region. For example, the calculated NEP becomes 1.73×10^{-13} W/$Hz^{0.5}$ and 5.52×10^{-13} W/$Hz^{0.5}$ and the specific detectivity (D^*) becomes 6.83×10^{10} Jones and 2.14×10^{10} Jones for the plasmonic graphene/WS_2-Ag and bare graphene/WS_2 devices, respectively (at λ = 410 nm, V_{ds} = 1 V). A lower NEP and higher detectivity indicate the superiority of the plasmon coupled device for weak light detection.

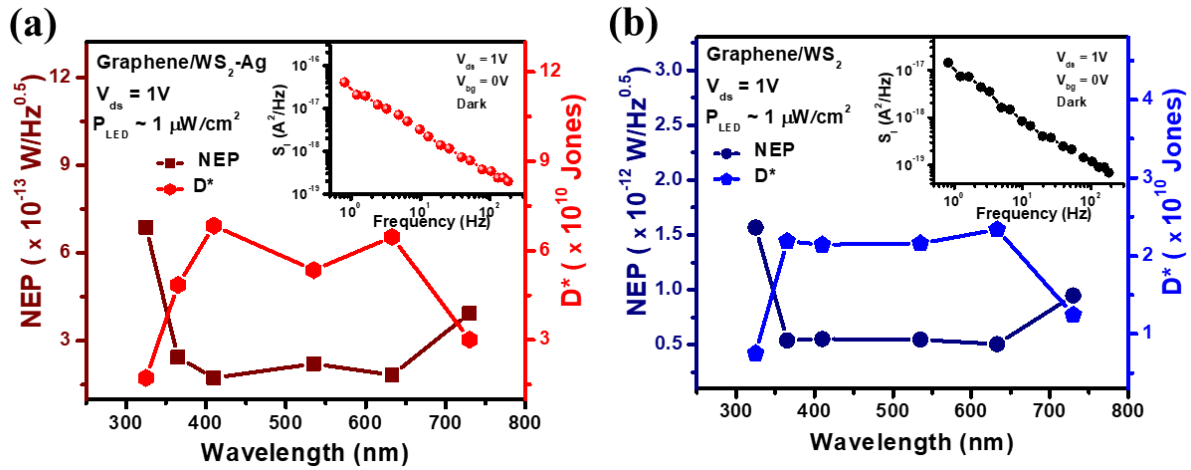

Figure 6.9: *Comparison of photoresponse characteristics of graphene/WS_2-Ag and graphene/WS_2 hybrid devices. Noise equivalent power (NEP) and the specific detectivity (D*) of (a) hybrid graphene/WS_2-Ag and (b) graphene/WS_2 devices. 1/f noise spectra of the respective devices are shown in the inset.*

6.3.4 Temporal photoresponse and speed

Figures 6.10a and **6.10b** represent the UV-Vis (325-730nm) broadband photo-switching characteristics of these two phototransistors with the same experimental conditions V_{ds} = 1 V, V_{bg} = 0 V and P_{LED} ~ 10 μW/ cm^2. Both the devices show stable and repeatable temporal photoresponse by following the multiple ON/OFF illumination cycles. The plasmonic graphene/WS_2-Ag device offers a significantly higher photocurrent with consistent reproducibility in the overall wavelength region compared to the bare graphene/WS_2 device.

This higher temporal photocurrent is consistent with the enhanced photoresponsivity and can be described by the strong exciton-plasmon coupling as explained before. The characteristic temporal response time is a very important parameter to evaluate the performance of a photodetector. The rise time (τ_{Rise}) and decay time (τ_{Fall}) of a photodetector (**Figure 6.10c** and **6.10d**) device are basically defined as the time gap for the current changes from 10% to 90% and vice-versa when light is turn ON or OFF[241]. The rise times (τ_{Rise}) of the graphene/WS_2 phototransistor with and without Ag nanoparticles are 0.49 sec and 0.52 sec, respectively, while the corresponding fall times (τ_{Fall}) are 0.50 sec and 0.57 sec.

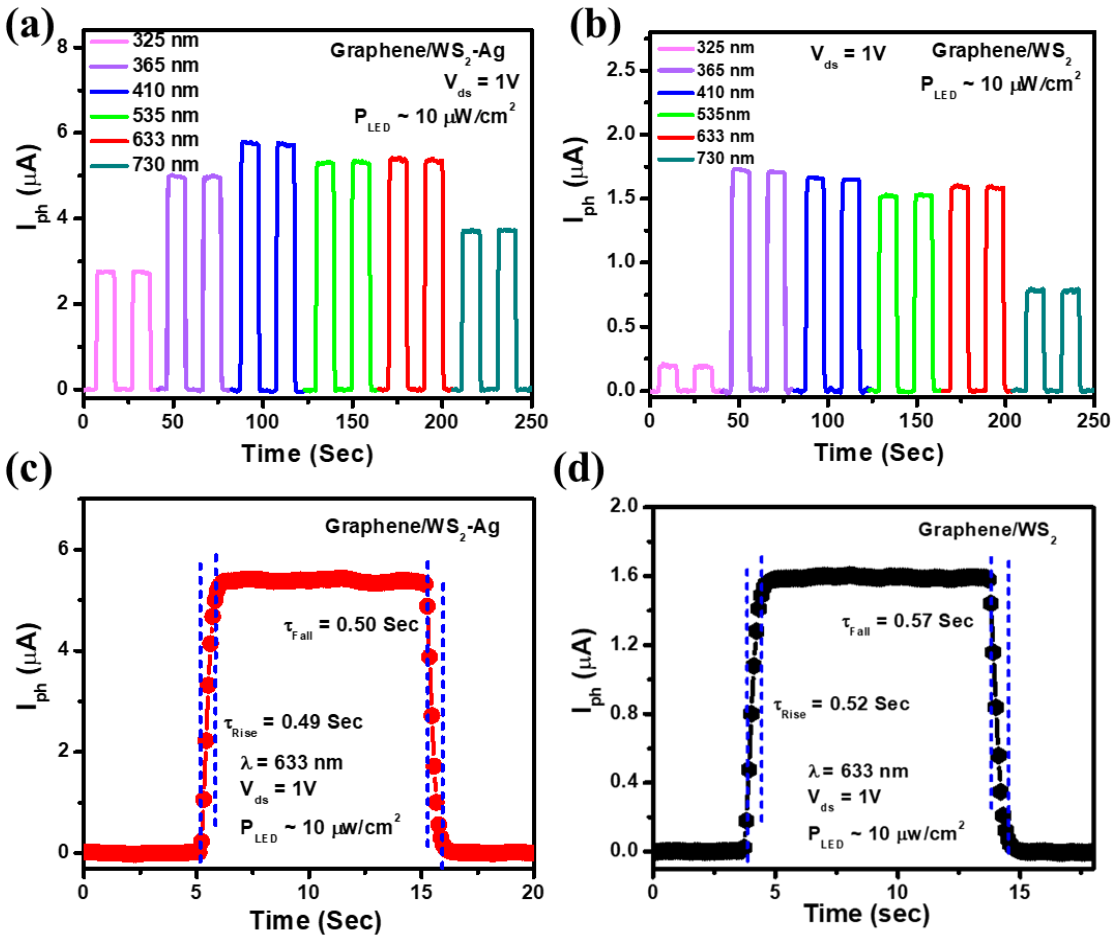

Figure 6.10: *Comparison of temporal photoresponse characteristics of graphene/WS_2-Ag and graphene/WS_2 hybrid devices. (a) and (b) the temporal photoresponse in the broadband UV-Vis (325-730 nm) region of the graphene/WS_2-Ag and graphene/WS_2 hybrid devices respectively. The enlarged one cycle view of temporal photoresponse characteristics of hybrid (c) graphene/WS_2-Ag and (d) graphene/WS_2 phototransistors with λ = 633 nm, V_{ds} = 1 V, V_{bg} = 0 V, P_{LED} ~ 10$\mu W/cm^2$.*

6.3.5 Gate tunable photoresponse and the simulated electric field

Figure 6.11a shows the transfer characteristics of the hybrid device before and after illuminating a 633 nm radiation (left axis) and the gate tunable photoresponsivity at V_{ds} = 0.5 V (right axis). It is seen that the photoresponsivity can be tuned significantly by the application of a gate voltage (V_{bg}). At 633 nm of illumination with 8 μW/cm^2 power, the photoresponsivity increases from 2.57×10^3 A/W to 3.32×10^3 A/W when the gate voltages (V_{bg}) changes from -15 V to 0 V, while photoresponsivity (R) again decreases to -3.06×10^2 A/W at V_{bg} = 45 V. Such a polarity tunable photoresponsivity can be described by a simple energy band diagram as shown in **Figure 6.11b**. Upon irradiation, electron-hole pairs are generated in Ag NPs decorated WS_2. The photogenerated holes are then transferred to graphene channel by trapping the electrons in WS_2 due to the upward band bending. While decreasing the gate voltage to a

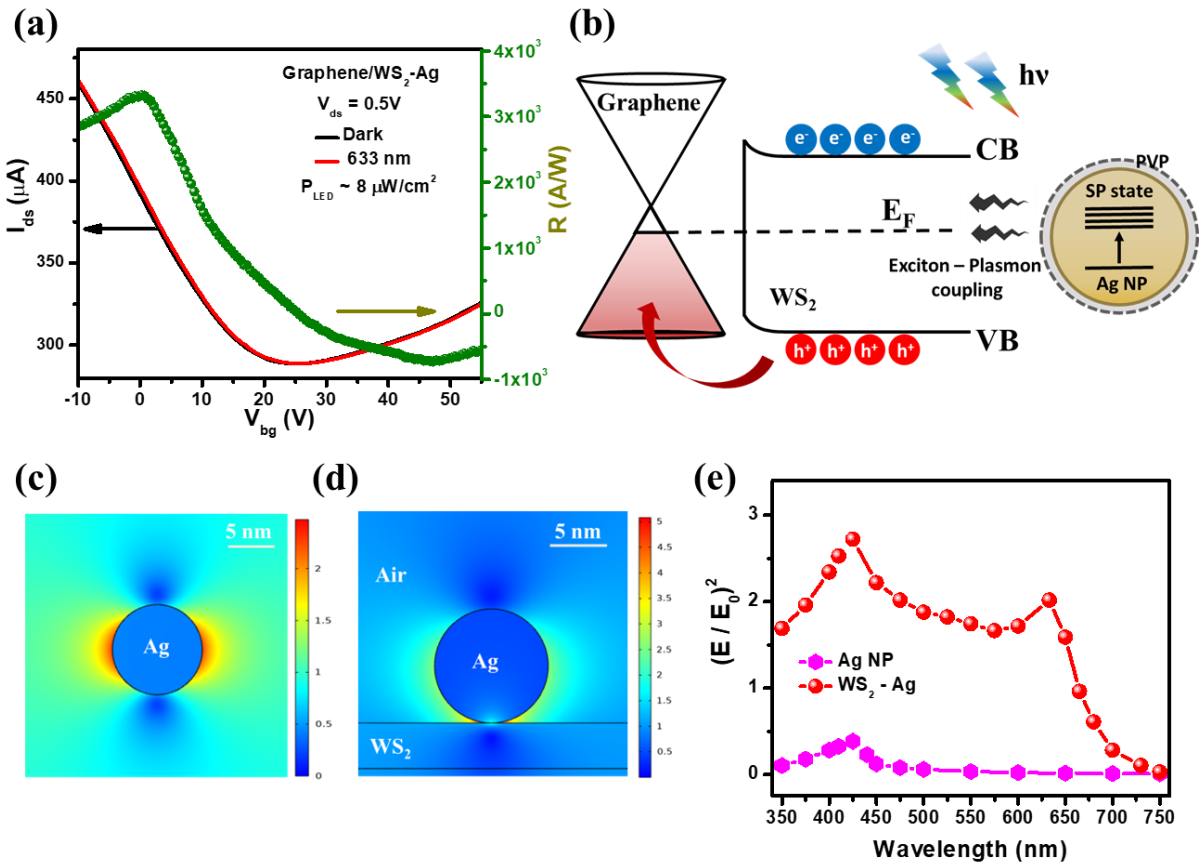

Figure 6.11: *Photodetection characteristics of graphene/WS_2-Ag heterostructure. (a) Transfer characteristics and the gate tunable photoresponse of the plasmonic hybrid device at λ = 633 nm, V_{ds} = 0.5V, P_{LED} ~ 8 μW/cm^2. (b) Suggested energy band diagram illustrating the gate tunable photoresponse in the hybrid device. (c) and (d) Electric field distribution of a single Ag NP and the WS_2-Ag interface under the excitation of 420 nm. (e) The simulated spectral electric field intensity of bare Ag NP and WS_2-Ag hybrid structure.*

value of $V_{bg} < V_D$, the Fermi level of the graphene is lowered and the graphene becomes hole doped. It helps to transfer more photogenerated holes to the graphene channel by enhancing the interfacial electric field. As a result, the photoresponsivity of the device increases. Similarly, when the applied gate voltages are higher than the Dirac voltage ($V_{bg} > V_D$), the graphene becomes electron doped. Now, increasing V_{bg} also increases the injection of photogenerated electrons from WS_2 to graphene due to downward band bending in WS_2, resulting in a negative photoresponsivity. Interestingly, the photoresponsivity becomes negligibly small near the photoresponsivity of the devices. The presence of an additional PVP layer in between WS_2 and Ag NPs effectively blocks all the transfer mechanism (charge, heat etc.) except the LSPR Dirac point ($V_D \sim 23$ V) making the gate voltages as an additional switch to tune the coupling. The dipole-dipole energy transfer effectively increases the electric field intensity at the locality of semiconducting WS_2 and results in an enhanced optical absorption accompanied by the generation of larger density of electron-hole pairs upon illumination. To understand the effect of surface plasmon (SP) coupling for synergistically enhanced absorption, emission and improved photoresponse in the WS_2-Ag hybrid, the electric field distribution is investigated by using COMSOL Multiphysics simulation. Under resonance excitation ~ 420 nm, the simulated electric field distribution of a single Ag NP and WS_2-Ag hybrid system are represented in **Figure 6.11c** and **6.11d,** respectively. This strong, tightly confined plasmonic mode of Ag NPs is responsible for the enhanced light matter interaction in the hybrid system. The excitation rate and the absorption cross-section of the excitonic system are enhanced by a factor ($\left|E/E_0\right|^2$), where E and E_0 are the local and incident electric fields respectively[242,243]. The simulated spectral distribution (350-750 nm) of the interfacial electric field is depicted in **Figure 6.11e** for a single Ag NP and WS_2-Ag hybrid system. The field enhances in the hybrid system for the overall spectrum region, which is consistent with the absorption spectra (**Figure 6.3a**). This enhancement of the interfacial electric field can be qualitatively explained by a simple image charge model. The electromagnetic field of the plasmonic Ag NP can effectively be screened due to the introduction of the WS_2 layer in the vicinity and therefore generates the image charges. The coupling between the plasmonic particle and its image charge pushes down the hot spot of the generated electric field and subsequently enhances the interfacial field of the hybrid WS_2-Ag system.

6.3.6 Stability

The stability of the plasmonic hybrid photodetector is checked by keeping it in the normal ambient conditions (in a vacuum desiccator). The device offers extremely stable photocurrent (**Figure 6.12**) even after 3 months of its fabrication. The insulating PVP capping therefore greatly helps to stabilize the device by preventing the direct contact of such Ag NPs with the WS_2 layers. Notably, highly enhanced photoresponsivity, along with good stability and durability, make this hybrid graphene/WS_2-Ag phototransistor superior to other reported results (presented in **Table 6.1**) and very promising for the future multifunctional optical devices.

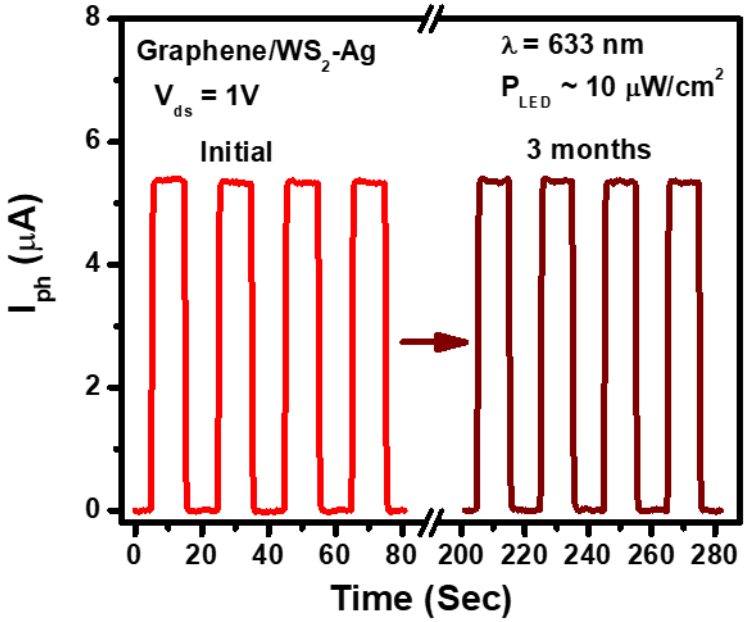

Figure 6.12: *The temporal photocurrent (I_{ph}) of the graphene/WS_2-Ag hybrid phototransistor after 3 months of its fabrication which suggests the excellent stability of the device. The experiments are performed with λ = 633 nm, V_{ds} = 1 V, V_{bg} = 0 V, P_{LED} ~ 10 $\mu W/cm^2$.*

Table 6.1: *Performance comparison of some graphene based plasmonic photodetectors*

SL No	Device Structure	Wavelength (Nm)	V_{ds} (V)	Responsivity (R) A/W	Rise time (sec)	Decay time (sec)	Ref
1.	Graphene-perovskite-Au nanoarray	375-808	2	18.71	0.33	0.27	17
2.	Graphene-$MAPbI_3$-Au NPs	532	10	2.1×10^3	1.5	1.5	18

3.	Graphene-WS_2- Ag NPs	400-750	0.8	11.4	0.3	1	35
4.	Graphene-$MAPbI_3$-Au nano stars	532	-5	5.9×10^4	2.5	11.9	19
5.	Graphene-Ag NP	225-450	0.5	14.5	6	17	50
6.	Graphene -Ag NP	250-450	0.35	82	1	4	52
7.	Graphene-perovskite-Au NPs	450-800	0.1	495.3	7	7	49
8.	Graphene/WS_2-Ag (PVP)	325-730	1	3.5×10^4	0.49	0.52	**This work**

.

6.4 Summary

In summary, we have demonstrated a stable, cost effective, scalable and gate tunable phototransistor based on monolayer graphene/WS_2-Ag NPs plasmonic heterostructure. The presence of strong surface plasmon resonance due to synthesized Ag NPs effectively enhances the light matter interactions in WS_2. The enhanced optical properties in the WS_2-Ag hybrid are originated from the dipole mediated exciton-plasmon coupling in the multiple integrated hot spots. Compared to the bare graphene/WS_2 device, the graphene/plasmonic Ag NPs coupled WS_2 hybrid device offers superior photodetection capabilities in the broadband UV-Vis (325-730 nm) region with an excellent gate tunability. Furthermore, it shows the photoresponsivity as high as ~ 3.2×10^4 A/W and ~ 2.9×10^4 A/W for 410 nm and 633 nm of illumination, respectively which are about 500% higher than the control graphene/WS_2 device. Also, considering 1/f noise, the plasmon coupled graphene/WS_2 phototransistor offers a very low noise equivalent power (NEP) ~10^{-13} W/$Hz^{0.5}$ and high specific detectivity (D*) ~10^{10} Jones in the wide (325-730 nm) wavelength region. The additional PVP capping in Ag NPs helps to supress the loss through the heat and energy transfer and most importantly increases the device stability by preventing any degradation. The strong exciton-plasmon coupling mediated enhanced optical properties of the plasmonic WS_2-Ag hybrid have been explained by COMSOL Multiphysics simulation. Our study provides a strategic route towards facile fabrication of a superior quality large area, broadband, plasmon based, highly stable hybrid phototransistor based on the exciton-plasmon coupling, a potential candidate for the next generation optoelectronic devices.

Chapter 7

Conclusions and Future Scope of Study

This Chapter concludes the current thesis and gives an insight about the drawbacks and the future scope of study which can be addressed in future.

7.1 Conclusions

The study of 2D materials has advanced at a lightning speed due to the extensive research on graphene and other layered materials. From both scientific and technological perspective, their distinctive electronic and optoelectronic properties, flexibility, and ultimate saleability down to single atomic layer are of great interest. Photodetectors are of utmost significance in optoelectronic technology, and the expanding variety of application fields necessitates new material systems and device designs. These must not only fulfil essential criteria like high sensitivity, quick response, and affordable manufacturing, but also add new features like tunable spectral selectivity, mechanical flexibility, or even partial transparency. In this thesis, by customized experimental setups, several noble device structures have been discussed towards the large scale, cost effective broadband photodetection. The major outcomes of this thesis are summarized below:

- A highly sensitive visible phototransistor made of atomically thin bilayer MoS_2 has been reported. To make the back gated device, the mechanically exfoliated MoS_2 ultrathin sheet is dry transferred to a Si/SiO_2 substrate using an optical microscope. The fabricated phototransistor has a very high responsivity ($>10^6$ A/W) at 633 nm illumination, with superior gate tunability even at ultralow illumination. Furthermore, when 1/f noise is considered, the device has a low noise equivalent power (10^{-15} $W/Hz^{0.5}$) and a higher specific detectivity (10^{12} Jones).

- The most straightforward method for fabricating a super large (~ 0.75 mm^2), mixed-dimensional, UV-Vis broadband (365-633 nm) phototransistor with an active channel made of WS_2 QDs decorated CVD graphene is discussed. Colloidal crystalline 0D WS_2 QDs serve as the photo-absorbing material, and graphene serves as the conducting channel. A high photoresponsivity (3.1×10^2 A/W), moderately high detectivity

(8.9×10^{8} Jones), and low noise equivalent power (9.7×10^{-11} W/Hz$^{0.5}$) are obtained at a low bias voltage (V_{ds} = 1 V) and an optical power as low as 0.8 μW/cm^2, which can be further tuned by modulating the gate bias. This chapter also discusses the role of WS_2 morphology in hybrid device photocurrent generation.

- The photoresponse properties are systematically investigated by covering a large area of graphene with various composites of $MoS_{2x}Se_{2(1-x)}$ (x = 0 to 1) ternary alloys in 2D-2D device configurations. Among them, the hybrid graphene-MoSSe phototransistor performs better than its binary counterparts in terms of optoelectronic characteristics. With excellent gate tunability, the device has a very high photoresponsivity (>10^4 A/W), low noise equivalent power (10^{-14} W/Hz$^{0.5}$), and a higher specific detectivity (10^{11} Jones) in the UV-NIR (365-810 nm) range. This chapter ends with a potential justification for the engineering of controllable defects in MoSSe, which makes this device very alluring.

- A large area broadband superior gate-tunable hybrid phototransistor fabricated without the use of lithography and using monolayer graphene decorated with WS_2-Ag NPs in a three-terminal device configuration is reported. In addition to having a very low noise equivalent power (NEP) (10^{-13} W/Hz$^{0.5}$) and a higher specific detectivity (10^{10} Jones) in the broad (325-730 nm) wavelength region, the fabricated device has an extremely high photoresponsivity (up to 3.2×10^{4} A/W), which is more than 5 times higher than the bare graphene/WS_2 hybrid device. The surface plasmon-exciton coupling effect of the polyvinylpyrrolidone (PVP) capped silver (Ag) nanoparticles (NPs) limits the direct charge, energy, and heat transfer and improves the optical properties of tungsten disulphide (WS_2). According to COMSOL Multiphysics simulation, the increased electromagnetic field near the WS_2-Ag hybrid causes the amplified optical signal. This work demonstrates a method for achieving an eco-friendly, scalable, high-performance broadband phototransistor for new generation opto-electronic devices by adjusting the exciton-plasmon coupling.

7.2 Future Scope of Study

In this thesis, some experimental setups are developed and new device structures towards the graphene based broadband phototransistors are addressed. The focus of the thesis was to fabricate the devices for technological applications while also addressing some fundamental

issues. There are many aspects which remain unaddressed in this work and can be extended for future work.

- The large area chemical vapour deposited (CVD) graphene serves as the foundation for most of the devices fabricated for this thesis. Such CVD-grown graphene has lower charge carrier mobilities, which also affects optoelectronics. The capabilities of the device can be increased by using high mobility graphene and as well as device engineering (heterostructure formation and using flexible substrate) is an important prospect.

- Instead of graphene, fabrication of other 2D heterostructures by combining different TMDC materials (MoS_2, WS_2, WSe_2 etc) in order to minimize the dark current and off current of fabricated phototransistors.

- In one of the works, the composition tunable $MoS_{2x}Se_{2(1-x)}$ alloys are used to fabricate the broadband phototransistor devices. The reduced defect density and the conversion from deep to shallow level vacancies are considered to be responsible for the enhanced optoelectronic properties of MoSSe. By developing some experimental tools, such as deep level transient spectroscopy (DLTS), one can address the quantitively the defect densities, for the purpose of fundamental interest.

- Exciton-plasmon coupling is found to be interesting which also helps to improve the photodetection capabilities of graphene-WS_2-Silver (Ag) hybrid phototransistors. Now, the understanding of charge and the energy transfer mechanism in WS_2-Ag hybrid system and graphene-TMDC interfaces can be explored by ultrafast pump-probe spectroscopy technique.

References

1. K. S. Novoselov, 1 A. K. Geim, 1, * S. V. Morozov, 2 D. Jiang, 1 & Y. Zhang, 1 S. V. Dubonos, 2 I. V. Grigorieva, 1 A. A. Firsov2. Electric Field Effect in Atomically Thin Carbon Films. *Science (80-.).* **306**, 666–669 (2004).

2. Novoselov, K. S. *et al.* Two-dimensional atomic crystals. *Proc. Natl. Acad. Sci. U. S. A.* **102**, 10451–10453 (2005).

3. Novoselov, K. S. *et al.* Two-dimensional gas of massless Dirac fermions in graphene. *Nature* **438**, 197–200 (2005).

4. Zhang, Y., Tan, Y. W., Stormer, H. L. & Kim, P. Experimental observation of the quantum Hall effect and Berry's phase in graphene. *Nature* **438**, 201–204 (2005).

5. Mak, K. F. *et al.* Tightly bound trions in monolayer MoS 2. *Nat. Mater.* **12**, 207–211 (2013).

6. Low, T. *et al.* Polaritons in layered two-dimensional materials. *Nat. Mater.* **16**, 182–194 (2017).

7. Gorbachev, R. V. *et al.* Strong Coulomb drag and broken symmetry in double-layer graphene. *Nat. Phys.* **8**, 896–901 (2012).

8. Lee, C. *et al.* Anomalous lattice vibrations of single- and few-layer MoS2. *ACS Nano* **4**, 2695–2700 (2010).

9. Rao, C. N. R., Sood, A. K., Subrahmanyam, K. S. & Govindaraj, A. Graphene: The new two-dimensional nanomaterial. *Angew. Chemie - Int. Ed.* **48**, 7752–7777 (2009).

10. Article, P. The rise of graphene. **6**, 183–191 (2007).

11. Du, X. U., Skachko, I., Barker, A. & Andrei, E. V. A. Y. Approaching ballistic transport in suspended graphene. *naturenanotechnology* **3**, 491–495 (2008).

12. Wallace, P. R. No Title. *Phys. Rev.* **71**, 622–634 (1947).

13. Neto, A. H. Castro, F. Guinea, N. M. R. Peres, K. S. N. and A. K. G. The electronic properties of graphene. *Rev. Mod. Phys.* **81**, 109–162 (2009).

14. Sarma, S. Das, Adam, S. & Rossi, E. Electronic transport in two-dimensional graphene. **83**, (2011).

15. Katsnelson, M. I., Novoselov, K. S. & Geim, A. K. Chiral tunnelling and the Klein paradox in graphene. *Nat. Phys.* **2**, 620–625 (2006).

16. Baringhaus, J. *et al.* Exceptional ballistic transport in epitaxial graphene nanoribbons. *Nature* (2014) doi:10.1038/nature12952.

17. Hwang, E. H., Adam, S. & Sarma, S. Das. Carrier transport in two-dimensional graphene layers. *Phys. Rev. Lett.* **98**, 2–5 (2007).

18. Adam, S., Hwang, E. H., Galitski, V. M. & Sarma, S. Das. A self-consistent theory for graphene transport. *PNAS* **2007**, (2007).

19. Nair, R. R. *et al.* Fine Structure Constant Defines Visual Transparency of Graphene. *Science (80-.).* **320**, 1308 (2008).

20. Yan, J., Ruan, W. Y. & Chou, M. Y. Phonon dispersions and vibrational properties of monolayer , bilayer , and trilayer graphene : Density-functional perturbation theory. *Phys. Rev. B* **77**, 125401 (2008).

21. Ferrari, A. C. *et al.* Raman Spectrum of Graphene and Graphene Layers. *Phys. Rev. Lett.* **187401**, 1–4 (2006).

22. Gupta, A. *et al.* Raman Scattering from High-Frequency Phonons in Supported n-Graphene Layer Films. *Nano Lett.* **6**, 2667–2673 (2006).

23. Graf, D. *et al.* Spatially Resolved Raman Spectroscopy of Single- and Few-Layer Graphene. *Nano Lett.* **7**, 238–242 (2007).

24. Casiraghi, C., Novoselov, S. P. S. & Ferrari, A. K. G. C. Raman fingerprint of charged impurities in graphene Raman fingerprint of charged impurities in graphene. *Appl. Phys. Lett.* **233108**, 1–4 (2007).

25. Malard, L. M., Pimenta, M. A., Dresselhaus, G. & Dresselhaus, M. S. Raman spectroscopy in graphene. *Phys. Rep.* **473**, 51–87 (2009).

26. Wang, Q. H., Kalantar-zadeh, K., Kis, A., Coleman, J. N. & Strano, M. S. transition metal dichalcogenides. *Nat. Publ. Gr.* **7**, 699–712 (2012).

27. Mak, K. F., Lee, C., Hone, J., Shan, J. & Heinz, T. F. Atomically thin MoS2: A new

direct-gap semiconductor. *Phys. Rev. Lett.* **105**, 2–5 (2010).

28. Kuc, A., Zibouche, N. & Heine, T. Influence of quantum confinement on the electronic structure of the transition metal sulfide T S 2. *Phys. Rev. B* **83**, 245213 (2011).

29. Mo, M. X. M. *et al.* First principles study of structural , vibrational and electronic properties of. *Phys. B Phys. Condens. Matter* **406**, 2254–2260 (2011).

30. Ataca, C. & Ciraci, S. Stable, Single-Layer MX 2 Transition-Metal Oxides and Dichalcogenides in a Honeycomb-Like Structure. *J. Phys. Chem. C* (2012).

31. Fraser, S. = 3. 86. *Phys. Rev. B* **43**, 53–56 (1991).

32. Ahmed, T. *et al.* Thermodynamically stable octahedral MoS 2 in van der Waals hetero-bilayers Thermodynamically stable octahedral MoS 2 in van der Waals. *2D Mater.* **6**, 041002 (2019).

33. Eda, G. *et al.* Photoluminescence from Chemically Exfoliated MoS 2. *Nano Lett.* **11**, 5111–5116 (2011).

34. Lebègue, S. & Eriksson, O. Electronic structure of two-dimensional crystals from ab initio theory. *Phys. Rev. B* **79**, 115409 (2009).

35. Severin, R., Mu, A., Janowitz, C., Manzke, R. & Bo, T. Angle-resolved photoelectron spectroscopy and ab initio calculations. *Phys. Rev. B* **64**, 235305 (2001).

36. Li, T. & Galli, G. Electronic Properties of MoS 2 Nanoparticles. *J. Phys. Chem. C* **12**, 16192–16196 (2007).

37. Radisavljevic, B., Radenovic, A., Brivio, J., Giacometti, V. & Kis, A. Single-layer MoS 2 transistors. *Nat. Nanotechnol.* **6**, 147–150 (2011).

38. Wang, Q. H., Kalantar-zadeh, K., Kis, A., Coleman, J. N. & Strano, M. S. Electronics and optoelectronics of two-dimensional transition metal dichalcogenides. *Nat. Publ. Gr.* **7**, 699–712 (2012).

39. Kaasbjerg, K., Thygesen, K. S. & Jacobsen, K. W. Phonon-limited mobility in n -type single-layer MoS 2 from first principles. *Phys. Rev. B* **115317**, 1–16 (2012).

40. Ma, N. & Jena, D. Charge Scattering and Mobility in Atomically Thin Semiconductors. *Phys. Rev. X* **011043**, 1–9 (2014).

41. Cui, X. *et al.* device platform. *Nat. Nanotechnol.* **10**, 534–540 (2015).

42. Schmidt, H. & Eda, G. Chem Soc Rev dichalcogenide field-effect devices : surface and interface effects. *Chem Soc Rev* **44**, 7715–7736 (2015).

43. Splendiani, A. *et al.* Emerging Photoluminescence in Monolayer. 1271–1275 (2010) doi:10.1021/nl903868w.

44. Xiao, D., Liu, G., Feng, W., Xu, X. & Yao, W. Coupled Spin and Valley Physics in Monolayers of MoS 2 and Other Group-VI Dichalcogenides. *Phys. Rev. Lett.* **196802**, 1–5 (2012).

45. Mos, F. *et al.* Anomalous Lattice Vibrations of Single-. *ACS Nano* **4**, 2695–2700 (2010).

46. Wirtz, L. Phonons in single-layer and few-layer MoS 2 and WS 2. *Phys. Rev. B* **155413**, 1–8 (2011).

47. Hernandez, Y. *et al.* High-yield production of graphene by liquid-phase exfoliation of graphite. *Nat. Nanotechnol.* **3**, 563–568 (2008).

48. Coleman, J. N. *et al.* Produced by Liquid Exfoliation of Layered Materials. *Science (80-.).* **331**, 568–571 (2011).

49. Chang, C. *et al.* Growth of Large-Area and Highly Crystalline MoS 2 Thin Layers on Insulating Substrates. *Nano Lett.* **12**, 1538–1544 (2012).

50. Wang, S. *et al.* Shape Evolution of Monolayer MoS 2 Crystals Grown by Chemical Vapor Deposition. *Chem. Mater.* **26**, 6371–6379 (2014).

51. Lin, L. *et al.* Sulfur-Depleted Monolayered Molybdenum Disulfide Nanocrystals for Superelectrochemical Hydrogen Evolution Reaction. *ACS Nano* **10**, 8929–8937 (2016).

52. Nguyen, T. P., Sohn, W., Oh, J. H., Jang, H. W. & Kim, S. Y. Size-Dependent Properties of Two-Dimensional MoS2 and WS2. *J. Phys. Chem. C* **120**, 10078–10085 (2016).

53. Bhattacharya, D., Mukherjee, S. & Mitra, R. K. Size-dependent optical properties of MoS 2 nanoparticles and their photo-catalytic applications. (2020).

54. Zhou, W. *et al.* Intrinsic Structural Defects in Monolayer Molybdenum Disul fi de. *Nano Lett.* **13**, 2615–2622 (2013).

55. Xi, J., Zhao, T., Wang, D. & Shuai, Z. Tunable Electronic Properties of Two-

Dimensional Transition Metal Dichalcogenide Alloys: A First-Principles Prediction. *J. Phys. Chem. Lett.* **5**, 285–291 (2014).

56. Huang, B., Yoon, M., Sumpter, B. G., Wei, S. & Liu, F. Alloy Engineering of Defect Properties in Semiconductors : Suppression of Deep Levels in Transition-Metal Dichalcogenides. *Phys. Rev. Lett.* **126806**, 1–5 (2015).

57. Linder, C., Rahm, J. M. & Erhart, P. High-Throughput Characterization of Transition Metal Dichalcogenide Alloys : Thermodynamic Stability and Electronic Band Alignment. *Chem. Mater.* **34**, 9364–9372 (2022).

58. Komsa, H. & Krasheninnikov, A. V. Two-Dimensional Transition Metal Dichalcogenide Alloys: Stability and Electronic Properties. *J. Phys. Chem. C* **3**, 3652–3656 (2012).

59. Chen, H., Su, L., Jiang, M. & Fang, X. Highly Desirable Photodetectors Derived from Versatile Plasmonic Nanostructures. *Adv. Funct. Mater.* **27**, 1704181 (2017).

60. Zhang, J., Wang, Y., Li, D., Sun, Y. & Jiang, L. Engineering Surface Plasmons in Metal/ Nonmetal Structures for Highly Desirable Plasmonic Photodetectors. *acs matterials Lett.* **4**, 343–355 (2022).

61. Tame, M. S. *et al.* Quantum plasmonics. *Nat. Phys.* **9**, 329–340 (2013).

62. Xuanhua Li, J. Z. and B. W. Hybrid nanostructures of metal/two-dimensional nanomaterials for plasmon-enhanced applications. *Chem Soc Rev* **45**, 3145–3187 (2016).

63. Liu, W. *et al.* Strong Exciton − Plasmon Coupling in MoS 2 Coupled with Plasmonic Lattice. *Nano Lett.* **16**, 1262–1269 (2016).

64. Butun, S., Tongay, S. & Aydin, K. Enhanced Light Emission from Large-Area Monolayer MoS 2 Using Plasmonic Nanodisc Arrays. *Nano Lett.* **15**, 2700–2704 (2015).

65. Lee, H. S. *et al.* Effi cient Exciton – Plasmon Conversion in Ag Nanowire / Monolayer MoS 2 Hybrids : Direct Imaging and Quantitative Estimation of Plasmon Coupling and Propagation. *Adv. Opt. Mater.* 1–5 (2015) doi:10.1002/adom.201500021.

66. Li, Y. *et al.* Plasmonics of 2D Nanomaterials: Properties and Applications. *Adv. Sci.* **4**, (2017).

67. Klitzing, K. v., G. D. and M. P. New et od for High-Accuracy Determination of th F -S e ine- tructure Constant Based on Quantized Hall Resistance. *Phys. Rev. Lett.* **6**, 11–14 (1980).

68. Murakami, S., Nagaosa, N. & Zhang, S. Dissipationless Quantum Spin. *Science (80-.).* **301**, 1348–1351 (2003).

69. B. Andrei Bernevig, Taylor L. Hughes, S.-C. Z. Quantum Spin Hall Effect and Topological Phase Transition in HgTe Quantum Wells. *Science (80-.).* 1757–1761 (2006) doi:10.1126/science.1133734.

70. T. Dekorsy, R. Ott, and H. K. and K. K. Bloch oscillations at room temperature. *Phys. Rev. B* **51**, 275–278 (1995).

71. Byrnes, T., Kim, N. Y. & Yamamoto, Y. Exciton–polariton condensates. *Nat. Phys.* 1–11 (2014) doi:10.1038/NPHYS3143.

72. Wang, L. *et al.* One-Dimensional Electrical Contact to. *Science (80-.).* **342**, 614–617 (2013).

73. Dean, C. R. *et al.* Boron nitride substrates for high-quality graphene electronics. *Nat. Nanotechnol.* **5**, 722–726 (2010).

74. Jariwala, D., Marks, T. J. & Hersam, M. C. Mixed-dimensional van der Waals heterostructures. *Nat. Mater.* **16**, 170–181 (2017).

75. Koppens, F. H. L. *et al.* Photodetectors based on graphene, other two-dimensional materials and hybrid systems. *Nat. Publ. Gr.* **9**, (2014).

76. Hadfield, R. H. Single-photon detectors for optical quantum information applications. *Nat. Photonics* **3**, (2009).

77. Long, M. *et al.* Broadband Photovoltaic Detectors Based on an Atomically Thin Heterostructure. *Nano Lett.* **16**, 2254−2259 (2016).

78. Xu, X., Gabor, N. M., Alden, J. S., Zande, A. M. Van Der & Mceuen, P. L. Photo-Thermoelectric Effect at a Graphene Interface Junction. *Nano Lett.* **10**, 562–566 (2010).

79. Song, J. C. W., Rudner, M. S., Marcus, C. M. & Levitov, L. S. Hot Carrier Transport and Photocurrent Response in Graphene. *Nano Lett.* **11**, 4688–4692 (2011).

80. Wei, J. *et al.* Ultrasensitive hot-electron nanobolometers for terahertz astrophysics. *Nat.*

Nanotechnol. **3**, 496–500 (2008).

81. Dyakonov, M. & Shur, M. Shallow Water Analogy for a Ballistic Field Effect Transistor: New Mechanism of Plasma Wave Generation by dc Current Michael. *Phys. Rev. Lett.* **71**, 2465–2469 (1993).

82. Konstantatos, G. & Sargent, E. H. Nanostructured materials for photon detection. *Nat. Publ. Gr.* **5**, 391–400 (2010).

83. Gong, X. *et al.* High-Detectivity Polymer from 300 nm to 1450 nm. *Science (80-.).* **325**, 1665–1667 (2009).

84. Mak, K. F. & Shan, J. Photonics and optoelectronics of 2D semiconductor transition metal dichalcogenides. *Nat. Publ. Gr.* **10**, 216–226 (2016).

85. Hooge, F. N. 1/f NOISE. *Phys. B Phys. Condens. Matter* 14–23 (1976) doi:10.1016/0378-4363(76)90089-9.

86. F N Hooge, T. G. M. K. and L. K. J. V. Experimental studies on 1 / f noise Experimental studies on. *Reports Prog. Phys. Rev.* **44**, (1981).

87. Rai, S. S. Low Frequency Noise Modeling in Single- and Double-Gate MOSFETs. (2005).

88. H. NYQUIST. THERMAL AGITATION OF ELECTRIC CHARGE IN CONDUCTORS. *Phys. Rev.* **32**, 110–113 (1928).

89. Novoselov, K. S., Mishchenko, A., Carvalho, A. & Castro Neto, A. H. 2D materials and van der Waals heterostructures. *Science (80-.).* **353**, (2016).

90. Nathaniel M. Gabor, Justin C. W. Song, Qiong Ma, Nityan L. Nair, Thiti Taychatanapat, Kenji Watanabe, Takashi Taniguchi, Leonid S. Levitov, P. J.-H. Hot Carrier–Assisted Intrinsic Photoresponse in Graphene. *Science (80-.).* **334**, 648–652 (2011).

91. Liu, C. H., Chang, Y. C., Norris, T. B. & Zhong, Z. Graphene photodetectors with ultra-broadband and high responsivity at room temperature. *Nat. Nanotechnol.* **9**, 273–278 (2014).

92. Zhang, B. Y. *et al.* monolayer graphene photodetector. *Nat. Commun.* 1–11 (2013) doi:10.1038/ncomms2830.

93. Chen, X., Yang, C., Sun, H., Ning, S. & Zhou, H. Enhanced photoresponsivity in carbon

quantum dots-coupled graphene / silicon Schottky-junction photodetector. *laser Phys. Lett.* **16**, 076201 (6pp) (2019).

94. Gong, M. *et al.* All-Printable ZnO Quantum Dots/Graphene van der Waals Heterostructures for Ultrasensitive Detection of Ultraviolet Light. *ACS Nano* 4114–4123 (2017) doi:10.1021/acsnano.7b00805.

95. Spirito, D. *et al.* UV Light Detection from CdS Nanocrystal Sensitized Graphene Photodetectors at kHz Frequencies. *J. Phys. Chem. C* **119**, 23859−23864 (2015).

96. Shao, Y. *et al.* Stable Graphene-Two-Dimensional Multiphase Perovskite Heterostructure Phototransistors with High Gain. *Nano Lett.* **17**, 7330–7338 (2017).

97. Wang, Y. *et al.* Hybrid Graphene-Perovskite Phototransistors with Ultrahigh Responsivity and Gain. *Adv. Opt. Mater.* **3**, 1389–1396 (2015).

98. Ni, Z. *et al.* Plasmonic Silicon Quantum Dots Enabled High-Sensitivity Ultrabroadband Photodetection of Graphene-Based Hybrid Phototransistors. *ACS Nano* **11**, 9854–9862 (2017).

99. Ulrich Nguétchuissi Noumbé,⊥ Charlie Gréboval,⊥ Clément Livache, Chu, A. *et al.* Recon fi gurable 2D/0D p − n Graphene/HgTe Nanocrystal Heterostructure for Infrared Detectioń. *ACS Nano* **14**, 4567–4576 (2020).

100. Yu, X. *et al.* Narrow bandgap oxide nanoparticles coupled with graphene for high performance mid-infrared photodetection. *Nat. Commun.* **9**, 1–8 (2018).

101. Konstantatos, G. *et al.* Hybrid grapheneĝquantum dot phototransistors with ultrahigh gain. *Nat. Nanotechnol.* **7**, 363–368 (2012).

102. Yu, W. J. *et al.* generation in vertical heterostructures of layered materials. *Nat. Nanotechnol.* **8**, 952–958 (2013).

103. Roy, K. *et al.* Graphene-MoS 2 hybrid structures for multifunctional photoresponsive memory devices. *Nat. Nanotechnol.* **8**, 826–830 (2013).

104. Mehew, J. D. *et al.* Fast and Highly Sensitive Ionic-Polymer-Gated WS2–Graphene Photodetectors. *Adv. Mater.* **29**, 1700222 (2017).

105. Jinshui Miao , Weida Hu , * Nan Guo , Zhenyu Lu , Xingqiang Liu , Lei Liao , * Pingping Chen , Tao Jiang , Shiwei Wu , Johnny C. Ho , Lin Wang , Xiaoshuang Chen,

and W. L. High-Responsivity Graphene InAs Nanowire Heterojunction Near-Infrared Photodetectors with Distinct_smll 2015.pdf. 936–942 (2015) doi:10.1002/smll.201402312.

106. Liu, Y. *et al.* Planar carbon nanotube–graphene hybrid films for high-performance broadband photodetectors. *Nat. Commun.* 1–7 (2015) doi:10.1038/ncomms9589.

107. Wu, D. *et al.* Highly Polarization-Sensitive, Broadband, Self-Powered Photodetector Based on Graphene/PdSe 2 /Germanium Heterojunction. *ACS Nano* **13**, 9907−9917 (2019).

108. Nicolosi, V., Chhowalla, M., Kanatzidis, M. G., Strano, M. S. & Coleman, J. N. Liquid exfoliation of layered materials. *Science (80-.).* **340**, 72–75 (2013).

109. Hayashi, H. & Hakuta, Y. Hydrothermal Synthesis of metal oxide nanoparticles in supercritical water. *Materials (Basel).* **3**, 3794–3817 (2010).

110. Ren, X. *et al.* One-step hydrothermal synthesis of monolayer MoS2 quantum dots for highly efficient electrocatalytic hydrogen evolution. *J. Mater. Chem. A* **3**, 10693–10697 (2015).

111. Novoselov, K. S. *et al.* A roadmap for graphene. *Nature* **490**, 192–200 (2012).

112. Moram, M. A. & Vickers, M. E. X-ray diffraction of III-nitrides. *Reports Prog. Phys.* **72**, (2009).

113. Shinato, K. W., Huang, F. & Jin, Y. Principle and application of atomic force microscopy (AFM) for nanoscale investigation of metal corrosion. *Corros. Rev.* **38**, 423–432 (2020).

114. John, R. & Chris, W. *Introductory Raman Spectroscopy*. *Introductory Raman Spectroscopy* (1994). doi:10.1016/c2009-0-21238-4.

115. Eaton-Magaña, S. & Breeding, C. M. An introduction to photoluminescence spectroscopy for diamond and its applications in gemology. *Gems Gemol.* **52**, 2–17 (2016).

116. Scofield, J. H. Ac Method for Measuring Low-Frequency Resistance Fluctuation Spectra. *Rev. Sci. Instrum.* **58**, 985–993 (1987).

117. Clifford, J. P. *et al.* Fast, sensitive and spectrally tuneable colloidal-quantum-dot photodetectors. *Nat. Nanotechnol.* **4**, 40–44 (2009).

118. Yao, J. & Yang, G. 2D material broadband photodetectors. *Nanoscale* **12**, 454–476 (2020).

119. Tan, C. L. & Mohseni, H. Emerging technologies for high performance infrared detectors. *Nanophotonics* **7**, 169–197 (2018).

120. Xie, C., Mak, C., Tao, X. & Yan, F. Photodetectors Based on Two-Dimensional Layered Materials Beyond Graphene. *Adv. Funct. Mater.* **27**, 1603886 (2017).

121. Yin, Z. *et al.* Single-layer MoS 2 phototransistors. *ACS Nano* **6**, 74–80 (2012).

122. Sundaram, R. S. *et al.* Electroluminescence in Single Layer MoS 2. *Nano Lett.* **13**, 1416–1421 (2013).

123. Guo, K. *et al.* High-performance flexible inverted organic light-emitting diodes by exploiting MoS2 nanopillar arrays as electron-injecting and light-coupling layers. *Nanoscale* **9**, 14602–14611 (2017).

124. Splendiani, A. *et al.* Emerging photoluminescence in monolayer MoS 2. *Nano Lett.* **10**, 1271–1275 (2010).

125. Ghatak, S., Pal, A. N. & Ghosh, A. Nature of electronic states in atomically thin MoS2 field-effect transistors. *ACS Nano* **5**, 7707–7712 (2011).

126. Zhang, W. *et al.* High-gain phototransistors based on a CVD MoS2 monolayer. *Advanced Materials* vol. 25 3456–3461 (2013).

127. Koppens, F. H. L. *et al.* Photodetectors based on graphene, other two-dimensional materials and hybrid systems. *Nat. Nanotechnol.* **9**, 780–793 (2014).

128. Liu, K., Sakurai, M. & Aono, M. ZnO-based ultraviolet photodetectors. *Sensors* **10**, 8604–8634 (2010).

129. Velazquez, R., Aldalbahi, A., Rivera, M. & Feng, P. Fabrications and application of single crystalline GaN for high-performance deep UV photodetectors. *AIP Adv.* **6**, (2016).

130. Das, K., Mukherjee, S., Manna, S., Ray, S. K. & Raychaudhuri, A. K. Single Si nanowire (diameter ≤ 100 nm) based polarization sensitive near-infrared photodetector with ultra-

high responsivity. *Nanoscale* **6**, 11232–11239 (2014).

131. Ray, S. K., Katiyar, A. K. & Raychaudhuri, A. K. One-dimensional Si/Ge nanowires and their heterostructures for multifunctional applications - A review. *Nanotechnology* **28**, (2017).

132. Zhou, H., Maize, K., Qiu, G., Shakouri, A. & Ye, P. D. β-Ga2O3 on insulator field-effect transistors with drain currents exceeding 1.5 A/mm and their self-heating effect. *Appl. Phys. Lett.* **111**, (2017).

133. Radisavljevic, B., Radenovic, A., Brivio, J., Giacometti, V. & Kis, A. Single-layer MoS2 transistors. *Nat. Nanotechnol.* **6**, 147–150 (2011).

134. Morozov, S. V. *et al.* Giant intrinsic carrier mobilities in graphene and its bilayer. *Phys. Rev. Lett.* **100**, 11–14 (2008).

135. Bonaccorso, F., Sun, Z., Hasan, T. & Ferrari, A. C. Graphene photonics and optoelectronics. *Nat. Photonics* **4**, 611–622 (2010).

136. Fang, Z. *et al.* Plasmon-induced doping of graphene. *ACS Nano* **6**, 10222–10228 (2012).

137. Furchi, M. *et al.* Microcavity-integrated graphene photodetector. *Nano Lett.* **12**, 2773–2777 (2012).

138. Konstantatos, G. *et al.* Hybrid grapheneĝquantum dot phototransistors with ultrahigh gain. *Nat. Nanotechnol.* **7**, 363–368 (2012).

139. Gong, M. *et al.* All-Printable ZnO Quantum Dots/Graphene van der Waals Heterostructures for Ultrasensitive Detection of Ultraviolet Light. *ACS Nano* **11**, 4114–4123 (2017).

140. Sun, Z. *et al.* Infrared Photodetectors Based on CVD-Grown Graphene and PbS Quantum Dots with Ultrahigh Responsivity. 1–6 (2012) doi:10.1002/adma.201202220.

141. Spirito, D. *et al.* UV Light Detection from CdS Nanocrystal Sensitized Graphene Photodetectors at kHz Frequencies. (2015) doi:10.1021/acs.jpcc.5b07895.

142. Pradhan, B. *et al.* Ultrasensitive and ultrathin phototransistors and photonic synapses using perovskite quantum dots grown from graphene lattice. *Sci. Adv.* **6**, 1–12 (2020).

143. Eda, G. *et al.* Photoluminescence from Chemically Exfoliated MoS 2. 5111–5116 (2011) doi:10.1021/nl201874w.

144. Ghorai, A., Bayan, S., Gogurla, N., Midya, A. & Ray, S. K. Highly Luminescent WS 2 Quantum Dots/ZnO Heterojunctions for Light Emitting Devices. (2017) doi:10.1021/acsami.6b12859.

145. Ghorai, A., Midya, A., Maiti, R. & Ray, S. K. Exfoliation of WS2 in the semiconducting phase using a group of lithium halides: A new method of Li intercalation. *Dalt. Trans.* **45**, 14979–14987 (2016).

146. Nanocomposites, L. W. S. *et al.* Superior Field Emission Properties of Layered WS2-RGO Nanocomposites Chandra. *Sci. Rep.* 1–8 (2013) doi:10.1038/srep03282.

147. Yin, W. *et al.* Rational Control of Size and Photoluminescence of WS 2 Quantum Dots for White Light-Emitting Diodes. (2018) doi:10.1021/acsami.8b17966.

148. Thin, A. Evolution of Electronic Structure in. 791–797 (2013) doi:10.1021/nn305275h.

149. Anupama, S. & Kaul, B. As featured in : enhancement in environmentally-friendly solution. *J. Mater. Chem. C* **5**, 5323–5333 (2017).

150. Carvalho, A., Ribeiro, R. M. & Neto, A. H. C. Band nesting and the optical response of two-dimensional semiconducting transition metal dichalcogenides. **115205**, 1–6 (2013).

151. Wang, L. *et al.* hot carriers in MoS 2 monolayer. (2017) doi:10.1038/ncomms13906.

152. McCreary, A. *et al.* Distinct photoluminescence and Raman spectroscopy signatures for identifying highly crystalline WS2 monolayers produced by different growth methods. *J. Mater. Res.* **31**, 931–944 (2016).

153. Lan, C. *et al.* Zener Tunneling and Photoresponse of a WS2/Si van der Waals Heterojunction. *ACS Appl. Mater. Interfaces* **8**, 18375–18382 (2016).

154. Ferrari, A. C. & Basko, D. M. studying the properties of graphene. *Nat. Publ. Gr.* **8**, 235–246 (2013).

155. Alamri, M., Gong, M., Cook, B., Goul, R. & Wu, J. Z. Plasmonic WS2 Nanodiscs/Graphene van der Waals Heterostructure Photodetectors. *ACS Appl. Mater. Interfaces* **11**, 33390–33398 (2019).

156. Gong, M. *et al.* Broadband Photodetectors Enabled by Localized Surface Plasmonic Resonance in Doped Iron Pyrite Nanocrystals. *Adv. Opt. Mater.* **6**, 1–11 (2018).

157. Luther, J. M., Jain, P. K., Ewers, T. & Alivisatos, A. P. Localized surface plasmon

resonances arising from free carriers in doped quantum dots. *Nat. Mater.* **10**, 361–366 (2011).

158. Notley, S. M. High yield production of photoluminescent tungsten disulphide nanoparticles. *Journal of Colloid and Interface Science* vol. 396 160–164 (2013).

159. Lin, W. *et al.* Electron redistribution and energy transfer in graphene/MoS2 heterostructure. *Appl. Phys. Lett.* **114**, (2019).

160. Kim, S. *et al.* Robust graphene wet transfer process through low molecular weight polymethylmethacrylate. *Carbon N. Y.* **98**, 352–357 (2016).

161. Pal, A. N. *et al.* Microscopic mechanism of 1/f noise in graphene: Role of energy band dispersion. *ACS Nano* **5**, 2075–2081 (2011).

162. Gao, S. *et al.* Graphene / MoS 2 / Graphene Vertical Heterostructure-Based Broadband Photodetector with High Performance. *Adv. Mater. Interfaces* **2001730**, 1–6 (2020).

163. Liu, X. *et al.* Epitaxial Ultrathin Organic Crystals on Graphene for High- Effi ciency Phototransistors. 5200–5205 (2016) doi:10.1002/adma.201600400.

164. Ahmad, S. *et al.* Strong Photocurrent from Two-Dimensional Excitons in Solution-Processed Stacked Perovskite Semiconductor Sheets. *ACS Appl. Mater. Interfaces* **7**, 25227–25236 (2015).

165. Lan, C., Li, C., Yin, Y. & Liu, Y. Correction: Large-area synthesis of monolayer WS2 and its ambient-sensitive photo-detecting performance. **4**, 610054 (2015).

166. Mueller, T., Xia, F. & Avouris, P. Graphene photodetectors for high-speed optical communications. *Nat. Photonics* **4**, 297–301 (2010).

167. Xu, H., Wu, J., Feng, Q., Mao, N. & Wang, C. High Responsivity and Gate Tunable Graphene-MoS 2 Hybrid Phototransistor. 1–7 (2014) doi:10.1002/smll.201303670.

168. Chen, T. *et al.* High Photoresponsivity in Ultrathin 2D Lateral Graphene:WS 2 :Graphene Photodetectors Using Direct CVD Growth. *ACS Appl. Mater. Interfaces* (2019) doi:10.1021/acsami.8b20321.

169. Phys, A. Enhancing photoresponsivity using MoTe 2 - graphene vertical heterostructures. **063506**, (2016).

170. Xiao, R. *et al.* High Performance Van der Waals Graphene – WS 2 – Si Heterostructure

Photodetector. **1901304**, 1–7 (2019).

171. Xu, J., Song, Y. J., Park, J. H. & Lee, S. Graphene/black phosphorus heterostructured photodetector. *Solid. State. Electron.* **144**, 86–89 (2018).

172. García De Arquer, F. P., Armin, A., Meredith, P. & Sargent, E. H. Solution-processed semiconductors for next-generation photodetectors. *Nat. Rev. Mater.* **2**, 1–16 (2017).

173. Maiti, R. *et al.* Strain-engineered high-responsivity MoTe2 photodetector for silicon photonic integrated circuits. *Nat. Photonics* **14**, 578–584 (2020).

174. De Fazio, D. *et al.* High Responsivity, Large-Area Graphene/MoS2 Flexible Photodetectors. *ACS Nano* **10**, 8252–8262 (2016).

175. Nan Guo,* Lin Xiao, Fan Gong, Man Luo, Fang Wang, Yi Jia, H. C. & Junku Liu, Qing Li, Yang Wu, Yang Wang, Chongxin Shan, Yang Xu, Peng Zhou, and W. H. Light-Driven WSe2-ZnO Junction Field-Effect Transistors for High-Performance Photodetection_advsci2020.pdf. 1901637 (2020) doi:10.1002/advs.201901637.

176. Mukherjee, S. *et al.* High-Responsivity Gate-Tunable Ultraviolet–Visible Broadband Phototransistor Based on Graphene–WS 2 Mixed-Dimensional (2D-0D) Heterostructure . *ACS Appl. Mater. Interfaces* (2022) doi:10.1021/acsami.1c18999.

177. Rao, C. N. R., Sood, A. K., Subrahmanyam, K. S. & Govindaraj, A. Graphene: The new two-dimensional nanomaterial. *Angew. Chemie - Int. Ed.* **48**, 7752–7777 (2009).

178. Riazimehr, S. *et al.* High Responsivity and Quantum Efficiency of Graphene/Silicon Photodiodes Achieved by Interdigitating Schottky and Gated Regions. *ACS Photonics* **6**, 107–115 (2019).

179. Guo, W. *et al.* Oxygen-assisted charge transfer between ZnO quantum dots and graphene. *Small* **9**, 3031–3036 (2013).

180. Nie, B. *et al.* Monolayer graphene film on zno nanorod array for high-performance schottky junction ultraviolet photodetectors. *Small* **9**, 2872–2879 (2013).

181. Zhou, W. *et al.* Intrinsic structural defects in monolayer molybdenum disulfide. *Nano Lett.* **13**, 2615–2622 (2013).

182. Huang, B., Yoon, M., Sumpter, B. G., Wei, S. H. & Liu, F. Alloy Engineering of Defect Properties in Semiconductors: Suppression of Deep Levels in Transition-Metal

Dichalcogenides. *Phys. Rev. Lett.* **115**, 1–5 (2015).

183. Komsa, H. & Krasheninnikov, A. V. Two-Dimensional Transition Metal Dichalcogenide Alloys: Stability and Electronic Properties. *J. Phys. Chem. Lett.* **3**, 3652−3656 (2012).

184. Lim, Y. R. *et al.* Atomic-Level Customization of 4 in. Transition Metal Dichalcogenide Multilayer Alloys for Industrial Applications. *Adv. Mater.* **31**, 1–14 (2019).

185. Sahoo, A., Reiss, P., Quesnel, E. & Hyot, B. Optical modulation frequency mediated tunable response time and responsivity in graphene-PbS QD based hybrid photodetectors. *Nanotechnology* **32**, 405205 (2021).

186. Tan, C. *et al.* Preparation of Single-Layer MoS2xSe2(1-x) and MoxW1-xS2 Nanosheets with High-Concentration Metallic 1T Phase. *Small* **12**, 1866–1874 (2016).

187. Qingliang Feng, Nannan Mao, JuanxiaWu, Hua Xu, ChunmingWang, Jin Zhang*, and L. X. Controlled Morphology by Physical Vapor Deposition. *ACS Nano* **9**, 7450–7455 ’ (2015).

188. Lee, H. I., Yu, H., Rhee, C. K. & Sohn, Y. Electrochemical hydrogen evolution and CO2 reduction over hierarchical MoSxSe2-x hybrid nanostructures. *Appl. Surf. Sci.* **489**, 976–982 (2019).

189. He, H. *et al.* Anion Vacancies Regulating Endows MoSSe with Fast and Stable Potassium Ion Storage. *ACS Nano* **13**, 11843–11852 (2019).

190. Gong, Q. *et al.* Ultrathin MoS2(1-x)Se2x Alloy Nanoflakes for Electrocatalytic Hydrogen Evolution Reaction. *ACS Catal.* **5**, 2213–2219 (2015).

191. Kiran, V., Mukherjee, D., Jenjeti, R. N. & Sampath, S. Active guests in the MoS2/MoSe2 host lattice: Efficient hydrogen evolution using few-layer alloys of MoS2(1-x)Se2x. *Nanoscale* **6**, 12856–12863 (2014).

192. Li, H. *et al.* Lateral growth of composition graded atomic layer MoS2(1-x)Se2x nanosheets. *J. Am. Chem. Soc.* **137**, 5284–5287 (2015).

193. Zhang, W. *et al.* CVD synthesis of Mo(1-x)WxS2 and MoS2(1-x)Se2x alloy monolayers aimed at tuning the bandgap of molybdenum disulfide. *Nanoscale* **7**, 13554–13560 (2015).

194. Islam, S. *et al.* Ultra-sensitive graphene-bismuth telluride nano-wire hybrids for infrared detection. *Nanoscale* **11**, 1579–1586 (2019).

195. Qiao, H. *et al.* Broadband photodetectors based on graphene-Bi2Te3heterostructure. *ACS Nano* **9**, 1886–1894 (2015).

196. Wu, C. Y. *et al.* Graphene-Assisted Growth of Patterned Perovskite Films for Sensitive Light Detector and Optical Image Sensor Application. *Small* **15**, 1–9 (2019).

197. Lan, C. *et al.* Highly responsive and broadband photodetectors based on WS2-graphene van der Waals epitaxial heterostructures. *J. Mater. Chem. C* **5**, 1494–1500 (2017).

198. Dang, V. Q. *et al.* High-Performance Flexible Ultraviolet (UV) Phototransistor Using Hybrid Channel of Vertical ZnO Nanorods and Graphene. *ACS Appl. Mater. Interfaces* **7**, 11032–11040 (2015).

199. Lee, Y. *et al.* High-performance perovskite-graphene hybrid photodetector. *Adv. Mater.* **27**, 41–46 (2015).

200. Xu, Y. *et al.* Solvent-Based Soft-Patterning of Graphene Lateral Heterostructures for Broadband High-Speed Metal–Semiconductor–Metal Photodetectors. *Adv. Mater. Technol.* **2**, 1–8 (2017).

201. Balandin, A. A. Low-frequency 1/f noise in graphene devices. *Nat. Nanotechnol.* **8**, 549–555 (2013).

202. Rajbanshi, B., Sarkar, S. & Sarkar, P. The electronic and optical properties of MoS2(1-x)Se2x and MoS2(1-x)Te2x monolayers. *Phys. Chem. Chem. Phys.* **17**, 26166–26174 (2015).

203. Li, X. *et al.* Suppression of Defects and Deep Levels Using Isoelectronic Tungsten Substitution in Monolayer MoSe2. *Adv. Funct. Mater.* **27**, 1603850 (2017).

204. Zhou, G., Li, Z., Ge, Y., Zhang, H. & Sun, Z. A self-encapsulated broadband phototransistor based on a hybrid of graphene and black phosphorus nanosheets. *Nanoscale Adv.* **2**, 1059–1065 (2020).

205. Goyal, N., Kaushik, N., Jawa, H. & Lodha, S. Enhanced stability and performance of few-layer black phosphorus transistors by electron beam irradiation. *Nanoscale* **10**, 11616–11623 (2018).

206. Sun, Z., Aigouy, L. & Chen, Z. Plasmonic-enhanced perovskite-graphene hybrid photodetectors. *Nanoscale* **8**, 7377–7383 (2016).

207. Liu, Y. *et al.* Van der Waals heterostructures and devices. *Nat. Rev. Mater.* **1**, (2016).

208. Mak, K. F. & Shan, J. Photonics and optoelectronics of 2D semiconductor transition metal dichalcogenides. *Nat. Photonics* **10**, 216–226 (2016).

209. Chuancheng Jia , Xinxi Li , Na Xin , Yao Gong , Jianxin Guan , Linan Meng , Sheng Meng, and X. G. Interface-Engineered Plasmonics in Metal Semiconductor Heterostructures _ aem 2021.pdf. 1600431 (2016) doi:10.1002/aenm.201600431.

210. Lee, H. S. *et al.* Selective Amplification of the Primary Exciton in a Mo S2 Monolayer. *Phys. Rev. Lett.* **115**, 2–6 (2015).

211. Zhao, W. *et al.* Exciton-Plasmon Coupling and Electromagnetically Induced Transparency in Monolayer Semiconductors Hybridized with Ag Nanoparticles. *Adv. Mater.* **28**, 2709–2715 (2016).

212. Bang, S. *et al.* Augmented Quantum Yield of a 2D Monolayer Photodetector by Surface Plasmon Coupling. *Nano Lett.* **18**, 2316–2323 (2018).

213. Giannini, V., Fernández-Domínguez, A. I., Heck, S. C. & Maier, S. A. Plasmonic nanoantennas: Fundamentals and their use in controlling the radiative properties of nanoemitters. *Chem. Rev.* **111**, 3888–3912 (2011).

214. Feng, F. *et al.* Plasmonic and Graphene-Functionalized High-Performance Broadband Quasi-Two-Dimensional Perovskite Hybrid Photodetectors. *ACS Appl. Mater. Interfaces* **13**, 61496–61505 (2021).

215. Sun, Z., Aigouy, L. & Chen, Z. Plasmonic-enhanced perovskite-graphene hybrid photodetectors. *Nanoscale* **8**, 7377–7383 (2016).

216. Lee, Y. H. *et al.* Flexible high-performance graphene hybrid photodetectors functionalized with gold nanostars and perovskites. *NPG Asia Mater.* **12**, 1–12 (2020).

217. Zheng, D. *et al.* Manipulating coherent plasmon-exciton interaction in a single silver nanorod on monolayer WSe2. *Nano Lett.* **17**, 3809–3814 (2017).

218. Soni, B. & Biswas, S. Stability of microstructure at high temperatures in silver nanoparticles coated with an in situ grown thin graphitic carbon layer. *J. Alloys Compd.*

779, 784–793 (2019).

219. Goudarzi, M., Mir, N., Mousavi-Kamazani, M., Bagheri, S. & Salavati-Niasari, M. Biosynthesis and characterization of silver nanoparticles prepared from two novel natural precursors by facile thermal decomposition methods. *Sci. Rep.* **6**, 1–13 (2016).

220. Fedutik, Y., Temnov, V. V., Schöps, O., Woggon, U. & Artemyev, M. V. Exciton-plasmon-photon conversion in plasmonic nanostructures. *Phys. Rev. Lett.* **99**, 1–4 (2007).

221. Chowdhury, R. K., Sinha, T. K., Katiyar, A. K. & Ray, S. K. Synergistic effect of polymer encapsulated silver nanoparticle doped WS2 sheets for plasmon enhanced 2D/3D heterojunction photodetectors. *Nanoscale* **9**, 15591–15597 (2017).

222. Backes, C. *et al.* Edge and confinement effects allow in situ measurement of size and thickness of liquid-exfoliated nanosheets. *Nat. Commun.* **5**, 1–10 (2014).

223. Merkl, P. *et al.* Plasmonic Coupling in Silver Nanoparticle Aggregates and Their Polymer Composite Films for near -Infrared Photothermal Biofilm Eradication. *ACS Appl. Nano Mater.* **4**, 5330–5339 (2021).

224. Alamri, M. *et al.* Graphene/WS2Nanodisk Van der Waals Heterostructures on Plasmonic Ag Nanoparticle-Embedded Silica Metafilms for High-Performance Photodetectors. *ACS Appl. Nano Mater.* **3**, 7858–7868 (2020).

225. Gutiérrez, H. R. *et al.* Extraordinary room-temperature photoluminescence in triangular WS 2 monolayers. *Nano Lett.* **13**, 3447–3454 (2013).

226. Zhang, D. *et al.* Surface enhanced Raman scattering of monolayer MX2 with metallic nano particles. *Sci. Rep.* **6**, 1–8 (2016).

227. Sun, Y. *et al.* Evolution of local strain in Ag-deposited monolayer MoS2 modulated by interface interactions. *Nanoscale* **11**, 22432–22439 (2019).

228. Bong Gyu Shin,* Gang Hee Han, Seok Joon Yun, Hye Min Oh, Jung Jun Bae, Young Jae Song, Chong-Yun Park, and Y. H. L. Indirect Bandgap Puddles in Monolayer MoS2 by Substrate-Induced Local Strain adv mat 2016.pdf. 9378–9384 (2016) doi:10.1002/adma.201602626.

229. Shi, Y. *et al.* Hot Electron of Au Nanorods Activates the Electrocatalysis of Hydrogen

Evolution on MoS2 Nanosheets. *J. Am. Chem. Soc.* **137**, 7365–7370 (2015).

230. Cheng, F. *et al.* Enhanced Photoluminescence of Monolayer WS2 on Ag Films and Nanowire-WS2-Film Composites. *ACS Photonics* **4**, 1421–1430 (2017).

231. Zhang, C., Wang, H., Chan, W., Manolatou, C. & Rana, F. Absorption of light by excitons and trions in monolayers of metal dichalcogenide Mo S2: Experiments and theory. *Phys. Rev. B - Condens. Matter Mater. Phys.* **89**, 12–16 (2014).

232. Lee, H. S., Kim, M. S., Kim, H. & Lee, Y. H. Identifying multiexcitons in Mo S2 monolayers at room temperature. *Phys. Rev. B* **93**, 1–6 (2016).

233. Fan, X. *et al.* Nonlinear photoluminescence in monolayer WS2: Parabolic emission and excitation fluence-dependent recombination dynamics. *Nanoscale* **9**, 7235–7241 (2017).

234. Bhanu, U., Islam, M. R., Tetard, L. & Khondaker, S. I. Photoluminescence quenching in gold-MoS 2 hybrid nanoflakes. *Sci. Rep.* **4**, 1–5 (2014).

235. Giugni, A. *et al.* Hot-electron nanoscopy using adiabatic compression of surface plasmons. *Nat. Nanotechnol.* **8**, 845–852 (2013).

236. Halas, N. J., Lal, S., Chang, W. S., Link, S. & Nordlander, P. Plasmons in strongly coupled metallic nanostructures. *Chem. Rev.* **111**, 3913–3961 (2011).

237. Manjavacas, A., Abajo, F. J. G. De & Nordlander, P. Quantum plexcitonics: Strongly interacting plasmons and excitons. *Nano Lett.* **11**, 2318–2323 (2011).

238. Savasta, S. *et al.* Nanopolaritons: Vacuum rabi splitting with a single quantum dot in the center of a dimer nanoantenna. *ACS Nano* **4**, 6369–6376 (2010).

239. Mukherjee, S., Bhattacharya, D., Ray, S. K. & Pal, A. N. High-Performance Broad-Band Photodetection Based on Graphene−MoS2xSe2(1−x) Alloy Engineered Phototransistors. *ACS Appl. Mater. Interfaces* **2**, 34875−34883 (2022).

240. Liu, B. *et al.* Using Silver Nanoparticles-Embedded Silica Metafilms as Substrates to Enhance the Performance of Perovskite Photodetectors. *ACS Appl. Mater. Interfaces* **11**, 32301–32309 (2019).

241. Paria, D. *et al.* Graphene-silver hybrid devices for sensitive photodetection in the ultraviolet. *Nanoscale* **10**, 7685–7693 (2018).

242. Deshpande, P. *et al.* Investigating photoresponsivity of graphene-silver hybrid

nanomaterials in the ultraviolet. *J. Chem. Phys.* **152**, (2020).

243. Mukherjee, S. *et al.* Plasmon Triggered, Enhanced Light-Matter Interactions in Au-MoS2Coupled System with Superior Photosensitivity. *J. Phys. Chem. C* **125**, 11023–11034 (2021).